

---

# X-ray and Optical observations of Globular Clusters and Pulsars

Hsiu-Hui Huang

---



München 2010



---

# **X-ray and Optical observations of Globular Clusters and Pulsars**

**Hsiu-Hui Huang**

---

Dissertation  
an der Fakultät für Physik  
der Ludwig–Maximilians–Universität  
München

vorgelegt von  
Hsiu-Hui Huang  
aus Taiwan

München, den 22 April 2010

Erstgutachter: Prof. Dr. Werner Becker

Zweitgutachter: PD Dr. Markus Kissler-Patig

Tag der mündlichen Prüfung: 10 June 2010

# Contents

<b>Summary</b>	<b>xiii</b>
<b>1 Introduction I – Globular Clusters</b>	<b>1</b>
1.1 Properties . . . . .	2
1.2 Structural and Dynamical Properties . . . . .	2
1.3 Binary Systems . . . . .	8
<b>2 Introduction II – Neutron Stars and Pulsars</b>	<b>19</b>
2.1 A brief History of Neutron Stars . . . . .	19
2.2 Physics and Astrophysics of Neutron Stars . . . . .	20
2.2.1 Rotation-powered Pulsars: the Magnetic Braking Model . . . . .	21
2.2.2 High-energy Emission Models . . . . .	22
2.2.3 Rotation-powered Millisecond Pulsars . . . . .	30
<b>3 Observatories &amp; Telescopes</b>	<b>33</b>
3.1 X-ray Observatories . . . . .	33
3.1.1 Chandra X-ray Observatory . . . . .	33
3.1.2 XMM-Newton X-ray Observatory . . . . .	37
3.2 The Hubble Space Telescope . . . . .	40
<b>4 XMM-Newton Observations of PSR B1957+20</b>	<b>45</b>
4.1 Abstract . . . . .	45
4.2 Introduction . . . . .	45
4.3 Observations and Data Analysis . . . . .	48
4.3.1 Spatial Analysis . . . . .	48
4.3.2 Spectral Analysis . . . . .	48
4.3.3 Timing Analysis . . . . .	51
4.4 Summary and Discussion . . . . .	53
<b>5 X-rays from the Eclipsing Millisecond Pulsar PSR J1740–5340 in NGC 6397</b>	<b>57</b>
5.1 Abstract . . . . .	57
5.2 Introduction . . . . .	57
5.3 Observations and Data Analysis . . . . .	59

5.3.1	Search for Orbital Modulation . . . . .	59
5.3.2	Spectral Analysis . . . . .	61
5.4	Summary and Discussion . . . . .	63
<b>6</b>	<b>X-ray counterparts of millisecond pulsars in Globular Clusters</b>	<b>67</b>
6.1	Abstract . . . . .	67
6.2	Introduction . . . . .	68
6.3	Observation and Data Reduction . . . . .	70
6.3.1	Source Detection and Identification . . . . .	71
6.3.2	Search for Temporal Variability . . . . .	72
6.3.3	Spectral Analysis . . . . .	83
6.4	Discussion . . . . .	86
<b>7</b>	<b>Chandra X-ray Observatory Observations of the Globular Cluster M71</b>	<b>101</b>
7.1	Abstract . . . . .	101
7.2	Introduction . . . . .	101
7.3	Observations, Data Reprocessing, and Source Detection . . . . .	103
7.4	Distributions . . . . .	111
7.5	Power-law Spectral Fits . . . . .	115
7.6	X-ray Color–Color Diagram . . . . .	119
7.7	Searches for Counterparts . . . . .	119
7.7.1	2MASS, USNO, & TYCHO-2 Catalogs . . . . .	119
7.7.2	HST data . . . . .	121
7.7.3	Variable Sources . . . . .	122
7.7.4	X-ray Catalogs . . . . .	122
7.7.5	The Milli-second Pulsar . . . . .	122
7.8	Individual Sources . . . . .	125
7.9	Discussion . . . . .	127
<b>8</b>	<b>Study of HST counterparts to Chandra X-ray sources in M71</b>	<b>131</b>
8.1	Abstract . . . . .	131
8.2	Introduction . . . . .	131
8.3	X-ray Observations . . . . .	133
8.4	Optical Observations . . . . .	134
8.4.1	Data Reduction and Photometry . . . . .	135
8.4.2	Astrometry . . . . .	137
8.5	Source Identification and Classification . . . . .	139
8.6	Summary and Discussion . . . . .	145
<b>9</b>	<b>Conclusion and Future Prospect</b>	<b>151</b>
9.1	Eclipsing Binary Pulsars . . . . .	151
9.2	Millisecond Pulsars in Galactic Globular Clusters . . . . .	155
9.3	Globular Clusters . . . . .	157

9.4 Future Prospects . . . . .	158
<b>Bibliography</b>	<b>161</b>
<b>Acknowledgements</b>	<b>173</b>
<b>Curriculum Vitae</b>	<b>174</b>



# List of Figures

1.1	Schematic color-magnitude diagram of a typical globular cluster . . . . .	3
1.2	The evolution of a globular cluster . . . . .	4
1.3	The various types of objects suggested as X-ray sources in globular clusters . . .	10
1.4	An artists impression of the flow of material onto a compact object. . . . .	12
1.5	Diagram of a Polar . . . . .	14
1.6	Diagram of an Intermediate Polar . . . . .	15
2.1	Diagram of the magnetic dipole model of a pulsar . . . . .	25
2.2	The $P - \dot{P}$ diagram . . . . .	31
3.1	Illustration of the Chandra X-ray Observatory . . . . .	34
3.2	Chandra's X-ray mirror assembly . . . . .	35
3.3	Sketch of the XMM-Newton payload . . . . .	38
3.4	The Hubble Space Telescope and its instruments . . . . .	40
4.1	A composite X-ray and optical image of the black widow pulsar . . . . .	47
4.2	XMM-Newton MOS1/2 image of the PSR B1957+20 . . . . .	49
4.3	Energy spectrum of PSR B1957+20 . . . . .	50
4.4	X-ray orbital light curve of PSR B1957+20 . . . . .	52
4.5	The EPIC-PN count rate of PSR B1957+20 vs. the orbital phase . . . . .	54
5.1	Orbital phase coverages of Chandra observations targeted on PSR J1740–5340. .	60
5.2	X-ray orbital light curve of PSR J1740–5340 . . . . .	62
5.3	The cumulative distribution function from the observed data of PSR J1740–5340	64
5.4	ACIS-S3 count rates of PSR J1740–5340 vs. observation dates . . . . .	64
6.1	A histogram of radio and X-ray detected MSPs in globular clusters . . . . .	69
6.2	Chandra ACIS-S view on the globular clusters Terzan 5 and 47 Tucanae . . . . .	73
6.3	Chandra images of M28 and M15 . . . . .	74
6.4	Chandra ACIS-S view on the globular clusters NGC 6440 and M62 . . . . .	75
6.5	Chandra ACIS-S view on the globular clusters NGC 6752 . . . . .	76
6.6	Chandra ACIS-S view on the globular clusters M3 and M5 . . . . .	77
6.7	Chandra images of M13 and NGC 6441 . . . . .	78
6.8	Chandra ACIS-S view on the globular clusters M30 and NGC 6544 . . . . .	79

6.9	Chandra ACIS-S view on the globular clusters M4 and M71 . . . . .	80
6.10	Chandra ACIS-S view on the globular clusters NGC 6397 . . . . .	81
6.11	Orbital light curves of the pulsars M28G and M28H . . . . .	82
6.12	Energy spectrum of the millisecond pulsar PSR J1824–2452A in M28 . . . . .	85
6.13	Confidence contours showing the blackbody normalization versus temperature . . . . .	87
6.14	The $L_x - \dot{E}$ relations for the GC and field MSPs . . . . .	90
6.15	Cumulative luminosity functions for the GC and field MSPs . . . . .	91
7.1	ACIS-S S3 0.3–8.0 keV image of the globular cluster M71 for $r_{M71} \leq 2r_h$ . . . . .	104
7.2	Number of sources, $N(\leq r_{M71})$ , inside radius $r_{M71}$ (') vs. $r_{M71}$ . . . . .	113
7.3	The M71 log $N$ –log $C_x$ distribution for sources with $r_{M71} \leq 2r_h$ . . . . .	116
7.4	Color-color diagram for sources with $r_{M71} \leq 2r_h$ . . . . .	120
7.5	The 0.3–8.0 keV light curve for PSR J1953+1846A . . . . .	124
7.6	Light curves for the 14 Chandra X-ray sources . . . . .	126
7.7	Number of background-subtracted sources vs. $L_{0.5-2.5keV}$ for 4 GCs . . . . .	129
8.1	Chandra ACIS-S3 image of the globular cluster M71 . . . . .	136
8.2	Color magnitude diagrams of M71 . . . . .	138
8.3	HST/ACS $V_{606}$ finding charts (I) . . . . .	140
8.4	HST/ACS $V_{606}$ finding charts (II) . . . . .	142
8.5	X-ray luminosity $L_x$ as a function of absolute magnitude $M_v$ . . . . .	146
8.6	Number of X-ray sources $N$ vs. the normalized collision number $\Gamma$ . . . . .	149

# List of Tables

3.1	Chandra characteristics . . . . .	36
3.2	XMM-Newton characteristics . . . . .	38
3.3	Basic imaging parameters of NICMOS instrument on board HST . . . . .	41
4.1	Photon arrival times and its corresponding orbital phase of PSR B1957+20 . . . . .	53
5.1	List of Chandra observations of PSR J1740–5340 in NGC 6397 . . . . .	59
5.2	Significance for intra-orbital flux modulation . . . . .	61
5.3	Spectral fits to the PSR J1740 – 5340 binary system . . . . .	65
6.1	Chandra observations of globular clusters . . . . .	92
6.1	Continued . . . . .	93
6.2	Characteristics of the X-ray counterparts of 31 GC pulsars . . . . .	94
6.3	Properties of globular clusters which are known to host pulsars . . . . .	95
6.4	Properties of X-ray detected GC pulsars . . . . .	96
6.5	Counting rate upper limits for X-ray emission from GC pulsars . . . . .	97
6.6	Properties of X-ray non-detected GC pulsars . . . . .	98
6.7	Spectral parameters and X-ray luminosities of GC pulsars . . . . .	99
6.7	Continued . . . . .	100
7.1	CXO X-ray sources detected with $r_{M71} \leq 2r_h$ . . . . .	106
7.1	Continued . . . . .	107
7.2	CXO X-ray sources detected with $2r_h \leq r_{M71}$ . . . . .	108
7.2	Continued . . . . .	109
7.2	Continued . . . . .	110
7.3	Best-fit King model parameters. . . . .	112
7.4	Predicted No. of S3 sources inside radius $r_{M71}$ ('). . . . .	114
7.5	Power-law spectral fits for selected X-ray sources. . . . .	117
7.6	X-ray sources within 30'' of a CXO source. . . . .	123
7.7	MEKAL and MEKAL+MEKAL spectral fits. . . . .	127
7.8	Background-subtracted source numbers for selected globular clusters. . . . .	128
8.1	Spectral fits of the X-ray source . . . . .	134
8.2	HST Optical Counterparts to Chandra X-ray Sources in M71 . . . . .	141

8.3 Scaling parameters of some globular clusters . . . . . 148

9.1 Eclipsing binary pulsars in globular clusters and in the Galactic disk . . . . . 153

# Summary

Utilizing the state-of-art X-ray observatories – Chandra and XMM-Newton, and the optical Hubble Space Telescope, I have accomplished several research projects which covered a wide range of topics on studying the high-energy emission from binary pulsar systems in the field and in globular clusters and their environment, as well as studies of the globular cluster M71. In the following description, I would like to give the highlights of the research that I have done.

## **X-ray studies of millisecond pulsars in binary systems**

Eclipsing binary pulsars have the potential of providing a wealth of information on both the evolutionary history of isolated millisecond pulsars and the relativistic winds and pulse emission mechanisms in these systems. I report on X-ray observations of two eclipsing millisecond pulsars in binary systems, PSR B1957+20 and PSR J1740–5340.

A  $\sim 30$ -kilosecond XMM-Newton observation of the “Black Widow pulsar”, PSR B1957+20, was conducted in my study. Through the spectral analysis, the pulsar’s X-ray emission was found to be non-thermal and best modeled with a single power-law spectrum, suggesting that the observed X-rays from PSR B1957+20 originate from the interaction of the relativistic pulsar wind with the interstellar medium or with the ablated material from the companion star. Its diffuse X-ray emission with the orientation to the north-east and a size of about 16 arcsec was detected with the MOS1/2 cameras, which is consistent with previous results derived from Chandra observations. No coherent X-ray pulsations at the pulsar’s spin-period were reported. Furthermore, I investigated if the pulsar’s X-ray emission is a function of its orbital phase by examining how significant the orbital light curve differs from a constant level. No variation during  $\sim 90\%$  of one binary orbit was indicated. The limited photon statistics and the incomplete orbital coverage prevented us from doing any orbital-phase resolved imaging and spectral analysis and searching for a fully-covered orbital modulation.

The millisecond pulsar, PSR J1740–5340, in the globular cluster NGC 6397 has its radio emission eclipsed for  $\sim 40\%$  of its orbit which suggests the pulsar is orbiting within an extended envelope of matter released from the companion. It has long been speculated that the X-ray emission of this binary system should also vary across the orbital phase. In this study, I searched for this possible orbital modulation of the X-ray emission. Utilizing five archival Chandra observations of PSR J1740–5340, I performed a systematic analysis of this binary system. A marginal temporal variability for the whole orbit of the binary system was detected. The possible origin of the X-ray flux is discussed in three different scenarios, namely: 1) the coronal emission from

the companion star, 2) from the magnetosphere of the pulsar, and 3) from the intrabinary shock. Based on the present data, it is not possible to firmly distinguish three different possible contributions of X-ray emission of the binary system of PSR J1740–5340. However, I stress that the shape of the light curve as well as the orbital phase-resolved spectroscopy are the important tools to constrain the nature of the system. Further studies are required to place tighter constraints on its emission properties.

## **X-ray counterparts of millisecond pulsars in globular clusters**

We have conducted a systematic census of the X-ray population of rotation-powered pulsars in globular clusters by using the imaging data obtained with the Chandra X-ray observatory. So far  $\sim 140$  radio pulsars have been detected in globular clusters. Among them, only  $\sim 20\%$  have been identified with X-ray counterparts. Therefore, our current understanding of the high-energy emission nature of the cluster pulsars is seriously biased. By cross-correlating the radio timing positions of the cluster pulsars with the high resolution X-ray images, thirty-one possible X-ray counterparts have been identified in nine different globular cluster systems, including the 47 Tuc population. These include the newly identified X-ray counterparts of PSR J1824–2452G and PSR J1824–2452H in M28 and PSR J1748–2021B in NGC 6440. We have also characterized their spectral properties as well as searched for the possible temporal variability. In order to compare with the pulsar population in the Galactic field, we have re-examined the relation between the X-ray luminosity and the spin-down power of pulsar population in globular clusters by using the enlarged sample reported in this work and found their X-ray conversion efficiency spans a wide range, which is not consistent with the linear  $L_X - \dot{E}$  relation. We have also constructed the cumulative luminosity functions for the millisecond pulsar population in globular clusters as well as in the Galactic field. No significant difference between these two cumulative luminosity functions was found in our study. Therefore, we cannot conclude the discrepancy between the globular cluster pulsar population and the Galactic millisecond pulsars in terms of the current knowledge of their X-ray conversion efficiency and luminosity functions.

## **Study of the globular cluster M71 in the X-ray and optical band**

Globular clusters provide us with a unique laboratory to investigate various aspects of astrophysics. Due to the high stellar densities, globular clusters have high efficiency for producing tight binary systems. One of the most powerful ways to probe their binary content is by studying the X-ray source populations. We observed the nearby, low-density globular cluster M71 (NGC 6838) with the Chandra X-ray Observatory to study its faint X-ray populations. Five X-ray sources were found inside the cluster core radius ( $r_h = 0.63$ ), including the known eclipsing binary MSP PSR J1953+1846A. The X-ray light curve of the source coincident with this millisecond pulsar shows marginal evidence for periodicity at the binary period of 4.2 h. Its hard X-ray spectrum and luminosity resemble those of other eclipsing binary millisecond pulsars in 47 Tuc, suggesting a similar shock origin of the X-ray emission. A further 24 X-ray sources were found within the half-mass radius ( $r_h = 1.65$ ), reaching to a limiting luminosity of  $1.5 \times 10^{30}$  ergs s $^{-1}$  (0.3–8 keV). From a radial distribution analysis, we found that 18 of these 29

sources are associated with M71, and the other 11 sources are background sources, both galactic and extragalactic. Both of the two estimated numbers have a  $1-\sigma$  uncertainty of 6 sources.

I also report on archival Hubble Space Telescope observations of M71. These observations, covering the core of the globular cluster, were performed by the Advanced Camera for Surveys (ACS) and the Wide Field Planetary Camera 2 (WFPC2). Inside the half-mass radius of M71, I found 33 candidate optical counterparts to 25 out of 29 Chandra X-ray sources, while outside the half-mass radius, 6 possible optical counterparts to 4 X-ray sources were detected. Based on the X-ray and optical properties of the identifications, I found 1 certain and 7 candidate cataclysmic variables (CVs). I also classified 2 X-ray sources as certain and 12 as potential chromospherically active binaries (ABs), respectively. The only star in the error circle of the known millisecond pulsar is inconsistent with being the optical counterpart. The number of X-ray sources with  $L_X > 4 \times 10^{30}$  ergs s<sup>-1</sup> (0.5–6.0 keV) found in M71 is higher than the predicted value extrapolated from other clusters on the basis of either collision frequency or mass. Since the core density of M71 is relatively low, we suggest that those CVs and ABs are primordial in origin. Study of other low-density globular clusters will help us to better understand their evolution and dynamics.



# Chapter 1

## Introduction I – Globular Clusters

Studies of globular clusters have been crucial to making progress in solving a variety of astronomical problems, such as the shape and the size of the galaxy (e.g. Shapley 1918), the age of the universe (e.g. Reid 1997; Krauss & Chaboyer 2003), the behavior of self-gravitating N-body systems (e.g. Spitzer 1987), the initial mass function of stars (e.g. Richer et al. 2002), the metallicity evolution of the universe (e.g. Sneden & Cowan 2003), and the effects of close stellar encounters (e.g. Bailyn & Pinsonneault 1995).

Globular clusters are very old stellar systems which have the typical age of  $\sim 10^{10}$  years and contain  $\sim 10^4 - 10^7$  stars. They are very dense and tightly bound by gravity, which gives them their spherical shapes and relative high stellar density towards the center. The dense stellar environment in globular clusters triggers various dynamical interactions, ie. exchanges in encounters with binaries, direct collisions, destruction of binaries, and tidal capture. These dynamical interactions not only can change the evolution of individual stars, but also can produce tight binary systems (see, e.g., Ashman & Zepf 1998; Verbunt & Lewin 2004, for review). Globular clusters represent an ideal workbench to study stellar dynamics and to test most exquisite theoretical dynamical models. In addition, if we consider each globular cluster as an individual system, they constitute fossil records of the dynamical and chemical evolution of the parent galaxy and can be used as test particles to evaluate both the total mass and the radial distribution of the galaxy. Furthermore, due to the homogeneity of the stars in their ages and metallicities, globular clusters provide an excellent vantage point for studying stellar populations and evolution. Among all the globular clusters, those within the Milky Way are the best-studied due to their relative vicinity. There are about 158 currently known globular clusters in our Milky Way.

In the subsequent sections, I first give a brief introduction to the physical (in §1.1), structural, and dynamical (in §1.2) properties of the Galactic globular clusters. To identify the X-ray sources in the globular clusters is one of the subjects of my thesis. In the final section (§1.3), the detailed descriptions of various types of X-ray sources that may be detected in globular clusters are presented. I also discuss the formation of the binary systems and the relation between the number of X-ray sources and the properties of the globular clusters, i.e. the stellar encounter frequency and the cluster mass.

## 1.1 Properties

Globular clusters exhibit a variety of properties and characteristics. Most of the typical properties described here are based on the observations of Galactic globular clusters (GGCs). Besides the high central density, Galactic globular clusters are very old, i.e. with the age of  $\sim (1.2-1.3)\times 10^{10}$  years, and typically metal-poor stellar systems with metal abundances in the range  $-0.7 < [\text{Fe}/\text{H}] < -2.5$  (where  $[\text{Fe}/\text{H}] = \log(N_{\text{Fe}}/N_{\text{H}}) - \log(N_{\text{Fe}}/N_{\text{H}})_{\odot}$  and  $N$  is the number of atoms of the given element; our Sun has  $[\text{Fe}/\text{H}] = 0.0$ ). Owing to the low metallicity, Galactic globular clusters were presumably born during the very early stages of the Galaxy's formation. Since GGCs are the oldest objects observed in our Milky Way so far, they provide a convincing lower limit to the age of the universe by estimating the ages of the Galactic globulars. On the other hand, studies of their age distribution, the relation between their ages and metallicity, and their spatial location in the Galaxy allow us to directly trace back the first epoch of star formation in the Galactic halo. In addition, combined with the investigation of kinematic properties, it may help in understanding the whole process of galaxy formation.

The luminosity and temperature of a star are dependent on its mass, age, and chemical composition. Color-magnitude diagrams (CMDs) of globular clusters have been studied for a long time since they reflect these fundamental properties of the constituent stars. The observational CMD as well as its twin, the Hertzsprung-Russell diagram (HR diagram), reports on the X-axis the color (temperature) of the stars and on the Y-axis the observed apparent magnitude (the star brightness). Figure 1.1 displays the schematic CMD of a typical globular cluster. Labels indicate the main branches of the diagram. Due to the large number of stars having the same chemical composition but different initial masses, almost every evolutionary stage is present at the appropriate statistical significance. The CMD is a basic and powerful tool which allows us not only to calibrate the observables in terms of fundamental intrinsic parameters (e.g. age, metallicity) but also to examine the validity of the detailed evolutionary theory.

## 1.2 Structural and Dynamical Properties

The evolution of a globular cluster is believed to be very similar to the evolution of a star, and passes through three main phases (Fregeau 2008). In the adolescent phase of the evolution – the “core-contraction phase”, the cluster's core collapse inward on a relaxation timescale, much like a pre-main-sequence star. Once the core density becomes large enough for binary stars to strongly dynamically interact, and therefore generating energy via superelastic encounters, the cluster settles into the “binary-burning phase,” analogous to the main sequence in stars. In this phase the interactions of these double stars near the center of the cluster prevents it from further collapse and the dynamical properties of the cluster core remain roughly constant (e.g., Gao et al. 1991; Heggie & Hut 2003; Fregeau & Rasio 2007). Once the binary population is exhausted in the cluster core, it will collapse via the gravothermal instability, leading to extremely high central densities (“core collapse”). Deep in collapse, an energy producing event, such as an interaction of a dynamically formed binary, will reverse the collapse, causing the core to rebound and enter the “gravothermal oscillation phase,” in which the core continues to collapse and rebound

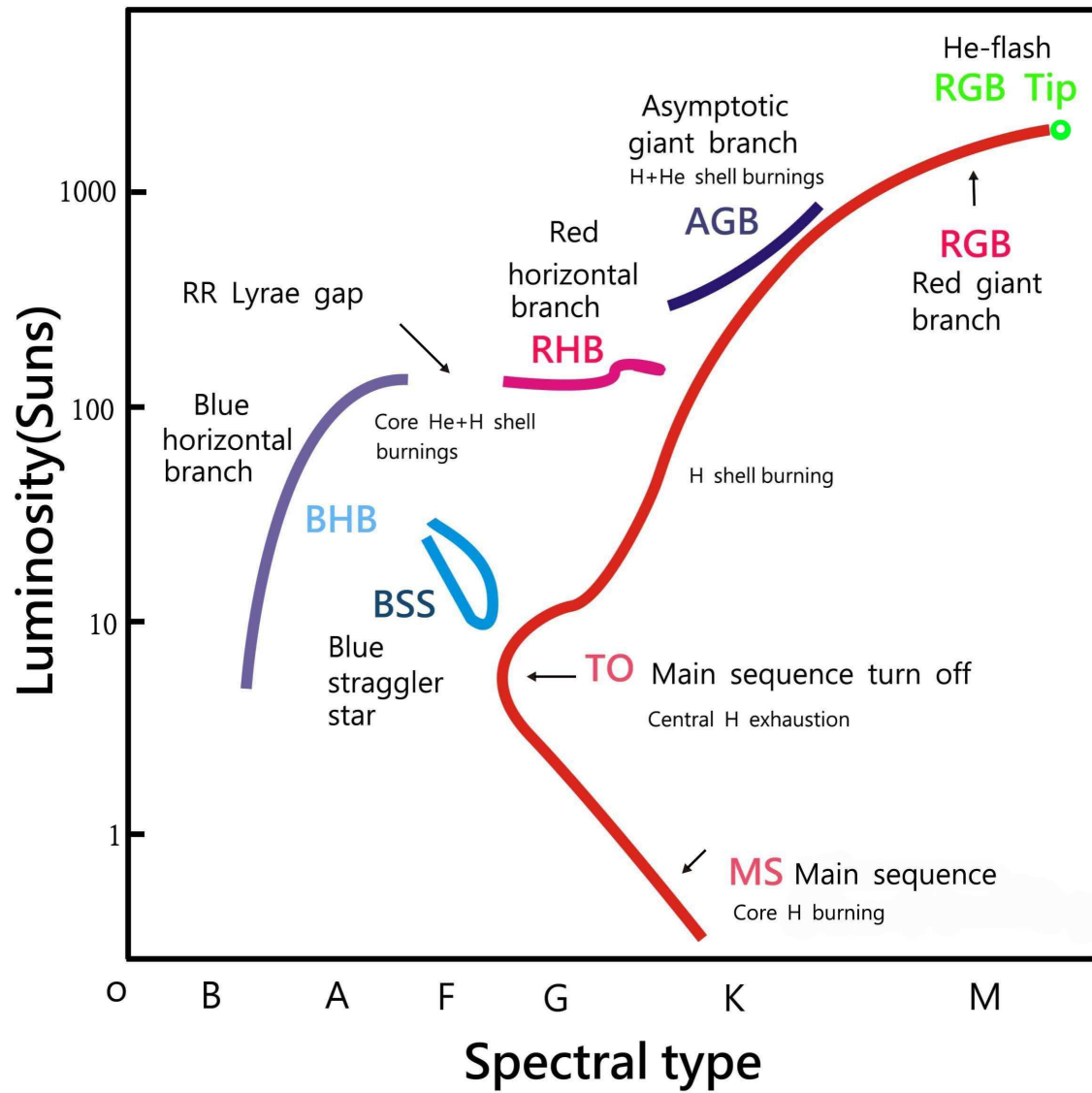


Figure 1.1: Schematic color-magnitude diagram of a typical globular cluster. Labels indicate the main branches of the diagram.

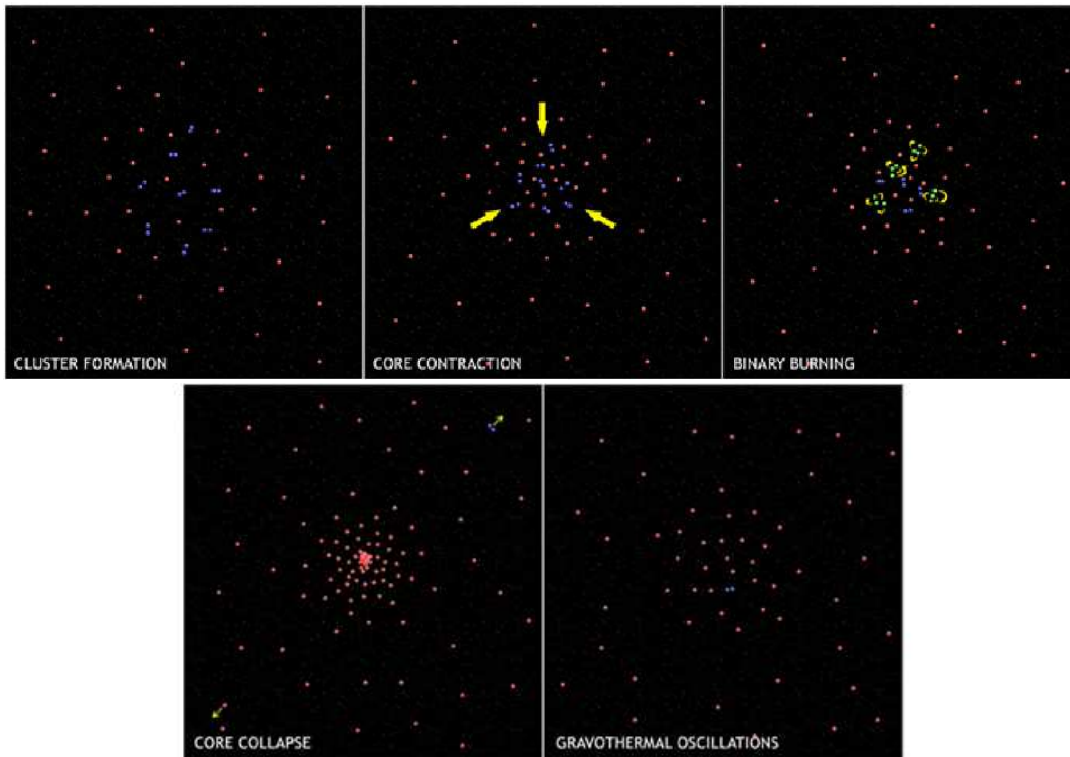


Figure 1.2: This figure shows a sequence of artist’s impressions explaining the evolution of a globular cluster. From left to right: the first graphic shows a globular cluster forming, where single stars are shown in red and double stars in blue. A globular cluster then comprises three main phases of evolution, corresponding to adolescence (“core contraction”), middle age (“binary burning”), and old age (“core collapse”), as shown in the next three graphics. In ‘binary burning’ phase the stars in green are those currently undergoing interactions. These “ages” refer to the evolutionary state of the cluster, not the physical ages of the individual stars. The final graphic shows a period of extended old age, when the central region of the cluster expands and contracts (“gravothermal oscillations”) after new binary systems are formed. (Courtesy of Northwestern/W. Finney)

(Heggie & Hut 2003). For a graphical representation of the cluster evolution, see Figure 1.2. It is very difficult to trace the evolution of a globular cluster backward. However, studies of the dynamical processes acting on globular clusters can provide us with the valuable information on the general evolution of star clusters.

The overall structure of a globular cluster can be described in terms of a nearly spherical N-body system with an averaged central density of  $\sim 10^4 M_{\odot}/\text{pc}^3$ . The important characteristic radii of a globular cluster are the core radius  $r_c$ , the half-mass radius  $r_h$ , and the tidal radius  $r_t$ . The overall luminosity of the cluster steadily decreases with distance from the core. The core radius is defined to be the radius at which the surface brightness has dropped to half the central value. The half-mass radius is the radius that contains half the mass of the cluster. The tidal radius is defined as the radius beyond which the external gravitational field of the galaxy dominates

the dynamics. The core radius is susceptible to change through dynamical processes, whereas the tidal radius is determined by the location within the Galaxy and the orbital characteristics of a given globular cluster.

There are also some important characteristic time scales that govern the dynamics of globular clusters. These are the crossing time  $t_{\text{cross}}$ , the relaxation time  $t_{\text{relax}}$ , and the evaporation time  $t_{\text{evap}}$ . Estimates of these time scales for a particular cluster tell us which physical processes are likely to be the most important in determining its dynamical state.

The crossing time is the typical time required for a star in the cluster to pass through the characteristic size  $R$  of the cluster (typically taken to be the half-mass radius). Thus,  $t_{\text{cross}} \sim R/v$ , where  $v$  is a typical velocity ( $\sim 10$  km/s). The most important parameter to determine the lifetime of the cluster is the relaxation time (Lee 2002) which measures the time for the velocity of a star to be changed by gravitational interactions with other stars in the globular cluster to remove the history of a stars original velocity. Since the relaxation time correlates closely with the number and strength of the gravitational encounters of a typical cluster star, it is related to the number and the average energy of the stars in the cluster. Thus, it can be shown that the mean relaxation time for a cluster is

$$t_{\text{relax}} \approx \frac{0.1N}{\ln N} t_{\text{cross}} \quad (1.1)$$

where  $N$  is the number of stars (Binney & Tremaine 1987; Padmanabhan 2000). For a typical cluster with  $N = 10^5$ , a characteristic size of  $R \sim r_h \sim 10$  pc, a velocity of  $v \sim 10$  km/s, the crossing time and relaxation time are  $t_{\text{cross}} \sim 10^5 - 10^6$  years and  $t_{\text{relax}} \sim 10^8 - 10^9$  years.

The evaporation time for a cluster is the time required for the cluster to dissolve through the gradual loss of stars that acquire sufficient velocity through encounters to escape its gravitational potential. The evaporation time can be estimated by assuming that a fraction  $\gamma$  of the stars in the cluster are escaping every relaxation time without considering stellar evolution and tidal interactions with the host galaxy. Therefore, the rate of loss of stars can be described by the equation

$$\frac{dN}{dt} = -\gamma \frac{N}{t_{\text{relax}}} = -\frac{N}{t_{\text{evap}}} \quad (1.2)$$

(King 1966a). The value of  $\gamma$  depends very sensitively on the ratio of escape velocity  $v_e$  to root-mean-square (RMS) velocity. If we assume the cluster is virialized and the velocities of stars distribute as a Maxwellian, those stars with velocities higher than twice RMS velocity will be evaporated and the fraction  $\gamma$  will be  $7.38 \times 10^{-3}$  (Spitzer 1984; Benacquista 2006). Thus, the evaporation time can be expressed as:

$$t_{\text{evap}} = \frac{t_{\text{relax}}}{\gamma} = 136 t_{\text{relax}}. \quad (1.3)$$

The typical  $t_{\text{evap}}$  is  $\sim 10^{10}$  years, which is comparable to the observed age of globular clusters (Benacquista 2006). If considering stellar evolution and tidal interactions, the evaporation process will be accelerated (Gnedin & Ostriker 1997). The characteristic time scales of globular clusters differ significant from each other:  $t_{\text{cross}} \ll t_{\text{relax}} \ll t_{\text{evap}}$ .

Galactic globular clusters are embedded in galactic potential. Various processes such as dynamical friction, tidal field, and shocks by Galactic disk and bulge contribute to the dissolution of globular clusters. Besides, the evaporation of stars from cluster is also an important process that affects the internal dynamics. Understanding of the destructive processes acting on Galactic globular clusters can provide us with the valuable information on the general evolution of star clusters. In the following, I briefly describe three dominant dynamical processes, i.e. evaporation, disk-shocking, and dynamical friction.

- Through stellar encounters, the velocity distribution of stars in the globular clusters tends to be towards a Maxwellian. Stars in the high-velocity tail of this distribution obtain sufficient energy to escape from the cluster. This process is known as evaporation. The evaporation process could be accelerated due to the presence of the external gravitational field, e.g. the host galaxy, and energy equipartition of stars, e.g. all stars in a given cluster have the same kinetic energy. Since the stellar population of a globular cluster consists of a range of stellar masses, the more massive stars slow down and sink towards the cluster center, while the lighter stars pick up speed and tend to occupy the outer cluster regions – a process termed mass segregation (Spitzer 1987), which leads to the preferential loss of low-mass stars. Through the progress of mass segregation, the core will be overabundant in binaries and degenerate objects since the higher concentration of more massive stars in the center of the cluster increases the probability of the stellar encounter. The typical evaporation time scale for a cluster is about  $10^{10}$  years.
- Disk-shocking (Ostriker et al. 1972) occurs when a globular cluster crosses the high-density disk of the Milky Way. The stars within the globular cluster will obtain the energy through the gravitational shock which is produced by the disk. As a result of the increase in stellar velocities, the stars are induced to escape from the cluster. This process is also called ‘tidal relaxation’ because it is similar to what the two-body relaxation does to the globular cluster (Lee 2002). The disk shock time scale at the half-mass radius is defined as (Elson 1999, and reference therein)

$$t_{\text{disk}} = \frac{-E_h}{dE/dt} = \frac{3GM P_{\text{orb}} V_z^2}{20r_h^3 g_m^2}, \quad (1.4)$$

where  $E_h$  is the mean energy of a cluster with mass  $M$  and the half-mass radius  $r_h$ ,  $dE/dt$  is evaluated at  $r_h$ ,  $V_z$  is the vertical component of the cluster orbital velocity, and  $g_m$  is the maximum vertical gravitational acceleration produced by the disk, and  $P_{\text{orb}}$  is the orbital period. For the Galaxy we can take  $g_m = 4.7 \times 10^{-9} \text{ cm s}^{-2}$ . Then

$$t_{\text{disk}} = 9 \times 10^{12} \left( \frac{M}{10^5 M_{\odot}} \right) \left( \frac{r_h}{5 \text{ pc}} \right)^{-3} \left( \frac{P_{\text{orb}}}{4 \times 10^8 \text{ yr}} \right) \left( \frac{V_z}{300 \text{ km s}^{-1}} \right)^2 \text{ yr}. \quad (1.5)$$

Disk shock is more effective in the low density clusters with short orbital periods and slow orbital velocities.

- Globular clusters experience dynamical friction through the interaction with stars (Binney and Tremaine 1987). This process leads globular clusters to spiral in towards the Galactic center. Disruption is the possible end-point for those clusters before they reach the center of the Milky Way. The dynamical friction time scale for a cluster with mass  $M$  in a isothermal sphere with rotation velocity  $v_c$  is (Binney and Tremaine 1987)

$$t_{\text{fric}} = 2.6 \times 10^{10} \left( \frac{r_i}{2 \text{ kpc}} \right)^2 \left( \frac{v_c}{250 \text{ km s}^{-1}} \right) \left( \frac{10^6 M_\odot}{M} \right) \text{ yr}, \quad (1.6)$$

where  $r_i$  is the initial orbital radius and  $M$  is the cluster's mass. The dynamical friction preferentially destroys massive globular clusters with the short distance to the Galactic center.

In addition, supernova explosions in the early phase of cluster evolution could be destructive if the mass loss takes place rather faster than the internal dynamical time scales. The  $\sim 50\%$  of the total mass loss is required to destroy the cluster instantaneously. However, the condition is not easily satisfied unless the cluster contains a large fraction of massive stars. Besides, the cluster could be also destroyed even with much smaller amount of mass loss by stellar evolution, but it does not seem to be an important mechanism for disruption of early population of clusters.

Astronomers have constructed models of globular clusters for over 100 years. These models mainly fall into two categories: (1) static (equilibrium) models, such as King's model (King 1962, 1966b,c) and its variants. These models are used to estimate mass-to-light ratios and mass segregation, and to combine data from proper motions and radial velocities. (2) Dynamic evolutionary models have been developed for a few objects using the gaseous model (Angeletti et al. 1980), the Fokker-Planck model (Grabhorn et al. 1992; Dull et al. 1997), Monte Carlo models (Giersz & Heggie 2003) and N-body models. These models play a significant role in the search for massive black holes in globular clusters, for instance. In the following, I briefly introduce King's model which is related to my thesis.

King (1962) found an empirical density law which represented the projected star distribution in globular clusters. A few year later he explored a set of analytical models based on the internal stellar dynamics of globular cluster to quantify the surface brightness profiles (King 1966b). These models, widely referred to as "King models," form the basis of all studies of the dynamical evolution of rich star clusters. In general the surface brightness profiles of globular clusters display a core with roughly constant surface brightness. The surface density  $f$  in the inner parts of the globular clusters can be represented by the formula

$$f = \frac{f_0}{1 + (r/r_c)^2}, \quad (1.7)$$

where  $f_0$  is the central surface density and the scale factor  $r_c$  is the core radius. However, outside the core, the surface brightness fall off approximately as power law until the outermost regions, where a sharp turndown indicates the tidal limit of the cluster. The surface density  $f$  falls with radius according to

$$f = f_1 \left( \frac{1}{r} - \frac{1}{r_t} \right)^2, \quad (1.8)$$

where  $f_1$  is a constant and  $r_t$  is the radius at which  $f = 0$ , in other words, the tidal radius. A single expression that shares the characteristic of both Equations (1.7) and (1.8) is

$$f = k \left[ \frac{1}{(1 + (r/r_c)^2)^{1/2}} - \frac{1}{(1 + (r_t/r_c)^2)^{1/2}} \right]^2. \quad (1.9)$$

In a typical cluster,  $r_t/r_c \approx 30$  so the second term of Equation (1.9) has a value  $\approx 0.03$ . For the case  $r \ll r_t$ , we recover Equation (1.7) from Equation (1.9). On the other hand, if  $r \gg r_c$  then Equation (1.9) becomes

$$f = k \left( \frac{r_c}{r} - \frac{r_c}{r_t} \right)^2. \quad (1.10)$$

If we consider the constant  $f_1$  as  $kr_c^2$ , Equation (1.10) reduces to Equation (1.8) in the outer part of the globular cluster. Indeed, Equation (1.9) provides good representations of the observed density profile and furthermore provides a convenient expression for quickly estimating the core radius  $r_c$  and a concentration parameter  $c = \log(r_t/r_c)$  for a globular cluster. As a result, King models not only represent the observed cluster profiles remarkably well but also allows general studies of relations between their structure, Galactocentric radius, and height above the Galactic disk (cf. Djorgovski & Meylan 1994).

### 1.3 Binary Systems

Due to the high stellar densities, globular clusters have high efficiency for producing tight binary systems, such as low-mass X-ray binaries (LMXBs), cataclysmic variables (CVs), millisecond pulsars (MSPs), and chromospherically active binaries (ABs), through frequent dynamical interactions. Binaries are thought to play a key role in the dynamical evolution of the globular clusters (Hut et al. 1992). Theoretical considerations and numerical calculations show that the presence of binaries can postpone deep core collapse. Even a handful of very close binaries can significantly modify the evolution of a globular cluster (Goodman & Hut 1989). Globular clusters have proved to be an excellent place to study binary systems, because of their known distances, ages, and reddening, which allow system parameters and histories to be better understood than in the field. One of the most powerful ways to probe their binary content is by studying the X-ray source populations.

The launch of the Uhuru and OSO-7 Observatories in the early 1970s allowed X-ray sources with luminosity greater than  $10^{36}$  ergs  $s^{-1}$  to be detected for the first time (Giacconi et al. 1972; Clark et al. 1975; Canizares & Neighbours 1975). It was realized that Galactic globular clusters are overabundant by orders of magnitude in bright X-ray sources per unit mass relative to the disk population (Clark et al. 1975; Katz 1975). Strong dynamical scattering interactions of binaries in the dense cluster cores should be responsible for this overabundance (Verbunt & Hut 1987). Following the Einstein and ROSAT era, the number of known faint X-ray sources ( $L_x < 10^{34.5}$  ergs  $s^{-1}$ ) was dramatically increased. Those bright X-ray sources have been identified with low-mass X-ray binaries (LMXBs; Grindlay et al. 1984) while the identification of the weaker sources remained limited due to low photon statistics and insufficient spatial resolution. The

launch of the Chandra X-ray Observatory ushered in a new age of studying the crowded centers of Galactic globular clusters with a far greater sensitivity and resolving power than ever before (e.g., Grindlay et al. 2001a,b). With the unparalleled resolution of the Hubble Space Telescope (HST), identifications of many of these faint X-ray sources in the globular clusters, e.g., 47 Tuc (Grindlay et al. 2001a; Edmonds et al. 2003a,b; Heinke et al. 2005), NGC 6397 (Grindlay et al. 2001b), M 4 (Bassa et al. 2004), NGC 288 (Kong et al. 2006), M 55 and NGC 6366 (Bassa et al. 2008), have been made.

To sort out the X-ray sources in the globular clusters is one of the subjects of my thesis. Understanding the properties of the various types of X-ray sources that may be detected in globular clusters in advance can help us to do the source identification. Figure 1.3 displays the sketch of those potential X-ray sources and the detailed descriptions are presented in the following.

- Low-Mass X-ray Binaries (LMXBs)

Low-mass X-ray binaries are semi-detached binaries consisting of either a neutron star or a black hole primary, and a low-mass secondary which is filling its Roche lobe<sup>1</sup>. The donor orbiting the compact object in the period range from ten minutes to hundreds of days can be a main sequence star, a degenerate dwarf, or an evolved star (red giant). Due to the intense gravity of the compact object, the material from the companion is pulled into an accretion disk around the compact object through Roche lobe overflow and spirals into the compact object. This process heats up the material in the disk to the temperature of more than  $10^6$  K and emits X-rays. When actively accreting, LMXBs are among the brightest objects in the X-ray sky with the luminosity of  $L_x \sim 10^{36} - 10^{38}$  ergs  $s^{-1}$  (hereafter, the use of “LMXBs” refers only to active LMXBs). The brightest part of the system is the accretion disk around the compact object. There are 13 LMXBs located in 12 Galactic globular clusters (Liu et al. 2001; White & Angelini 2001). Compared with  $\sim 100$  such systems in our Milky Way, LMXBs are substantially over-represented with 100 times more common per unit mass in globular clusters than in the field (Clark et al. 1975; Katz 1975). All of the LMXBs in Galactic globular clusters with the orbital period on the order of a day or less contain an accreting neutron star and 12 from the 13 sources exhibit type I X-ray bursts (in’t Zand et al. 2003), indicating thermonuclear flashes on the surface of the neutron star (Johnston & Verbunt 1996).

If the X-ray binary contains a neutron star, it might be seen to pulse in X-rays or give off bursts of X-rays. Figure 1.4 shows an artist impression that the material is funnelled by the strong magnetic field of the neutron star onto its magnetic poles. The material falling in

---

<sup>1</sup> Roche lobe is the region surrounding each star in a binary system, within which any material is gravitationally bound to that star. The boundary of the Roche lobes is an equipotential surface, and the lobes touch at the inner Lagrangian point, L1, through which mass transfer may occur if one of the components expands to fill its lobe. It is named after the French mathematician Édouard Albert Roche. The radius of the Roche Lobe of the star with mass  $M_1$  is

$$R_{L1} = \frac{0.49a}{0.6 + q^{\frac{2}{3}} \ln(1 + q^{\frac{1}{3}})}, \quad (1.11)$$

where  $q \equiv M_1/M_2$  and  $a$  is the distance between these two stars.

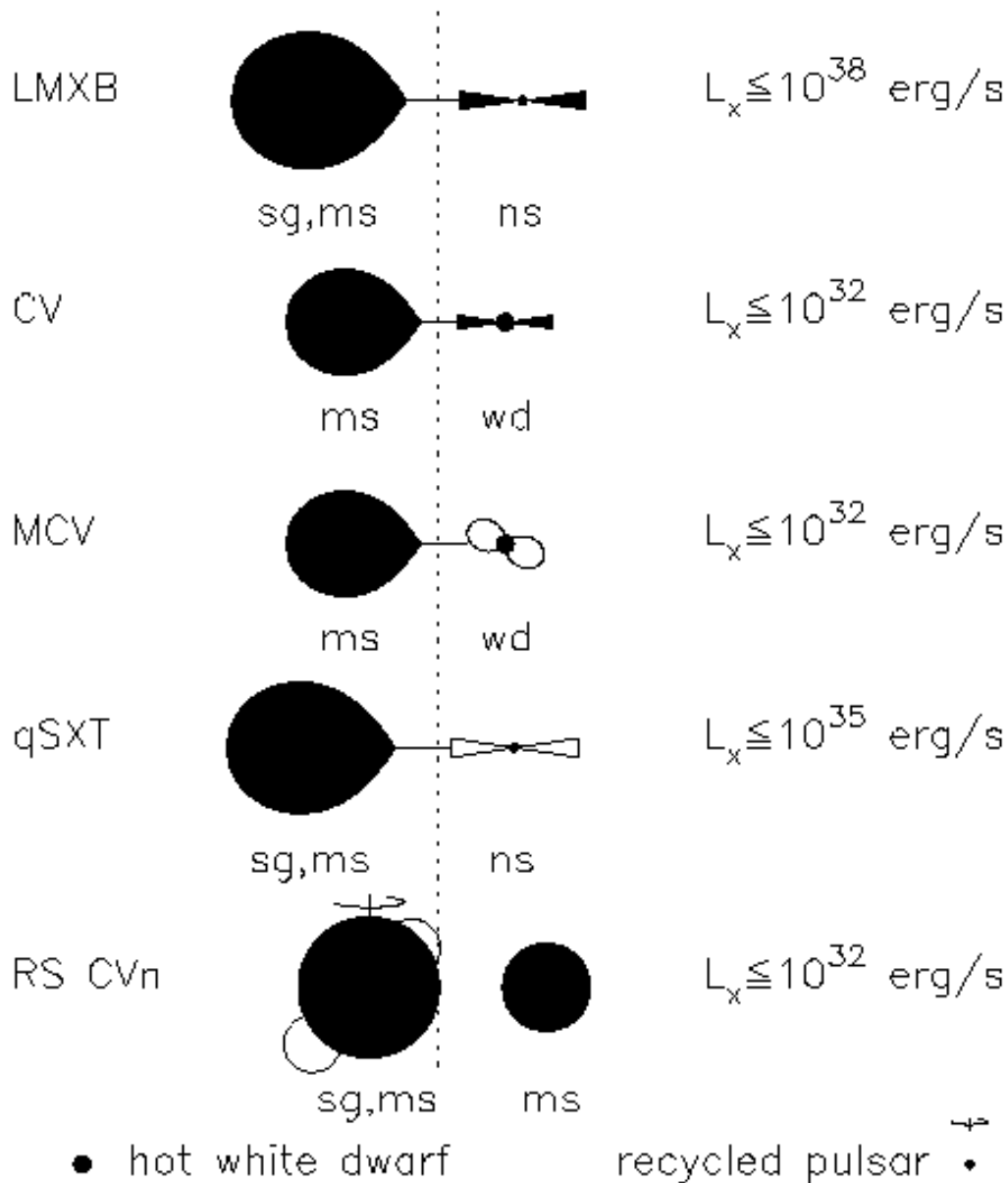


Figure 1.3: The various types of objects suggested as X-ray sources in globular clusters. Binaries from top to bottom: low-mass X-ray binaries (LMXBs), cataclysmic variables (CVs), magnetic cataclysmic variables (MCVs), quiescent soft X-ray transients (qSXT) – in all of these the luminosity is due to mass transfer – and RS CVn binaries – a type of X-ray active binaries containing one main-sequence star and one (sub)giant, in which magnetic activity produces the X-rays. Luminosities in the 0.5–2.5 keV range are indicated on the right. Single stars that emit X-rays include hot white dwarfs, and recycled pulsars. Recycled pulsars also occur in binaries, with an undermassive white dwarf or a swapped evolved companion. ‘sg’, ‘ms’, ‘ns’ and ‘wd’ stand for (sub)giant, main-sequence star, neutron star and white dwarf. This figure is from Verbunt (2002).

from the companion will hit the neutron star surface and will shine in X-rays as an intense hot spot. Not all neutron star systems have such intense magnetic fields, and it appears that many of the low mass X-ray binary systems in the field is much weaker. In these cases the flow of material onto the neutron star is more erratic, with the pulsations unstable. Many of these low magnetic field systems show what are called quasi-periodic oscillations (QPO). These oscillations seem to originate from the interaction of the neutron star with the surrounding accretion disk, or from instabilities in the captured material caused by the overwhelming intensity of the X-ray emission.

In addition to active LMXBs, Galactic globular clusters may contain 10 times as many LMXBs in their quiescent states (qLMXB; Pooley et al. 2003). A typical qLMXB emits its radiation in X-rays with the luminosity of  $L_x \sim 10^{32} - 10^{34}$  ergs  $s^{-1}$  (Heinke et al. 2003). The X-ray spectra of qLMXBs are dominated by a soft component with the temperature about 0.1 to 0.3 keV, which is thought to be thermal emission from the neutron-star surface due to the cooling of the neutron-star core, which has been heated during the outbursts (Campana et al. 1998; Brown et al. 1998). Identifying the nature of X-ray sources usually requires deep multiwavelength data. However, with the unique X-ray spectral signature, it offers the possibility of identifying qLMXBs without multiwavelength follow-up observations since they are among the brightest objects in the X-ray sky, but relatively faint in the optical band (see Grindlay et al. 2001b; Edmonds et al. 2002b).

- Cataclysmic Variables (CVs)

Cataclysmic variables are the systems containing a white dwarf accreting material from a low-mass companion, typically a main-sequence star, a white dwarf, or less often, a red giant. They irregularly increase in brightness by a large factor, then drop back down to a quiescent state with an orbital period generally between about 80 and 700 minutes. The stars are so close to each other that the gravity of the white dwarf distorts the secondary, and the white dwarf accretes matter from the companion. Therefore, the secondary is often referred to as the donor star. The infalling matter, usually rich in hydrogen, forms in most cases an accretion disk around the white dwarf, which radiates over a broad energy range from the optical through the far-UV band. Furthermore, X-ray emission also can be detected when material accretes onto the white dwarf.

CVs are classified into various subgroups based primarily on the strength of the white dwarf's magnetic field. The majority of CVs are non-magnetic, e.g. dwarf novae and classical novae. The accretion disk may be prone to an instability leading to dwarf nova outbursts, when a portion of the disk material falls onto the white dwarf; the classical nova outbursts occur when the density and temperature at the bottom of the accumulated hydrogen layer rise high enough to ignite nuclear fusion reactions, which rapidly burn the hydrogen layer to helium. If the accretion process continues long enough to bring the white dwarf close to the Chandrasekhar limit, the increasing interior density can ignite runaway carbon fusion and trigger a Type Ia supernova explosion, which completely disrupts the white dwarf.

There are two other kinds of cataclysmic variables with a very strong magnetic field of B

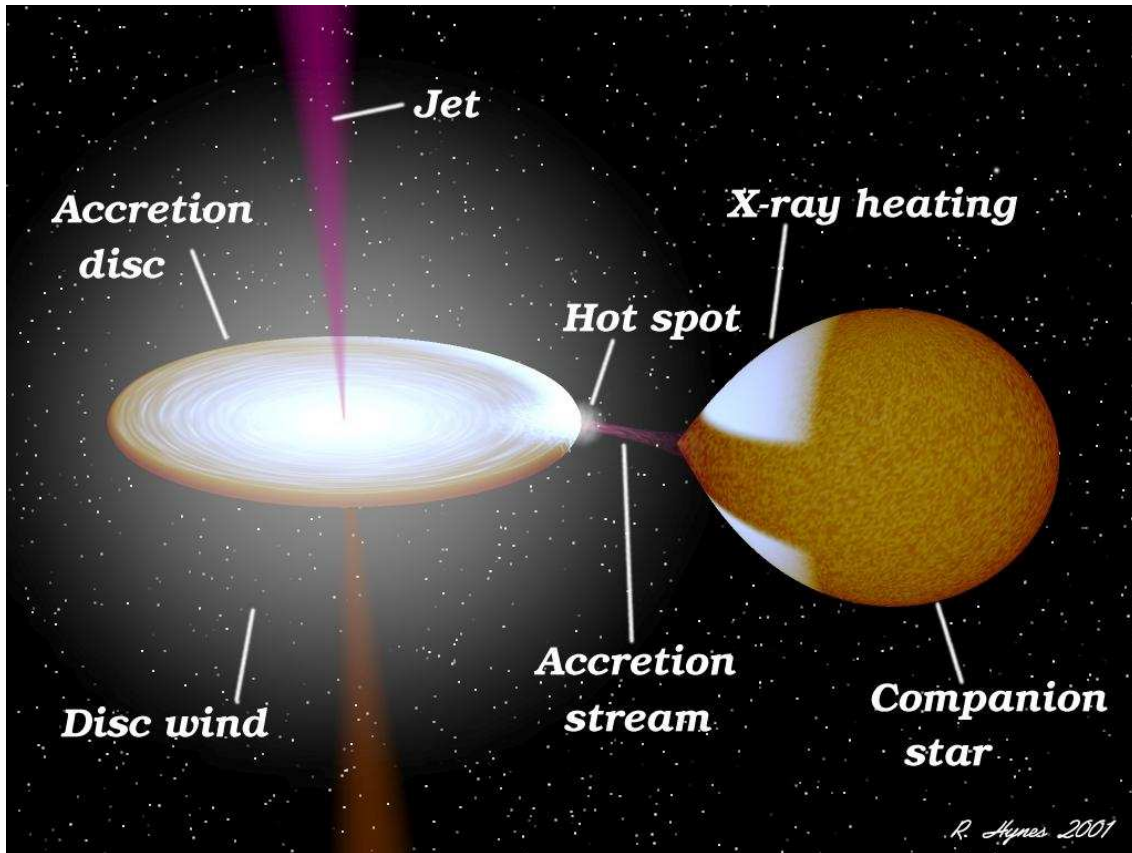


Figure 1.4: This is an interacting binary stars containing a companion feeding an accretion disk around a black hole or a neutron star. X-rays are produced as material from the companion star is drawn to the compact object either through Roche-lobe overflow into an accretion disk (LMXB) or through direct impact of a stellar wind onto the compact object (HMXB). The illustration shows an impression of what an LMXB might look like. (Courtesy of Rob I. Hynes)

$> 10^6$  Gauss. These magnetic CVs are further subdivided into: Polars or AM Herculis type systems with magnetic field strengths  $\sim (10 - 200) \times 10^6$  Gauss, and Intermediate Polars (IPs) or DQ Her stars with magnetic field strengths  $\sim (1 - 10) \times 10^6$  Gauss. In Polar systems (see Figure 1.5), the magnetic field of the white dwarf is too strong to form an accretion disk. Infalling gas will form an accretion stream, following the dipole magnetic field lines of the white dwarf. Optical/infrared cyclotron emission is strongly detected, and the white dwarf spins synchronously with the binary orbit. However, the Intermediate Polars (see Figure 1.6) are generally less magnetic and only partial accretion disks are probably present since the disk is disrupted by the magnetic field of the white dwarf. Infalling gas from the companion star will form a disk when the matter is still far from the primary star, but will follow magnetic field lines in accretion streams when the matter falls closer to the white dwarf. In the transition region between the accretion disk and the accretion stream, infalling gas may also fall as curved sheets called accretion curtains. The cyclotron emission is weak or undetected, and the white dwarf spin period is shorter than the orbital period. In both these subclasses, accretion proceeds quasi-radially along field lines onto the magnetic polar regions. There a strong shock forms, heating the plasma to X-ray temperatures ( $kT > 10$  keV). The white dwarf surface below the shock is heated to  $kT \sim 20$  keV by these X-rays and by direct injection of kinetic energy by dense blobs. The IPs are the strongest source of 2–10 keV X-rays among CVs, with estimated luminosities in excess of  $10^{33}$  ergs  $s^{-1}$ , while the Polars are generally strong ( $10^{32}$  ergs  $s^{-1}$ ) soft X-ray sources.

Cataclysmic variables are best identified when an optical counterpart is found. A good indicator is that the optical counterpart in U versus U-V color-magnitude diagrams (CMDs) is bluer than the main sequence, usually lying between the main sequence and the white dwarf cooling sequence. A strong contributor to this blue color, the accretion disk, will also generate  $H\alpha$  emission and cause short-timescale nonperiodic variability (flickering) and sometimes large-amplitude outbursts. In V versus V-I CMDs, CVs generally appear redder because of the increased contribution of the secondary light, and in globular clusters they have often been observed to fall on or near the main sequence (Edmonds et al. 2003a). The secondary, filling its Roche lobe, will often show ellipsoidal variations, and this periodic, low-amplitude signal is detectable if the noise from flickering is not too large. However, quiescent neutron-star low-mass X-ray binaries also have blue spectra with Balmer emission, but can be distinguished from CVs through their soft X-ray spectra and by the fact that they are more luminous than CVs. In addition, the X-ray to optical flux ratio for CVs should be smaller than for qLMXBs, and a CV at a given X-ray luminosity will display much bluer colors than a qLMXB at the same luminosity, since it must be accreting at a much higher rate. On the basis of these characteristics, X-ray sources can be identified as CVs with high confidence.

- Millisecond Pulsars (MSPs)

The widely accepted scenario for the formation of millisecond pulsars (MSPs) is that an old neutron star has been spun up in a past accretion phase by mass and angular momentum transfer from a binary late-type companion (Alpar et al. 1982; Radhakrishnan & Srinivasan

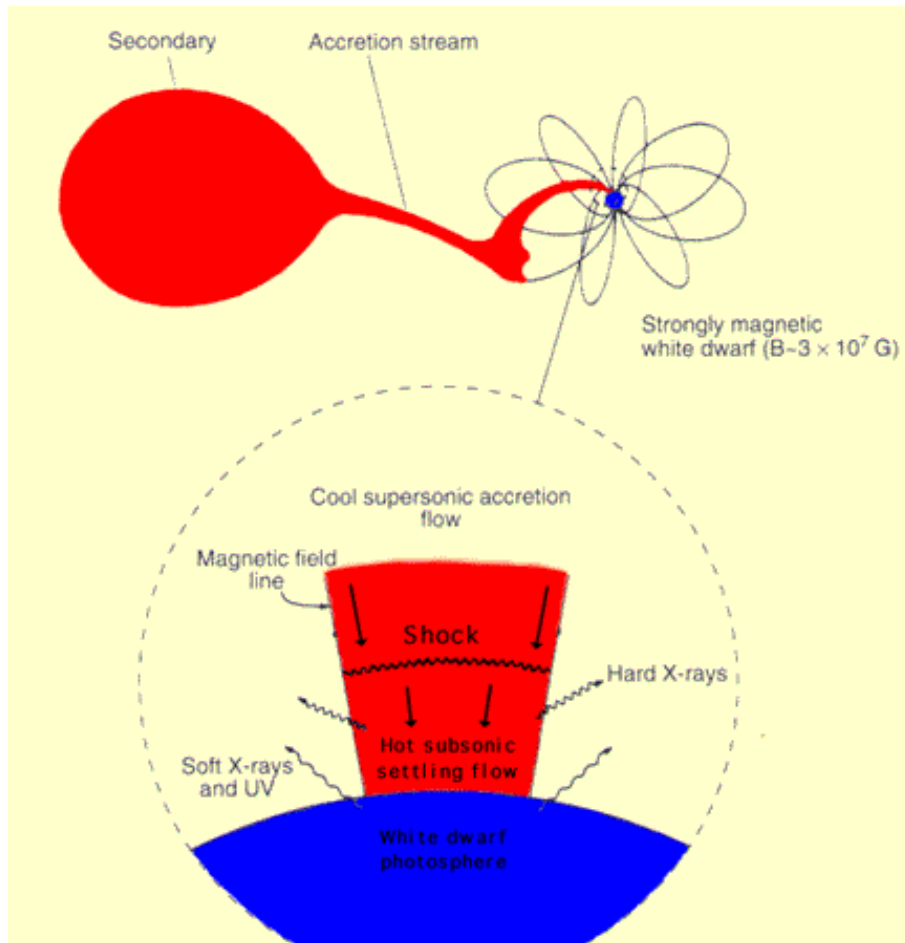


Figure 1.5: Diagram of a Polar: The strong magnetic field of the white dwarf prevents the formation of an accretion disk. Instead, the overflowing material from the companion will form an accretion stream, following the dipole magnetic field lines of the white dwarf and impact on the surface of the white dwarf at its magnetic pole. (Courtesy of NASA)

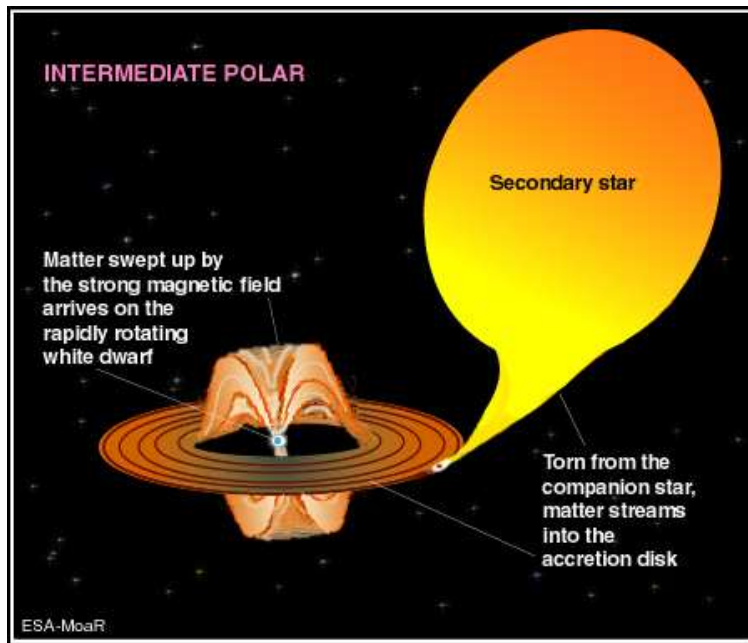


Figure 1.6: Diagram of an Intermediate Polar (IP): Matter flows from the companion star into an accretion disk around the white dwarf, but is disrupted by the white dwarf's magnetic field. (Courtesy of ESA)

1982). Due to the high stellar densities, globular clusters have high efficiency for producing tight binary systems, such as MSPs, through frequent dynamical interactions. Until now, more than 180 MSPs are detected in the radio surveys. Among them about 70% are located in globular clusters.

In globular clusters, the MSP progenitor binaries can be formed from direct two-body tidal capture (Mardling 1995a,b) or three-body encounters and may be also formed from main-sequence binaries by exchange of a neutron star into the binary (Rasio et al. 2000). Globular clusters also allow the exchange of the original mass donor with a replacement main-sequence star. The optical identifications of MSPs in globular clusters, PSR J1740–5340 in NGC 6397 (hereafter 6397A; D’Amico et al. 2001a,b; Ferraro et al. 2001) and PSR J0024–7204W in 47 Tucanae (hereafter 47 Tuc W; Edmonds et al. 2001, 2002a), have provided direct evidence that some MSPs in globular clusters have swapped their original binary companions.

Most identification of X-ray sources in globular clusters with recycled radio pulsars are based on positional coincidence. The exceptions are the identifications of the pulsar in M28 (PSR B1821–24A, hereafter M28A), which is based on the pulsar spin period, and of pulsars in NGC 6397 (6397A; Ferraro et al. 2001) and in 47 Tuc (47 Tuc W; Edmonds et al. 2002a) which are based on their orbital periods.

The first and brightest X-ray globular cluster MSP, PSR B1821–24A, was detected with the ROSAT HRI in the cluster M28 (Danner et al. 1997). It is the only MSP in globular clusters

identified with an X-ray source before the Chandra observations (Saito et al. 1997). With the sub-arcsecond spatial resolution of Chandra, Becker et al. (2003) have well-resolved the X-ray contribution from M28A and obtained the phase-averaged power-law spectrum with photon index  $\sim 1.2$ . The X-ray emission from M28A is most likely to have a magnetospheric origin. However, in contrast to the bright and hard pulsar in M28, 19 of 23 MSPs located in the globular cluster 47 Tuc are found to have X-ray counterparts and are dim and soft X-ray emitters (Grindlay et al. 2001a, 2002; Bogdanov et al. 2006). The X-ray luminosities of the 47 Tuc pulsars are in range of  $L_X \sim 10^{30} - 10^{31}$  ergs $^{-1}$  (Bogdanov et al. 2006), which are orders of magnitudes smaller than that of M28A. The X-ray spectra of the majority of these pulsars can be well-described by a thermal model (blackbody or neutron star hydrogen atmosphere model; Zavlin et al. 1996) with temperature  $T_{\text{eff}} \sim (1-3) \times 10^6$  K and emission radius  $R_{\text{eff}} \sim 0.1 - 3$  km (Bogdanov et al. 2006).

Based on the first Chandra observations of 47 Tuc, Grindlay et al. (2002) suggested the X-ray conversion efficiency (i.e. the dependence of  $L_X$  on  $\dot{E}$ ) for 47 Tuc pulsars to be  $L_X \propto \dot{E}^{0.5}$ , where  $\dot{E}$  is the spin-down power of the pulsar. Such dependence is obviously shallower than the linear relation  $L_X \sim 10^{-3} \dot{E}$  found for the pulsars in the Galactic field and in the globular clusters (see Becker & Trümper 1997, 1999, 2009). However, including all systematic uncertainties, subsequent observations did not confirm this evidence, albeit more significant data became available meanwhile (Bogdanov et al. 2006).

As aforementioned, the brightness and hardness of globular cluster pulsars in the X-ray regime span a very wide range. Of the 140 globular cluster radio pulsars known today, only a small fraction of them are found to have an X-ray counterpart. Moreover, more than half of these X-ray sources are located in a single cluster, namely 47 Tuc. It is obvious that our current understanding of the X-ray emission nature of cluster pulsars is seriously biased. Therefore, to enlarge the sample and to study their X-ray emission properties more systematically is very important. This provides the motivation for our study.

- Chromospherically Active Binaries (ABs)

Differential rotation in late-type stars with convective envelopes drives a magnetic dynamo leading to strong chromospheric emission and the formation of a corona. X-ray sources in globular clusters can be classified as chromospherically or magnetically active binaries when a stellar flare is observed in the X-ray band. There are three types of active binaries: detached binaries of two main-sequence stars (BY Dra systems), detached binaries of one main-sequence star and one giant or subgiant (RS CVn systems), and contact binaries (W UMa systems).

One or both stars in these close binaries are kept in corotation with the orbit. The rapid rotation combines with the convective motion to act as a dynamo which enhances the magnetic field and coronal activity. The loops of the magnetic field sticking out of the stellar surface contain hot, X-ray emitting gas. In principle, single stars can be rapid rotators, but in an old globular cluster all single stars have slowed down long ago. Only binary stars are magnetically active. Strong X-ray and non-thermal radio emission in late-type stars are well-known indicators of enhanced coronal activity (Drake et al. 1992). Thereby

X-ray emission is an efficient way of detecting close binaries in a stellar cluster (e.g. M 67: Belloni et al. 1998, Van den Berg et al. 2004). However, without detailed optical photometric and spectroscopic studies, those binaries could not be correctly classified into known types.

Most magnetically active binaries have been identified on the basis of color-magnitude diagrams. These ABs located on or slightly above the main sequence belong to the BY Dra star systems with the soft X-ray luminosities  $L_{x,0.1-2.0\text{keV}} \approx 10^{29} - 10^{30} \text{ ergs s}^{-1}$  (Dempsey et al. 1993) while those lying on the giant branch are thought to be the RS CVn stars with higher X-ray luminosities of  $L_{x,0.1-2.0\text{keV}} \approx 10^{29} - 10^{32} \text{ ergs s}^{-1}$  (Drake et al. 1989).

In the galactic plane, all binary X-ray sources evolve from primordial binaries (e.g. Verbunt 1993). However, in globular clusters, two additional processes are possible: tidal capture and exchange encounter (reviewed by Hut et al. 1992). In a tidal capture, one star (in particular a neutron star or white dwarf) raises tides on a main-sequence or (sub)giant star in a close passage; the energy of the tides is taken from the relative motion, and the stars become bound, as the tidal energy is dissipated. In an exchange encounter, a star come across a binary system and forms a temporary triple system with it; one star is then expelled (usually the star with the lowest mass) and the other two remain bound. In this way, a neutron star or white dwarf can be exchanged into a binary.

In globular clusters, as suggested by Verbunt (2002), magnetically ABs are most likely primordial binaries, i.e. formed as binaries when the component stars formed, while the low-mass X-ray binaries in globular clusters are thought to be formed through tidal capture or exchange encounter (see the review by Verbunt & Lewin 2006 and references therein). Both formation mechanisms, evolution from a primordial binary (Davies 1997) and capture of a previously single white dwarf in a close encounter (Pooley et al. 2003), are viable for cataclysmic variables, depending on the circumstances. The progenitor binary of a cataclysmic variable must be wide enough to allow the more massive star to evolve into a fairly big giant, before it reaches its Roche lobe. Such wide binaries are easily destroyed through binary interactions in dense cores of globular clusters. However, according to the computations by Davies (1997), in a relatively low-density cluster with the stellar number density of  $1000 \text{ pc}^{-3}$ , most CVs may have evolved from primordial binaries. In addition, it has been pointed out that CVs which evolved in the low-density outskirts of globular clusters can sink towards the core at late times. Thus, the population of cataclysmic variables in dense cores can be a mixture of locally produced products of stellar encounters and recently arrived products of the evolution of primordial binaries (Ivanova et al. 2006; see also Hurley et al. 2007).

In a globular cluster, binary systems may change due to their internal evolution and/or due to external encounters. The over-abundance of bright X-ray binaries in globular clusters is the consequence of stellar encounters. These mechanisms, i.e. tidal capture or exchange encounter, scale with the *encounter rate*  $\Gamma$  in a globular cluster

$$\Gamma = \int_V n_1 n_2 A v dV, \quad (1.12)$$

where  $n_1$  and  $n_2$  are the number densities of the neutron stars and of the objects (giants, single stars, binaries) with which they interact, respectively,  $A$  is the encounter cross section,  $v$  is the velocity dispersion as a function of radius, and the integral is over the cluster volume. The integral is often approximately as

$$\Gamma \propto \int \frac{n_1 n_2 R}{v} dV \propto \frac{\rho_0^2 r_c^3}{v} \propto r_c^2 \rho_0^{1.5} \equiv \Gamma'. \quad (1.13)$$

The proportionality follows because the cross section is dominated by gravitational focusing and scales as  $A \propto R/v^2$ , with the size of the object  $R$ . The second term assumes that the encounter rate is dominated by the cluster core (radius  $r_c$ , mass density  $\rho_0$ ), where most encounters occur, and the number density  $n_1$  and  $n_2$  scales with the total mass density  $\rho_0$ . We then relate  $v$ ,  $\rho_0$ , and  $r_c$  via  $v \propto r_c \rho_0^{1/2}$  through the virial theorem. The last equality  $\Gamma'$  is referred to as the *collision number*, which is usually used to scale with the number of the dynamically-formed X-ray binaries in a globular cluster.

With the advances in X-ray astronomy, Pooley et al. (2003) has quantitatively studied the relationship between the number of X-ray sources in each cluster and properties of the cluster itself by using Chandra observations of many Galactic globular clusters with the X-ray luminosity down to a limit of  $4 \times 10^{30}$  ergs s<sup>-1</sup> in the 0.5–6 keV range (which includes low-mass X-ray binaries in outburst and quiescence, cataclysmic variables, millisecond pulsars, and magnetically active main sequence binaries). They found the strongest correlation between the encounter frequency,  $\Gamma$ , and the number of X-ray sources within the half-mass radius of the globular cluster. More recently, Heinke et al. (2003) and Pooley & Hut (2006) have isolated the qLMXBs and CVs, respectively, from the X-ray source populations, and have shown that their numbers are indeed consistent with dynamical formation.

However, the number of the primordial binaries may be expected to depend on the total mass  $M$  of a cluster, which can be estimated from the total luminosity of a cluster with use of a mass-to-light ratio appropriate for a cluster star population. Since the information on low-luminosity X-ray sources in most clusters is limited to the region within the half-mass radius, the masses within this radius should be reliable to use. Following Kong et al. (2006), the half masses is calculated by  $10^{-0.4M_V}$ , where  $M_V$  is the absolute visual magnitude. Kong et al. (2006) reported that the predicted number of active binaries  $L_{0.5-6\text{keV}} > 4 \times 10^{30}$  erg s<sup>-1</sup> in NGC 288 is indeed similar to those in NGC 6397 and M 4, and about one tenth of those in 47 Tuc, by scaling the half masses of the globular clusters.

It is now thought that X-ray binary systems in dense globular clusters are created principally through exchange interactions between primordial binaries and other stars (see, e.g. Hut et al. 1991). On the other hand, in low-density globular clusters a large part of X-ray binaries are believed to be primordial in origin since fewer primordial binaries may have been destroyed through binary interactions. The number of X-ray sources in a globular cluster then may be expected to depend both on the collision number (dynamical origin) and on the cluster mass (primordial origin) (Bassa et al. 2008). Therefore, studying binary systems in globular clusters can give us insight into the characteristics of accreting binary systems and populations and also can help us to better understand their evolution and dynamics.

# Chapter 2

## Introduction II – Neutron Stars and Pulsars

### 2.1 A brief History of Neutron Stars

In the 1930's, Subrahmanyan Chandrasekhar discovered that a collapsed stellar core with a mass higher than  $1.4M_{\odot}$  could not hold itself up against gravity once the nuclear fusion no longer takes place in the interior of the star. After the discovery of the neutron by Chadwick (1932), Walter Baade & Fritz Zwicky (1934) proposed that the neutron star, a star almost entirely composed of neutrons with a radius on the order of  $R \sim 10^5$  cm, could be created in the aftermath of the gravitational collapse of the core of a massive star at its final evolution stage, which triggers a Type II supernova explosion. First models for the structure of neutron stars were worked out in 1939 by Oppenheimer & Volkoff (Oppenheimer–Volkoff limit). However, their pioneering work did not predict anything that could be observed by astronomers. And then the idea of neutron stars was not seriously considered in the following two decades.

Compact stars, either white dwarfs or neutron stars, were predicted to be observed in X-rays by Hayakawa & Matsuoka (1964) and Zeldovich & Guseynov (1966), who independently predicted that binary systems consisting of a compact object and a massive companion could generate thermal X-ray emission through the matter accretion from the companion star onto the condensed star. In 1962, the brightest extra-solar X-ray source located in the constellation Scorpio, Sco X-1, was detected with the X-ray detectors onboard the Aerobee rocket by the team led by Bruno Rossi and Riccardo Giacconi. The discovery had motivated people to speculate that neutron stars could be observable in the X-ray regime. And searching for the thermal emission from the surface of neutron stars had become a strong motivation to improve the instrumentation for X-ray astronomical observations.

Hoyle, Narlikar, & Wheeler (1964) had predicted that neutron stars could be fast rotating compact objects with strong magnetic field. The first radio pulsar, PSR B1919+21 (PSR stands for pulsating sources of radio), with a spin period of 1.3 sec was unexpectedly discovered by Jocelyn Bell in November 1967 (Hewish et al. 1968). After a few more similar pulsating sources, pulsars, have been detected, it became clear that a new kind of celestial objects was discovered.

The connection between these radio pulsars and fast spinning neutron stars was provided by Pacini (1967) and Gold (1968). Pacini (1967), just before the discovery of pulsars, proposed that the rapid rotation of a highly magnetized neutron star could be the source of energy in the Crab Nebula. In addition, Gold (1968) provided the most fundamental ideas on the nature of the pulsating radio sources. He introduced that the rotational-powered pulsar spins down as rotation energy is radiated away and recognized that the rotational energy is lost via electromagnetic radiation of the rotating magnetic dipole and emission of relativistic particles. These particles are accelerated in the pulsar magnetosphere along the curved magnetic field lines and emit the observed intense curvature and synchrotron radiation. These exciting radio discoveries triggered subsequent pulsar searches at all wavelength.

The discovery of two most famous pulsars, the Crab pulsar and the Vela pulsar, located within the supernova remnants provided conspicuous confirmation that neutron stars are born in core collapse supernovae from massive main sequence stars (see Badde & Zwicky 1934).

Rotation-powered neutron stars are generally referred to as “radio pulsars” since it is that the vast majority of the population is observed at radio wavelengths. Nowadays, more than 1800 radio pulsars have been detected (see e.g., the ATNF pulsar database<sup>1</sup>). X-ray observatories during the past few decades, including Einstein, ROSAT, ASCA, BeppoSAX, Chandra, and XMM-Newton, have helped us to make a big leap in studying X-ray pulsar astronomy. 98 radio pulsars have been detected in the X-ray band by spring 2010. In the past ten years, operation of Chandra, with the outstanding sub-arcsecond imaging capability, and XMM-Newton, with the unprecedentedly high spectral sensitivity and collecting power allowed us to detect pulsars as various categories at X-ray energies and to obtain detailed X-ray imaging, timing, and spectral information of pulsars. With the increase in sensitivity of today’s observatories, a growing number of neutron stars are detected in more than one wavelength, which makes it possible to carry out the multiwavelength studies of the pulsar emission.

## 2.2 Physics and Astrophysics of Neutron Stars

Neutron stars are one of the densest manifestations of massive objects in the universe. They are ideal astrophysical laboratories for testing gravitational physics and high energy physics and provide connections among nuclear physics and particle physics under the most extreme conditions which are not observed elsewhere. The detailed description of the theory of formation, structure, and internal composition of neutron stars is beyond the scope of my PhD thesis. The basic properties and X-ray emission mechanism of neutron stars based on observations will be briefly summarized in this section.

---

<sup>1</sup><http://www.atnf.csiro.au/research/pulsar/psrcat/>

### 2.2.1 Rotation-powered Pulsars: the Magnetic Braking Model

The total available spin luminosity in a rotation-powered pulsar is given by the rate of loss of rotational kinetic energy,

$$\frac{dE_{\text{rot}}}{dt} \equiv \dot{E}_{\text{rot}} \equiv I\omega\dot{\omega} \equiv \frac{4\pi^2 I \dot{P}}{P^3}, \quad (2.1)$$

where  $\omega \equiv 2\pi/P$  is the angular velocity with the spin period  $P$  and  $I$  is the stellar moment of inertia, typically taken to be  $10^{45}$  g cm<sup>2</sup> if assumed a neutron star with a canonical radius of 10 km and a mass of  $1.4 M_{\odot}$ . Thus the rotational power of an isolated neutron star can be determined by a simple measurement of  $P$  and  $\dot{P}$  in a model-independent way. The observed values of  $\dot{E}$  for the pulsar population are in the range of  $\sim 5 \times 10^{38}$  ergs s<sup>-1</sup> for the Crab pulsar and PSR J0537–6910 down to  $3 \times 10^{28}$  ergs s<sup>-1</sup> for the slowest known pulsar, PSR J2144–3933 (Manchester et al. 2005). Ostriker & Gunn (1969) suggested that the pulsar spin-down is due to the braking torque exerted on the neutron star by its magnetic dipole radiation, that yields

$$\dot{E}_{\text{brake}} = -\frac{32\pi^4}{3c^3} B_{\perp}^2 R^6 P^{-4} \quad (2.2)$$

for the energy loss of a rotating magnetic dipole, where  $B_{\perp}$  is the component of the equatorial magnetic field orthogonal to the rotation axis. Equating  $\dot{E}_{\text{rot}}$  with  $\dot{E}_{\text{brake}}$ , we find

$$B_{\perp} = 3.2 \times 10^{19} (P\dot{P})^{1/2} \text{ Gauss}. \quad (2.3)$$

Magnetic field strengths inferred from Equation (2.3) range between  $10^8$  G for recycled (or “millisecond”) pulsars up to  $> 10^{15}$  G for “magnetars”. We can assume a pulsar is formed with a high angular velocity  $\omega$ , the relation between  $P$  and  $\dot{P}$  can be generalized as  $\dot{P} = kP^{2-n}$ , where  $k$  is a constant and  $n$  is the “braking index”. Assuming the initial rotation period  $P_0$  at the time of the neutron star formation was much smaller than today, i.e.  $P_0 \ll P$ , the age of the system is (Manchester & Taylor 1977):

$$\tau = \frac{P}{(n-1)\dot{P}} \left[ 1 - \left( \frac{P_0}{P} \right)^{n-1} \right] \approx \frac{P}{(n-1)\dot{P}}, \quad (2.4)$$

where  $n \neq 1$ . For the case of magnetic dipole braking  $n=3$ ,

$$\tau \equiv \frac{P}{2\dot{P}}, \quad (2.5)$$

where  $\tau$  is defined as the characteristic spin-down age even though the real value of  $n$  may differ from 3. A direct measurement of  $n$  is obtainable if the second period derivative can be found. In terms of angular velocity  $\omega$  or period  $P$ :

$$n = \frac{\omega\ddot{\omega}}{\dot{\omega}^2} = 2 - \frac{P\ddot{P}}{\dot{P}^2}. \quad (2.6)$$

The values of the braking index  $n$  found for some pulsars, e.g., the Crab pulsar ( $n = 2.509 \pm 0.001$ ; Lyne et al. 1988), PSR B1509–58 ( $n = 2.837 \pm 0.001$ ; Kaspi et al. 1994), and PSR B0540–69

( $n = 1.81 \pm 0.07$ ; Zhang et al. 2001) show the deviation from  $n = 3$ , which implies that a significant fraction of the pulsar's rotational energy is carried away by a pulsar wind, e.g., a mixture of electromagnetic field and charge particles. And a pulsar wind nebular (PWN) could be formed under some appropriate conditions, which is observable from the radio through  $\gamma$ -ray regions of the spectrum.

However, the observed luminosity of the pulsars is found to account only for a small fraction of the spin-down energy  $\dot{E}$ . The efficiencies,  $\eta = L/\dot{E}$ , observed in the radio and optical bands are typically in the range  $\sim 10^{-7} - 10^{-5}$ , whereas they are  $\sim 10^{-4} - 10^{-3}$  and  $\sim 10^{-2} - 10^{-1}$  at X-ray and  $\gamma$ -ray energies, respectively. There is still a mystery how rotation-powered pulsars lose large amounts of their rotational energy.

The popular model of magnetic braking provides plausible estimates for neutron star rotational energy loss  $\dot{E}$ , magnetic field  $B_{\perp}$ , and the characteristic age  $\tau$ . However, it does not give detailed information about the physical processes which operate in the pulsar magnetosphere and which are responsible for the broad-band spectrum, from the radio to the X-ray and  $\gamma$ -ray bands.

### 2.2.2 High-energy Emission Models

Rotation-powered pulsars are most widely known for their radio emission, but the mechanism of the radio emission is poorly understood. However, it is certainly different from those responsible for the high-energy (from infrared to  $\gamma$ -ray) radiation. The most promising radio emission mechanism is proposed to be the coherent curvature radiation. On the other hand, the optical, X-ray, and  $\gamma$ -ray emission from the pulsars must be incoherent with different radiation processes, e.g., synchrotron radiation, curvature radiation, and inverse Compton scattering. In addition, the fluxes in these energy bands are directly proportional to the densities of the radiating high-energy electrons in the acceleration regions. The thesis will focus on the X-ray studies of the rotation-powered pulsars.

So far, the high-energy radiation detected from rotation-powered pulsars has been attributed to various thermal and non-thermal emission processes described in the following:

- Thermal emission

Photospheric thermal emission comes from the hot surface of a cooling neutron star. A modified black-body spectrum and smooth, low-amplitude intensity variations with the rotational period could be observable from the optical through the soft X-ray range (cf. Greenstein & Hartke 1983; Romani 1987; Pavlov et al. 1994). In addition, the relativistic particles streaming back and bombarding the neutron star's polar caps from the pulsar magnetosphere also generate soft thermal X-ray emission (Kundt & Schaaf 1993; Zavlin et al. 1995; Gil & Krawczyk 1996).

- Non-thermal pulsed emission

The non-thermal pulsed emission is resulted from the charge relativistic particles accelerated in the pulsar magnetosphere. The X-ray broad band spectra can be described well

with a power-law-like model (cf. Michel 1991 and references therein). The emitted radiation can be observed from the optical to the gamma-ray bands. The X-ray luminosity of the rotation-powered pulsar as a function of the spin period can be detected as well.

- Non-thermal non-pulsed emission

Extended non-thermal X-ray emission could come from the pulsar-driven synchrotron nebulae (cf. Michel 1991 and reference therein), where the charged particles emit synchrotron radiation as they move along the magnetic field lines. Interaction between the relativistic pulsar wind which carries away the pulsar's rotational energy and the surrounding interstellar medium is also expected to create detectable diffuse non-thermal emission. These nebulae can be observed from radio through hard X-ray energies. Non-thermal radiation can also arise from a shock wave resulting from the interaction between the pulsar wind and the outflowing matter from the companion star.

The X-ray spectra of most of the spin-powered pulsars show a mixture of thermal and non-thermal components. Usually the available data do not allow to fully discriminate between these different emission scenarios.

The basic concepts of magnetospheric emission models, thermal emission from the neutron star surface, the emission mechanism of pulsar wind nebulae as well as shock emission in binary systems are briefly presented in the following.

- Magnetospheric emission models

Particle acceleration inside the pulsar magnetosphere gives rise to pulsed non-thermal radiation and possibly also thermal emission from backflowing particles that heat the neutron star surface. Rotating, magnetized neutron stars behave as natural unipolar inductors, generating huge electric field in vacuum. However, as was first noted by Goldreich & Julian (1969), a rotating neutron star will not be surrounded by vacuum, since a large surface charge will build up on the star. This surface charge is unstable because the induced vacuum electric field has a component parallel to the magnetic field ( $E_{\parallel}$ ) at the stellar surface that exceeds the gravitational force by many orders of magnitude and is capable of pulling charges out of the star. If charges are not trapped in the surface by binding forces, a charge density, known as the Goldreich-Julian or corotation charge density:

$$\rho_{GJ} = \frac{\nabla \cdot E}{4\pi} \simeq -\frac{\omega \cdot \mathbf{B}}{2\pi c}, \quad (2.7)$$

builds up in the neutron star magnetosphere. If the magnetospheric charge reaches the Goldreich-Julian value everywhere, it is able to short out the electric field parallel to the magnetic field (i.e.  $E \cdot B = 0$ ), and the dipole magnetic field will corotate with the star. Nevertheless, the corotation of the pulsar magnetosphere must break down at certain large distances from the neutron star as a result of the finite inertia of the particles. Where and how this happens is not well-known yet, but it is certain that corotation cannot pass the

speed-of-light cylinder radius (the distance at which the corotation velocity reaches  $c$ , see Figure 2.1):

$$R_{LC} = \frac{c}{\omega} = 5 \times 10^9 P \text{ cm}, \quad (2.8)$$

where  $P$  is the spin period of the pulsar in the unit of second. In this view, the magnetosphere can be divided into two regions: (1) The corotating closed field-lines region with the last closed field touching the light cylinder, and (2) the open field-line region with the last open field-line defining the conventional polar cap size  $R_{PC}$  on the stellar surface:

$$R_{PC} = R \left( \frac{2\pi R}{cP} \right)^{1/2}, \quad (2.9)$$

where  $R$  is the radius of the neutron star. It is believed that in the outer parts of the magnetosphere there must be a transition to the wind zone, where the energy density of the particles is large enough to distort the poloidal dipole field ( $B_p$ ) into a toroidal ( $B_\phi$ , which is perpendicular to the poloidal component) relativistic wind flow that carries the spin-down energy of the pulsar, in the form of magnetic and particle energy, into a surrounding nebula where it is dissipated as synchrotron (Rees & Gunn 1974; Kennel & Coroniti 1984).

The non-thermal pulsed emission is presumed to originate inside the corotating magnetosphere, and strong  $E_{\parallel}$  may develop to accelerate particles at two possible sites where  $E \cdot B \neq 0$ . Various emission models had been proposed. Despite the fact that these models are fundamentally different from each other, they do incorporate acceleration of electron/positron in the charge depletion regions (or gaps) of certain forms. High energy photons are produced when the charged particles are accelerated in these regions. According to the location of the accelerating regions, these models can be divided into two main classes: *Polar cap models* and *Outer-gap models* (see Figure 2.1). Polar-cap models (Sturrock 1971; Ruderman & Sutherland 1975) advocate that particle acceleration occurs near the neutron star surface and that high-energy emission results from a curvature radiation or inverse Compton induced pair cascade in a strong magnetic field while Outer-gap models (Cheng et al. 1986) assume that acceleration occurs in vacuum gaps that develop in the outer magnetosphere, along the last open field line above the null charge surfaces, where the Goldreich-Julian charge density changes sign, and that high-energy emission results from photon-photon pair production-induced cascades (for recent review, see Harding 2009 and Cheng 2009 and references therein).

- Thermal evolution of neutron stars

Neutron stars are born in the core-collapsed supernova explosions with a central temperature of  $T_c \sim 10^{11}$  K. Various processes of neutrino emission from the interior of the star carry away lots of initial thermal energy, leaving a one-day-old neutron star with the temperature of  $T_c \sim 10^9 - 10^{10}$  K. Within 10 to 100 years, the crust and the core of the neutron star become thermally adjust and the interior of the star becomes isothermal. The energy balance of the cooling neutron star is determined by the following equation:

$$C(T_i) \frac{dT_i}{dt} = -L_\nu(T_i) - L_\gamma(T_s) + \sum_k H_k, \quad (2.10)$$

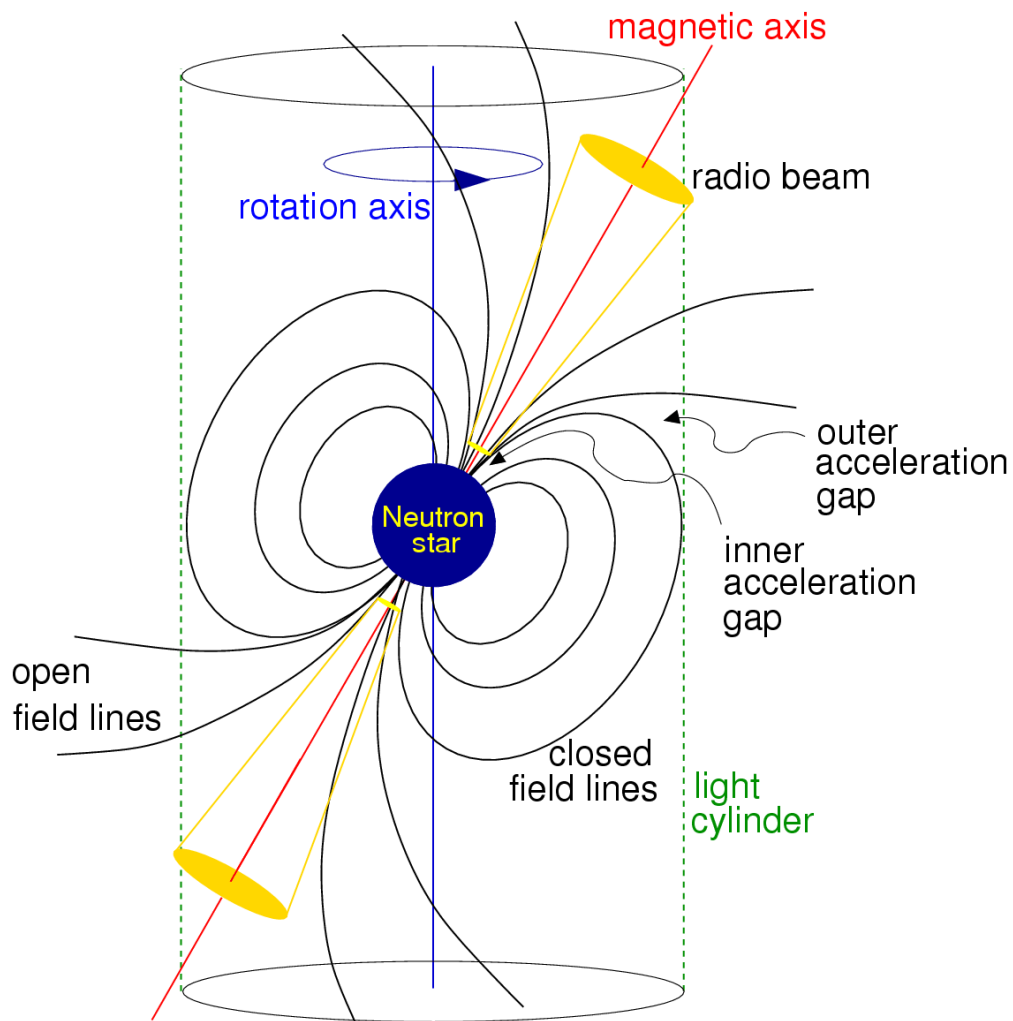


Figure 2.1: A diagram of the traditional magnetic dipole model of a pulsar. The figure is from the Handbook of Pulsar Astronomy by Lorimer and Kramer

where  $C(T_i)$  is the heat capacity of the neutron star and  $T_i$  and  $T_s$  are the internal and surface temperatures. Neutron star cooling means a decrease of thermal energy due to energy loss by neutrinos from the interior ( $L_\nu = \int Q_\nu dV$ ,  $Q_\nu$  is the neutrino emissivity) and by thermal photons from the surface ( $L_\gamma = 4\pi R^2 \sigma T_s^4$ ). However, the cooling rate might be reduced by some heating mechanisms  $H_k$ , such as frictional heating of superfluid neutrons in the inner crust or some exothermal nuclear reactions. In the following  $\sim 10^3$  yr or more likely  $\sim 10^5 - 10^6$  yr (depending on leading neutrino emission process), neutrino emission dominates over photon emission until  $T_c \sim 10^7 - 10^8$  K. The thermal behavior before  $10^6$  yr depends strongly on cooling model. After  $t \simeq 10^6$  yr, photon emission from the neutron star surface takes over as the main cooling mechanism and various internal and external heating mechanisms dominate thermal emission over the initial cooling.

During the first  $\sim 10^5 - 10^6$  yr, a neutron star cools mainly via neutrino emission. The main cooling mechanism in the core is neutrino emission via the Urca process<sup>2</sup>. The most efficient cooling mechanisms are the so-called direct Urca process (Lattimer et al. 1991), which is a sequence of a  $\beta$ -decay and an electron capture:



and



The process is only permitted if energy and momentum can be simultaneously conserved. This requires that the proton-to-neutron ratio exceeds 1/8, or the proton fraction  $x \geq 1/9$ , which is far above the value found in neutron star matter in the vicinity of  $n_0$ . If the neutrons and protons are the only baryons in the star and the proton fraction is not sufficiently high, the direct Urca process will be forbidden. In this case, a so-called standard cooling scenario will take place with the “modified” Urca process (Chiu & Salpeter 1964) as the cooling mechanism:



and



where  $N$  is a nucleon (neutron or proton). To proceed at interesting rates in the neutron-star interior for a wide range of expected interior properties, the modified Urca process requires a spectator reactant to simultaneously conserve energy and momentum. Comparing with the direct Urca reactions, the cooling rate of the modified Urca process is considerably slower. Therefore, the surface thermal emission of a neutron star is expected to remain observable for a few million years within the context of a standard cooling scenario.

Studies of neutron star cooling has been proposed to be a promising probe to unriddle the interior structure and physics of neutron stars and measuring the surface temperatures of

---

<sup>2</sup>Urca is the name of a long-since-closed casino in Rio de Janeiro, and was adopted as a name for these reactions by Gamow & Schoenberg (1941) who saw a parallel between how casinos extract money from players and how nature extracts energy in these reactions.

neutron stars is an important tool to study super-dense matter. The thermal emission from the cooling neutron stars can be observed with the X-ray detectors sufficiently sensitive at  $E \lesssim 1$  keV.

- Pulsar wind nebulae (PWNe)

The high energy radiation within the light cylinder which contributes to the non-thermal pulsed emission of a pulsar can be explained by the magnetospheric emission models. However, the pulsed component only consumes a small fraction ( $\lesssim 10\%$ ) of the spin-down energy of a pulsar (Gaensler & Slane 2006). It is generally accepted that most of the rotational energy leaves the pulsar's magnetosphere in the form of a magnetized wind (Michel 1969), which contributes the non-thermal non-pulsed component of the observed emission.

The charged particles flow outward with the magnetic field forming a magnetized wind which is ultimately accelerated to very high energies. This highly magnetized relativistic wind eventually interacts with the surrounding medium and emits synchrotron radiation from radio to  $\gamma$ -ray wavelengths. This synchrotron emission caused by the pulsar wind is generally termed pulsar wind nebula (PWN). To characterize the pulsar wind, a magnetization parameter,  $\sigma$ , introduced to describe the efficiency of the conversion of energy contained in the pulsar wind into synchrotron radiation, is commonly used which is defined as the ratio of the Poynting flux,  $F_{\text{E}\times\text{B}}$ , to the particle energy flux,  $F_{\text{particle}}$ :

$$\sigma \equiv \frac{F_{\text{E}\times\text{B}}}{F_{\text{particle}}} = \frac{B^2}{4\pi\rho\gamma_w c^2}, \quad (2.15)$$

where  $B$ ,  $\rho$ , and  $\gamma_w$  are the magnetic field, the mass density of the wind particles, and the corresponding Lorentz factor, respectively. All pulsar emission models predict that just inside the light cylinder the wind leaving the pulsar magnetosphere is dominated by the magnetic energy density, with a much smaller contribution from the particle energy density. And the typical value of the magnetization parameter  $\sigma$  is  $> 10^4$  when the pulsar wind flows through the light cylinder (Gaensler & Slane 2006). However, as suggested by Kennel & Coroniti (1984), the magnetization parameter must be small (for the Crab Nebula, de Jager & Harding (1992) have found  $\sigma \sim 0.003$  just behind the termination shock) in order to pressure boundary conditions at the outer edge of the PWN and transfer the bulk flow energy to random particle motion and produce the observed synchrotron radiation. This implies the nature of the wind must dramatically change in a region between the pulsar light cylinder and the wind termination shock although the mechanism for this transition is still unclear (see Arons 2002).

The standard theoretical picture for PWNe from young pulsars (Pacini & Salvati 1973; Rees & Gunn 1974; Reynolds & Chevalier 1984; Kennel & Coroniti 1984) is of a synchrotron bubble being blown at the center of an expanding supernova remnant. Initially, the outer edge expands supersonically into the supernova ejecta, so is presumably bounded by a forward shock. The corresponding reverse shock is near the center of the nebula, where the relativistic wind from the pulsar is terminated. The bulk flow energy is then

converted into random particle motion with a power-law distribution of particle energies. The wind continuously injects high-energy electrons and positrons as well as magnetic field into the bubble. The particles gyrate in the magnetic field, emitting synchrotron radiation from the radio through  $\gamma$ -ray regions of the spectrum.

Physical models for describing PWN emission can be divided into two main classes, depending on whether the pulsar is moving subsonically or supersonically (see Cheng et al. 2004). For a pulsar with the subsonic velocity, the shock termination radius  $R_s$  is determined by the balance between the wind ram pressure and the total magnetic and particle pressure within the nebula (Rees & Gunn 1974):

$$R_s \simeq \left( \frac{\dot{E}}{B^2 c} \right)^{1/2} \quad (2.16)$$

where  $\dot{E}$  is the spin-down power of the pulsar. This will result in a wind bubble with the pulsar located at the center. In the case of the supersonic motion, the nebula will form a bow shock morphology.  $R_s$  is then obtained via the balance of the ram pressure between the wind particle and the interstellar medium (ISM) at the head of the bow shock:

$$R_s = \left( \frac{\dot{E}}{2\pi\rho_{\text{ISM}}v_p^2 c} \right)^{1/2} \quad (2.17)$$

where  $\rho_{\text{ISM}}$  and  $v_p$  are the density of the ISM and the pulsar's proper motion velocity, respectively. Apart from the non-thermal emission, the fast-moving pulsar could also produce an  $H\alpha$  shock, which results from the collisional excitation and charge exchange of the neutral hydrogen atoms in the ISM. This is essentially a thermal process.

Recent discoveries of TeV emission associated with PWNe have opened a new channel for investigations of the structure and evolution of these objects (de Jager & Djannati-Ataï 2008). This emission in the TeV band probably originates from Inverse-Compton (IC) scattering of ambient soft photons with energetic electrons in the nebula (Atoyan & Aharonian 1996). The seed soft photons for the IC processes are possibly contributed by the cosmic microwave background, interstellar dust, starlight and the synchrotron photons emitted by the accelerated particles (see Gallant et al. 2006). Apart from the leptonic model, a hadronic model, which involves the decay of neutral pions produced in collisions of energetic ions with ambient hadronic material, has also been proposed for the TeV emission from the pulsar wind nebulae (Horns et al. 2006).

The details of the structure and luminosity of the PWN should depend on the pulsar's spin-down energy history and space velocity as well as the density profile of the surrounding medium. It may also depend upon the magnetic inclination angle of the pulsar, although the details on how the wind properties depend on this angle is poorly understood. Doppler boosting is also a non-negligible factor in the surface brightness distribution of the PWN due to the dependence of the the observer's viewing angle. There appears to be a minimum spin-down energy necessary to create bright PWNe with a significant drop in

PWN emission efficiency from pulsars with  $\log \dot{E} \lesssim 36$  (Frail & Scharringhausen 1997; Gaensler et al. 2000; Gotthelf 2003), and generally only the youngest isolated pulsars are observed to have PWNe. However, millisecond pulsars can also have a substantial  $\dot{E}$ , and both  $H\alpha$  (Bell et al. 1995) and X-ray (Stappers et al. 2003) nebulae have been observed around them.

- Intra-binary shock emission

Non-thermal non-pulsed radiation can also arise from a shock wave resulting from the interaction between the pulsar wind and the outflowing matter from the companion stars (Arons & Tavani 1993; Stella et al. 1994; Tavani & Arons 1997). The nature of their X-ray emission is very similar to that in a PWN. For high- $\dot{E}$  pulsars in binary systems, the confining medium can be the wind of the companion star. In this case, the confinement, particularly for eccentric binaries, is strongly orbital-phase dependent, leading to a PWN of luminosity that varies systematically with orbital phase. Even circular orbits are of interest since the orientation of the PWN, which is not expected to be isotropic, changes with orbital phase.

In the shock, the extended matter in the orbit is compressed and gives rise to a power law distribution of synchrotron-emitting particles,  $N(\gamma) \propto \gamma_w^{-p}$ , by accelerating a fraction of these particles to very high energies, where  $\gamma_w$  is the Lorentz factor of the emitting particles. This should lead to an enhancement of X-ray emission from the system as the pulsar enters the eclipsing region and a subsequent decrease due to the increased absorption in this region. The termination radius of the pulsar wind is given by the pressure balance between the pulsar and companion outflow and can be expressed as

$$\left( \frac{R_s}{R_c + R} \right)^2 = \frac{\dot{E}}{\dot{M} v_w c}, \quad (2.18)$$

where  $R_s$  is the shock wave termination radius as measured from the neutron star surface,  $R_c$  is the radius of the companion,  $R$  is the distance of the shock from the surface of the companion star,  $v_w$  is the outflow velocity, and  $\dot{M}$  is the mass loss rate of the companion star.

In the Galactic field only two such systems have been detected in X-rays: PSRs B1259–63 (Chernyakova et al. 2006) and B1957+20 (Stappers et al. 2003; Huang & Becker 2007). The recent Chandra X-ray studies of the millisecond pulsars (MSPs) in globular clusters reveal that MSPs J, O, and W in 47 Tucanae (hereafter 47 Tuc; Bogdanov et al. 2005, 2006), PSR J1740–5340 in NGC 6397 (Huang & Becker 2009), and PSR J1953+1846A in M71 (Elsner et al. 2008) exhibit a non-thermal component. It is believed that the non-thermal spectral components are produced in an intrabinary shock formed by the interaction between the relativistic wind and matter from the stellar companion. Of these MSPs, only 47 Tuc W exhibits dramatic X-ray variability as a function of orbital phase. Their rarity is because of the need to have a high  $\dot{E}$  pulsar in a binary system in which the two components come sufficiently close to each other for the shock to be strong, but not too close so that accretion occurs. In principle, such systems are an excellent diagnostic of shock

acceleration and the pulsar wind as they have regular, repeating and predictable dynamical properties.

### 2.2.3 Rotation-powered Millisecond Pulsars

Figure 2.2 shows the  $P-\dot{P}$  diagram with all catalogued rotation-powered neutron stars, which is very useful for classification purposes. There are two different populations of rotation-powered neutron stars: (1) the majority of ordinary field pulsars with spin periods longer than 20 ms and the magnetic fields of  $B_{\perp} \sim 10^{11} - 10^{12}$  Gauss and (2) the fast-rotating millisecond pulsars (MSPs) with the very short spin periods of  $P \leq 20$  ms and small period derivatives of  $\dot{P} \approx 10^{-18} - 10^{-21}$  s s<sup>-1</sup>. In the frame of the magnetic braking model this corresponds to very old spin-down ages of typically  $10^9 - 10^{10}$  years and low magnetic field strengths of  $\sim 10^8 - 10^{10}$  Gauss. The millisecond pulsars are often referred to as “recycled” pulsars as they are thought to be formed in a past accretion phase by mass and angular momentum transfer from a binary late-type companion (Alpar et al. 1982; Radhakrishnan & Srinivasan 1982). More than  $\sim 70\%$  of the known disk MSPs are in binaries, usually with a low-mass white dwarf companion, compared to  $\simeq 1\%$  binaries among the ordinary pulsars. This gives support to the idea that these neutron stars have been spun-up in the past. Further evidence for this came from the discovery of seven accreting MSPs which seem to confirm this scenario (see Wijnand 2005 for a review). The unusually high magnetic sources with  $B_{\perp} \gtrsim 10^{14}$  Gauss, e.g., soft gamma-ray repeaters (SGR) and anomalous X-ray pulsars (AXP), are thought to be “magnetars” (Duncan & Thompson 1992).

By early 2010, about 10% of the  $\sim 1900$  known radio pulsars fall into the category of MSPs, i.e. are recycled (cf. Manchester et al. 2005). The majority of them ( $\sim 70\%$ ) are located in 26 globular clusters<sup>3</sup> which apparently provide a favorable environment for the recycling scenario. Of these globular cluster MSPs 74 ( $\sim 60\%$ ) are in binaries, the others are solitary. The ratio of binary MSPs in GCs is a bit lower than the 70% observed in the population of Galactic disk MSPs. The formation of solitary recycled pulsars is not well-understood, but it is widely believed that either the pulsar’s companion was evaporated (a process which is believed to be at work in the PSR B1957+20 binary system) or the system was tidally disrupted after the formation of the MSP.

Recycled pulsars had been studied merely in the radio domain until the 1990s, when ROSAT, ASCA, RXTE and BeppoSAX were launched. The first millisecond pulsar discovered as pulsating X-ray source was PSR J0437–4715 (Becker & Trümper 1993), a nearby 5.75 ms pulsar which is in a binary orbit with a low-mass white dwarf companion. With further detections,  $\sim 49\%$  of all X-ray detected rotation-powered pulsars are MSPs by March 2010. With the aid of the improved sensitivity of Chandra and XMM-Newton X-ray observatories, it not only provided the high quality spectral, temporal and spatial information but also provide a step forward in classifying the MSPs X-ray emission properties, indicating that there is a dichotomy between thermal and non-thermal dominated emitters, similar to what is observed from non-recycled pulsars.

<sup>3</sup><http://www.naic.edu/~pfreire/GCpsr.html>

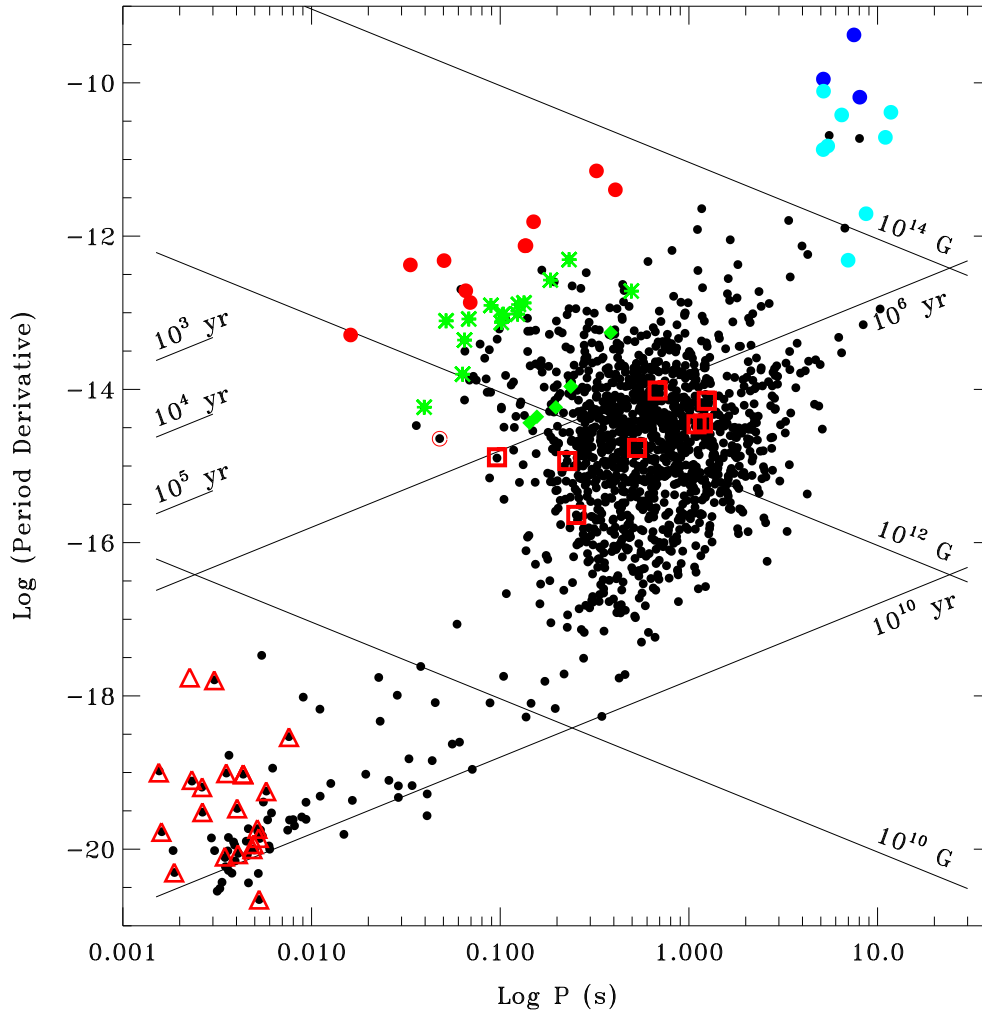


Figure 2.2: The  $P - \dot{P}$  diagram. Small black dots show the distribution of rotation-powered pulsars. The straight lines of constant characteristic ages  $\tau$  and surface magnetic field strengths  $B_{\perp} = 3.2 \times 10^{19} (P\dot{P})^{1/2}$  as deduced in the frame of the magnetic braking model are indicated. Millisecond pulsars are distinguished from the majority of ordinary field pulsars and located in the lower left corner, while the high magnetic field pulsars ( $B_{\perp} \gtrsim 10^{14}$  Gauss), e.g., soft gamma-ray repeaters (SGR; dark blue) and anomalous X-ray pulsars (AXP; light blue), are located in the upper right corner. The Crab-like pulsars, the Vela-like pulsars, and the X-ray detected cooling neutron stars mark by the red circles, green stars, and green diamonds. Red squares and red triangles indicate the million-year old pulsars and the X-ray detected millisecond pulsars, respectively. Figure from Becker (2009).



# Chapter 3

## Observatories & Telescopes

### 3.1 X-ray Observatories

Since X-ray radiation is absorbed by the Earth's atmosphere, the X-ray detectors must be placed high above the Earth's surface, in the past with balloons and sounding rockets. Nowadays, X-ray astronomy is part of space research and X-ray telescopes are placed on satellites. In 1949, X-rays from the Sun were first detected by the Navy's experiment on board the V-2 rocket. The first known celestial X-ray source (Scorpius X-1) apart from the Sun was discovered in 1962 during a sounding-rocket flight. In the following ~40 years, studies of high-energy astrophysics continue to be carried out. In the 1990s ROSAT detected more than 150,000 X-ray objects used to construct the catalog by the all-sky survey. The ASCA mission then made the first sensitive measurements of the X-ray spectra from these objects, and RXTE studied the timing properties. In 1999 the launch of the Chandra and XMM-Newton observatories brought high-resolution imaging, spectral information, and high-throughput capability to X-ray astronomy. These missions combined with Suzaku/Astro-E2, launched in 2005, have ushered in a new age of studying the nature of X-ray sources and their mechanisms with a far greater sensitivity and resolving power than ever before. In my thesis, I reported on several research projects by utilizing the Chandra and XMM-Newton observatories. The following sections give an overview on these two observatories.

#### 3.1.1 Chandra X-ray Observatory

On the 23 of July 1999, NASA's Advanced X-ray Astrophysics Facility, (AXAF), renamed the Chandra X-ray Observatory in honor of Indian-American physicist Subrahmanyan Chandrasekhar, was boosted into a 64-hour highly-eccentric Earth orbit by the Space Shuttle Columbia, which allows long-duration uninterrupted exposures (~ 55 hours) of celestial objects. The Chandra observatory carries a high resolution four-nested paraboloid-hyperboloid (Wolter-I) mirror, two imaging detectors – the Advanced CCD Imaging Spectrometer (ACIS) and the High Resolution Camera (HRC), and two sets of transmission gratings (LETG and HETG). Sub-arcsecond spatial resolution, large effective area, and high sensitivity in the energy range of 0.1–10.0 keV

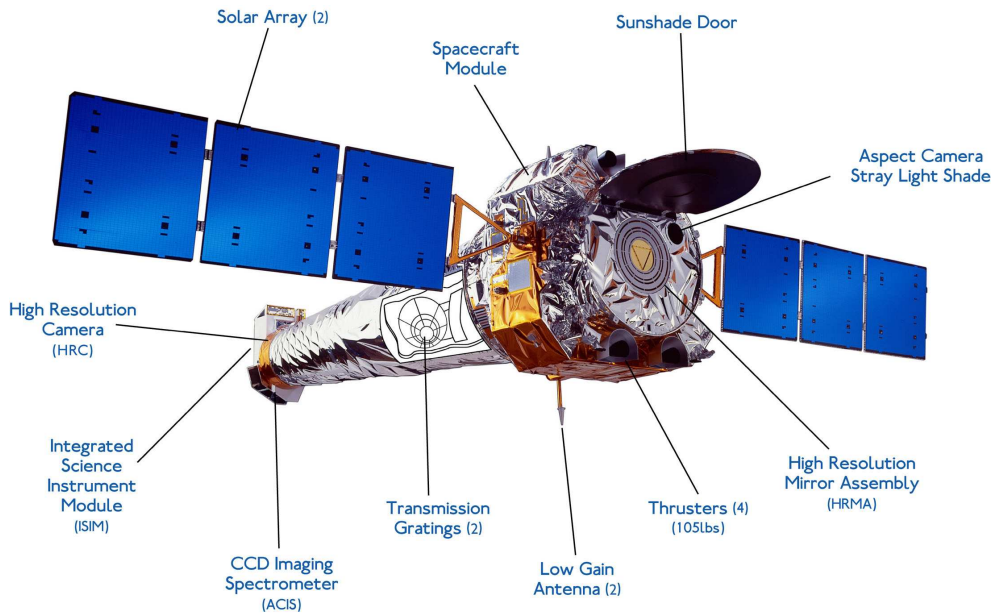


Figure 3.1: Image of the Chandra X-ray Observatory and its science payload. (Courtesy of NASA/CXC/SAO)

make it possible for Chandra to study extremely faint source, especially those in the crowded regions (e.g. globular clusters).

A labeled sketch of the Chandra X-ray observatory is shown in Figure 3.2. It consists of a spacecraft and a telescope/science-instrument payload. The principal elements onboard Chandra are described below:

1. High Resolution Mirror Assembly (HRMA):

The HRMA comprises four pairs of concentric thin-walled grazing-incidence X-ray mirrors in the Wolter Type-I configuration. i.e. the front mirror of each pair is a paraboloid while the back is a hyperboloid. The eight mirrors are made of Zerodur glass and coated with iridium (Ir) on a binding layer of chromium (Cr). The focal length is  $\sim 10$  m and their diameters range from 0.63 m to 1.23 m. A detailed overview on X-ray optics is given by Aschenbach (1985).

2. Focal-plane Science Instruments (SIs):

A summary of the characteristics of Chandra science instruments is give in Table 3.1.

- Advanced CCD Imaging Spectrometer (ACIS)

ACIS provides the capability to simultaneously obtain high-resolution images and moderate resolution spectral information in the energy range of 0.2 – 10 keV. It contains ten  $1024 \times 1024$  pixel CCDs, four of which are arranged in a  $2 \times 2$  array (ACIS-I) which are optimized for imaging and the other six CCDs arrange in a  $1 \times 6$  array

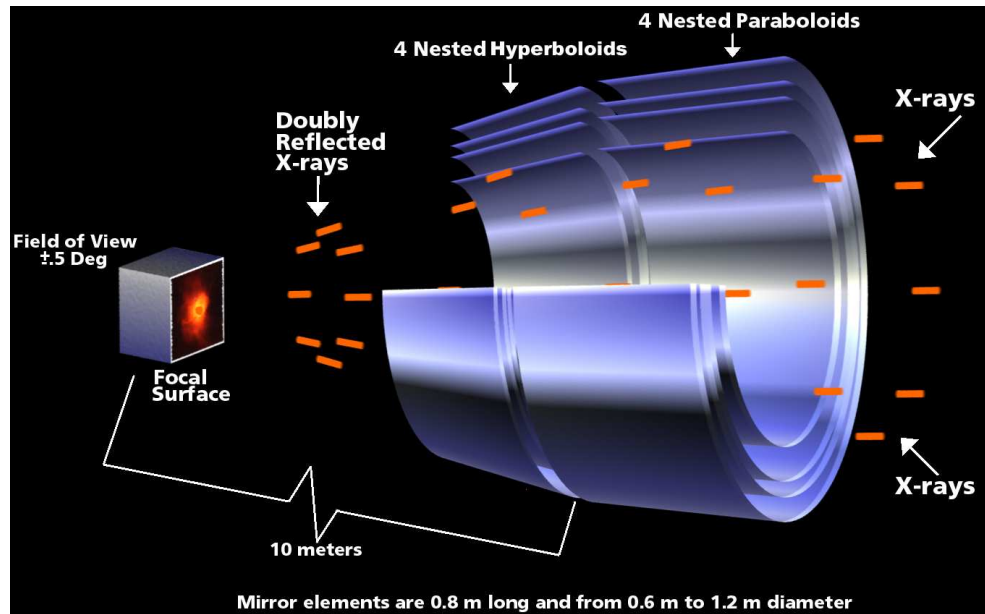


Figure 3.2: Chandra's X-ray mirror assembly focuses X-rays onto a detector to produce an image. This is a Wolter type-I telescope, which contains two mirrors, a paraboloid and a hyperboloid, to reflect incident X-rays to a common focus. (Courtesy of NASA/CXC/D.Berry)

(ACIS-S) which can be used either for imaging or for high-resolution spectroscopy in conjunction with the High Energy Transmission Grating (HETG). There are two types of CCD chips. ACIS-I is comprised of four front-illuminated (FI) CCDs while ACIS-S is comprised of four FI and two back-illuminated (BI) CCDs, one of which (i.e. ACIS-S3) is at the best focus position. The BI CCDs have better quantum efficiency at the soft X-ray band, whereas the FI CCD response is more efficient at higher energies but the energy resolution varies with position due to radiation damage caused by protons reflecting through the telescope during radiation-zone passages in the early part of the mission. The chip-averaged energy resolution of the BI devices is better than that of the FI devices. The field of view (FOV) for the ACIS-I array and for the ACIS-S array is  $\sim 16.9' \times 16.9'$  and  $\sim 8.3 \times 50.6'$ , respectively. The spatial resolution for on-axis imaging with the ACIS instrument is limited by the pixel size of  $\sim 0.492$  arcsecond.

ACIS is a complex instrument having many different characteristics and operating modes – the Timed Exposure (TE) mode and the Continuous Clocking (CC) Mode. Operating in the TE mode, frame times are selectable within a range of values spanning the time interval from 0.2 to 10.0 seconds. Typically the nominal read-out time in the full-frame mode is 3.2 s, which can cause pile-up (i.e. when two or more photons are detected in the same pixel at the same time causing a single event) during observations of bright X-ray sources. Selecting subarrays (i.e. restricting the region of the CCD in which the data will be taken) yields a faster frame time and therefore

also lowers the pile-up ratio. For an even faster timing response, CCDs can be operated in the CC mode with a high temporal resolution of  $\sim 2.85$  milliseconds (ms), which allows us to investigate the short time variability of observed sources but at the expense of one dimension of spatial resolution.

- High Resolution Camera (HRC)

The HRC is comprised of two CsI-coated microchannel plate (MCP) imaging detectors. One is the HRC-I optimized for wide-field imaging with a field of view of  $30' \times 30'$  and the other HRC-S is designed to serve as a readout for the Low Energy Transmission Grating (LETG). The HRC detectors have the highest spatial resolution ( $\sim 0.4''$ ) among all the detectors aboard Chandra, albeit without comparable spectral resolution. Under certain circumstances, the HRC-S detector also offers the fastest time resolution ( $16 \mu\text{s}$ ).

There are a number of optional operating modes that might be invoked to optimize a particular observation. The HRC-S is normally operated in spectroscopy mode, where signals from any of the three MCP segments can be recognized as triggers. An alternate operation mode, timing mode, ties the signals from the outer segments to ground so that only signals from the center MCP generate triggers. For the edge- or center-blanking mode, it is possible to define a rectangular region, other than the default region, on both the HRC-I and the HRC-S in order to prevent events from a nearby bright source from contributing to telemetry. Events from either inside (edge-blanking) or outside (center-blanking) the defined regions are telemetered.

Table 3.1: The basic characteristics of Chandra science instruments. All values are from the Chandra proposers' observatory guide.

Instruments	ACIS-S	ACIS-I	HRC-S	HRC-I
Field of view (FOV)	$8.3' \times 50.6'$	$16.9' \times 16.9'$	$6' \times 99'$	$30' \times 30'$
Bandpass (keV)	0.2–10.0		0.08–10.0	
PSF (FWHM) <sup>a</sup>	$\sim 0.492''$		$\sim 0.4''$	
Pixel size	$\sim 0.492''$		$\sim 0.132''$	
Time resolution	TE <sup>b</sup> : 0.2–10.0 s ; CC <sup>b</sup> : $\sim 2.85$ ms		16 $\mu\text{s}$	
Spectral resolution (E/ $\Delta$ E)	FI <sup>c</sup> : 20–50 ; BI <sup>c</sup> : 9–35		$\sim 1$	
Effective area (cm <sup>2</sup> @1 keV)	FI: 340 ; BI: 340		N/A	227

a. PSF: point spread function; FWHM: full width half maximum

b. TE: Timed Exposure Mode; CC: Continuous Clocking Mode

c. FI: front-illuminated CCDs; BI: back-illuminated CCDs

### 3. Objective Transmission Gratings:

- High Energy Transmission Grating (HETG)

In operation with the ACIS-S, the HETG forms the High-Energy Transmission Grating Spectrometer (HETGS) for high resolution spectroscopy with a resolving power ( $E/\Delta E$ ) up to 1000 in the energy band between 0.4 keV and 10.0 keV. The HETG is comprised of two grating assemblies – the High Energy Grating (HEG) and the Medium Energy Grating (MEG). The HEG intercepts X-rays from the two inner mirror shells and is optimized for high energies while the MEG intercepts X-rays from the two outer mirror shells in the medium energy range. The HEG and MEG dispersion directions are offset by 10 degrees so the two patterns can be easily distinguished.

- Low Energy Transmission Grating (LETG)

The Low Energy Transmission Grating Spectrometer (LETGS) comprises the LETG, the High Resolution Mirror Assembly (HRMA), and a focal plane imaging detector, ACIS-S or HRC-S. The LETGS provides the highest spectral resolution ( $E/\Delta E \geq 1000$ ) on Chandra at low (0.07 – 0.15 keV) energies. The nominal LETGS energy range accessible with the HRC-S is 0.07 – 10.0 keV and the useful coverage for ACIS-S is ~0.2 – 10.0 keV.

### 3.1.2 XMM-Newton X-ray Observatory

The European Space Agency's X-ray Multi-Mirror Mission (XMM-Newton) was launched into a 48-hour orbit on December 10, 1999. Three co-aligned high throughput Wolter type-I X-ray telescopes and one co-aligned 30-cm optical/UV telescope are on board XMM-Newton observatory. Each of the X-ray telescopes consists of 58 gold-coated nested mirrors in order to obtain the highest possible mirror geometric effective area, which reflects the ability of the mirrors to collect radiation at different photon energies, over a wide range of energies. Each mirror shell consists of a paraboloid and an associated hyperboloid which were replicated together in one piece to facilitate alignment and integration. The unprecedented collecting area of  $\sim 1550 \text{ cm}^2$  at 1.5 keV energy for each X-ray telescope, i.e.,  $\sim 4650 \text{ cm}^2$  in total, enables highly sensitive observations. Besides its three X-ray telescopes, XMM-Newton was designed to have an optical telescope which consists of an  $f/12.7$  modified Ritchey Chrétien optical system. This provides the possibility to observe simultaneously in the X-ray and optical/UV regime from a single platform for the first time.

In the following, we briefly describe the capabilities of three types of science instrument onboard XMM-Newton and summarize the most important characteristics of XMM-Newton in Table 3.2. A sketch of the XMM-Newton observatory is displayed in Figure 3.3.

1. European Photon Imaging Camera (EPIC):

Each of the X-ray telescopes is equipped with an X-ray CCD camera in the focal plane, called European Photon Imaging Camera. It comprises two Metal Oxide Semi-conductor (MOS1/2) CCD arrays and one Positive-Negative depleted Silicon CCD camera (PN). Each of the MOS camera consists of 7 front-illuminated CCDs and the orientation of MOS1 and MOS2 are perpendicular to one another so that the gaps between the CCD chips of one camera can be covered by the other. However, the PN camera was made of

Table 3.2: The basic characteristics of XMM-Newton. All values are from XMM-Newton Users' Handbook.

Instruments	EPIC/MOS	EPIC/PN	RGS	OM
Bandpass	0.15–12 keV	0.15 – 15 keV	0.35–2.5 keV <sup>(1)</sup>	180–600 nm
Field of view (FOV)	~ 30'	~ 30'	~5'	17'
PSF (FWHM/HEW)	5"/14"	6"/15"	N/A	1'4–2'0
Pixel size	40 $\mu\text{m}$ (~ 1'1)	150 $\mu\text{m}$ (~ 4'1)	81 $\mu\text{m}$ ( $9 \times 10^{-3} \text{\AA}$ )	0'476513
Timing resolution <sup>(2)</sup>	1.5 ms	0.03 ms	0.6 s	0.5 s
Spectral resolution <sup>(3)</sup>	~ 70 eV	~ 80 eV	0.04/0.025 $\text{\AA}$ <sup>(4)</sup>	350 <sup>(5)</sup>
Effective area ( $\text{cm}^2$ @ 1 keV)	922	1227	185	N/A

Notes:

- 1) In the -1. grating order (wavelength range: 5–35  $\text{\AA}$ )
- 2) In fast data acquisition mode (i.e., fast mode for OM and timing mode for EPIC, spectroscopy mode for RGS, reading out only one of nine CCDs). The EPIC pn burst mode offers an even higher timing resolution of 7  $\mu\text{s}$ , but has a very low duty cycle of 3%
- 3) At 1 keV energy. At the energy of Fe  $K_{\alpha}$  (6.4 keV), the energy resolution of both EPIC cameras is ca. 150 eV
- 4) In -1. and -2. order, resp.; at 1 keV, this corresponds to 3.2/2.0 eV (HEW)
- 5) Resolving power ( $\lambda/\Delta\lambda$ ) with UV and optical grism

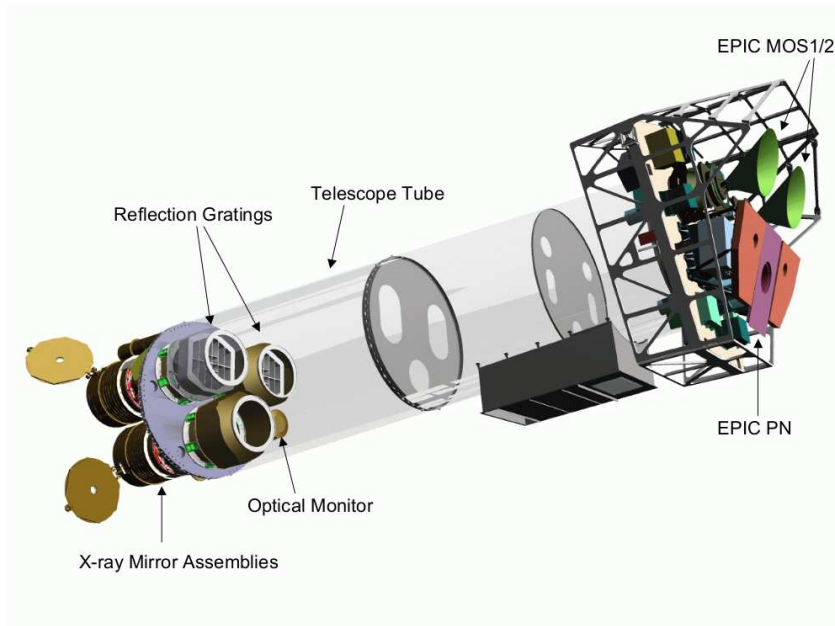


Figure 3.3: An image of the XMM-Newton observatory with three X-ray telescopes, an optical monitor, the grating assemblies, and the EPIC MOS1/2 and PN cameras. (Courtesy of ESA).

12 back-illuminated CCDs which provide the camera to have a better spectral sensitivity at the soft X-ray band. The physical size of each pixel for the MOS1/2 and the PN CCDs is  $\sim 1''.1$  and  $\sim 4''.1$ , respectively. The EPIC CCDs are designed to perform highly sensitive imaging observations over a  $30'$  field of view in the energy range of 0.15 – 15 keV with moderate spectral ( $E/\Delta E \sim 20 - 50$ ) and angular resolution (FWHM:  $6''$ ; HEW:  $15''$ ).

Those cameras can be operated parallel and provide a variety of data collection modes which are very well suited for pulsar studies. To operate the PN camera in the small-window mode is the most beneficial for timing studies of pulsars and the sources located in supernova remnants (SNRs) and crowded regions since it can prevent the source confusion and provide spectral and imaging information for a sky field of  $\sim 4'.4 \times 4'.4$  with a  $\sim 6$  millisecond temporal resolution. For even faster rotating recycled pulsars, the timing mode of the PN CCD can be employed with temporal resolutions of  $\sim 0.03$  ms. However, the spatial information in the Y-direction is lost because the two dimensional spectral and spatial information from a  $64 \times 199$  CCD pixel array is collapsed into one dimensional  $64 \times 1$  pixel array (1-D image). The burst mode with very high temporal resolution of 0.007 ms is designed for the very bright source up to 6.3 Crab only.

## 2. Reflection Grating Spectrometer (RGS):

It consists of Reflection Grating Assemblies (RGAs) and RGS Focal Cameras (RFCs) which are placed on two of the three X-ray telescopes and intercept about 58% of the total light collected by the mirror module onto an array of 9 MOS CCD chips. The rest about 42% of the original incoming flux reaches the MOS1/2 cameras. The RGS MOS chips are back-illuminated in order to maximize the soft energy response and aluminium-coated on the exposed side in order to suppress optical and UV light. The RGS provides high spectral resolution ( $E/\Delta E$  from 200 to 800) X-ray spectroscopy over the energy range 0.35–2.5 keV (5–35 Å).

## 3. Optical Monitor (OM):

The OM detector consisting of a micro-channel plate (MCP) intensified CCD (MICs) is a compact image-intensified photon-counting instrument. The  $2048 \times 2048$  pixel CCD provides sensitivity from 180 nm to 600 nm with a field of view of  $17' \times 17'$  and its pixel size is about  $0'.476 \times 0'.476$ . The FWHM of the on-axis PSF depending on different filters is from  $1''.4$  to  $2''.0$  and the  $5\text{-}\sigma$  detection limit can be down to the B-band apparent magnitude of  $m_B \sim 20.7$ . Although small in size, the OM is very well appropriate for observing faint stars due to its extreme sensitivity and the absence of atmospheric extinction, diffraction and background and also offers the opportunity to monitor and identify the optical/UV counterparts to X-ray sources observed by the X-ray telescope as well as imaging of the surrounding field.

There are in total six science instruments on board XMM-Newton, which can be operated independently and simultaneously. The high throughput of the instruments provide high resolution spatial, spectral and temporal information from a source during a single observation and make XMM-Newton unique and best suited for pulsar studies.

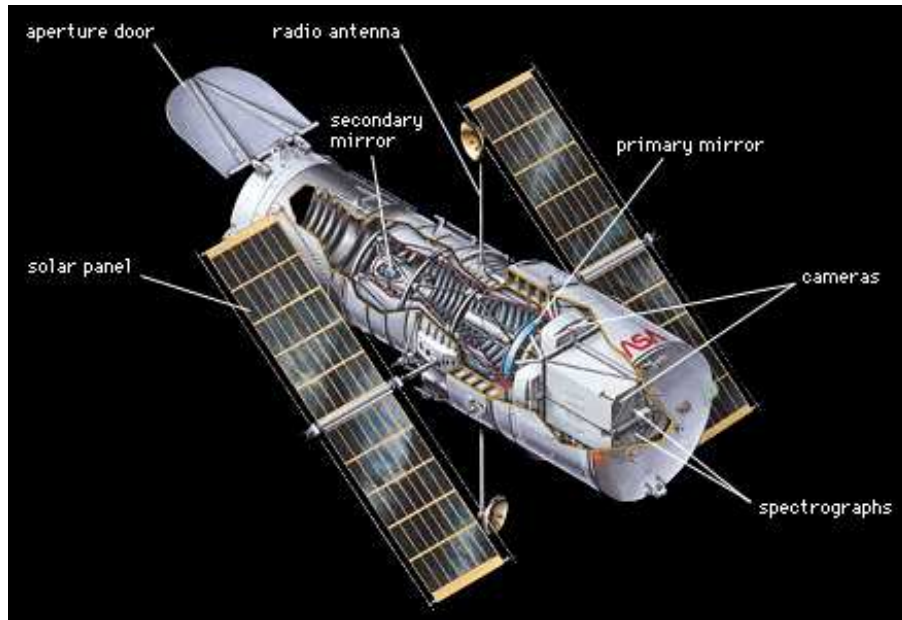


Figure 3.4: Image of the Hubble Space Telescope and its instruments. The image is from [http://www.nasa.gov/mission\\_pages/hubble/spacecraft/index.html](http://www.nasa.gov/mission_pages/hubble/spacecraft/index.html).

## 3.2 The Hubble Space Telescope

The Hubble Space Telescope (HST) is a cooperative program of the European Space Agency (ESA) and the National Aeronautics and Space Administration (NASA) to operate a long-lived space-based observatory for the benefit of the international astronomical community. HST is a 2.4-meter reflecting telescope (Figure 3.4), which was launched into a low-Earth orbit of ~600 kilometers by the crew of the space shuttle Discovery (STS-31) on 25 April 1990. Because of HST's location above the Earth's atmosphere, these science instruments can produce high-resolution images of astronomical objects. Ground-based telescopes are limited in their resolution by the Earth's atmosphere, which causes a variable distortion in the images. Hubble can observe ultraviolet as well as infrared radiation, which is blocked by the atmosphere and therefore unavailable to ground-based telescopes.

Hubble is a type of telescope known as a Cassegrain reflector. Light bounces off the concave primary mirror and then is reflected to the convex secondary mirror. The secondary mirror focuses the light through a hole in the center of the primary mirror that leads to the telescope's science instruments. Its science instruments can work together or individually to provide the observation. Each instrument is designed to examine the universe in a different way.

The Hubble Space Telescope is the only one ever designed to be serviced in space by astronauts. By now, there have been five servicing missions. The last servicing mission, STS-125, was launched in May 2009, and installed two new instruments, repaired two inactive ones, and performed the component replacements that will keep the telescope functioning at least into 2014. Assuming testing and calibration of the new equipment goes well, the Hubble should resume

routine operation in September 2009.

HST's current complement of science instruments include three cameras— Advanced Camera for Surveys (ACS), Near Infrared Camera and Multi-Object Spectrometer (NICMOS), and Wide Field Camera 3 (WFC3; the previous generation instrument is the Wide Field Planetary Camera 2 (WFPC2)), two spectrographs – Cosmic Origins Spectrograph (COS) and Space Telescope Imaging Spectrograph (STIS), and the Fine Guidance Sensors (FGS; primarily used for accurate pointing, but also for astrometric observations).

1. Advanced Camera for Surveys (ACS):

ACS has three independent cameras that provide wide-field, high spatial resolution imaging from near-UV to near-IR wavelengths, using a broad assortment of filters designed to address a large range of scientific goals. There are three different channels: Wide Field Channel (WFC), High Resolution Channel (HRC), and Solar Blind Channel (SBC). Each of the three channels is optimized for a different specific goal.

The ACS CCDs are thinned, backside-illuminated full-frame devices cooled by thermoelectric cooler (TEC) stacks housed in sealed, evacuated dewars with fused silica windows. The spectral response of the WFC CCDs is optimized for imaging at visible to near-IR wavelengths, while the HRC CCD spectral response is optimized specifically for near-UV wavelengths. The SBC MAMA (Multi-Anode Microchannel Plate Array) is a photon-counting detector which provides a two-dimensional ultraviolet capability.

2. Near Infrared Camera and Multi-Object Spectrometer (NICMOS):

NICMOS is an HST instrument providing the capability for infrared imaging and spectroscopic observations of astronomical targets. It contains three cameras designed for simultaneous operation and detects light with wavelengths between 0.8 and 2.5 microns. Each camera can be operated independently. The basic imaging properties of each of the cameras are summarized in Table 3.3.

Table 3.3: The basic imaging parameters of NICMOS instruments. All values are referred to the HST/NICMOS Instrument Handbook for cycle 17.

Parameter	Camera NIC1	Camera NIC2	Camera NIC3
Pixel Size (arcsec)	0.043	0.075	0.2
Field of View (arcsec × arcsec)	11 × 11	19.2 × 19.2	51.2 × 51.2
<i>f</i> ratio	<i>f</i> /80	<i>f</i> /45.7	<i>f</i> /17.2

3. Wide Field Camera 3 (WFC3) and Wide Field Planetary Camera 2 (WFPC2):

WFC3 is the fourth generation instrument that has been built for installation on the Hubble Space Telescope during Servicing Mission 4 (SM4). WFC3 features two independent imaging cameras: the UV/optical channel (UVIS) and the near-infrared channel (IR). The

UVIS channel uses two butted  $4096 \times 2051$  thinned, back-illuminated CCD detectors to support imaging between  $2000\text{\AA}$  and  $10000\text{\AA}$ . The IR channel uses a  $1024 \times 1024$  Teledyne HgCdTe detector array, with the central  $1014 \times 1014$  pixels useful for imaging, and covering the near-infrared between  $8000\text{\AA}$  and  $17000\text{\AA}$ .

WFPC2 was removed in the 2009 servicing mission (SM4) and was replaced by the WFC3. This instrument is a two-dimensional imaging photometer, located at the center of the Hubble Space Telescope focal plane and covers the spectral range between approximately  $1150\text{\AA}$  to  $10500\text{\AA}$ . The WFPC2 field-of-view is divided into four cameras by a four-faceted pyramid mirror. Each of the four cameras contains an  $800 \times 800$  pixel Loral CCD detector. Three cameras operate at a spatial resolution of  $0''.1$  per pixel and comprise the Wide Field Camera (WFC) with a  $150'' \times 150''$  L-shaped region. The fourth camera images a smaller  $34'' \times 34''$  square field with  $0''.046$  per pixel and is referred to as the Planetary Camera (PC). There are thus four sets of relay optics and CCD sensors in WFPC2.

#### 4. Cosmic Origins Spectrograph (COS):

The Cosmic Origins Spectrograph is a fourth-generation instrument to be installed on the Hubble Space Telescope during SM4. COS is designed to perform high sensitivity, moderate- and low-resolution spectroscopy of astronomical objects in the  $1150\text{--}3200\text{\AA}$  wavelength range. The primary design goal of COS is to improve the sensitivity to point sources in the far-UV (from about  $1100\text{\AA}$  to  $1800\text{\AA}$ ). COS has two channels, one for the Far Ultraviolet (FUV), and one for the Near Ultraviolet (NUV). Both channels use photon-counting detectors. Only one of the two channels may be in use at any one time.

#### 5. Space Telescope Imaging Spectrograph (STIS):

The STIS is a versatile imaging spectrograph. The instrument provides spatially resolved spectroscopy from  $1150\text{\AA}$  to  $10300\text{\AA}$  with low to medium spectral resolution and high spatial resolution. The spectrograph spreads out the light gathered by a telescope so that it can be analyzed to determine such properties of celestial objects as chemical composition and abundances, temperature, radial velocity, rotational velocity, and magnetic fields. STIS has three detectors, each with  $1024 \times 1024$  pixels. One detector is a Scientific Image Technologies (SITE) CCD for detecting optical and near-infrared light, and the other two are Multi-Anode Microchannel Plate Array (MAMA) detectors for detecting near- and far-ultraviolet light. Due to the failure of a power supply, the STIS stopped science operations in August 2004. During the servicing mission in 2009, astronauts have repaired the STIS by removing the circuit card containing the failed power supply and replacing it with a new card.

#### 6. Fine Guidance Sensors (FGS):

The Fine Guidance Sensors provide HST observers with the capability of precision astrometry and milliarcsecond (mas) resolution over a wide range of magnitudes ( $3 < V < 16.8$ ). The FGS has two modes of operation: Position mode and Transfer mode. In Position mode

the FGS locks onto and tracks a star's interferometric fringes to precisely determine its location in the FGS FOV. In Transfer mode an object is scanned to obtain its interferogram with sub-mas sampling. Its two observing modes have been used to determine the parallax and proper motion of astrometric targets to a precision of 0.2 mas, and to detect duplicity or structure around targets as close as 8 mas (visual orbits can be determined for binaries as close as 12 mas).



# Chapter 4

## XMM-Newton Observations of PSR B1957+20

This chapter is a revision of the refereed paper entitled “XMM-Newton Observations of PSR B1957+20” published in *Astronomy & Astrophysics* (Huang & Becker 2007).

### 4.1 Abstract

We report on XMM-Newton observations of the “Black Widow pulsar”, PSR B1957+20. The pulsar’s X-ray emission is non-thermal and best modeled with a single powerlaw spectrum of photon index  $2.03^{+0.51}_{-0.36}$ , suggesting that the observed X-rays from PSR B1957+20 originate from the interaction of the relativistic pulsar wind with the interstellar medium or with the ablated material from the companion star. Its diffuse X-ray emission with the orientation to the north-east and the size of about 16 arcsec was detected, which is consistent with the previous result derived from the Chandra observations. No coherent X-ray pulsations at the pulsar’s spin-period could be detected. By using the limited photon statistics and the incomplete orbital coverage, no orbital modulation of the eclipsing pulsar system during  $\sim 90\%$  of one binary orbit was found. A repeated coverage of the binary orbit in a longer X-ray observation would provide us not only a better photon statistic but would also allow us to search for the orbital modulation and determine the X-ray emission geometry with a much higher accuracy.

### 4.2 Introduction

Until now, more than 1700 rotation-powered radio pulsars are detected. Among them are about 10% which are millisecond pulsars (MSPs) (Manchester et al. 2005). They form a separate population. The majority of them resides in Globular Clusters (c.f. Bogdanov et al. 2006). MSPs are presumed to have been spun up in a past accretion phase by mass and angular transfer from a binary companion (Alpar et al. 1982). About 40% of them are seen to be solitary. It is believed that they lost their companion, e.g. in a violent supernova event. All MSPs possess very short

spin periods of less than 20 ms and show a high spin stability with period derivatives in the range  $\approx 10^{-18} - 10^{-21} \text{ s s}^{-1}$ . MSPs are generally very old neutron stars with spin-down ages  $\tau = P/2\dot{P}$  of  $\sim 10^9 - 10^{10}$  years and low surface magnetic fields in the range  $B \propto \sqrt{P\dot{P}} \sim 10^8 - 10^{10} \text{ G}$ .

At present, about 50% of all X-ray detected rotation-powered radio pulsars are MSPs (c.f. Bogdanov et al. 2006 and references therein). Among them an extraordinarily rich astrophysics binary system which is formed by the millisecond pulsar PSR B1957+20 and its  $0.025 M_{\odot}$  low mass white dwarf companion (Fruchter et al. 1988b). The binary period of the system is 9.16 hours. The spin period of the pulsar is 1.6 ms which is the third shortest among all known MSPs. Its period derivative of  $\dot{P} = 1.69 \times 10^{-20} \text{ s s}^{-1}$  implies a spin-down energy of  $\dot{E} = 10^{35} \text{ ergs s}^{-1}$ , a characteristic spin-down age of  $> 2 \times 10^9$  years, and a dipole surface magnetic field of  $B_{\perp} = 1.4 \times 10^8 \text{ Gauss}$ . Optical observations by Fruchter et al. (1988a) and van Paradijs et al. (1988) revealed that the pulsar wind consisting of electromagnetic radiation and high-energy particles is ablating and evaporating its white dwarf companion star. This rarely observed property gave the pulsar the name *black widow pulsar*. Interestingly, the radio emission from the pulsar is eclipsed for approximately 10% of each orbit by material expelled from the white dwarf companion. For a radio dispersion measure inferred distance of 1.5 kpc (Taylor & Cordes 1993) the pulsar moves through the sky with a supersonic velocity of  $\sim 220 \text{ km s}^{-1}$ . The interaction of a relativistic wind flowing away from the pulsar with the interstellar medium (ISM) produces an  $H_{\alpha}$  bow shock which was the first one seen around a “recycled” pulsar (Kulkarni & Hester 1988).

In 1992 Kulkarni et al. published a contour map of the X-ray emission of PSR B1957+20 which was derived from ROSAT PSPC observations. Although this ROSAT data were very sparse in statistics it led the authors to predict faint diffuse X-ray emission with constant surface brightness to be present along a cylindrical trail formed when the relativistic pulsar wind expands into pressure equilibrium with the interstellar medium behind the nebula. The much improved sensitivity of the Chandra and XMM-Newton observatories made it possible to probe and investigate the structure and properties of this unique binary system in much higher detail than it was possible with ROSAT, ASCA or BeppoSAX. A narrow X-ray tail with the extent of 16 arcsec and the orientation to the north-east was detected from it in deep Chandra observations by Stappers et al. (2003). Figure 4.1 shows the composite X-ray and optical image of the pulsar.

Searching in ROSAT data for a modulation of the pulsar’s X-ray emission as a function of its orbital phase revealed a suggestive but insignificant increases in flux before (at phase  $\phi \sim 0.17$ ) and after (at phase  $\phi \sim 0.4 - 0.5$ ) the pulsar radio eclipse ( $\phi = 0.25$ ) (Kulkarni et al. 1992). Taking Chandra data into account revealed a hint that the lowest and highest fluxes are located during and immediately after the radio eclipse, respectively. The statistical significance of this modulation observed by Chandra, though, is only 98% and thus prevents any final conclusion on it (Stappers et al. 2003).

In this paper we report on XMM-Newton observations of PSR B1957+20 and its white dwarf companion. The paper is organized as follows. In §4.2 we describe the observations and data analysis. §4.3 gives a summary and discussion.

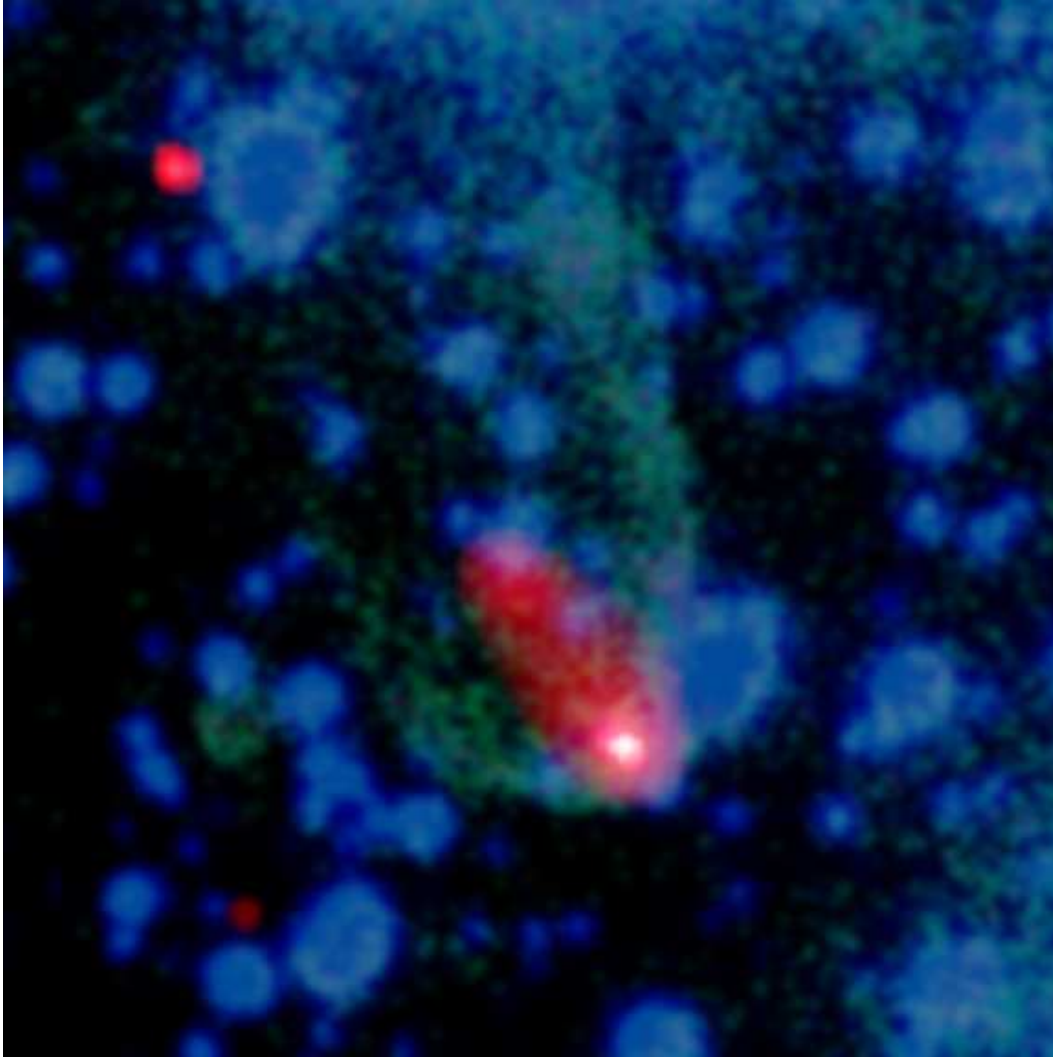


Figure 4.1: The composite X-ray (red/white) and optical (green/blue) image reveals an elongated cloud of high-energy particles flowing behind the black widow pulsar, PSR B1957+20 (white point-like source). The pulsar is moving through the galaxy at a supersonic velocity of  $\sim 220 \text{ km s}^{-1}$ . A bow shock wave due to this motion is visible to optical telescopes, shown in this image as the greenish crescent shape. The pressure behind the bow shock creates a second shock wave that sweeps the cloud of high-energy particles back from the pulsar to form the cocoon. The image is 1.2 arcmin per side. Credit: X-ray: NASA/CXC/ASTRON/B.Stappers et al.; Optical: AAO/J.Bland-Hawthorn & H.Jones.

### 4.3 Observations and Data Analysis

PSR B1957+20 was observed with XMM-Newton on October 31, 2004 for a 30 ksec effective exposure. In this observation, the EPIC-MOS1 and MOS2 instruments were operated in full-frame mode using the thin filter to block optical stray light. The EPIC-PN detector was setup to operate in the fast timing mode. Because of the reduced spatial information provided by the PN in timing mode we use the MOS1/2 data for imaging and spectral analysis of the pulsar and its diffuse X-ray nebula while the PN data having a temporal resolution of 0.02956 ms allowed us to search for X-ray pulsations from the pulsar. All the data were processed with the XMM-Newton Science Analysis Software (SAS) package (Version 6.5.0). Spatial and spectral analyses were restricted to the 0.3 – 10.0 keV energy band while for timing analysis events were selected for the energy range 0.3 – 3.0 keV.

#### 4.3.1 Spatial Analysis

Figure 4.2 shows the combined EPIC-MOS1/2 image of the PSR B1957+20 system. The image was created with a binning factor of 6 arcsec and by using an adaptive smoothing algorithm with a Gaussian kernel of  $\sigma < 4$  pixels in order to better make visible faint diffuse emission. The extent of the diffuse emission with its orientation to the north-east is about 16 arcsec which is consistent with the previous result derived from the Chandra Observations. However, the detailed structure of the X-ray emission from XMM-Newton can not be as clearly seen as from Chandra due to the 10 times wider Point Spread Function (PSF) of XMM-Newton.

Inspecting the XMM-Newton MOS1/2 image two faint features (denoted as A and B) which contribute to only about 3% of the total X-ray flux are apparent. In order to investigate whether this faint features are associated with nearby stars we inspected the Digitized Sky Survey data (DSS) and the USNO-B1.0 Catalogue for possible sources. These catalogues which are limited down to 22 mag (Krongold et al. 2001) and 21 mag (Monet et al. 2003) do not reveal possible counterparts. These features are not seen in the Chandra image though (Stappers et al. 2003).

#### 4.3.2 Spectral Analysis

Combined EPIC-MOS1/2 data of PSR B1957+20 were extracted from a circle of 30 arcsec radius centered at the pulsar position (RA (J2000) =  $19^h59^m36^s.77$ , Dec =  $20^\circ48'15''.12$ ). The selection region contains about 85% of all source counts. Background photons were selected from a source-free region near to the pulsar position. Response files were derived by using the XMM-Newton SAS tasks RMFGEN and ARFGEN.

After subtracting background photons, in total 338 sources counts were available for a spectral analysis. The extracted spectra were binned with at least 30 source counts per bin. Assuming that the emission originates from the interaction of the pulsar wind with the ISM or with the stellar wind we expect synchrotron radiation to be the emission mechanism of the detected X-rays. To test this hypothesis we fitted the spectrum with a power law model. Indeed, this model describes the observed spectrum with a reduced  $\chi^2_\nu$  of 1.09 (for 8 D.O.F.). The photon-index is

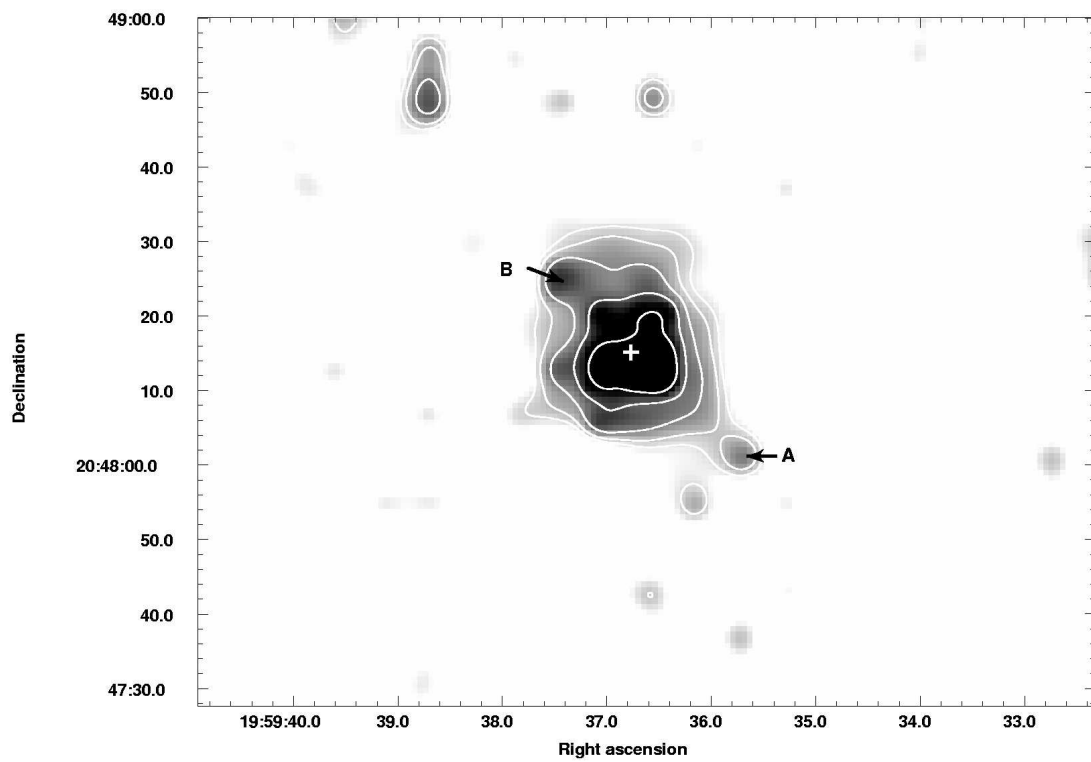


Figure 4.2: XMM-Newton MOS1/2 image of the PSR B1957+20 -WD system with contour lines overlaid. The contour lines are at the levels of  $(5.1, 6.1, 9.4, 16.3, 32.4, 69.0) \times 10^{-6} \text{ cts s}^{-1} \text{ arcsec}^{-2}$ . The position of the pulsar is indicated.

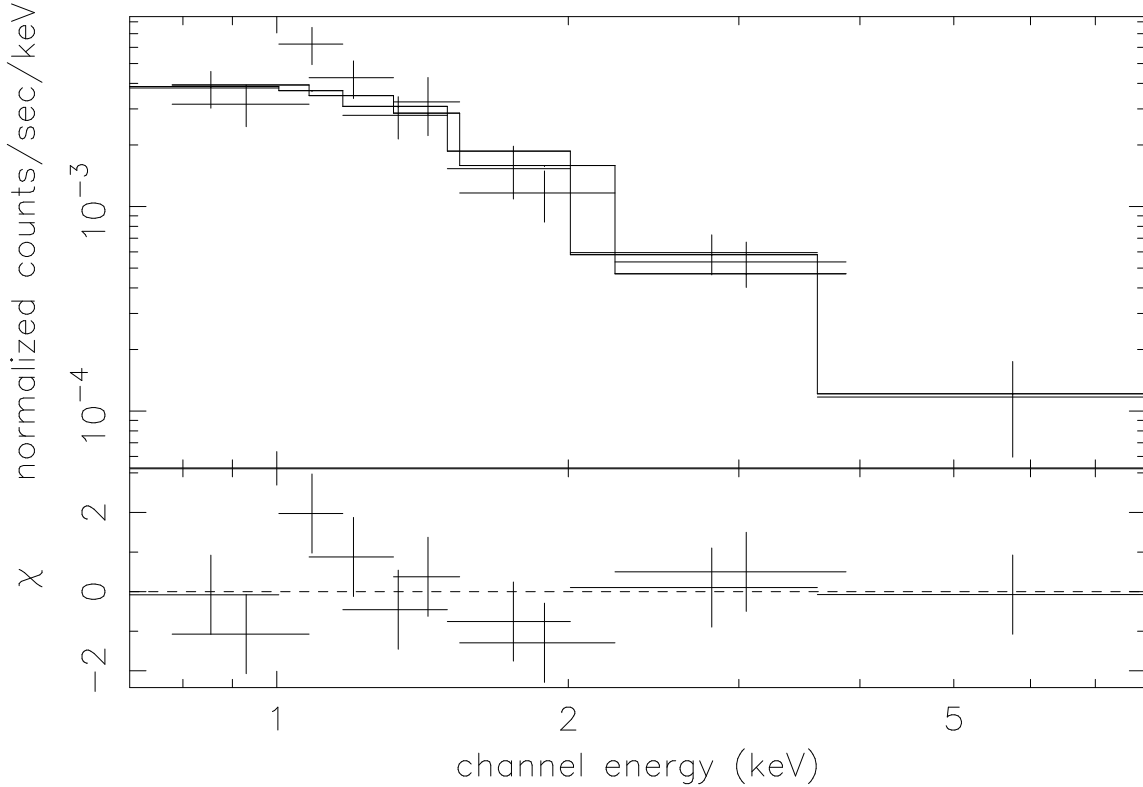


Figure 4.3: Energy spectrum of PSR B1957+20 obtained from the XMM-Newton MOS1/2 data. The plot shows the X-ray spectrum fitted with an absorbed power law model (upper panel) and contribution to the  $\chi^2$  fit statistic (lower panel).

found to be  $\alpha = 2.03^{+0.51}_{-0.36}$ . The column absorption  $N_H$  is  $8.0 \times 10^{20} \text{ cm}^{-2}$ . For the normalization at 1 keV we find  $1.5^{+0.9}_{-0.3} \times 10^{-5} \text{ photons keV}^{-1} \text{ cm}^{-2} \text{ sec}^{-1}$  ( $1\text{-}\sigma$  confidence for 1 parameter of interest). The spectrum (data and model) and the fit residuals are shown in Figure 2.

The unabsorbed X-ray flux derived from the best fitting model parameters is  $f_x = 8.35 \times 10^{-14} \text{ ergs s}^{-1} \text{ cm}^{-2}$  and  $f_x = 7.87 \times 10^{-14} \text{ ergs s}^{-1} \text{ cm}^{-2}$  in the 0.3 – 10 keV and 0.1 – 2.4 keV energy band, respectively. The X-ray luminosities in these energy bands – calculated for a pulsar distance of 1.5 kpc – are  $L_x(0.3 - 10.0 \text{ keV}) = 2.24 \times 10^{31} \text{ ergs s}^{-1}$  and  $L_x(0.1 - 2.4 \text{ keV}) = 2.12 \times 10^{31} \text{ ergs s}^{-1}$ , respectively. The conversion efficiency  $L_x/\dot{E}$  in the 0.1 – 2.4 keV band is found to be  $\sim 2.12 \times 10^{-4}$ .

In order to check whether the spectral emission characteristics changes for photons detected in a smaller compact region of 10 arcsec radius at the pulsar position we applied a spectral fit to this events only. The encircled energy within 10 arcsec is 60 %. In total, 186 sources counts were available for spectral fits. We did not find any significant change in the spectral parameters than reported above.

### 4.3.3 Timing Analysis

The EPIC-PN camera observed the pulsar in the fast timing mode. In this mode the spatial and spectral information from a  $64 \times 199$  CCD pixel array is condensed into a one dimensional  $64 \times 1$  pixel array (1D-image), i.e. the spatial information in Y-direction is lost due to the continuous read-out of the CCD. The complete photon flux (source plus DC emission from foreground or background sources located along the read-out direction) is accumulated and collapsed in the final 1D-image, severely reducing the signal-to-noise ratio of pulsed emission and preventing the detection of weak X-ray pulsations from the target of interest.

In order to search for X-ray pulsations from PSR B1957+20 we extracted 1615 counts from the CCD columns 33 – 41 in which the pulsar got located. For the purpose of increasing the signal-to-noise ratio we restricted the analysis to the energy range 0.3 – 3.0 keV. Below and beyond this energy band the accumulative sky and instrument background noise exceeds the contribution from the pulsar itself (c.f. Becker & Aschenbach 2002). However, still 80 % of the counts are estimated to be derived from the background.

In many observations there are some time intervals that show a very high background. In order to avoid this in our study, we first created a histogram file on the TIME column of the input event file which was selected with the energy greater than 10 keV and chose those time intervals where the counts are lower than 2 per 1000 sec as a Good Time Interval (GTI) file. A GTI file can be used to create a filtered event file that only accepts the good times where the background is low. We then filtered the time value which lies within the GTI.

The photon arrival times were corrected to the solar system barycentre with the BARYCEN tool (version: 1.17.4, JPL DE200 Earth ephemeris) of the SAS package. As the pulsar is in a binary we also corrected for the orbital motion of the pulsar by using the method of Blandford & Teukolsky (1976).

As millisecond pulsars are known to be extremely stable clocks we used the pulsar ephemeris from the ATNF Catalogue,  $f = 622.122030511927$  Hz and  $\dot{f} = -6.5221 \times 10^{-15} \text{sec}^{-2}$  (at MJD = 48196.0) to perform a period folding. By using the  $Z_n^2$  statistics (Buccheri et al. 1983) with the harmonics number (n) from one to ten no significant signal was detected at the radio spin period extrapolated for the epoch of the XMM-Newton observation. Restricting the period search to the various smaller energy bands did not change the result. A pulsed fraction upper limit of 9% ( $1-\sigma$ ) is deduced by assuming a sinusoidal pulsed profile.

Arons & Tavani (1993) predicted that depending on the flow speed and the degree of absorption and/or scattering by the companion wind the X-ray emission from PSR B1957+20 increases by up to a factor of 2.2 at the orbital phase before and after the radio eclipse. In order to test this prediction we created a lightcurve by binning all events in bins of 1.5 ksec width with the signal-to-noise ratio higher than 6 per bin. With an effective exposure time of about 30 ksec and an orbit period of 9.16-h the XMM-Newton MOS1/2 and PN data cover roughly 83 % and 92 % of one binary orbit, respectively. Table 4.1 lists the first and the last photon arrival times recorded by the MOS1/2 and EPIC-PN detectors and the corresponding pulsar binary orbital phase. The lightcurves resulting from the EPIC-PN and MOS1/2 data are shown in Figure 4.4. For the lightcurve deduced from the PN-data (upper solid curve) it is clearly seen that before the

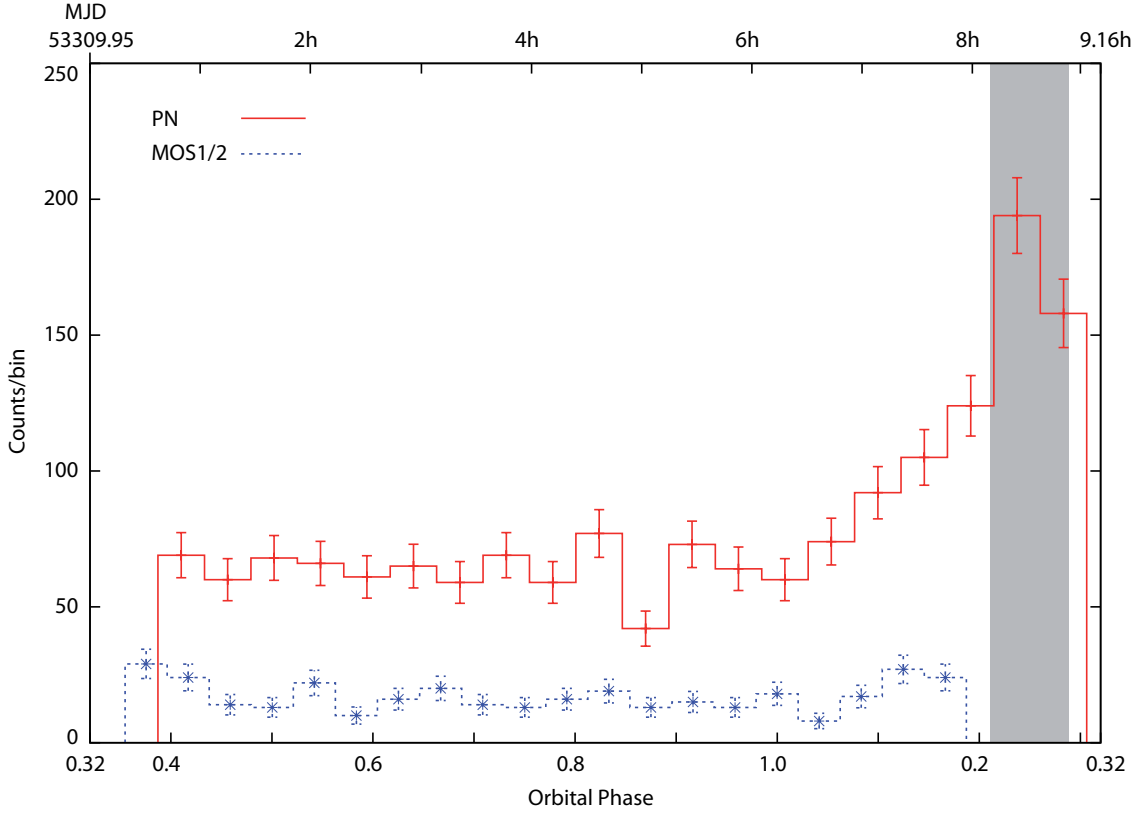


Figure 4.4: X-ray emission from PSR B1957+20 within 0.3 – 3.0 keV as function of the pulsar’s orbital phase ( $\phi$ ). We mapped one complete orbital period of this system at the starting point of  $MJD = 53309.95$ , i.e.  $\phi = 0.32$ .  $\phi = 1.0$  corresponds to the ascending node of the pulsar orbit. The upper curve was obtained from the XMM-Newton EPIC-PN (background level at 66 cts/bin). The lower lightcurve is obtained from the MOS1/2 data. The gray strip between the orbital angle 0.21 – 0.29 indicates the eclipse of the pulsar. Phase bins with zero counts correspond to phase angles not covered in the observation.

radio eclipse, i.e. between the orbital phase 0.1 and 0.25, the X-ray emission is about a factor of 3.0 higher than at other orbital phase angles before and after the radio eclipse.

Attention should be paid that at least  $\sim 80\%$  of the total photons could be from the background region. In order to examine if the increased X-ray emission really comes from the pulsar itself, we re-plotted the X-ray light curves by using the photons located in different CCD columns, i.e. the entire CCD strip, the on-pulsar position (RAWX 33–41), and the off-pulsar position (RAWX 1–32 and 42–64). We found that a soft PN background flare, detected over the entire one-dimensional spatial strip, occurs during the final  $\sim 4$  ksec of the observation, coinciding precisely with the orbital phase of radio eclipse, and when the MOS1/2 cameras have stopped collecting data (see the upper panel of Figure 4.5).

To properly search for flaring from the pulsar, the time-dependent count rate in the background region would have to be scaled for the relative numbers of pixels in the two extraction

Table 4.1: List of the first and the last photon arrival times and its corresponding orbital phase of PSR B1957+20 for the MOS1/2 and PN detectors. Arrival times are corrected to the solar system barycentre. The orbital phase is measured from the time of ascending node.

Date set	1st photon		last photon		Duration (s)
	Time (MJD)	Orbital Phase	Time (MJD)	Orbital Phase	
MOS1	53309.9688	0.3605	53310.2830	0.1830	27143.4
MOS2	53309.9666	0.3548	53310.2846	0.1871	27467.1
PN	53309.9791	0.3873	53310.3301	0.3063	30327.4

ranges and the result subtracted from the X-ray light curve of the pulsar PSR B1957+20. When this is done, the eclipse-boosted flux essentially disappears (see the lower panel of Figure 4.5).

## 4.4 Summary and Discussion

Interaction between relativistic pulsar winds which carry away the rotational energy of pulsars and the surrounding medium is expected to create detectable X-ray emission. Indeed, there are about 30 pulsar wind nebulae (PWNe) currently detected in the X-ray band (e.g. Kaspi et al. 2006; Gaensler & Slane 2006; Kargaltsev & Pavlov 2007). However, these PWNe are all powered by young and powerful pulsars with spin-down energies of more than  $\sim 3.6 \times 10^{36}$  ergs  $s^{-1}$ . Until now, only two MSPs are known to have X-ray nebulae. They are PSR B1957+20 (Stappers et al. 2003) and PSR J2124-3358 (Hui & Becker 2006). Both of them have tail-like structures behind the moving pulsars. These trails could be associated with the shocked relativistic wind confined by the ram pressure of the ambient ISM.

As PSR B1957+20 and its companion are separated by just  $1.5 \times 10^{11}$  cm, the intra-binary shock, formed where the pulsar and companion winds interact, is located in a strong magnetic field. Therefore, this intra-binary shock is a potential source of unresolved synchrotron emission at the location of the pulsar (Stappers et al. 2003), which is supported by the resultant spectral analysis. The downstream flow of the intra-binary shock is expected to undergo Doppler boosting as it passes around the companion and so the orbital modulation of the X-rays is expected (Arons & Tavani 1993). The X-ray emission near to the radio eclipse is supposed to be beamed in a forward cone because the shocked fluid is accelerated by the pressure gradient as it flows around the eclipse region. Relativistic beaming would tend to give the maximum flux just before and after the pulsar eclipse. On the other hand, the X-ray emission at the eclipse may be reduced because of the obscuration of the shock by the companion. However, the XMM-Newton data of PSR B1957+20 did not provided any observational evidence for a dependence of the pulsar's X-ray emission on its binary orbital phase. As the present XMM observation covers barely one binary orbit, i.e. the orbital angles  $0.30 - 0.38$  and  $0.18 - 0.36$  are not covered by EPIC-PN and MOS1/2 data at all, we stress that it cannot be fully excluded the existence of the orbital

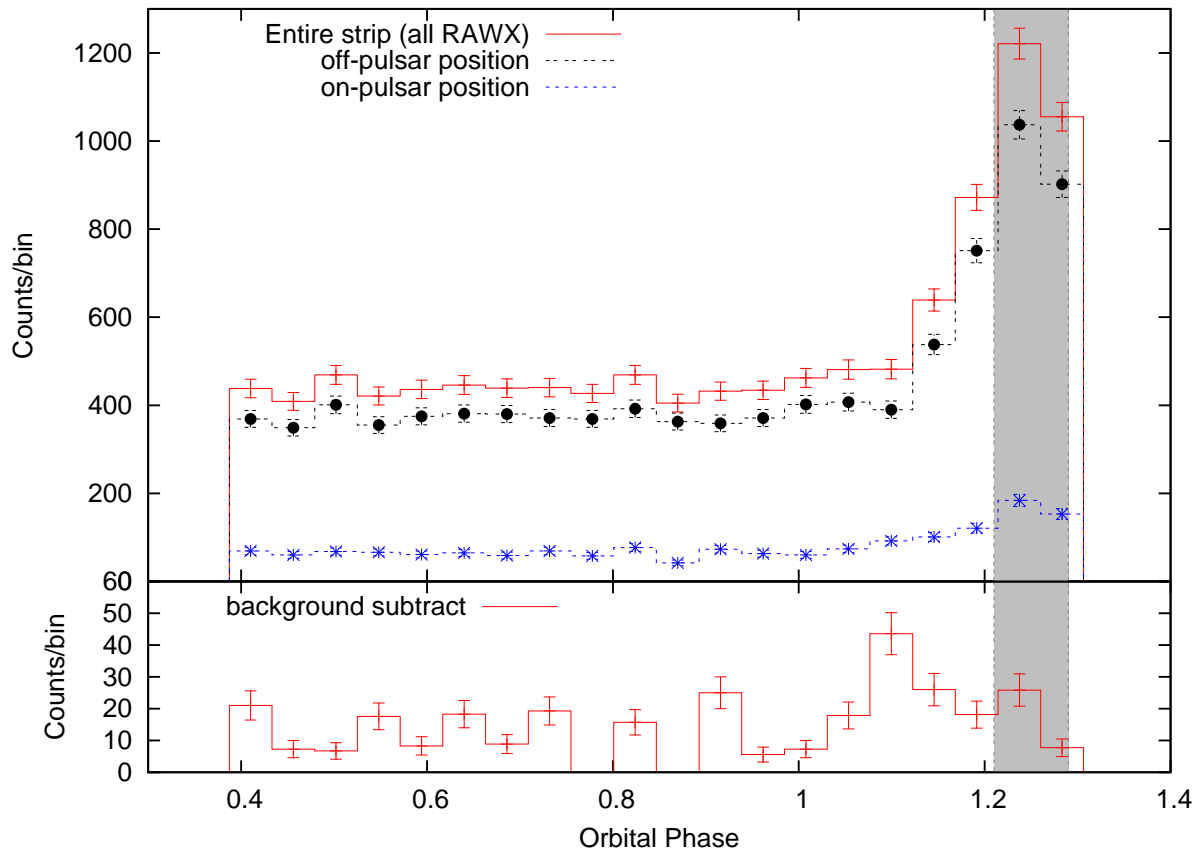


Figure 4.5: This figure shows the PN count rate of PSR B1957+20 vs. the orbital phase in the 0.3–3 keV band. The gray strip between the orbital angle 0.21 – 0.29 indicates the radio eclipse region of the pulsar. The upper panel shows the light curves by using the photons coming from the entire strip (red), the pixels away from the pulsar position (black) and the pixels covering the pulsar position (blue). It is clearly seen that the X-ray flux increase at the last few bins is not restricted to the pulsar position. The lower panel shows the background-subtracted light curve from the pulsar position.

modulation of the X-ray emission.

Given the limited photon statistics of the XMM-Newton data with the short observation time of 30 ksec, which is less than the time of one full binary orbit, it is not possible to investigate any binary-phase resolved imaging and spectral variation or to search for the X-ray emission as a function of the orbital phase. Clearly, a repeated coverage of the binary orbit in a longer XMM-Newton observation with higher accuracy and better photon statistic than currently possible and a comparison with the 2004 data would answer whether the X-ray emission from PSR B1957+20 is present during all orbit angles or is rasing only near to the radio eclipse while diffuse X-ray emission from the PWN is present at any orbital angle. This, in addition, would not only help us to better understand the pulsar's X-ray emission properties but also allow us to determine the emission geometry.



# Chapter 5

## X-rays from the Eclipsing Millisecond Pulsar PSR J1740–5340 in NGC 6397

This chapter is adopted from the refereed paper entitled “X-rays from the Eclipsing Millisecond Pulsar PSR J1740–5340 in NGC 6397” published in *Astronomy & Astrophysics* (Huang & Becker 2010).

### 5.1 Abstract

The millisecond pulsar PSR J1740 – 5340 in the globular cluster NGC 6397 shows radio eclipses over  $\sim 40\%$  of its binary orbit. A first Chandra observation revealed indications for the X-ray flux being orbit dependent as well. In this work, we analysed five datasets of archival Chandra data taken between 2000 and 2007 to investigate the emission across the pulsar’s binary orbit. Utilizing archival Chandra observations of PSR J1740–5340, we performed a systematic timing and spectral analysis of this binary system. Using a  $\chi^2$ -test, the significance for intra-binary orbital modulation was found to be between 88.5% and 99.6%, depending on the number of phase bins used to construct the light curve. Applying the unbiased statistical Kolmogorov-Smirnov (KS) test did not indicate any significant intra-binary orbital modulation. However, comparing the counting rates observed at different epochs, a flux variability on times scales of days to years is indicated. The possible origin of the X-ray emission is discussed in a number of different scenarios.

### 5.2 Introduction

The millisecond pulsar (MSP) PSR J1740–5340 (6397A), located in the core-collapsed globular cluster NGC 6397 at a distance of 2.5 kpc, was discovered during a systematic search for ms-pulsars in Galactic globular clusters using the Parkes Radio Telescope (D’Amico et al. 2001a). It is orbiting around a massive late type companion ( $> 0.14 M_{\odot}$ ; Orosz & van Kerkwijk 2003) with an orbital period of 1.35 day (D’Amico et al. 2001b). The inclination of the binary system

to the line of sight is  $i \sim 50^\circ$  (Orosz & van Kerkwijk 2003). The pulsar’s spin period and period derivative are  $P = 3.65$  ms (D’Amico et al. 2001a) and  $\dot{P} = 4.0 \times 10^{-20}$  s s $^{-1}$  (Possenti et al. 2005). The contribution to  $\dot{P}$  due to possible pulsar acceleration in the cluster’s gravitational field is estimated to be smaller than  $10^{-20}$  s s $^{-1}$  by its large offset of 0.6 arcmin (corresponding to eleven core radii) from the cluster center (D’Amico et al. 2001b). The spin parameters imply a spin-down luminosity, a characteristic age and a dipole surface magnetic field of PSR J1740–5340 of  $\dot{E} \sim 3.3 \times 10^{34}$  ergs s $^{-1}$ ,  $\tau_c = P/2\dot{P} \sim 1.4 \times 10^9$  years, and  $B_\perp \sim 3.9 \times 10^8$  G, respectively (Possenti et al. 2005).

The radio emission from PSR J1740–5340 is partially eclipsed in the orbital phase interval 0.05–0.45 for approximately 40% of each orbit (D’Amico et al. 2001a,b). Moreover, strong fluctuations of the radio signals were observed at nearly all orbital phases (D’Amico et al. 2001b), which led to the interpretation that the pulsar is orbiting within an extended envelope of matter released from the companion. The optical light curve of the companion showing tidal distortions provides strong evidence that PSR J1740–5340 is orbiting a companion whose Roche lobe is nearly completely filled (Ferraro et al. 2001). However, the system is in a radio-ejection phase in which accretion is inhibited by the radiation pressure exerted by the pulsar on the infalling matter. The strong interaction between the MSP flux and the plasma wind would explain the irregularities seen in the radio signals from PSR J1740–5340 (Ferraro et al. 2001; Burderi et al. 2002).

PSR J1740–5340 is in a wide orbit with a separation of  $\sim 6.5 R_\odot$ , so that the wind energy density impinging on the non-degenerate companion should be significantly less than that estimated for other much tighter eclipsing binary systems, such as the field ms-pulsar PSR B1957+20 which has a separation of  $\sim 0.04 R_\odot$  from its companion (Arzoumanian et al. 1994). PSR J1740–5340 therefore is unlikely to drive a wind of sufficient density off its companion (D’Amico et al. 2001b). Orosz & van Kerkwijk (2003) have studied the optical light curve of the companion and found no evidence of heating from the pulsar radiation, which supports the aforementioned inference. Sabbi et al. (2003) have investigated the chemical composition of the non-degenerate companion star and found a strong depletion of carbon. This suggests a scenario in which the companion is an evolved star that has lost most of its surface layers. In view of the high rotational velocity of the companion ( $\sim 50$  km/s; Sabbi et al. 2003), the stellar wind possibly can be strong enough to cause the mass-loss and result in an extended envelope of matter.

X-ray emission from this binary system was detected with the Chandra X-ray Observatory (Grindlay et al. 2001a). Based on an observation in 2000 (cf. Table 1) which only covered  $\sim 40\%$  of the binary orbit, Grindlay et al. (2002) reported evidence that the count rate of the system appears to increase by a factor of  $\sim 2$  at phase 0.4, just before the pulsar comes out of the radio eclipse. However, the short exposure time and the limited orbital phase coverage of this first observation (cf. top panel in Figure 1 and Table 1) did not support a detailed temporal and spectral analysis of the emission.

In this publication we report on a search for X-ray orbital modulation as well as on a spectral analysis of the PSR J1740–5340 binary system making use of archival Chandra data that cover various orbital phases ranges.

Table 5.1: List of Chandra observations of PSR J1740–5340 in NGC 6397

Obs. Date	Obs. ID	Instrument	Data Mode	Effective Exp. Time	Orbital Phase	Net count rate <sup>a</sup>	Off-axis(°)
2000-07-31	79	ACIS-I	Faint	48.3 ks	0.146 – 0.553	$1.89 \pm 0.25^b$	0.8745
2002-05-13	2668	ACIS-S	Faint	28.1 ks	0.035 – 0.267	$1.74 \pm 0.25$	0.9368
2002-05-15	2669	ACIS-S	Faint	26.7 ks	0.501 – 0.719	$2.89 \pm 0.33$	0.9214
2007-06-22	7461	ACIS-S	Very Faint	90.0 ks	0.189 – 0.950	$2.26 \pm 0.16$	0.3732
2007-07-16	7460	ACIS-S	Very Faint	149.6 ks	0.437 – 1.714 <sup>c</sup>	$2.92 \pm 0.14$	0.2129

<sup>a</sup>ACIS-S net count rates in units of  $10^{-3}$  counts/sec corrected to the on-axis.

<sup>b</sup>The ACIS-I on-axis net count rate is  $1.31 \pm 0.17$ . In order to derive a comparable ACIS-S net count rate from the observed ACIS-I rate we convert the ACIS-I rate by using the WebPIMMS tool (<http://heasarc.gsfc.nasa.gov/Tools/w3pimms.html>).

<sup>c</sup>The total exposure time covers more than one binary orbit.

## 5.3 Observations and Data Analysis

In total, five observations were targeted on the PSR J1740–5340 binary system using the Chandra Advanced CCD Imaging Spectrometer (ACIS). The first observation was performed on 2000 July 31 using the front-illuminated (FI) ACIS-I3 chip, while the other four observations taken on 2002 May 13 and 15, 2007 June 26, and July 16 used the back-illuminated (BI) chip ACIS-S3. We summarize the basic information of these observations in Table 1. Their binary orbit coverages are shown in Figure 5.1. As can be seen from this figure, only Obs. IDs 7460 and 7461 cover a larger fraction of the binary orbit. In the search for intra-orbital flux modulation and spectral variation, we therefore considered only these two datasets which have higher photon statistics and longer exposure times, while the other archival data were used to search for a possible flux variability on time scales of days or years. Data analysis was restricted to the energy range 0.3 – 8.0 keV. Searching for X-ray pulses from PSR J1740–5340 was precluded by the inappropriate temporal resolution of the observing modes used. Standard processed level-2 data were used. Correction for aspect offset was applied before analysis. All data were processed with Chandra Interactive Analysis Observations (CIAO) version 3.4 software and CALDB version 3.4.2.

### 5.3.1 Search for Orbital Modulation

In order to search for a modulation of the X-ray flux as a function of orbital phase, we extracted the photons from a circle of 2 arcsecond radius centered on the radio pulsar position RA (J2000) =  $17^h40^m44^s.59$ , Dec =  $-53^\circ40'40''.9$  (D’Amico et al. 2001b). In the 2007 observations,  $\sim 90\%$  of all source counts are located within this cut radius. The photon arrival times were corrected to the solar system barycenter with the CIAO tool AXBARY (JPL DE200 solar system ephemeris). We used the pulsar ephemeris from D’Amico et al. (2001b) and correct the photon arrival times for the orbital motion of the binary system (Blandford & Teukolsky 1976). Since PSR J1740–

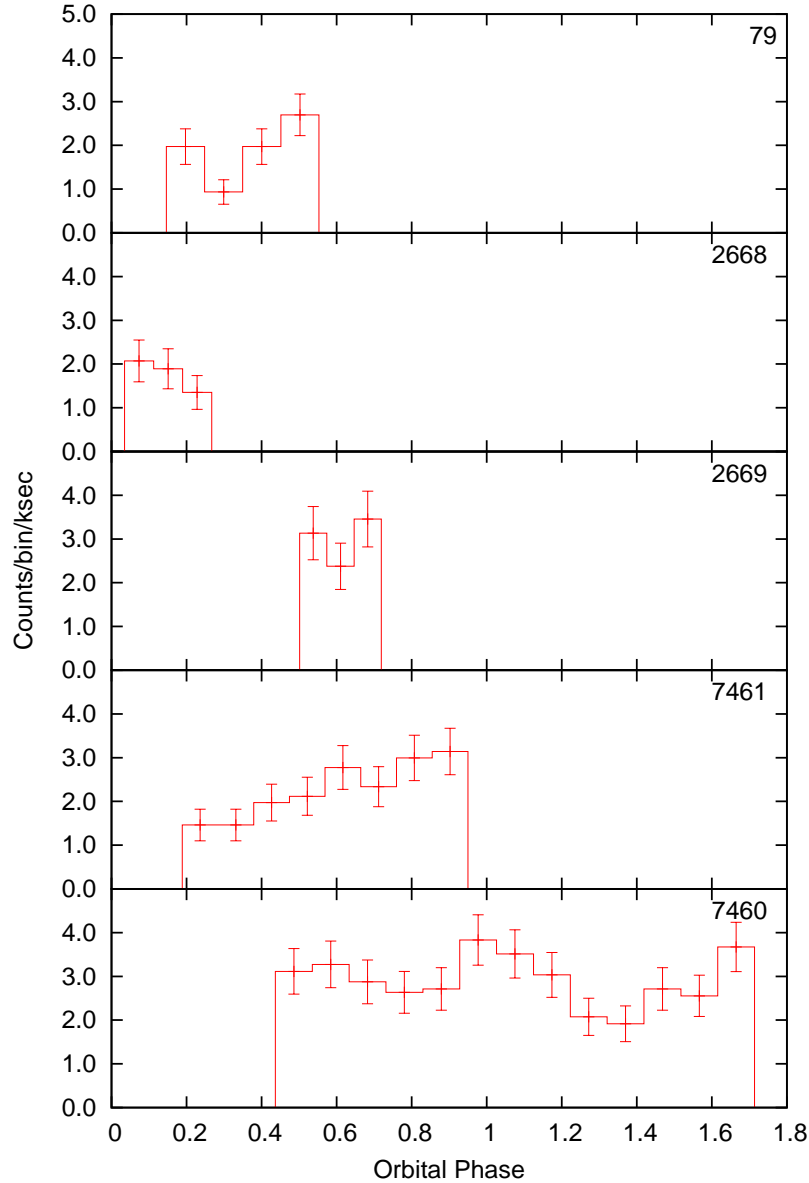


Figure 5.1: Orbital phase coverages of five Chandra observations targeted on the binary system PSR J1740–5340. The Y-axis shows the X-ray source counts per bin per kilosecond in the energy range 0.3 – 8.0 keV. The X-axis is the binary orbital phase (from ephemeris of D’Amico et al. 2001b).  $\phi=0.0$  is at the ascending node of the pulsar orbit. Binning is so that the signal-to-noise ratio in each bin is  $\geq 3$ . Error bars represent the  $1\sigma$  uncertainties. All X-ray light curves are corrected for vignetting and the various instrumental sensitivities of the different observing modes. Labels are the Obs. IDs (cf. Table 1).

Table 5.2: Significance for intra-orbital flux modulation by fitting the light curves of different phase bins against a constant by using the  $\chi^2$  test statistics. The best-fit mean levels are listed as well.

Number of bins	Mean level	$\chi^2_{\nu}$	Significance(%)
10	37.1±2.7	2.22	98.2
11	33.4±2.4	1.82	94.8
12	29.6±2.1	1.62	91.2
13	28.6±2.1	2.38	99.6
14	26.4±2.0	1.86	97.0
15	24.7±1.9	2.01	98.7
20	18.4±1.1	1.34	89.0
40	9.2±0.5	1.25	88.5

5340 is far out of the globular cluster core, the correction for gravitational acceleration in the cluster potential was ignored.

We tested the 2007 data for intra-orbital flux modulation by fitting a constant to the X-ray light curve. In order to have the signal-to-noise ratio for each phase bin higher than  $\sim 4$ , the numbers of phase bins were restricted to be within 10 to 15 bins per orbital period. In addition, we tested 20 and 40 bins per orbital period for comparison. Using a  $\chi^2$ -test, the significance for a flux modulation over the observed orbit was found to be between 88.5% and 99.6%, depending on the number of phase bins used to construct the light curve. Table 5.2 summarizes the results for various bin numbers. The X-ray light curve for 10 phase bins is shown in Figure 5.2.

The disadvantage of the  $\chi^2$ -test is its dependence on the number of phase bins. We therefore applied the Kolmogorov-Smirnov (KS) test to the unbinned light curve data in order to have a bin-independent statistical evaluation of the X-ray emission variability (see Figure 5.3). Calculating the corresponding KS probabilities between our data set and the cumulative distribution function generated by assuming a constant X-ray flux indicated no significant deviation between these two distributions. The significance for an intra-orbital flux modulation from this test is only at the level of  $\sim 68\%$ . A similar result is obtained if we restrict the analysis to the hard energy band above 2 keV.

### 5.3.2 Spectral Analysis

To investigate whether the X-ray spectral behavior of PSR J1740–5340 varies across the orbit, we analysed the X-ray spectrum within and outside the eclipsing region separately. The source and background spectra were extracted from the same region as mentioned in §2.1 and from a source-free region close to the pulsar. Response files for the corresponding observations were created by using the tools MKACISRMF and MKARF of CIAO. The background-subtracted

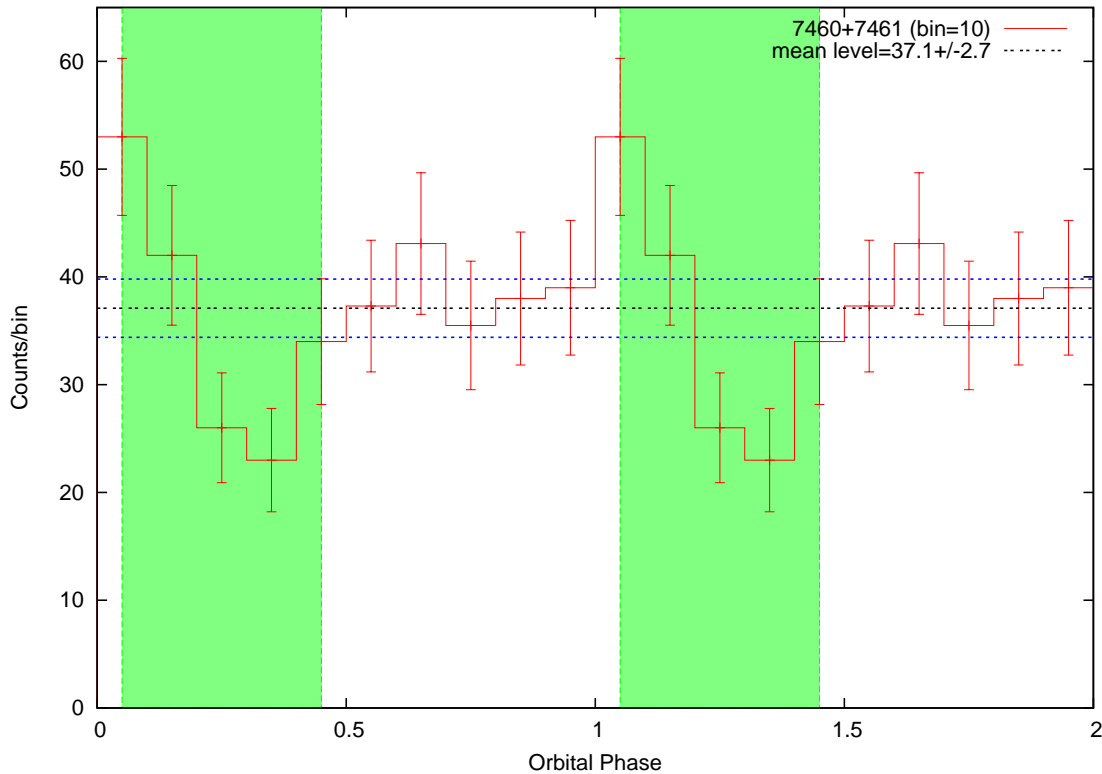


Figure 5.2: X-ray source counts (0.3–8.0 keV) vs. orbital binary phase according to the ephemeris of D’Amico et al. (2001b). Two orbital cycles are shown for clarity. The background noise level is found to be at  $\sim 0.35$  counts/bin.  $\phi = 0.0$  corresponds to the ascending node of the pulsar orbit. Error bars indicate the  $1\sigma$  uncertainty. The shaded regions between the orbital phases 0.05–0.45 and 1.05–1.45 mark the radio eclipse of the pulsar PSR J1740–5340. The dotted lines indicates the best-fit constant level and its  $1\sigma$  uncertainty.

count rates from the PSR J1740 – 5340 binary system per observation are given in Table 5.1. Extracted spectra were dynamically binned in accordance with the photon statistic in each dataset. Model spectra to Obs. IDs. 7460 and 7461 datasets were fitted using XSPEC 11.3.2. There are  $183 \pm 14$  and  $457 \pm 21$  net counts in total for the spectral analysis inside and outside the eclipsing region, respectively.

Assuming that the emission originates from the shock interaction of the pulsar wind with the wind of the companion star or from non-thermal emission processes in the pulsar magnetosphere, we expect the X-radiation to be synchrotron. To test this hypothesis, we fitted the spectrum with an absorbed power-law model (PL). For the PL fit, no significant variation of the spectral parameters is found between the spectrum inside and outside the eclipsing region. A thermal bremsstrahlung model (TB) was also tested, which physically implies that the X-ray emission is either from a hot plasma presented in the binary system or from the free-free radiation of the companion’s corona. We also tested whether a single blackbody (BB) can provide an appropriate modeling of the data. However, this BB model cannot provide any statistically acceptable description of the observed spectra (i.e.  $\chi^2_{\nu} > 2$ ) either inside the eclipsing region or outside.

The spectral parameters inferred from these fits are summarized in Table 5.3. The spectral parameters inferred from the PL/TB fits are found to be consistent with those reported by Grindlay et al. (2001a, 2002). The best-fitted  $N_H$  for each spectrum varies marginally, but is consistent with the values of  $\sim 1.03$  and  $\sim 2.22 \times 10^{21} \text{ cm}^{-2}$  inferred from the optical reddening of NGC 6397 and from the radio dispersion measure (DM) of PSR J1740–5340, respectively.

## 5.4 Summary and Discussion

We have searched for the orbital modulation of the X-ray emission from PSR J1740–5340 associated with NGC 6397. Only one of five archival datasets cover a full binary orbit. Analysing this data with a Kolmogorov-Smirnov test revealed no significant intra-orbital flux modulation. However, correlating the ACIS-S vignetting-corrected net counting rates observed at various orbital phases in 2000, 2002 and 2007 and assuming that the system in general shows no intra-orbital flux modulation reveals a  $\sim 3\sigma$  flux variability on time scales of days to years (cf. Col. 7 in Table 1). Figure 5.4 depicts the ACIS-S net count rates observed in the various observations.

In the following, we will discuss three scenarios which we believe could be the main source of the observed X-rays in the PSR J1740–5340 binary system.

### 1. The Companion star

The companion is observed to be a late-type star. It has an unusual position in the color-magnitude diagram (CMD) as being as luminous as a main-sequence turn-off star but redder (Ferraro et al. 2001; Orosz & van Kerkwijk 2003). This makes it quite similar to the “red straggler” active binaries which are identified to be X-ray sources in other globular clusters (Albrow et al. 2001; Edmonds et al. 2003a,b; Bassa et al. 2008). Detailed studies of X-ray sources

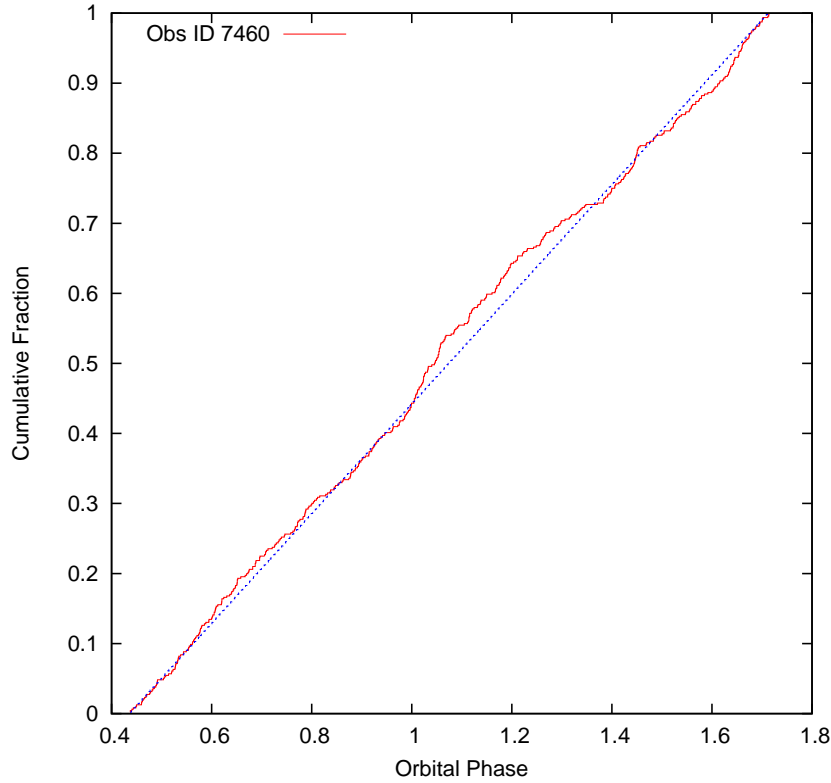


Figure 5.3: Kolmogorov-Smirnov test. The cumulative distribution function from the observed data is plotted in red and the blue dotted line shows the estimated cumulative distribution generated by assuming a constant X-ray flux.

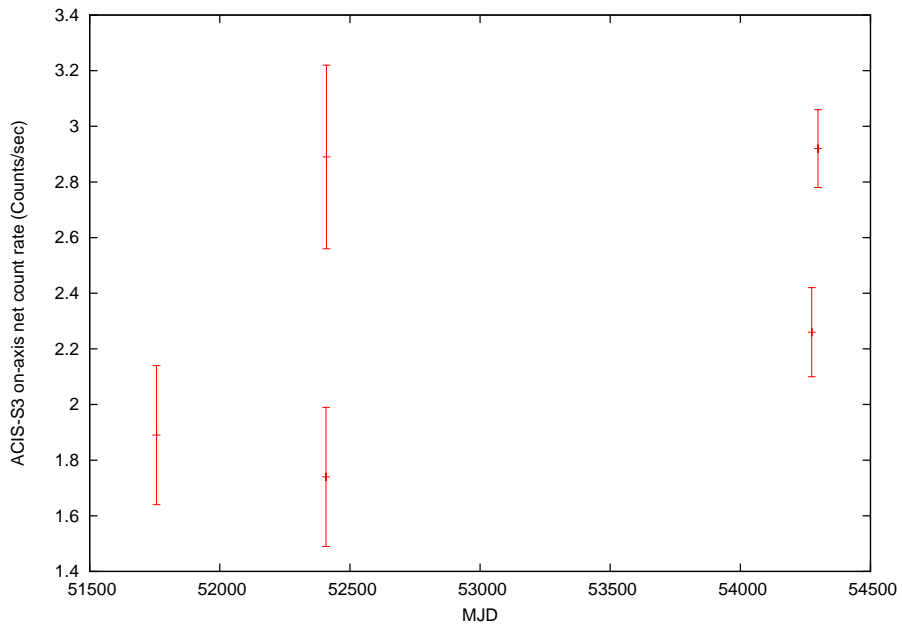


Figure 5.4: ACIS-S3 count rates of the PSR J1740–5340 binary system vs. observation dates.

Table 5.3: Parameters from spectral fits to the PSR J1740 – 5340 binary system.

Orbital Phase	Model <sup>a</sup>	$N_H$ <sup>b</sup>	$\Gamma/\text{kT}(\text{keV})$	$\chi^2_{\nu}/\text{dof}$	$F_x$ <sup>c</sup>	$L_x$ <sup>d</sup>	Note
0.05–0.45	PL	$< 1.4$	$1.8^{+0.4}_{-0.3}$	1.39/20	$1.9^{+1.8}_{-0.7}$	$1.4^{+1.3}_{-0.5} \times 10^{31}$	inside eclipsing region
	TB	$< 0.8$	$7.2^{+10.4}_{-3.4}$	1.42/20	$1.7^{+0.5}_{-0.4}$	$1.3^{+0.4}_{-0.3} \times 10^{31}$	
0.45–0.05	PL	$1.8^{+1.0}_{-0.7}$	$1.7^{+0.1}_{-0.2}$	0.96/19	$3.3^{+1.4}_{-0.8}$	$2.5^{+1.1}_{-0.6} \times 10^{31}$	outside eclipsing region
	TB	$1.3^{+0.6}_{-0.9}$	$7.3^{+9.6}_{-1.7}$	1.00/19	$2.9^{+0.4}_{-0.5}$	$2.2^{+0.3}_{-0.4} \times 10^{31}$	
0.0–1.0	PL	$0.6^{+0.4}_{-0.3}$	$1.5^{+0.2}_{-0.1}$	1.07/19	$2.8^{+0.9}_{-0.8}$	$2.1^{+0.7}_{-0.6} \times 10^{31}$	whole orbit
	TB	$< 0.7$	$16.1^{+23.2}_{-7.6}$	1.11/19	$2.6^{+0.3}_{-0.4}$	$1.9^{+0.2}_{-0.3} \times 10^{31}$	

Note: Col. 1 gives the orbital phase, Cols. 2–5 the spectral model, the hydrogen column density  $N_H$ , the best-fitted photon index or temperature, and the reduced  $\chi^2$  together with degrees of freedom. Cols. 6–7 list the unabsorbed X-ray flux and luminosity in the 0.3 – 8.0 keV energy range. Quoted errors indicate the 68% confidence level for one parameter of interest.

a. PL = powerlaw; TB = thermal bremsstrahlung

b. In units of  $10^{21} \text{ cm}^{-2}$

c. Unabsorbed X-ray flux in units of  $10^{-14} \text{ ergs cm}^{-2} \text{ s}^{-1}$  and in the energy range of 0.3–8.0 keV.

d. Unabsorbed X-ray luminosity in units of  $\text{ergs s}^{-1}$  and in the energy range of 0.3–8.0 keV for a distance of 2.5 kpc (Grindlay et al. 2001a).

in various globular clusters by Bassa et al. (2004) and Verbunt et al. (2008) have shown that the separatrix  $\log L_{0.5-2.5\text{keV}} = 34.0 - 0.4M_V$  allows one to distinguish between the population of cataclysmic variables and that of magnetically active binaries. Here,  $M_V$  is the absolute V-band magnitude, which for the PSR J1740 – 5340 binary system was observed to be  $M_V \sim 5$  (Orosz & van Kerkwijk 2003). Taking this together makes the properties observed from the companion star consistent with that from rapid rotating stars. The X-ray luminosities of late-type stars (i.e. F7 to M5) are found to be well correlated with their equatorial rotational velocities  $v_{\text{rot}}$ , according to  $L_X \simeq 10^{27} v_{\text{rot}}^2 \text{ ergs s}^{-1}$  (Pallavicini et al. 1981). Adopting the  $v_{\text{rot}} \sim 50 \text{ km/s}$  as reported by Sabbi et al. (2003) yields an expected X-ray luminosity of  $\sim 2.5 \times 10^{30} \text{ ergs s}^{-1}$ . Given that the  $L_X$  vs.  $v_{\text{rot}}^2$  correlation has a scatter of one order of magnitude (Pallavicini et al. 1981) it cannot be excluded that the X-ray emission observed from the PSR J1740–5340 binary is coronal emission from the companion star only. No significant X-ray intra-orbital modulation is observed, which is unlike what we have seen in the optical bands. The optical emission is expected to come from the surface of the companion star while the X-ray emission comes from the corona. As the companion star is interpreted to be tidal-distorted (Orosz & van Kerkwijk 2003), the emitting area responsible for the optical intensity appears to be modulated. However, the X-ray emission is coronal and may be less or not affected by this distortion.

## 2. The millisecond pulsar

Considering a possible contribution from the pulsar magnetosphere is justified by the pulsar's spin-down energy of  $\dot{E} \sim 3.3 \times 10^{34}$  ergs  $s^{-1}$ . By assuming the best-fit X-ray conversion efficiency found for other field and millisecond pulsars,  $L_X \sim 10^{-3} - 10^{-4} \dot{E}$  (Becker 2009), the spin-down power of PSR J1740–5340 implies an X-ray luminosity which is of the order of  $\sim 10^{30} - 10^{31}$  ergs  $s^{-1}$ , in agreement with the observed luminosity (cf. Table 3). Observing the pulsar in a mode suitable to resolve its X-ray pulses would be worthwhile and could constrain this interpretation.

## 3. Intrabinary shock emission

Grindlay et al. (2002) suggested that the X-ray emission they detected from the PSR J1740–5340 binary system is due to the interaction between the pulsar and shocked gas lifted from the stellar companion. In the shock, the extended matter in the orbit is compressed and gives rise to a power law distribution of synchrotron-emitting particles,  $N(\gamma) \propto \gamma^{-p}$ , by accelerating a fraction of these particles to very high energies, where  $\gamma$  is the Lorentz factor of the emitting particles. This should lead to an enhancement of X-ray emission from the system as the pulsar enters the eclipsing region and a subsequent decrease due to the increased absorption in this region. Cheng et al. (2006) found that the X-ray luminosity of intrabinary shock emission in the 2–10 keV band can be described by  $L_X^{\text{th}} \sim (0.3 - 1.2) \times 10^{32} D_{11}^{-(p-1)/2} \dot{E}_{35}^{(p+5)/4}$  ergs  $s^{-1}$ , assuming a Lorentz factor for the synchrotron-emitting particles of  $\gamma = (0.5 - 1.0) \times 10^6$ , the fractional energy density of electrons to be  $\epsilon_e = 0.5$  and the fractional energy density of the magnetic field to be  $\epsilon_B = 0.02 - 0.1$ .  $p$  and  $D_{11}$  denote the index of the postshock electron energy distribution  $N(\gamma) \propto \gamma^{-p}$ , and the orbital separation in units of  $10^{11}$  cm. The X-ray photon index inferred from the spectrum is  $\Gamma \sim 1.8$  which would suggest that the emission from the shock is in a slow cooling regime (Cheng et al. 2006). The photon index is related to  $p$  as  $\Gamma = (p + 1)/2$ . The observed  $\Gamma$  implies that  $p$  is  $\sim 2.6$ . With  $\dot{E}_{35} = 0.33$  and  $D_{11} = 4.5$ ,  $L_X^{\text{th}}$  is found to be in the range of  $\sim (0.1 - 4.4) \times 10^{30}$  ergs  $s^{-1}$ , which is at the observed level. Intrabinary shock emission thus can explain the observed X-ray luminosity though the modulation depth and amplitude, which is also a function of the inclination angle, is unconstrained from this model.

Based on the preceding discussion, it is not possible to firmly distinguish the possible emission scenarios which may, alone or in combination, be responsible for the observed X-ray emission. To disentangle them would require detailed orbital-phase resolved spectroscopy along with a search for X-ray pulses from the millisecond pulsar. Further dedicated X-ray observations covering more binary orbits are certainly needed to further constrain the emission processes at work in this binary system.

## Chapter 6

# X-ray counterparts of millisecond pulsars in Globular Clusters

This chapter corresponds to a draft of the paper entitled “X-ray counterparts of millisecond pulsars in globular clusters.” The paper is currently in preparation and supposed to be submitted to the *Astrophysical Journal* by Becker & Huang in early May, 2010.

### 6.1 Abstract

Recent radio surveys of globular clusters have increased the number of millisecond pulsars drastically. E.g. M28 is now the globular cluster with the third largest population of known pulsars, after Terzan 5 and 47 Tucanae. This prompted us to revisit the archival Chandra data on globular clusters to evaluate whether the newly discovered millisecond pulsars have an X-ray counterpart among the various X-ray sources seen in them. Cross-correlating the radio timing positions of the cluster pulsars with the high resolution Chandra images revealed 12 possible X-ray counterparts identified in eight different globular cluster systems, in addition to the 47 Tuc pulsar population. These include the newly identified X-ray counterparts of PSR J1824–2452G and PSR J1824–2452H in M28 and PSR J1748–2021B in NGC 6440. We have also characterized their spectral and temporal properties. In order to compare with the pulsar population in the Galactic field, we have re-examined the relation between the X-ray luminosity and the spin-down power of pulsar population in globular clusters by using the enlarged sample reported in this work and found their X-ray conversion efficiency spans a wide range, which is not consistent with the linear  $L_X - \dot{E}$  relation. We have also constructed the cumulative luminosity functions for the millisecond pulsar population in globular clusters as well as in the Galactic field. No significant difference between these two cumulative luminosity functions was found in our study. Therefore, we cannot conclude the discrepancy between the globular cluster pulsar population and the Galactic millisecond pulsars in terms of the current knowledge of their X-ray conversion efficiency and luminosity functions.

## 6.2 Introduction

In recent years it has become clear that globular clusters (GCs) are millisecond pulsar factories. Their high stellar density along with a frequent dynamical interaction of cluster constituents provides an efficient environment for the formation of short-period (binary) pulsars (Rasio et al. 2000; Fregeau 2008; Ivanova et al. 2008). Extensive surveys using radio telescopes with increased sensitivity keep the population of cluster pulsars persistently growing (Camilo & Rasio 2005; Ransom 2008). By March 2010, about 10% of  $\sim 1900$  cataloged radio pulsars fall into the category of millisecond pulsars, i.e. are recycled (Manchester et al. 2005). The majority ( $\sim 70\%$ ) of them are located in 26 GCs<sup>1</sup>. Of these globular cluster millisecond pulsars, 51 ( $\sim 40\%$ ) appear to be solitary, while the others are in binaries (cf. Table 6.9 in Becker 2009). The formation of solitary recycled pulsars is not well-understood, but it is widely believed that the pulsar's companion either gets evaporated (a process which is believed to be at work in the PSR B1957+20 millisecond pulsar/binary system) or that the system gets tidally disrupted after the formation of the millisecond pulsar. Whatever the mechanism is, it is interesting to note that the ratio of solitary to binary millisecond pulsars in globular clusters is almost identical to the 40% observed in the population of galactic disk millisecond pulsars (cf. Becker 2009). Figure 6.1 illustrates the current distribution of X-ray and radio millisecond pulsars in each of the 26 globular clusters known to host millisecond pulsars.

The first millisecond pulsar found in a globular cluster was PSR J1824–2452A (Lyne et al. 1987) which is located in NGC 6626 (M28). PSR J1824–2452A is not only the youngest ( $P/2\dot{P} = 3.0 \times 10^7$  yrs) but also the most powerful ( $\dot{E} = 2.24 \times 10^{36} I_{45} \text{ erg s}^{-1}$ ) and brightest X-ray pulsar in a globular cluster. Its X-ray emission was first detected in ROSAT HRI data (Danner et al. 1997). With an angular resolution of  $\sim 5''$  (HEW) the HRI, though, did not fully allow to resolve its emission into a point source. It therefore was unclear whether the pulsar powers a plerion or its X-ray emission was partly due to a superposition of multiple discrete cluster sources surrounding it. Today we know that sub-arcsecond spatial resolution is required to adequately study globular cluster sources in the X-ray band. Chandra resolved PSR J1824–2452A into a point source along with 12 other X-ray sources surrounding it within the cluster's  $0'.24$  core radius (Becker et al. 2003). Apparently, they cause the diffuse X-ray emission seen to surround PSR J1824–2452A in the ROSAT HRI data.

PSR J1824–2452A is a strong non-thermal X-ray emitter (cf. Becker et al. 2003 but see also Table 6.7 in Becker 2009 for a summary of spectral parameters from X-ray detected millisecond pulsars). Its relatively hard X-ray spectrum allowed to detect its X-ray pulses up to  $\sim 20$  keV with the Rossi X-ray Timing Explorer (Mineo et al. 2004). The X-ray pulse profile is characterized by narrow peaks and small features (Becker & Trümper 1999; Rutledge et al. 2004). The main X-ray pulse component appears to be almost aligned with the main radio pulse (cf. Figure 6.16 in Becker 2009). As thermal emission cannot be beamed strong enough as to explain the narrow pulse peaks, both the spectral and temporal emission properties are in agreement with the interpretation that its X-ray emission is caused by non-thermal radiation processes in the pulsar's magnetosphere. This inference is similar to what is observed in some other Galactic plane mil-

<sup>1</sup><http://www.naic.edu/~pfreire/GCpsr.html>

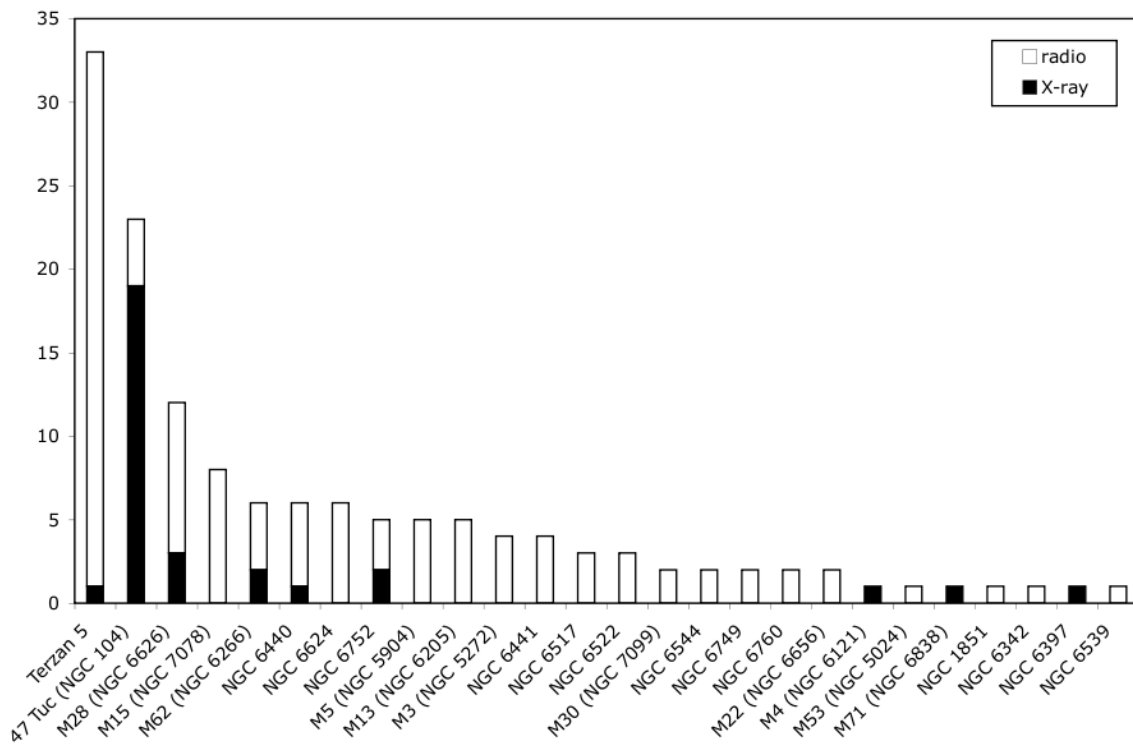


Figure 6.1: A histogram of radio and X-ray detected millisecond pulsars in globular clusters. (Status: spring 2010).

lisecond pulsars (Becker & Trümper 1999; Zavlin 2007; Becker 2009).

In the globular cluster 47 Tucanae (hereafter 47 Tuc), 19 millisecond radio pulsars are found to have X-ray counterparts. In contrast to the bright and hard PSR J1824–2452A, most of the 47 Tuc pulsars turned out to be dim and soft X-ray emitters (Grindlay et al. 2001a, 2002; Bogdanov et al. 2006). The X-ray luminosities of the 47 Tuc pulsars are in the range of  $L_X \sim 10^{30} - 10^{31}$  ergs s<sup>-1</sup> (Bogdanov et al. 2006), which are two orders of magnitudes smaller than that of PSR J1824–2452A. Furthermore, the X-ray spectra of the majority of the 47 Tuc pulsars can be well-described by a thermal model (blackbody or neutron star hydrogen atmosphere model) with temperatures in the range of  $T_{\text{eff}} \sim (1 - 3) \times 10^6$  K and emission radii  $R_{\text{eff}} \sim 0.1 - 3$  km (Bogdanov et al. 2006). Based on the first Chandra observations of 47 Tuc, the X-ray efficiency  $L_X/\dot{E}$  of its X-ray detected pulsars seemed to follow a different relation than seen in the disk pulsar population (Becker & Trümper 1997; Grindlay et al. 2001a). However, including all systematic uncertainties, subsequent observations did not confirm this evidence, albeit more significant data became available meanwhile (Bogdanov et al. 2006). With the current data the X-ray efficiency of the 47 Tuc pulsars is well within the scatter and at a comparable level of that observed in other millisecond pulsars (cf. Becker 2009).

As is demonstrated by the examples described above, the brightness and hardness of GC pulsars in the X-ray regime span a very wide range. Of the 140 GC radio pulsars known today, only a small fraction of them are found to have an X-ray counterpart. Moreover, more than half of these X-ray sources are located in a single cluster, namely 47 Tuc. Only these X-ray MSPs in 47 Tuc have been studied consistently as a unique class (Grindlay et al. 2001; Grindlay et al. 2002; Bogdanov et al. 2006). It is obvious that our current understanding of the X-ray emission nature of cluster pulsars is seriously biased. Therefore, to enlarge the sample and to study their X-ray emission properties more systematically is the motivation for the work we report in this paper. Its structure is as follows: in §6.3 we describe the source detection and identification along with the spectral and timing analysis of the detected millisecond pulsars. Their emission properties compared to those observed in Galactic plane millisecond pulsars are discussed in §6.4.

### 6.3 Observation and Data Reduction

A decade after the launch of Chandra 18 out of the 26 globular clusters which are known to host millisecond pulsars were observed with either the ACIS or HRC detector in focus. We made use of all available imaging data by spring 2010. For counterpart searches and/or spectral analysis there are 45 ACIS-S/I and 5 HRC-I observations available, summing up to a total of 1566.419 ksec and 52.442 ksec of good data. The corresponding observational details of these datasets are summarized in Table 6.1. Although several of them have been previously analyzed by various authors, leading to proposed counterpart assignments for some of the pulsars, new and so far unpublished data were available for NGC 6626 (M28), NGC 6266 (M4), and NGC 6752.

Standard processed level-2 data were used in all counterpart searches. Prior to the data analysis, aspect offsets for each observation, which is a function of the spacecraft roll angle, have

been carefully checked and corrected. The data analysis was restricted to the 0.3 – 8 keV energy range.

### 6.3.1 Source Detection and Identification

To search for X-ray counterparts in the available datasets we used the WAVELET algorithms as implemented in the CIAO 3.4 software package. Source positions were then correlated with the radio timing positions of the globular cluster millisecond pulsars. To assess all identifications we computed the probability for a chance coincidence according to  $P_{\text{coin}} = (N_{\text{X}}^{\text{all}}/r_s^2) \delta\text{RA} \delta\text{Dec}$ . Here  $N_{\text{X}}^{\text{all}}$  is the number of X-ray sources detected within a search region of radius  $r_s$ , and  $\delta\text{RA}$  and  $\delta\text{Dec}$  are the positional uncertainties in right ascension and declination. The latter was determined by combining the errors of the radio pulsar and X-ray source positions in quadrature, considering Chandra’s absolute astrometric accuracy to be 0’21. This astrometric accuracy was estimated from the distribution of aspect offsets for a sample of point sources with accurately known celestial positions<sup>2</sup>. There are 68% of 237 sources imaged with ACIS-S which have offsets smaller than or equal to  $\sim 0’21$ . As all the data used for counterpart searches were taken with the ACIS-S, we included this value in our error budget computation for each coordinate. For the search radius  $r_s$ , we used the globular cluster half-mass radius as most of the pulsars lie within this region. The pulsar PSR J1911 – 6000C in NGC 6752, though, is located outside this radius so that we expanded the search region for this pulsar to 3 arcmin (cf. Figure 6.5). The resulting identifications, counting rates and chance probabilities for finding an X-ray source by chance at the radio pulsar position are summarized in Table 6.2. Distance, half-mass radius and column density of the globular clusters which are known to host millisecond pulsars are summarized in Table 6.3. Basic pulsar parameters for those millisecond pulsars having an X-ray counterpart are listed in Table 6.4.

In total 31 X-ray sources in nine globular clusters were found to be coincident with the radio timing position of known millisecond pulsars. Among them are the 19 millisecond pulsars previously identified in 47 Tuc (Grindlay et al. 2001a, 2002; Bogdanov et al. 2006), PSR J1824–2452A (M28A) in NGC 6626 (Becker et al. 2003), PSR 1953+1846A (M71A) in NGC 6838 (Elsner et al. 2008), PSR J1701–3006B (M62B) in NGC 6266 (Cocozza et al. 2008), PSR J1740–5340 in NGC 6397 (Huang & Becker 2010) and few more for which an association has been assigned in the literature (cf. Table 6.9 in Becker 2009 and references therein). Pulsars for which X-ray counterparts are newly detected are PSR J1824–2452G (M28G) and PSR J1824–2452H (M28H) in NGC 6626, PSR J1748–2021B in NGC 6440, and PSR J1701–3006C (M62C) in NGC 6266. The tentative assignment of the X-ray counterparts for PSR J2140–3310A in M30 (Ransom et al. 2004) and PSR J1910–5959B in NGC 6752 (D’Amico et al. 2002) could not be confirmed by our analysis, albeit additional data were available for the latter pulsar compared to their analysis.

Counting rate upper limits were computed for those pulsars for which no X-ray counterpart could be detected. For this we measured the number of counts recorded at the radio pulsar position and computed the  $3\sigma$  upper limits according to  $C_{3\sigma} = 0.5 \times (S/N)^2 + (S/N) \times$

<sup>2</sup>See <http://cxc.harvard.edu/cal/ASPECT/celmon/> for details

$\sqrt{cts + 0.25 \times (S/N)^2}$ . Here  $S/N = 3$  is the signal-to-noise ratio and  $cts$  the counts obtained within a circle of 1 arcsec radius centered on the position of the radio pulsar. All upper limits are summarized in Table 6.5 along with the exposure time of the observation and the number of counts recorded at the pulsar position. Figures 6.2 to 6.10 show Chandra images of all globular clusters considered in this work. The location of the millisecond pulsars and the cluster core-radius are indicated.

### 6.3.2 Search for Temporal Variability

The 3.2 s frame time of the ACIS-S detector does not support to search for coherent X-ray pulsations from the clusters' millisecond pulsars. Most of the sources considered in this work, though, were in the focus of the ACIS-S for multiple times, permitting us to investigate their temporal behavior on longer time scales. The length of the time scales in the various datasets is given by the time gaps between the different observations, e.g. hours to years.

We checked the counting rates of all pulsars to search for the temporal variability (cf. Table 6.2). Binary pulsars (cf. Table 6.4) were tested on whether they show flux variability related to e.g. their orbital binary motion. This was observed in 47 Tuc W (Bogdanov et al. 2005) which exhibits large-amplitude X-ray variability, probably due to geometric occultations of an X-ray emitting intra-binary shock by the companion main-sequence star (Bogdanov et al. 2006). As an example, Figure 6.11 shows the light curves of the M28 pulsars PSR J1824–2452G and J1824–2452H as folded at their binary period. PSR J1824–2452G is in a 2.51 h binary system with a low-mass companion. PSR J1824–2452H has an orbit period of 10.87 h and has been observed to show radio eclipses (Bégin 2006). Indeed, inspecting the light curves by eye may reveal a flux variability with the pulsar's orbital binary motion. From the statistical point of view, though, the significance for variability is only at the  $\sim 1.5 - 2\sigma$  level for the light curves with 6, 8, or 10 phase bins. More stringent results were found for PSR J1748–2021B in NGC 6440 and for PSR J1740–5340 in NGC 6397.

PSR J1748–2021B has an orbital period of  $\sim 20$  days Freire et al. (2008). NGC 6440 was observed by Chandra twice, in 2000 July 4 and three years later in 2003 June 27. These observations cover the relatively narrow phase intervals<sup>3</sup> 0.124 – 0.137 and 0.058 – 0.072 of the pulsar's binary orbit. The vignetting corrected net counting rates of its possible X-ray counterpart in these two datasets are  $(1.68 \pm 0.28) \times 10^{-3}$  cts/s and  $(5.03 \pm 0.46) \times 10^{-3}$  cts/s, respectively. The counting rates measured in both data thus differ by a factor of  $\sim 3$  with a significance of  $\sim 6\sigma$ . On whether this variability is because of a modulation of the X-ray flux over the pulsar's binary orbit or because of a long term flux increase by other means can not be clarified with the available data.

The millisecond pulsar PSR J1740–5340 in NGC 6397 is in a  $\sim 1.35$  day binary orbit with a massive late type companion (D'Amico et al. 2001b). The pulsar's radio emission is seen to eclipse in the orbital phase interval 0.05 – 0.45 (D'Amico et al. 2001b). Five datasets are available in the Chandra archive from NGC 6397 (cf. Table 6.1), covering various phase ranges of the pulsar's binary orbit (see Huang & Becker 2010 for a more detailed discussion). The first

<sup>3</sup>The zero point is set to the ascending node.

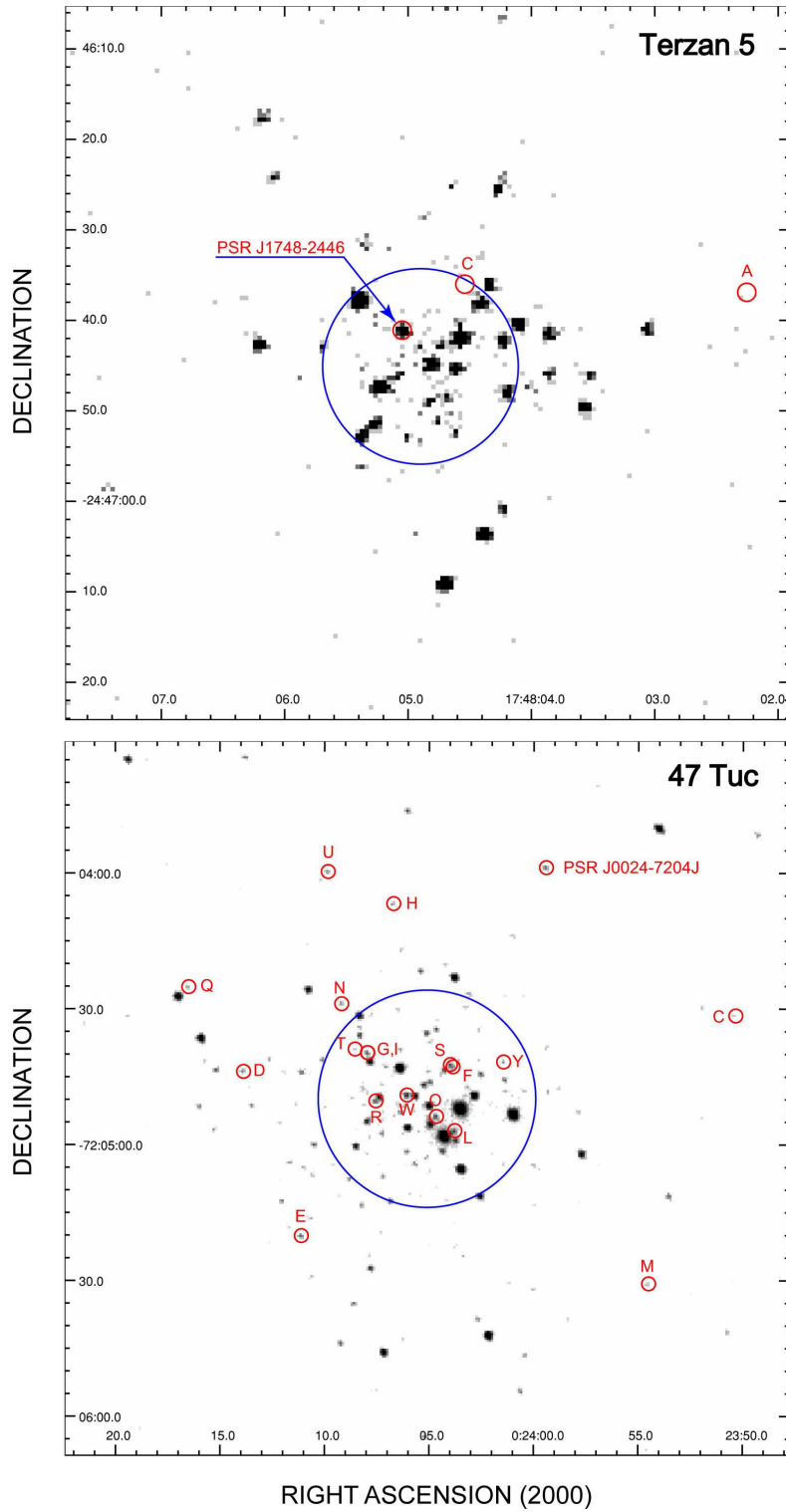


Figure 6.2: Chandra ACIS-S view on the globular clusters Terzan 5 and 47 Tuc. The clusters core radius and the position of known millisecond pulsars are indicated by blue and red circles, respectively. (Status: spring 2010).

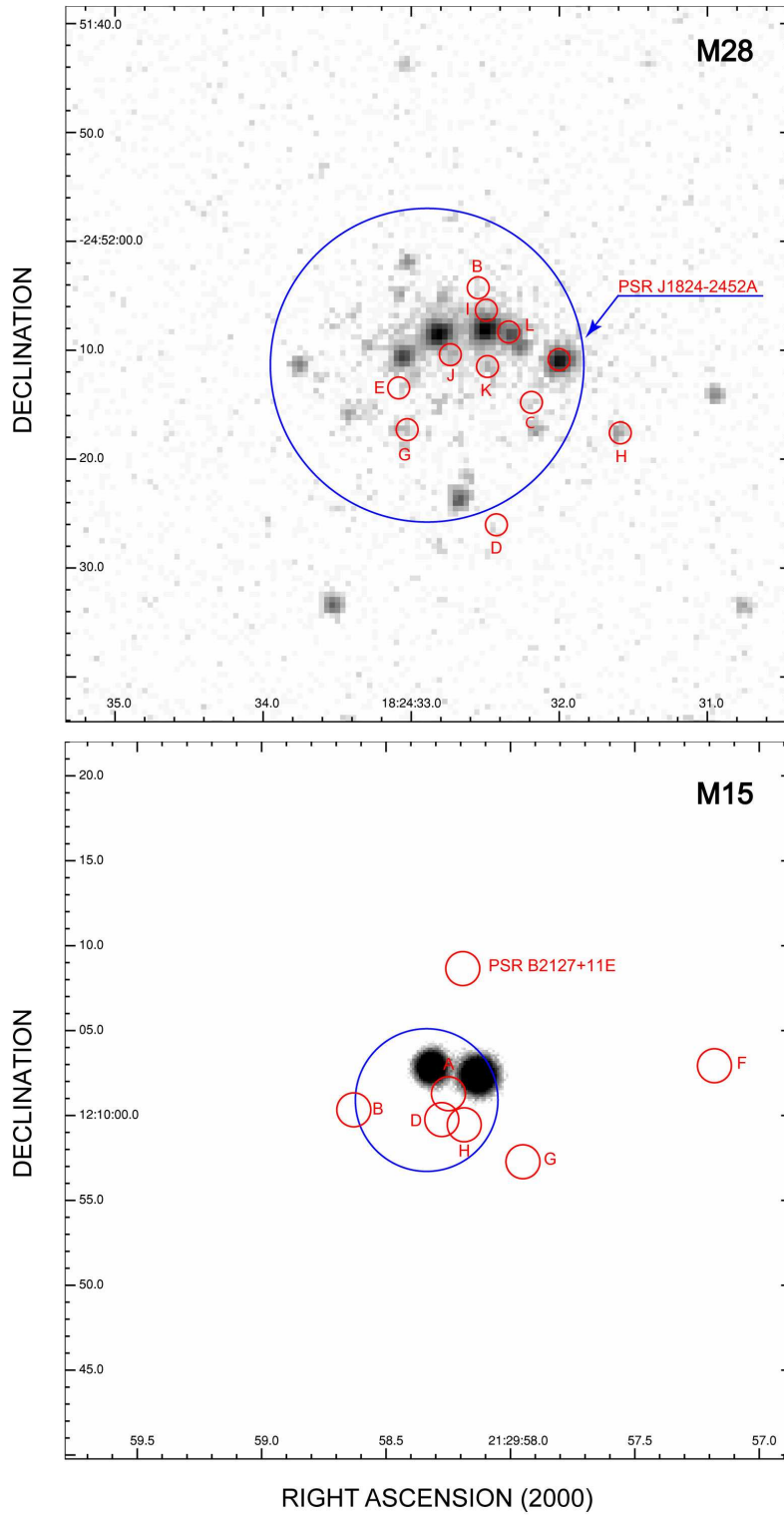


Figure 6.3: Chandra ACIS-S view on the globular clusters M28 (NGC 6626) and HRC-I image of M15 (NGC 7078). The clusters core radius and the position of known millisecond pulsars are indicated by blue and red circles, respectively. (Status: spring 2010).

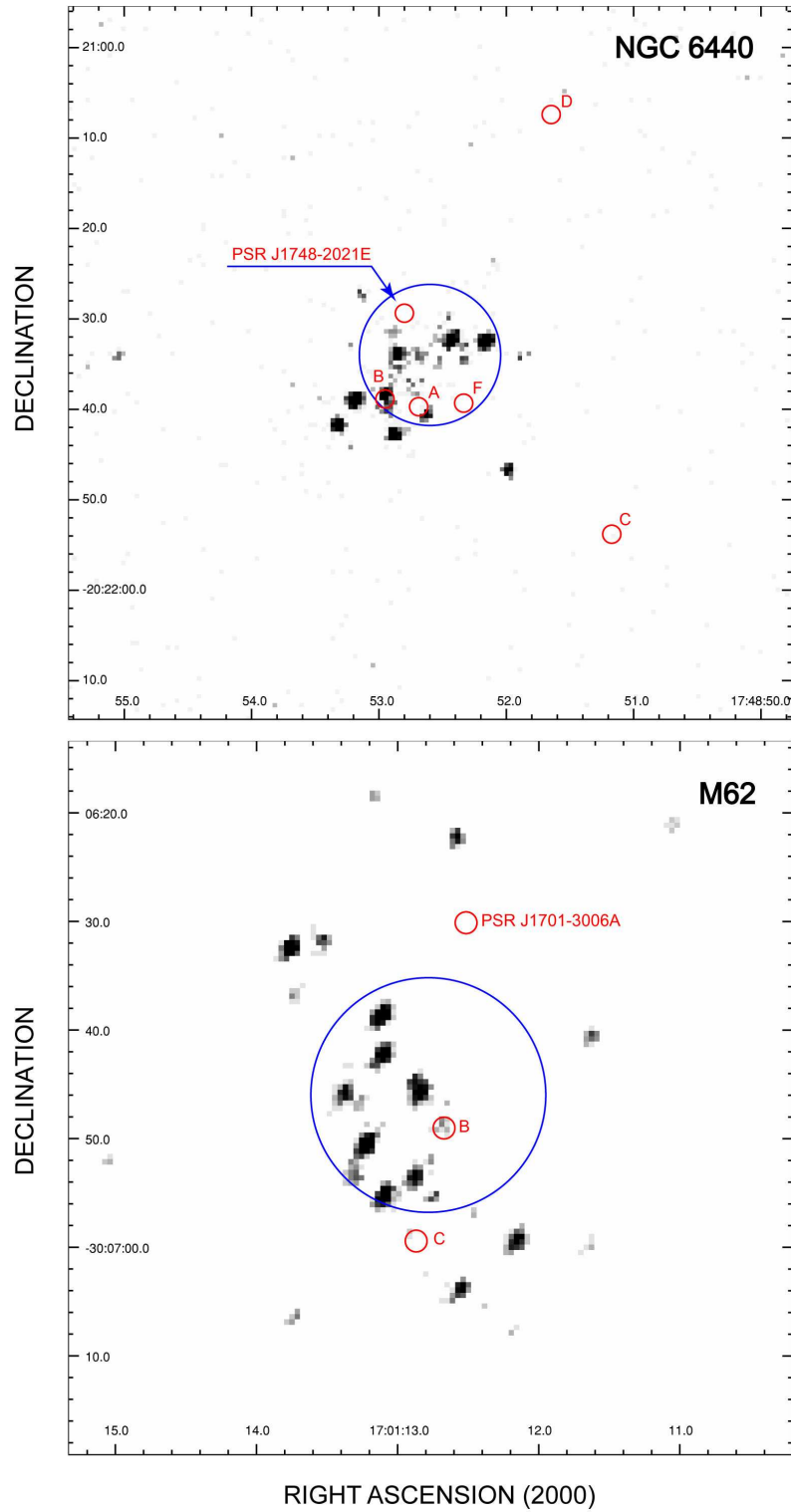


Figure 6.4: Chandra ACIS-S view on the globular clusters NGC 6440 and M62 (NGC 6266). The clusters core radius and the position of known millisecond pulsars are indicated by blue and red circles, respectively. (Status: spring 2010).

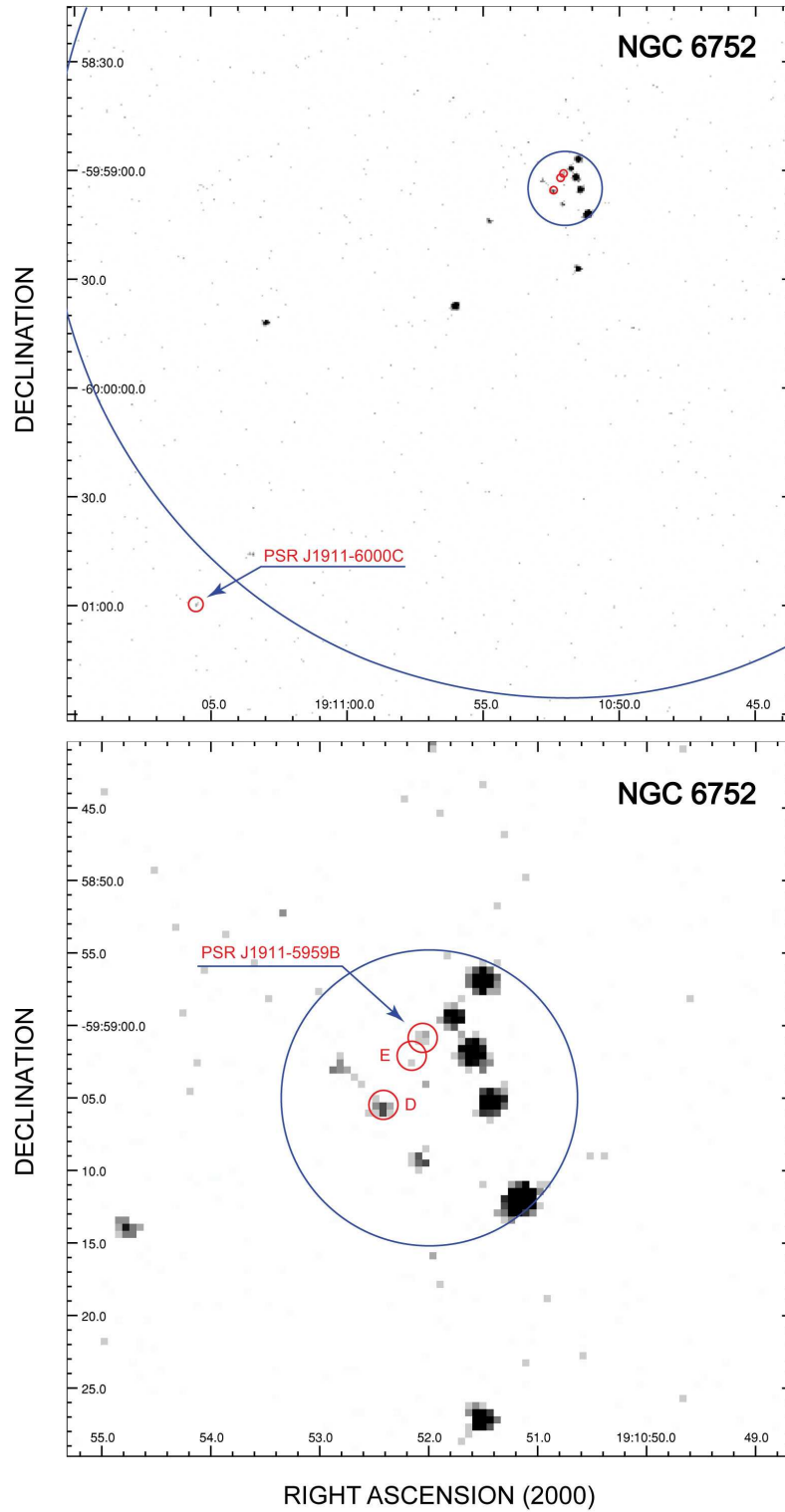


Figure 6.5: Chandra ACIS-S view on the globular clusters NGC 6752. The red circles show the positions of the known millisecond pulsars. The blue circles are centered on the nominal center of the cluster and have the core radius (inner circle) and the half-mass radius (outer circle). The bottom figure shows a zoom in of the top figure. (Status: spring 2010).

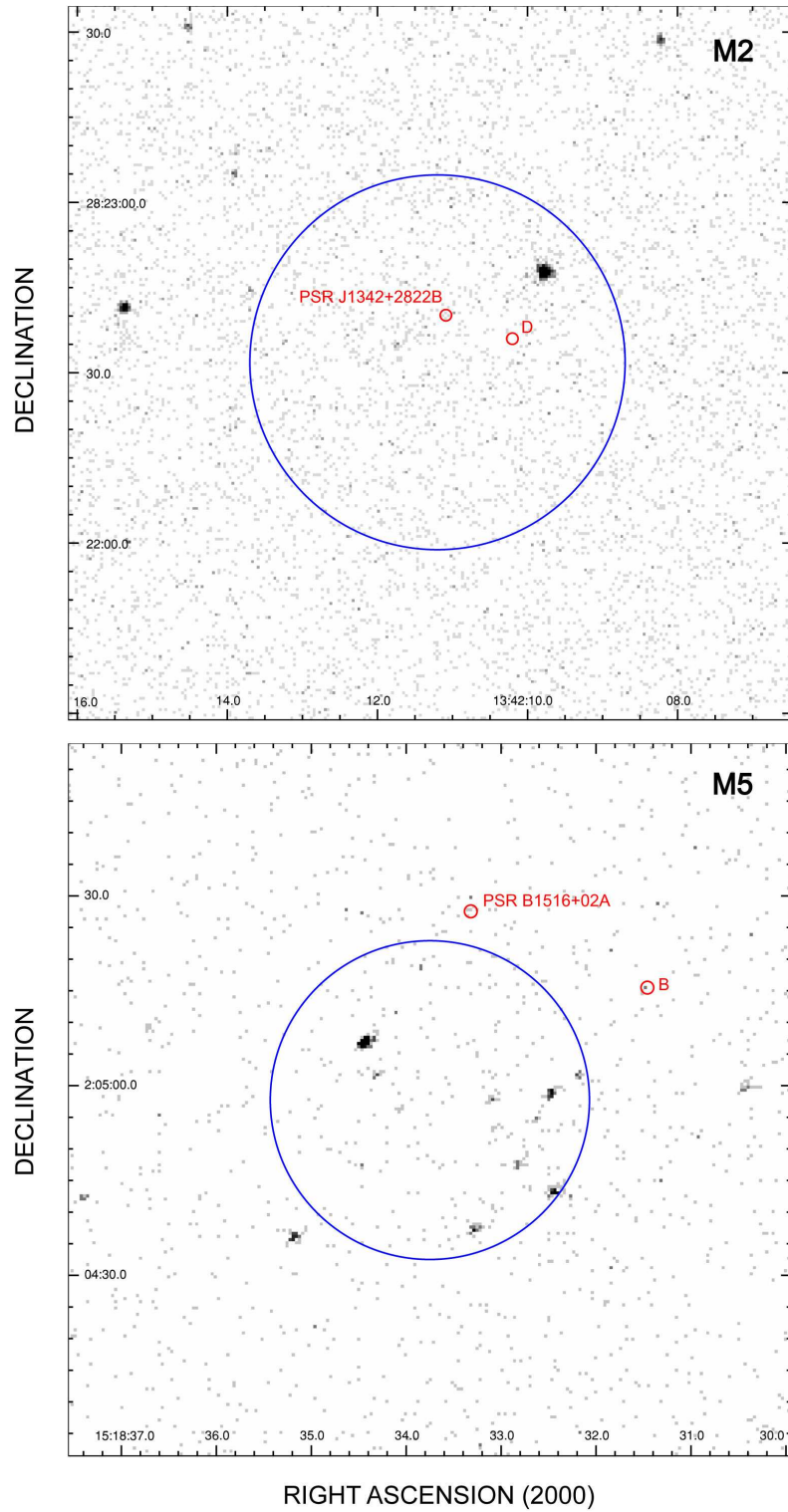


Figure 6.6: Chandra ACIS-S view on the globular clusters M3 (NGC 5272) and M5 (NGC 5904). The clusters core radius and the position of known millisecond pulsars are indicated by blue and red circles, respectively. (Status: spring 2010).

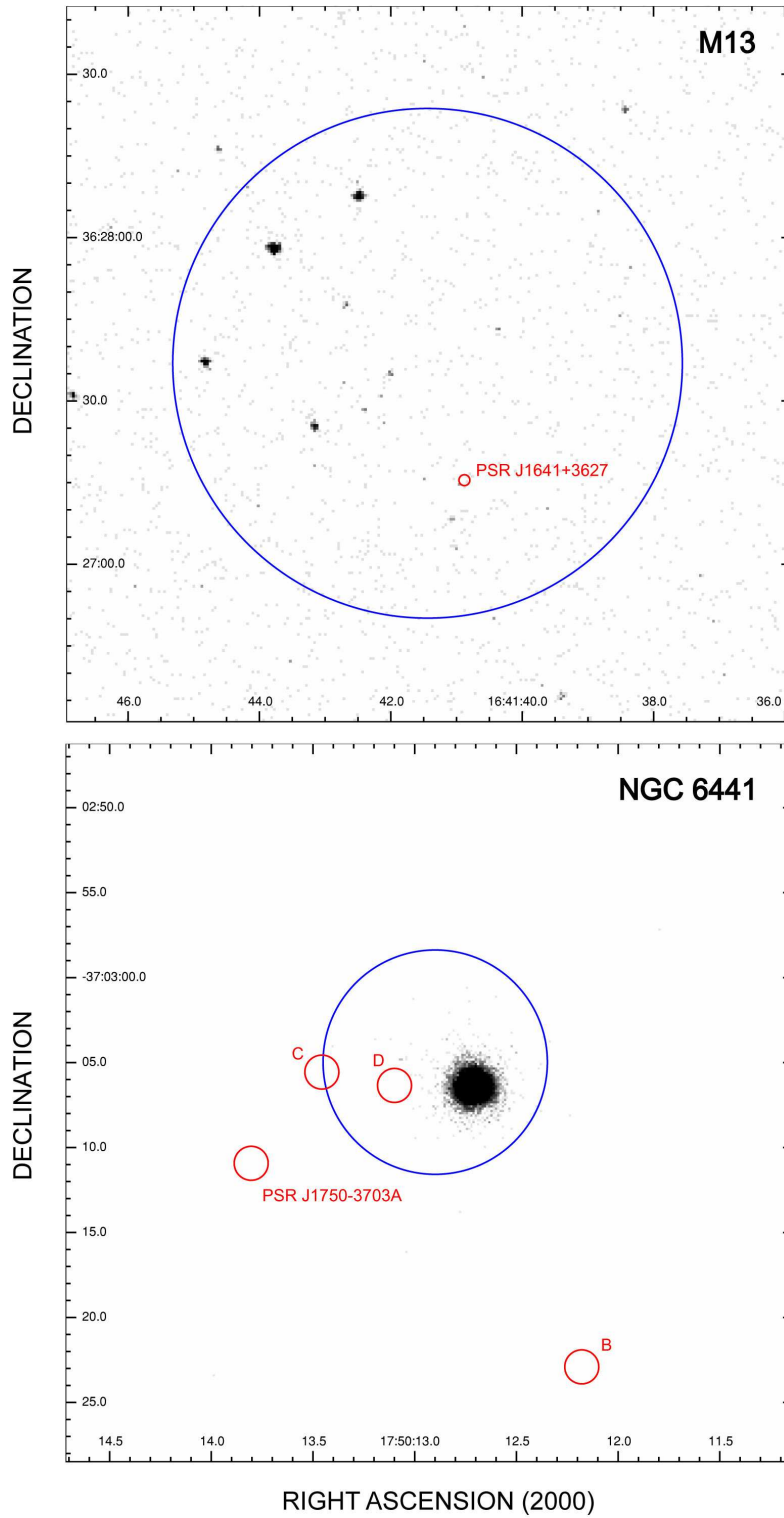


Figure 6.7: Chandra ACIS-S view on the globular clusters M13 (NGC 6205) and HRC-I image of NGC 6441. The clusters core radius and the position of known millisecond pulsars are indicated by blue and red circles, respectively. (Status: spring 2010).

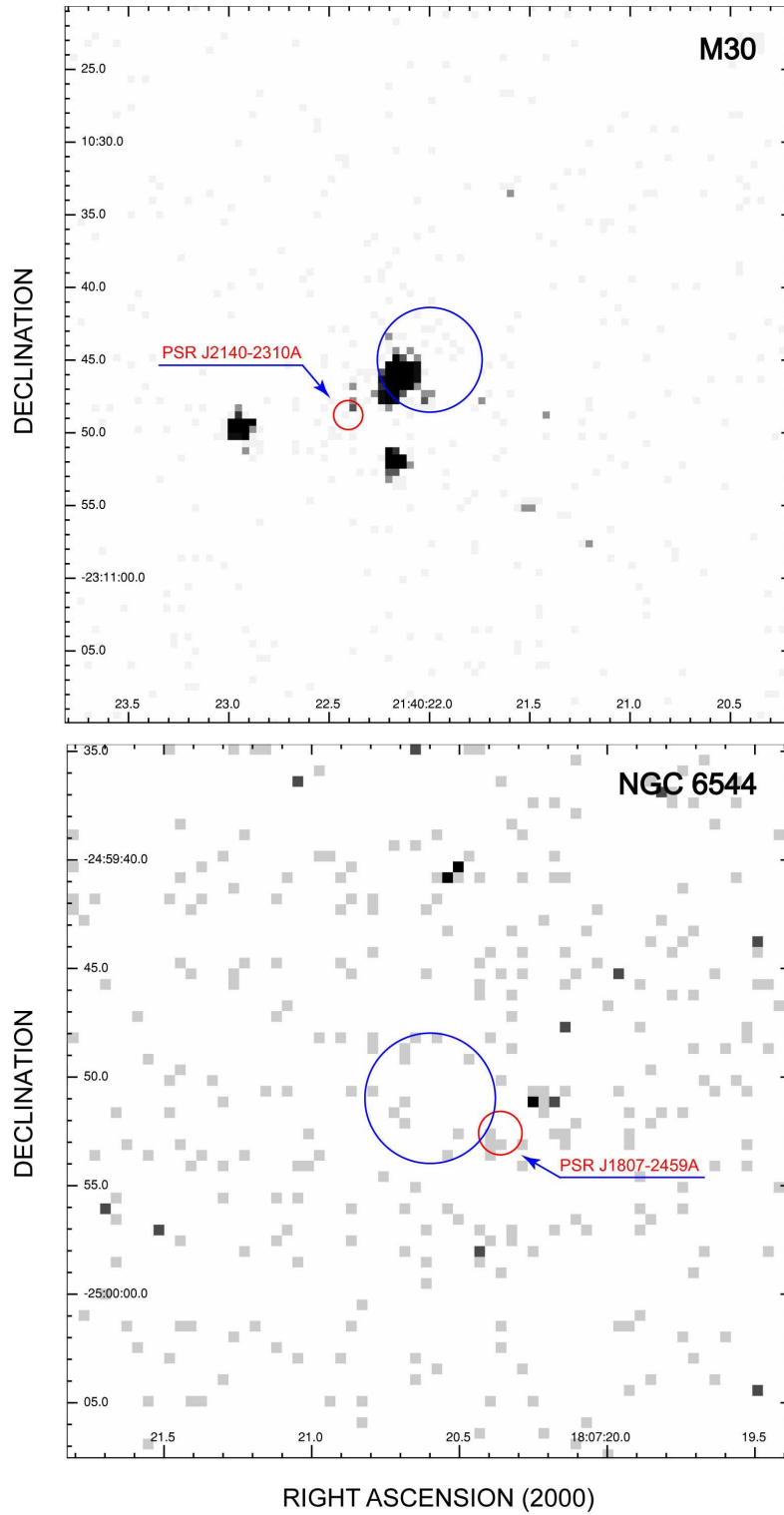


Figure 6.8: Chandra ACIS-S view on the globular clusters M30 (NGC 7099) and NGC 6544. The clusters core radius and the position of known millisecond pulsars are indicated by blue and red circles, respectively. (Status: spring 2010).

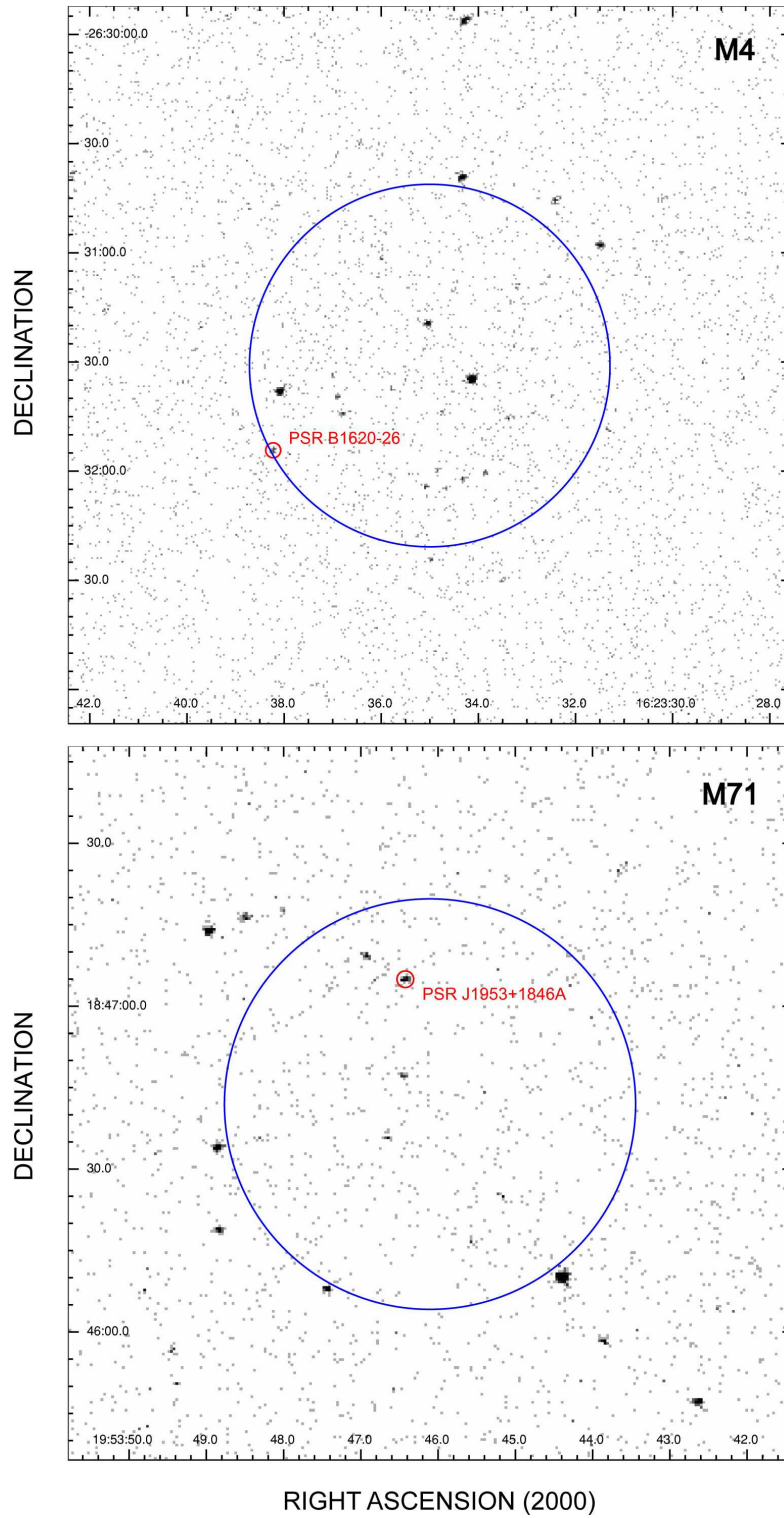


Figure 6.9: Chandra ACIS-S view on the globular clusters M4 (NGC 6121) and M71 (NGC 6838). The clusters core radius and the position of known millisecond pulsars are indicated by blue and red circles, respectively. (Status: spring 2010).

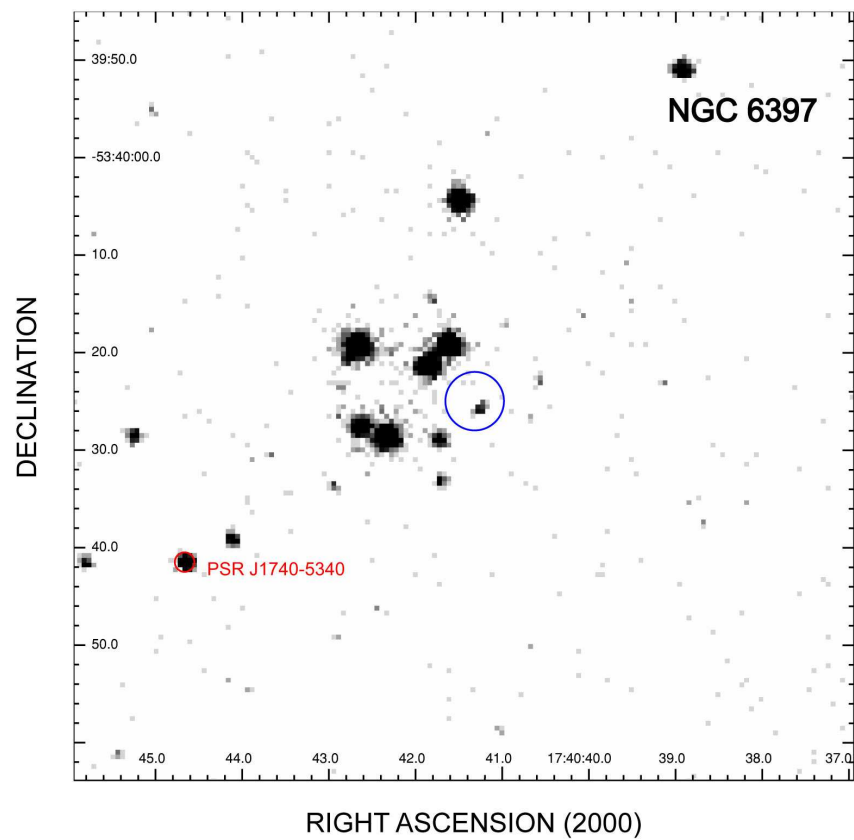


Figure 6.10: Chandra ACIS-S view on the globular clusters NGC 6397. The clusters core radius and the position of known millisecond pulsars are indicated by blue and red circles, respectively. (Status: spring 2010).

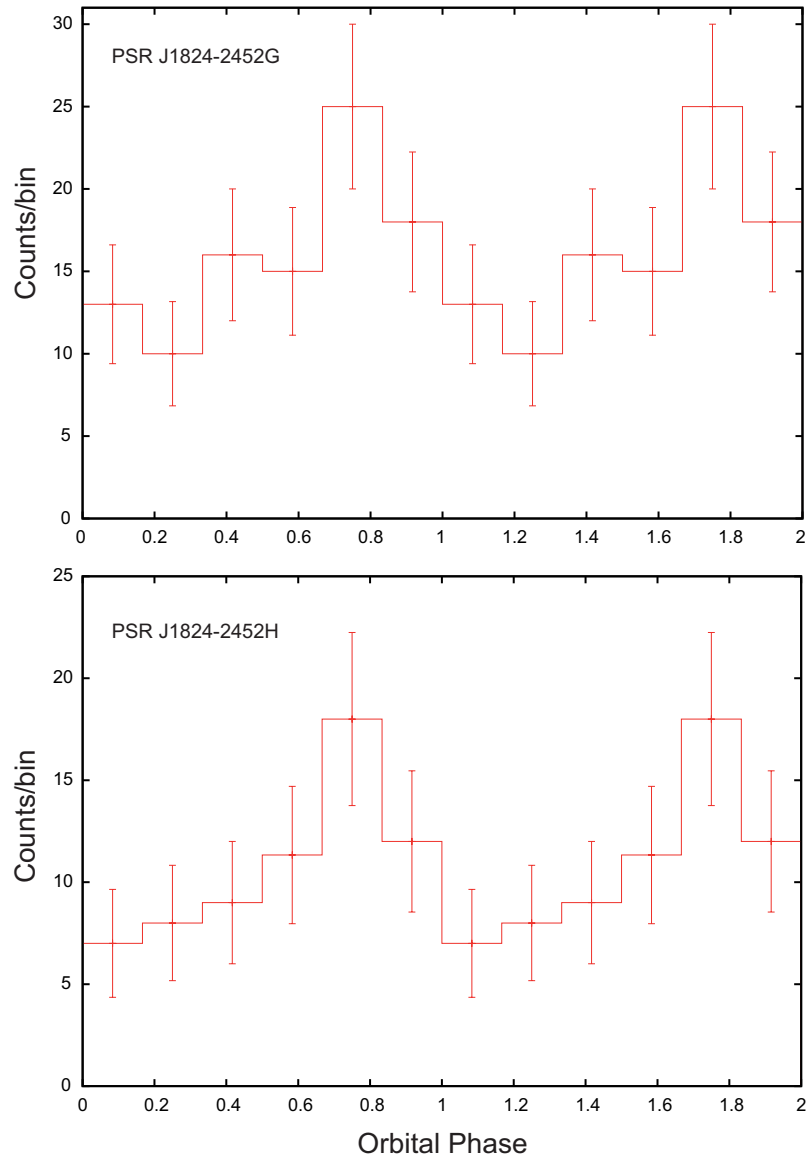


Figure 6.11: Orbital light curves of the pulsars PSR J1824–2452G (top) and J1824–2452H (bottom) in M28. The data were binned into six phase bins. Error bars indicate the  $1\sigma$  uncertainty. Two phase cycles are shown for clarity.

observation done in 2000 July 31 was aimed on the front-illuminated (FI) ACIS-I3 chip, while the other four observations were taken with the back-illuminated (BI) chip ACIS-S3. The pulsar's net counting rates obtained from this data are  $(1.31 \pm 0.17) \times 10^{-3}$  cts/s,  $(1.74 \pm 0.25) \times 10^{-3}$  cts/s,  $(2.89 \pm 0.33) \times 10^{-3}$  cts/s,  $(2.26 \pm 0.16) \times 10^{-3}$  cts/s and  $(2.92 \pm 0.14) \times 10^{-3}$  cts/s, respectively, revealing a  $\sim 3\sigma$  flux variability on time scales of month to years. The X-ray light curve of the pulsar as folded at the binary period is shown in Figure 5.2. The significance of the flux modulation over the observed orbit was found to be between 88.5% and 99.6%, depending on the number of phase bins used to construct the light curve (cf. Huang & Becker 2010).

### 6.3.3 Spectral Analysis

The ACIS-S CCDs provide spectral information for all cluster pulsars for which counterparts are detected. The quality of spectral fits and the constraint on the parameters of the model-spectra, however, is a function of photon statistics and thus varies significantly among the detected counterparts. In addition, the column absorption towards the various globular clusters shows a large diversity (cf. Table 6.3), meaning that the sensitivity to detect soft X-rays from e.g. thermal hot-spots on the neutron star surface may be higher for some clusters (e.g. in 47 Tuc) than in others (e.g. Terzan 5).

The extraction of the source and background spectra as well as the computation of the corresponding response and effective area files were performed with the data reduction package CIAO 3.4 by using the calibration data in CALDB 3.4. To extract the spectra we used circular regions of  $2''$  radius (corresponding to  $\sim 95\%$  encircled energy) centered at the radio pulsar's timing position. Net counting rates for the pulsar counterparts (cf. Table 6.3) were obtained by subtracting an averaged background rate which we obtained from combining two different source-free regions located near to the pulsar. Power law and blackbody model spectra were then fitted to the extracted spectra by using XSPEC 12.3.1. All datasets of a pulsar counterpart were fitted simultaneously unless a temporal counting rate variability was found for e.g. binary pulsars.

Most millisecond pulsar counterparts are detected with a relatively small photon statistics, requiring to fix the hydrogen column densities in order to better constrain the remaining model parameters. If so, we deduced  $N_{\text{H}}$  from the optical foreground reddening  $E(B-V)$  of the corresponding globular clusters (Harris 1996, updated 2003<sup>4</sup>). Only for PSR J1824–2452A in M28 and the two recent observations #7460 and #7461 of PSR J1740–5340 in NGC 6397, the photon statistics was sufficient to include  $N_{\text{H}}$  as an additional free parameter in the spectral fits.

For all 47 Tuc pulsars we grouped the extracted spectra so as to have at least 5 counts per spectral bin. 47 Tuc F+S and G+I were treated as single sources since their spectra could not be separated. The spectral parameters for most of the 47 Tuc pulsars are consistent with those reported by Bogdanov et al. (2006), except for 47 Tuc L and R. The spectral fits of these two pulsars are not well described by a single blackbody model albeit different background regions were included or  $N_{\text{H}}$  was let a free parameter in the fits. A composite model consisting of a

<sup>4</sup><http://physwww.mcmaster.ca/~harris/Databases.html>

blackbody plus power law model yields a better description of the observed spectra.

In order to investigate whether the binary pulsars PSR J1740–5340 in NGC 6397 and J1748–2021B in NGC 6440 show spectral changes along with their variable counting rates observed at different orbital phases, we analyzed each of their available datasets separately. As can be seen in Table 6.7, the photon indices obtained for a pulsar from each of the various datasets are all in agreement with each other (cf. also Huang & Becker 2010 for a more detailed discussion on PSR J1740–5340 in NGC 6397). The X-ray luminosity of PSR J1748–2021B in NGC 6440, though, changed by a factor of  $\sim 3$  for observations taken in 2000 July and 2003 June. PSR J1748–2021B furthermore shares the non-thermal nature of its X-ray spectrum with PSR J1953+1846A in M71 (cf. Elsner et al. 2008) and PSR J1701–3006C in M62. Their photon indices are in the range  $\sim 1.4 - 1.9$ . For the binary pulsars PSR J1824–2452H in M28 and PSR J1748–2446 in Terzan 5, the limited photon statistics does not support to discriminate between thermal or non-thermal emission models. A blackbody and a power law model both describe their spectra with comparable goodness (cf. Table 7). The fitted blackbody temperatures, however, are at the level of  $\gtrsim 10^7$  K, which is an order of magnitude higher than what is observed in other millisecond pulsar spectra (cf. Table 6.7 in Becker 2009). A non-thermal interpretation of their emission therefore seems more likely to us. Whether this non-thermal X-ray radiation is due to magnetospheric emission from within the pulsars’ co-rotating lightcylinder or whether it arises because of an intra-binary shock formed by the relativistic pulsar wind and the matter from the stellar companion is currently not clear.

For the brightest of all millisecond pulsars, PSR J1824–2452A, five observations are currently available in the Chandra data archive. Three of them were taken in 2002 and provided the basis for the results published on M28 by Becker et al. (2003). Two additional and significantly longer observations of M28 were taken in 2008, increasing the total on source exposure to 237 ksec which is almost five times as much as was available in 2002. To analyze the spectrum of PSR J1824–2452A we made use of all five datasets.

The spectra based on the 2002 data were grouped so as to have at least 30 counts per spectral bin. For the 2008 data we used a grouping of 50 and 30 counts per spectral bin for the longer (#9132) and shorter (#9133) observations (cf. Table 8.2). It has been shown previously that the pulsar’s X-radiation is dominated by non-thermal emission (Kawai & Saito 1999; Becker et al. 2003; Mineo et al. 2004). Fitting a power law spectral model to the data yields  $N_{\text{H}} = (0.22 \pm 0.02) \times 10^{22} \text{ cm}^{-2}$ , a photon-index  $\alpha = 1.13_{-0.04}^{+0.03}$ , and a normalization at 1 keV of  $3.43_{-0.15}^{+0.23} \times 10^{-5} \text{ photons cm}^{-2} \text{ s}^{-1} \text{ keV}^{-1}$  ( $\chi^2_{\nu} = 1.00$  for 168 dof). The column density is fully consistent with what is deduced from the reddening towards M28. The unabsorbed energy flux in the 0.3 – 8.0 keV band is  $f_x = 3.7_{-0.3}^{+0.4} \times 10^{-13} \text{ ergs s}^{-1} \text{ cm}^{-2}$ , yielding an X-ray luminosity of  $L_x = 1.36_{-0.11}^{+0.15} \times 10^{33} \text{ ergs s}^{-1}$ . If transformed to the 0.1 – 2.4 keV ROSAT band this corresponds to  $L_x = 3.76_{-0.22}^{+0.33} \times 10^{32} \text{ ergs s}^{-1}$ , which is comparable with the luminosity inferred from the ROSAT data (Verbunt 2001). These luminosities imply a rotational energy to X-ray energy conversion factor of  $L_{x,0.3-8.0 \text{ keV}}/\dot{E} = 6.1 \times 10^{-4}$  and  $L_{x,0.1-2.4 \text{ keV}}/\dot{E} = 2.1 \times 10^{-4}$ , respectively. The phase averaged photon index obtained in our spectral fits is identical to the one deduced for PSR J1824–2452A from the observations at pulse maximum using joint ASCA and RXTE data (Kuiper et al. 2003). This is in agreement with the interpretation that its fraction of pulsed X-ray

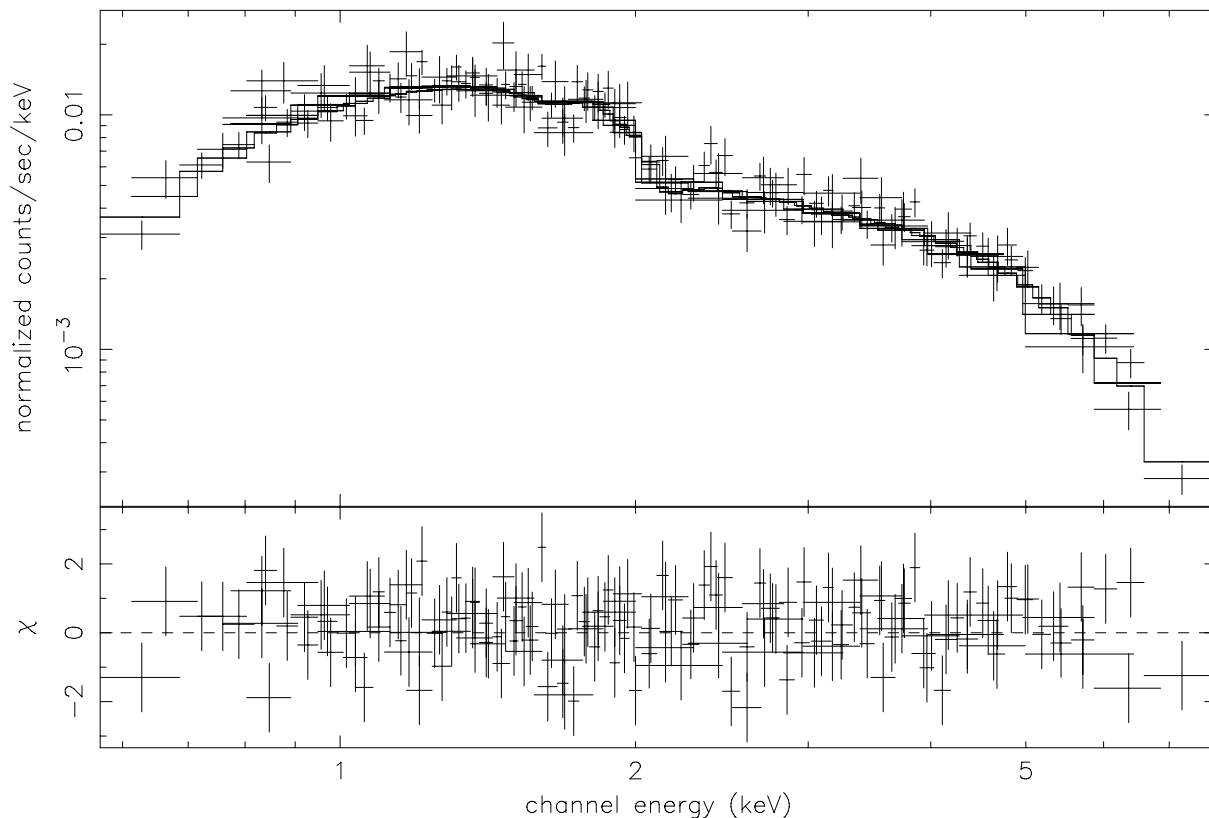


Figure 6.12: Energy spectrum of the millisecond pulsar PSR J1824–2452A in M28 obtained from the Chandra observations taken in 2002 and 2008 and fit to an absorbed power-law model (*upper panel*) and contribution to the  $\chi^2$  fit statistic (*lower panel*).

photons is 85% – 100%.

Using the 2002 Chandra data, Becker et al. (2003) found some evidence for a possible line feature centered at  $\sim 3.3$  keV in the X-ray spectrum of PSR J1824–2452A (cf. Figure 2 in Becker et al. 2003). The new data from 2008 supersede the previous data in photon statistics and sensitivity and do not confirm the presence of this line feature. Figure 6.12 shows the pulsar spectrum as fitted to an absorbed power law. No spectral feature is seen in the spectrum of PSR J1824–2452A.

Unlike for many other millisecond pulsars (cf. Table 6.7 of Becker 2009 for a summary), modeling the X-ray spectrum of PSR J1824–2452A with a power law does not require any additional blackbody component (e.g. associated with thermal emission from heated polar caps) to get an acceptable spectral fit. All combinations of blackbody normalizations and temperatures that were fitted along the power law model gave reduced  $\chi^2$ -values which didn't indicate a higher likelihood for such a model than the fits to a single power law. The F-test statistic for adding the extra blackbody spectral component to the power law model, thus, is very low.

Nevertheless, the high photon statistics provided by the archival Chandra data allows us to

constrain the temperature of a presumed thermal polar cap. Defining the size of the polar cap as the foot points of the neutron star's dipolar magnetic field, the radius of the polar cap area is given by  $\rho = \sqrt{2\pi R^3/cP}$  with  $R$  being the neutron star radius,  $c$  the velocity of light and  $P$  the pulsar rotation period (see e.g. Michel 1991). For PSR J1824–2452A, with a rotation period of 3.05 ms this yields a polar cap radius of  $\rho \sim 2.62$  km.

As a thermal spectral component of a heated polar cap contributes mostly below  $\sim 1$  keV, the fitted column absorption is found to be a steep function of the blackbody emitting area (normalization) and temperature. To determine a polar cap temperature upper limit which is in agreement with the fitted power law model and column absorption we fixed the absorption of the composite model as well as the power law photon index to the upper bound set by the  $1\sigma$  confidence range deduced in the power law fit. The power law normalization was fixed to the  $1\sigma$  lower bound as this led to a higher upper limit. We then computed the confidence ranges of the blackbody normalization and temperatures by leaving these parameters free. The resulting contours, computed for two parameters of interest, are shown in Figure 6.13.

The blackbody normalization in XSPEC is proportional to  $\rho_{km}^2/d_{10kpc}^2$  in which  $\rho_{km}$  is the blackbody radius of the emitting area and  $d_{10kpc}$  is the pulsar distance in units of 10 kpc. For a distance of 5.6 kpc towards M28 and a polar cap radius of 2.62 km we thus obtain a normalization of 21.87. Assuming a contribution from one polar cap only we can set a  $3\sigma$  temperature upper limit of  $T_{pc}^\infty < 1.3 \times 10^6$  K. This upper limit is at the same level as the temperatures fitted for the thermal components in the spectra of e.g. the solitary millisecond pulsar PSR J2124 – 3358 or of PSR J0437 – 4715 (cf. Table 6.7 in Becker 2009). That non-thermal radiation is the dominating emission component in PSR J1824–2452A thus does not exclude the existence of a thermal polar cap of similar properties than observed in other millisecond pulsars. Computing the  $3\sigma$  upper limit for a possible thermal polar cap contribution to the Chandra observed energy flux we find  $f_{bb,0.3-8 keV} \leq 1.5 \times 10^{-14}$  ergs s $^{-1}$  cm $^{-2}$ , corresponding to  $\leq 4\%$  of the non-thermal energy flux within 0.3 – 8 keV.

Table 6.7 summarizes all best fit parameters of the model spectra applied to the pulsar's X-ray counterparts. The quoted errors represent the 68% confidence level for one parameter of interest.

## 6.4 Discussion

We have systematically studied the X-ray emission from 31 GC pulsars. Their spectral properties and luminosities were evaluated in a consistent way. Therefore, this work provides a relatively less biased sample for studying the X-ray emission properties of GC pulsars, though, they reside in 9 different clusters.

Grindlay et al. (2002) have suggested the X-ray conversion efficiency (i.e. the dependence of  $L_X$  on  $\dot{E}$ ) for 47 Tuc pulsars to be  $L_X \propto \dot{E}^{0.5}$ , where  $\dot{E}$  is the spin-down power of the pulsar. Such dependence is obviously shallower than the linear relation  $L_X \sim 10^{-3} \dot{E}$  found for the pulsars in the Galactic field and in the globular clusters (see Becker & Trümper 1997, 1999, 2009). Reexamining the  $L_X - \dot{E}$  relation for the 47 Tuc pulsars, Bogdanov et al. (2006) have found a relation of  $L_X \propto \dot{E}^{0.2 \pm 1.1}$ . The larger uncertainty does not allow one to discriminate the  $L_X \propto \dot{E}^{0.5}$  relation

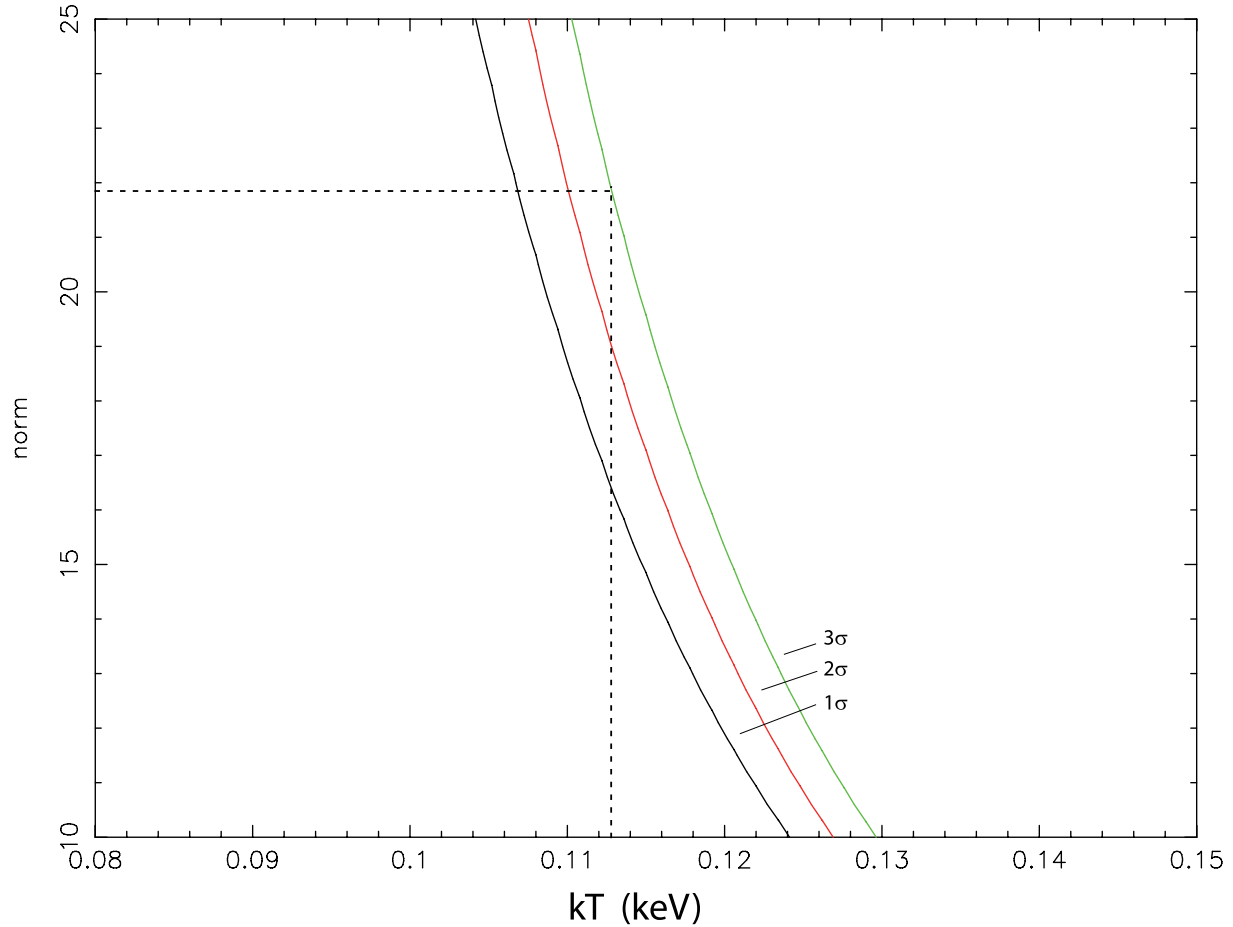


Figure 6.13: Portion of the confidence contours showing the blackbody normalization versus blackbody temperature for the composite model (see text). The horizontal line at a normalization of 21.87 corresponds to a polar cap radius of 2.62 km and a pulsar distance of 5.6 kpc. The contours correspond to  $\chi^2_{min} = 167.5$  plus 2.3, 6.17 and 11.8 which are the  $1\sigma$ ,  $2\sigma$  and  $3\sigma$  confidence contours for 2 parameters of interest.

and the linear one.

We attempted to reexamine the X-ray conversion efficiency of pulsar population in GCs by adding the results reported in this paper into the data pool, together with the 47 Tuc pulsars. The spin-down power  $\dot{E}$  of the GC pulsars was computed from the estimated intrinsic spin-down rate  $\dot{P}$  reported in the corresponding literature (see Table 6.4). Only 25 out of 31 GC pulsars which have their period derivative  $\dot{P}$  were used in this work. In addition, we excluded NGC 6440B in our fitting since its X-ray luminosity cannot be determined well by using two observations only covering part of the orbital phase in the binary system. We therefore examined the  $L_X - \dot{E}$  relation for the selected sample of 24 GC pulsars (see Figure 6.4). We adopted the absorption-corrected X-ray luminosities inferred from the best-fit model and have taken the  $1-\sigma$  error of the X-ray luminosities into account in the following statistical analysis. We found that the X-ray luminosities of these GC pulsars follow the empirical relation:  $L_X \propto \dot{E}^{0.48 \pm 0.11}$ . It is interesting to note that the best-fit parameters are consistent with those reported by Grindlay et al. (2002), which gives the relation of  $L_X \propto \dot{E}^{0.48 \pm 0.15}$ . However, if only taking the X-ray detected millisecond pulsars in the Galactic plane (see Table 9 of Becker 2009) into account, these data points can be described by a linear trend:  $L_X \propto \dot{E}^{0.99 \pm 0.24}$ .

Becker (2009) reported that the  $L_X - \dot{E}$  relation is in good agreement with  $L_X = 10^{-3} \dot{E}$  (Becker & Trümper 1997, 1999) by using the more significant data of all X-ray detected pulsars, including the pulsars in the Galactic field and in the globular clusters. However, only considering the millisecond pulsar population, we found their X-ray conversion efficiency spans a wide range (see Figure 6.4), which is not consistent with the expected linear relation. As suggested by Becker (2009), the  $L_X = 10^{-3} \dot{E}$  relation represents as an upper bound to the X-ray efficiency instead of a fixed correlation. With the higher sensitivity of XMM-Newton and Chandra, more faint pulsars, e.g. the orientation of the magnetic/rotational axes to the light of sight might not be optimal, have been detected. Since the beaming correction of the X-ray luminosity is not applied, the X-ray efficiency for those faint pulsars appears to be smaller.

An alternative possible reasons for the flattened  $L_X - \dot{E}$  relation for GC pulsars may be due to the lack of reliable measurement of the spin-down rate  $\dot{P}$  of many GC pulsars. This can be ascribed to two facts. First, the radio signals from these pulsars are relatively weak and therefore an accurate timing solution is difficult to obtain. Moreover, the gravitational effect of a cluster further complicates the estimation of  $\dot{P}$ . The subtraction of the gravitational acceleration of the cluster can possibly be done by numerical modeling (see Grindlay et al. 2002). However, the uncertainties of the intrinsic  $\dot{P}$  of an individual cluster pulsar can still be rather large (cf. Cheng & Taam 2003). Obtaining the intrinsic  $\dot{P}$  of GC pulsar is out of the scope of this paper, though it is very important. More reliable corrections for the effect of gravitational acceleration on the values of  $\dot{P}$  for the GC pulsars are required to verify the relation. Deeper observations of these pulsar may help to reduce the errors in determining their X-ray luminosities.

Besides the aforementioned possibilities, the various origins of the X-ray emission for the GC pulsars may lead to this flatness of the  $L_X - \dot{E}$  relation. The X-ray emission of some GC pulsars (excluding 47 Tuc pulsars) may come from the intra-binary shock since they are located in the binary systems, which is not that case for most field pulsars. Enlarging the X-ray popula-

tion of the GC pulsars may allow us not only to study their emission properties but also to better constrain the  $L_X - \dot{E}$  relation for the GC pulsars.

We have also constructed the cumulative luminosity functions for detected pulsar population in GCs as well as for the millisecond pulsars in the Galactic field. The luminosity functions are displayed in Figure 6.4 which can be described by  $N(> L_X) \propto L_X^{-0.38 \pm 0.04}$  and  $N(> L_X) \propto L_X^{-0.31 \pm 0.02}$  for the GC pulsars and the Galactic millisecond pulsars, respectively. However, the constructed luminosity function for the GC pulsars is not without bias. In particular, some of the pulsar-hosting GCs have not been observed deep enough (cf. Table 2 in Hui, Cheng & Taam 2009). For example, the detection limit for the point sources in NGC 6440 is as high as  $2 \times 10^{31}$  ergs  $s^{-1}$ . According to the relation  $\log L_X \simeq 14.49 + 0.48 \log \dot{E}$ , the pulsars PSRs B1745–20A, J1748–2021D and J1748–2021E in NGC 6440 are expected to have X-ray luminosities at the level of  $\sim (2-8) \times 10^{30}$  ergs  $s^{-1}$  which is well-below the detection threshold determined by the existing data. If a large number of faint X-ray pulsars is indeed detected in deeper observations, a steeper luminosity function will be resulted.

On the other hand, one should be aware that there is a large number of resolved X-ray sources in GCs which have their emission nature not yet been determined. It is not clear whether these unidentified sources are associated with the known pulsars because their positional determinations from the radio timing observations may be inaccurate. Grindlay et al. (2001a) have also suggested that  $\gtrsim 50\%$  of all the unidentified X-ray sources in 47 Tuc can possibly be pulsars. If many of these relatively bright sources are identified as pulsars, the luminosity function can be flattened. In view of the aforementioned biases, we cannot conclude the difference between the GC pulsar population and the Galactic millisecond pulsars in terms of the current knowledge of their luminosity functions.

Searching and studying millisecond pulsars in GCs not only provide us with the knowledge of the pulsars themselves, but also enable us to probe the interactions as well as the evolution of X-ray binaries inside the clusters. Traditional pulsar searches based on radio timing observations still play an important role in expanding the GC millisecond pulsar population. However, one should be aware of selection effects in timing observations. For example, it is difficult to detect pulsars with short periods and/or with large dispersion measure. Also, a fraction of GC millisecond pulsars can possibly be bounded in very tight binaries which have the orbital period as short as a few hours. This fact further complicates the pulsar searches. Parameters, including the positions, are inferred from minimizing the pulse arrival-time residuals. Since the signals from the GC millisecond pulsars are typically weak, the inferred pulsar parameters can possibly suffer from large errors. It is interesting to notice that the X-ray emission from a number of GC pulsars reported in this paper has already been detected before the radio pulsations were detected. This suggests that combining X-ray imaging with radio timing can be an efficient way for searching pulsars. With the aid of high spatial resolution X-ray data, one can test if the radio timing residual can be minimized by adopting the position of the unidentified X-ray sources in the clusters. Through this combined analysis, the pulsar parameters can possibly better constrained and provide a better sample of GC millisecond pulsar population for further studies. Deeper observations of globular clusters will add significant information to those faint sources for which a detailed spectral modeling was precluded by limited photon statistics in the existing datasets.

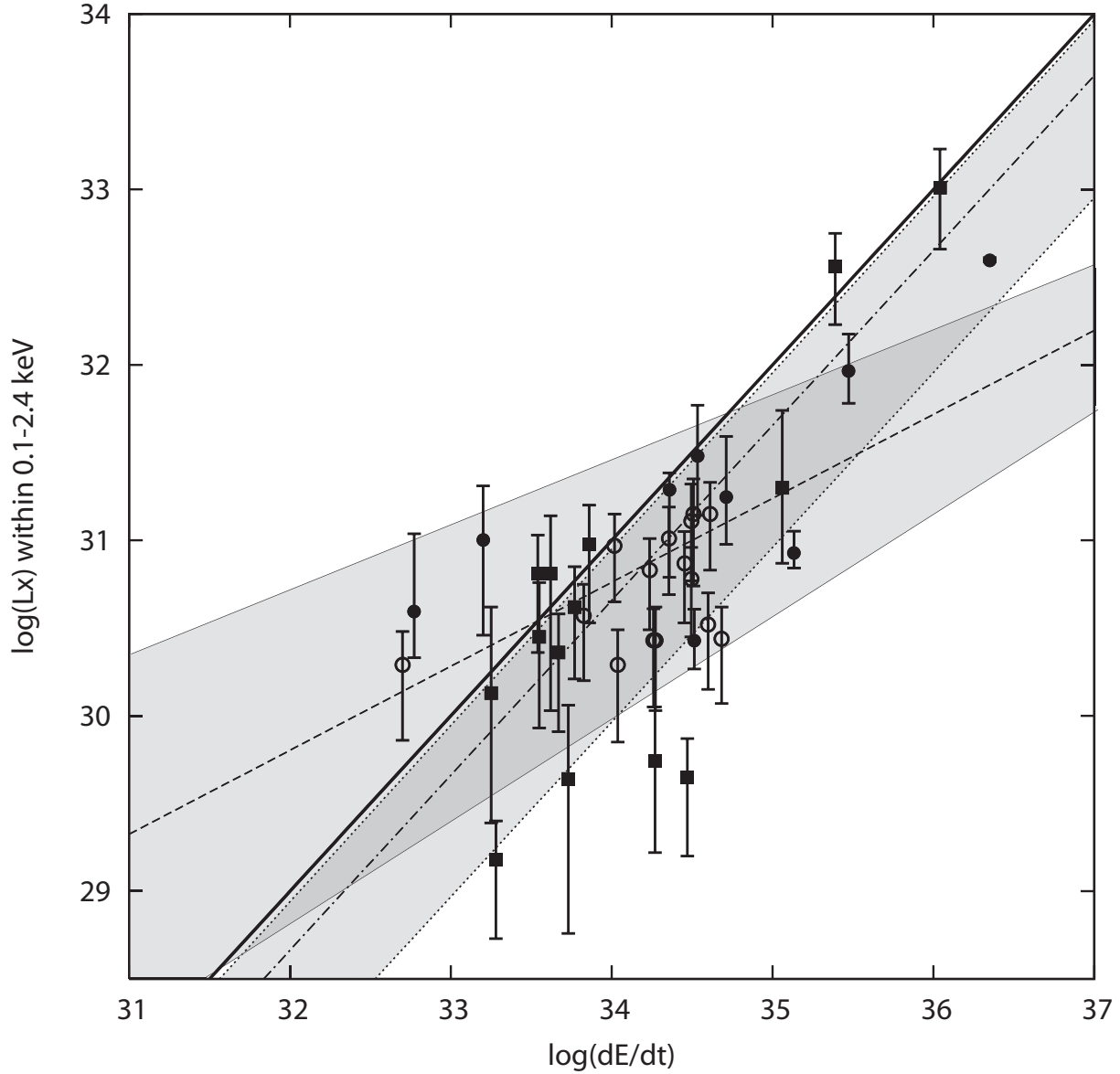


Figure 6.14: The best-fit  $L_{X,0.1-2.0\text{keV}} - \dot{E}$  relations for the GC millisecond pulsars (*filled circles*), 47 Tuc pulsars (*open circles*), and the field millisecond pulsars (*filled squares*). The solid line represents  $L_{X,0.1-2.4\text{keV}} = 10^{-3}\dot{E}$  (Becker & Trümper 1997, 1999). The best-fit  $L_X - \dot{E}$  relations for the GC millisecond pulsars and its  $1-\sigma$  uncertainty range are plotted with a dashed line and a gray shaded strip. The dot-dashed line and the corresponding gray shaded strip indicate the linear correlation  $L_{X,0.1-2.0\text{keV}} = 10^{-3.24}\dot{E}^{0.997}$  and its  $1-\sigma$  uncertainty range.

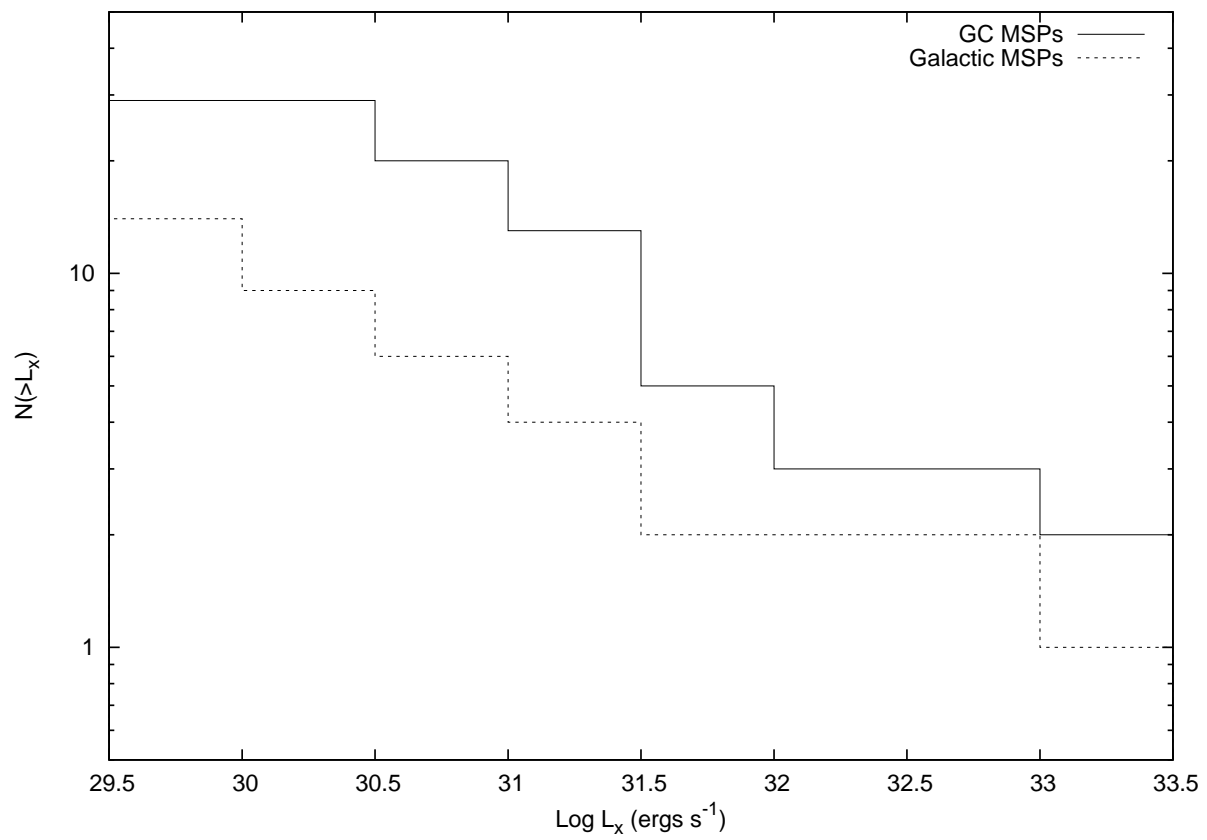


Figure 6.15: Cumulative luminosity functions for the GC pulsars and the MSPs in the Galactic field.

Table 6.1: Chandra observations of globular clusters which are known to host pulsars. The table is ordered top-down according to the number of radio pulsars known in each cluster. (Status: spring 2010).

Cluster	Obs-ID	Detector	Start Date	Exposure (s)
Terzan 5	654	ACIS-I	2000-07-29	5510 <sup>a</sup>
	655	ACIS-I	2000-07-24	42161 <sup>a</sup>
	3798	ACIS-S	2003-07-13	39344
47 Tucanae (NGC 104)	78	ACIS-I	2000-03-16	4050
	953	ACIS-I	2000-03-16	32080
	954	ACIS-I	2000-03-16	920
	955	ACIS-I	2000-03-16	32080
	956	ACIS-I	2000-03-17	4910
	2735	ACIS-S	2002-09-29	66100
	2736	ACIS-S	2002-09-30	66110
	2737	ACIS-S	2002-10-02	66110
	2738	ACIS-S	2002-10-11	69860
	3384	ACIS-S	2002-09-30	5580
	3385	ACIS-S	2002-10-01	5580
	3386	ACIS-S	2002-10-03	5830
	3387	ACIS-S	2002-10-11	6030
	5542	HRC-S	2005-12-19	50160
	5543	HRC-S	2005-12-20	51390
	5544	HRC-S	2005-12-21	50140
	5545	HRC-S	2005-12-23	51870
	5546	HRC-S	2005-12-27	50150
	6230	HRC-S	2005-12-28	49400
	6231	HRC-S	2005-12-29	47150
	6232	HRC-S	2005-12-31	44360
	6233	HRC-S	2006-01-02	97930
	6235	HRC-S	2006-01-04	50130
6236	HRC-S	2006-01-05	51920	
6237	HRC-S	2005-12-24	50170	
6238	HRC-S	2005-12-25	48400	
6239	HRC-S	2006-01-06	50160	
6240	HRC-S	2006-01-08	49290	
M28 (NGC 6626)	2683	ACIS-S	2002-09-09	14110
	2684	ACIS-S	2002-07-04	12746
	2685	ACIS-S	2002-08-04	13511
	9132	ACIS-S	2008-08-07	142260
	9133	ACIS-S	2008-08-10	54456
	2797	HRC-S	2002-11-08	49370
	6769	HRC-S	2006-05-27	41070
M15 (NGC 7078)	1903	HRC-I	2001-07-13	9096
	2412	HRC-I	2001-08-03	8821
	2413	HRC-I	2001-08-22	10790
	9584	HRC-I	2007-09-05	21445
NGC 6440	947	ACIS-S	2000-07-04	23279
	3799	ACIS-S	2003-06-27	24046

Table 6.1: Continued

Cluster	Obs-ID	Detector	Start Date	Exposure (s)
M62 (NGC 6266)	2677	ACIS-S	2002-05-12	62266
NGC 6752	948	ACIS-S	2000-05-12	29468
	6612	ACIS-S	2006-02-10	37967
M3 (NGC 5272)	4542	ACIS-S	2003-11-11	9932
	4543	ACIS-S	2004-05-09	10152
	4544	ACIS-S	2005-01-10	9441
M5 (NGC 5904)	2676	ACIS-S	2002-09-24	44656
M13 (NGC 6205)	5436	ACIS-S	2006-03-11	26799
	7290	ACIS-S	2006-03-09	27895
NGC 6441	721	HRC-I	2000-05-23	2290
M22 (NGC 6656)	5437	ACIS-S	2005-05-24	16020
M30 (NGC 7099)	2679	ACIS-S	2001-11-19	49435
NGC 6544	5435	ACIS-S	2005-07-20	16278
M4 (NGC 6121)	946	ACIS-S	2000-06-30	25816
	7446	ACIS-S	2007-07-06	46040
	7447	ACIS-S	2007-09-18	48540
M53 (NGC 5024)	6560	ACIS-S	2006-11-13	24565
M71 (NGC 6838)	5434	ACIS-S	2004-12-20	52446
NGC 6397	79	ACIS-I	2000-07-31	48343
	2668	ACIS-S	2002-05-13	28100
	2669	ACIS-S	2002-06-30	26660
	7460	ACIS-S	2007-07-16	147710
	7461	ACIS-S	2007-06-22	88898

a). Data unusable because of a bright flaring source in the field of view.

Table 6.2: X-ray counterparts of globular cluster pulsars and their Chandra ACIS-S counting rates.

Globular Cluster	Pulsar	RA (J2000) h m s	Dec (J2000) d m s	$\delta$ RA arcsec	$\delta$ dec arcsec	Net count rate $10^{-4}$ cts/s	$P_{\text{coincide}}$ %	References <sup>a</sup>
47 Tucanae	J0024-7204C	00 23 50.364	-72 04 31.54	0.308	0.226	$1.4 \pm 0.3$	0.018	1,2
	J0024-7204D	00 24 13.882	-72 04 43.84	0.242	0.213	$3.4 \pm 0.4$	0.013	1,2
	J0024-7204E	00 24 11.107	-72 05 20.27	0.249	0.214	$4.4 \pm 0.4$	0.014	1,2
	J0024-7204F	00 24 03.936	-72 04 42.50	0.231	0.212	$6.1 \pm 0.6$	0.013	1,2
	J0024-7204G	00 24 07.943	-72 04 39.65	0.210	0.210	$5.5 \pm 0.5$	0.011	1,2
	J0024-7204H	00 24 06.712	-72 04 06.95	0.256	0.214	$2.7 \pm 0.3$	0.014	1,2
	J0024-7204I	00 24 07.936	-72 04 39.65	0.210	0.210	$5.5 \pm 0.5$	0.011	1,2
	J0024-7204J	00 23 59.402	-72 03 58.93	0.262	0.219	$1.2 \pm 0.3$	0.015	1,2
	J0024-7204L	00 24 03.754	-72 04 56.87	0.210	0.210	$26.8 \pm 0.6$	0.011	1,2
	J0024-7204M	00 23 54.507	-72 05 30.77	0.286	0.219	$2.2 \pm 0.3$	0.016	1,2
	J0024-7204N	00 24 09.224	-72 04 28.95	0.252	0.214	$1.9 \pm 0.3$	0.013	1,2
	J0024-7204O	00 24 04.614	-72 04 53.83	0.210	0.210	$9.4 \pm 0.6$	0.011	1,2
	J0024-7204Q	00 24 16.518	-72 04 25.26	0.256	0.214	$2.5 \pm 0.3$	0.014	1,2
	J0024-7204R	00 24 07.551	-72 04 50.37	0.210	0.210	$5.4 \pm 0.4$	0.011	3
	J0024-7204S	00 24 03.936	-72 04 42.50	0.231	0.212	$6.1 \pm 0.5$	0.013	2
	J0024-7204T	00 24 08.552	-72 04 38.99	0.285	0.217	$0.8 \pm 0.2$	0.016	1,2
	J0024-7204U	00 24 09.873	-72 03 59.71	0.246	0.213	$3.1 \pm 0.4$	0.014	1,2
J0024-7204W	00 24 06.035	-72 04 49.17	0.214 <sup>b</sup>	0.210 <sup>b</sup>	$30.9 \pm 1.2^c$	0.012	3,4	
J0024-7204Y	00 24 01.454	-72 04 41.83	0.251 <sup>b</sup>	0.215 <sup>b</sup>	$1.3 \pm 0.3$	0.014	3	
M28 (NGC 6626)	J1824-2452A	18 24 32.007	-24 52 10.49	0.210	0.219	$280.8 \pm 5.8$	0.024	5
	J1824-2452G	18 24 31.591	-24 52 17.49	0.226	0.341	$2.9 \pm 0.6$	0.036	6
	J1824-2452H	18 24 31.591	-24 52 17.49	0.259	0.355	$2.0 \pm 0.7$	0.027	6
NGC 6440	J1748-2021B	17 48 52.953	-20 21 38.86	0.214	0.287	variable <sup>d</sup>	0.122	7
M62 (NGC 6266)	J1701-3006B	17 01 12.670	-30 06 49.04	0.225	0.228	$9.0 \pm 1.3$	0.048	8
	J1701-3006C	17 01 12.867	-30 06 59.44	0.237	0.232	$2.7 \pm 0.9$	0.051	8
NGC 6752	J1911-6000C	19 11 05.556	-60 00 59.68	0.297	0.248	$3.3 \pm 0.7$	0.007	9
	J1910-5959D	19 10 52.417	-59 59 05.45	0.304	0.228	$7.4 \pm 1.1$	0.007	9
M4 (NGC 6121)	B1620-26	16 23 38.222	-26 31 53.77	0.231	0.264	$4.3 \pm 1.1$	0.004	10
M71 (NGC 6838)	J1953+1846A	19 53 46.424	18 47 04.91	0.231 <sup>b</sup>	0.238 <sup>b</sup>	$5.6 \pm 1.0$	0.016	11
Terzan 5	J1748-2446	17 48 05.048	-24 46 41.10	0.220 <sup>b</sup>	0.219 <sup>b</sup>	$30.5 \pm 2.9^e$	0.008	12
NGC 6397	J1740-5340	17 40 44.589	-53 40 40.90	0.218	0.235	variable <sup>d</sup>	0.064	13

a.) <sup>1</sup>Freire et al. 2001; <sup>2</sup>Freire et al. 2003; <sup>3</sup>Heinke et al. 2005; <sup>4</sup>Edmonds et al. 2002; <sup>5</sup>Lyne et al. 1987 <sup>6</sup>Bégin 2006; <sup>7</sup>Freire et al. 2008; <sup>8</sup>Possenti et al. 2003; <sup>9</sup>D'Amico et al. 2002; <sup>10</sup>Thorsett et al. 1999; <sup>11</sup>Elsner et al. 2008; <sup>12</sup>Heinke et al. 2006; <sup>13</sup>D'Amico et al. 2001.

b.) Errors for the radio pulsar timing position are unpublished. Positional uncertainty of the X-ray counterpart only.

c.) Source exhibits variability at the binary period, count rate averaged over one orbit.

d.) The net counting rates for PSR J1748–2021B from observations in 2000-07-04 and 2003-06-27 are  $(16.8 \pm 2.8) \times 10^{-4}$  cts/s and  $(50.3 \pm 4.6) \times 10^{-4}$  cts/s, respectively. The net counting rates for PSR J1740–5340 from observations in 2000-07-31, 2002-05-13, 2002-06-30, 2007-06-22, 2007-07-16 are  $(13.1 \pm 1.7) \times 10^{-4}$  cts/s,  $(17.4 \pm 2.5) \times 10^{-4}$  cts/s,  $(28.9 \pm 3.3) \times 10^{-4}$  cts/s,  $(22.6 \pm 1.6) \times 10^{-4}$  cts/s and  $(29.2 \pm 1.4) \times 10^{-4}$  cts/s, respectively.

e.) Based on observation ID. 3798 only.

Table 6.3: Distance, half-mass radius and column density of globular clusters which are known to host pulsars. The table is ordered top-down according to the number of radio millisecond pulsars known in each cluster. (Status: spring 2010).

Cluster	Distance (kpc)	$r_{\text{hm}}$ (arcmin)	$N_{\text{H}}^{\text{a}}$ ( $10^{21} \text{ cm}^{-2}$ )
Terzan 5	10.3	0.83	12.0
47 Tucanae (NGC 104)	4.5	2.79	0.1
M28 (NGC 6626)	5.6	1.56	2.2
M15 (NGC 7078)	10.3	1.06	0.6
NGC 6440	8.4	0.58	5.9
M62 (NGC 6266)	6.9	1.23	2.6
NGC 6752	4.0	2.34	0.2
M3 (NGC 5272)	10.4	1.12	0.06
M5 (NGC 5904)	7.5	2.11	0.2
M13 (NGC 6205)	7.7	1.49	0.1
NGC 6441	11.7	0.64	2.6
M22 (NGC 6656)	3.2	1.10	1.9
M30 (NGC 7099)	8.0	1.15	0.2
NGC 6544	2.7	1.77	4.1
M4 (NGC 6121)	2.2	3.65	2.0
M53 (NGC 5024)	17.8	1.11	0.1
M71 (NGC 6838)	4.0	1.65	1.4
NGC 6397	2.3	2.33	1.0

a). The hydrogen column densities  $N_{\text{H}}$  inferred from the optical foreground reddening of the corresponding GCs (Harris 1996, updated 2003<sup>5</sup> estimated from the optical reddening.

Table 6.4: Period, spin-down energy and magnetic field strength of X-ray detected millisecond pulsars in globular clusters.

Cluster	Pulsar	$P^a$ $10^{-3}$ s	$\dot{E}$ ergs $s^{-1}$	$B_{\perp}$ $10^9$ G	Binary <sup>b</sup>
47 Tucanae <sup>c</sup> (NGC 104)	J0023-7204C	5.7568	$5 \times 10^{32}$	-	N
	J0023-7204D	5.3576	$6.7 \times 10^{33}$	-	N
	J0023-7204E	3.5363	$3.1 \times 10^{34}$	0.60	Y
	J0023-7204F	2.6236	$4.1 \times 10^{34}$	0.42	N
	J0023-7204G	4.0404	$< 1.7 \times 10^{34}$	-	N
	J0023-7204H	3.2103	-	-	Y
	J0023-7204I	3.4850	$< 7.1 \times 10^{34}$	-	Y
	J0023-7204J	2.1006	$3.2 \times 10^{34}$	-	Y
	J0023-7204L	4.3462	$1.0 \times 10^{34}$	-	N
	J0023-7204M	3.6766	-	-	N
	J0023-7204N	3.0540	$1.9 \times 10^{34}$	-	N
	J0023-7204O	2.6433	$3.1 \times 10^{34}$	0.29	Y
	J0023-7204Q	4.0332	$1.8 \times 10^{34}$	0.38	Y
	J0023-7204R	3.4805	$2.8 \times 10^{34}$	-	Y
	J0023-7204S	2.8304	$2.3 \times 10^{34}$	-	Y
	J0023-7204T	7.5885	$1.1 \times 10^{34}$	1.51	Y
	J0023-7204U	4.3428	$4.0 \times 10^{34}$	0.65	Y
J0023-7204W	2.3523	-	-	Y	
J0023-7204Y	2.1967	$4.8 \times 10^{34}$	-	Y	
M28 (NGC 6626)	J1824-2452A	3.0543	$2.2 \times 10^{36}$	2.25	N
	J1824-2452G	5.9091	$3.4 \times 10^{34}$	1.07	Y
	J1824-2452H	4.6294	$3.3 \times 10^{34}$	0.64	Y
NGC 6440	J1748-2021B	16.7601	$2.8 \times 10^{33}$	2.45	Y
M62 (NGC 6266)	J1701-3006B	3.5939	$3.0 \times 10^{35}$	1.17	Y
	J1701-3006C	3.8064	$2.3 \times 10^{34}$	0.36	Y
NGC 6752	J1911-6000C	5.2773	$5.9 \times 10^{32}$	0.11	N
	J1910-5959D	9.0353	$5.2 \times 10^{34}$	3.08	N
M4 (NGC 6121)	B1620-26	11.0758	$1.6 \times 10^{33}$	0.81	Y <sup>d</sup>
M71 (NGC 6838)	J1953+1846A	4.888	-	-	Y
Terzan 5	J1748-2446	-	-	-	-
NGC 6397	J1740-5340	3.6503	$3.3 \times 10^{34}$	0.82	Y

a.) From <http://www.naic.edu/~pfreire/GCpsr.html>.

b.) Indicates whether the pulsar is in a binary system.

c.)  $\dot{E}$  from Table 4 of Bogdanov et al. (2006).

d.) Long-orbit triple system with a white dwarf and a planet.

Table 6.5: Counting rate upper limits for X-ray emission from globular cluster millisecond pulsars.

Globular Cluster	Pulsar	RA (J2000) h m s	Dec (J2000) d m s	Counts <sup>a</sup>	Exp. Time sec	3- $\sigma$ upper limit <sup>b</sup> 10 <sup>-4</sup> cts/s	References <sup>c</sup>
NGC 6440	J1748-2021A	17 48 52.689	-20 21 39.7	16.3	47325.1	3.9	1
	J1748-2021C	17 48 51.173	-20 21 53.81	2.2		2.5	1
	J1748-2021D	17 48 51.647	-20 21 07.41	2.2		2.5	1
	J1748-2021E	17 48 52.800	-20 21 29.38	1.1		2.1	1
	J1748-2021F	17 48 52.334	-20 21 39.33	1.1		2.3	1
NGC 6441	J1750-3703A	17 50 13.802	-37 03 10.95	2.2	2290.1	50.7	1
	J1750-3703B	17 50 12.177	-37 03 22.93	1.1		47.0	1
	J1750-3703C	17 50 13.454	-37 03 05.58	5.4		59.7	1
	J1750-3703D	17 50 13.097	-37 03 06.37	15.2		78.8	1
NGC 6544	J1807-2459A	18 07 20.36	-24 59 52.6	3.3	16277.6	7.6	2
NGC 6752	J1910-5959B	19 10 52.056	-59 59 00.86	14.1	67435.9	2.6	3,4
	J1910-5959E	19 10 52.157	-59 59 02.09	8.7		2.3	3,4
M13 (NGC 6205)	J1641+3627A	16 41 40.880	36 27 15.44	2.2	54693.8	2.1	5
M15 (NGC 7078)	B2127+11A	21 29 58.247	12 10 01.26	1029.35 <sup>d</sup>	30851.3	34.2	6,7
	B2127+11B	21 29 58.632	12 10 00.31	60.9		9.7	6,7
	B2127+11C	21 30 01.204	12 10 38.21	1.1		3.5	6,7
	B2127+11D	21 29 58.274	12 09 59.74	150.0 <sup>d</sup>		14.1	6
	B2127+11E	21 29 58.187	12 10 08.63	81.5		10.9	6
	B2127+11F	21 29 57.178	12 10 02.91	6.5		4.6	6
	B2127+11G	21 29 57.948	12 09 57.26	65.2		9.9	6
	B2127+11H	21 29 58.184	12 09 59.43	155.4 <sup>d</sup>		14.3	6
M28 (NGC 6626)	J1824-2452B	18 24 32.545	-24 52 04.29	19.6	196713.4	1.0	8
	J1824-2452C	18 24 33.089	-24 52 13.57	21.7		1.0	8
	J1824-2452D	18 24 31.812	-24 49 25.03	9.8		0.8	8
	J1824-2452E	18 24 32.900	-24 52 12.00	14.1		0.9	8
	J1824-2452F	18 24 32.733	-24 52 10.18	7.8		0.7	8
	J1824-2452I	18 24 32.192	-24 52 14.66	31.5		1.2	8
	J1824-2452J	18 24 32.422	-24 52 25.90	117.4 <sup>d</sup>		2.0	8
M30 (NGC 7099)	J2140-2310A	21 40 22.406	-23 10 48.79	6.5	49435.3	2.9	9
M3 (NGC 5272)	J1342+2822B	13 42 11.087	28 22 40.14	3.3	29525.9	4.2	10
	J1342+2822D	13 42 10.200	28 22 36.00	1.1		3.3	10
M5 (NGC 5904)	B1516+02A	15 18 33.318	02 05 27.55	2.2	44656.1	2.6	11
	B1516+02B	15 18 31.458	02 05 15.47	2.2		2.6	11
M62 (NGC 6266)	J1701-3006A	17 01 12.513	-30 06 30.13	4.3	62266.2	2.1	12
Terzan 5	J1748-2446A	17 48 02.255	-24 46 36.90	2.2	39343.8	3.0	13,14
	J1748-2446C	17 48 04.540	-24 46 36.00	3.3		3.1	14

a.) The total counts were extracted from a circle of 1 arcsecond radius (corresponding to 92% of the encircled energy) and then rescaled to the 100%.

b.) The 3- $\sigma$  upper limits were computed by using  $C = 0.5 \times (S/N)^2 + (S/N) \times \sqrt{cts + 0.25 \times (S/N)^2}$ , in which  $S/N = 3$  is the signal-to-noise ratio and  $cts$  the counts obtained at the pulsar position.

c.) References: (1) Freire et al. 2008; (2) D'Amico et al. 2001; (3) D'Amico et al. 2002; (4) Corongiu et al. 2006; (5) Kulkarni et al. 1991; (6) Anderson et al. 2000; (7) Jacoby et al. 2006; (8) Bégin 2006; (9) Ransom et al. 2004; (10) Hessels et al. 2007; (11) Anderson et al. 1997; (12) Possenti et al. 2003; (13) Lyne et al. 1990; (14) Lyne et al. 2000

d.) Upper limit dominated by a bright nearby source.

Table 6.6: Period, spin-down energy and magnetic field strength of X-ray non-detected pulsars in globular clusters.

Cluster	Pulsar	$P^a$ $10^{-3}$ s	$\dot{E}$ ergs s $^{-1}$	$B_{\perp}$ $10^9$ G	Binary $^b$
NGC 6440	J1748-2021A	288.603	$6.6 \times 10^{32}$	344	N
	J1748-2021C	6.2269	-	-	N
	J1748-2021D	13.4958	$9.4 \times 10^{33}$	2.85	Y
	J1748-2021E	16.2640	$2.9 \times 10^{33}$	2.28	N
	J1748-2021F	3.7936	-	-	Y
	NGC 6441	J1750-3703A	111.608	$1.6 \times 10^{32}$	25.4
J1750-3703B		6.0745	$3.4 \times 10^{33}$	3.45	Y
J1750-3703C		26.5687	-	-	N
J1750-3703D		5.1399	$1.4 \times 10^{35}$	16.1	N
NGC 6544	J1807-2459A	3.0595	-	-	Y
NGC 6752	J1910-5959B	8.3578	-	-	N
	J1910-5959E	4.5718	-	-	N
M13 (NGC 6205)	J1641+3627A	10.3775	-	-	N
M15 (NGC 7078)	B2127+11A	110.665	-	-	N
	B2127+11B	56.1330	$2.1 \times 10^{33}$	23.4	N
	B2127+11C	30.5293	$6.9 \times 10^{33}$	12.5	Y
	B2127+11D	4.8028	-	-	N
	B2127+11E	4.6514	$7.0 \times 10^{34}$	0.92	N
	B2127+11F	4.0270	$1.9 \times 10^{34}$	0.36	N
	B2127+11G	37.6602	$1.5 \times 10^{33}$	8.78	N
	B2127+11H	6.7434	$3.1 \times 10^{33}$	0.41	N
M28 (NGC 6626)	J1824-2452B	6.5466	-	< 0.4	N
	J1824-2452C	4.1583	$9.3 \times 10^{34}$	< 1.2	Y
	J1824-2452D	79.8354	$7.6 \times 10^{34}$	$\sim 91.0$	Y
	J1824-2452E	5.4191	-	< 0.8	N
	J1824-2452F	2.4511	$2.5 \times 10^{34}$	< 0.5	N
	J1824-2452I	3.9318	-	-	Y
	J1824-2452J	4.0397	-	< 0.6	Y
M30 (NGC 7099)	J2140-2310A	11.0193	-	-	Y
M3 (NGC 5272)	J1342+2822B	2.389	$5.4 \times 10^{34}$	0.21	Y
	J1342+2822D	5.443	-	-	Y
M5 (NGC 5904)	B 1516+02A	5.5536	$9.5 \times 10^{33}$	0.48	N
	B 1516+02B	7.9469	-	-	Y
M62 (NGC 6266)	J1701-3006A	5.2416	-	-	Y
Terzan 5	J1748-2446A	11.5632	-	-	Y
	J1748-2446C	8.4361	-	-	N

a.) From <http://www.naic.edu/~pfreire/GCpsr.html>.

b.) Indicates whether the pulsar is in a binary system.

Table 6.7: Spectral parameters and X-ray luminosities of globular cluster pulsars.

Cluster	Pulsar	$N_H/10^{21}$ $\text{cm}^{-2}$	Model <sup>a</sup>	$\Gamma/kT(\text{KeV})$	$\chi^2_\nu$ (d.o.f)	$\log L_{0.3-8 \text{ keV}}^b$ $\text{ergs s}^{-1}$	$\log L_{0.1-2.4 \text{ keV}}^b$ $\text{ergs s}^{-1}$
47 Tucanae	J0024-7204C	0.1	BB	$0.24^{+0.05}_{-0.05}$	0.63(5)	$30.20^{+0.09}_{-0.12}$	$30.22^{+0.09}_{-0.10}$
	J0024-7204D	0.1	BB	$0.21^{+0.04}_{-0.03}$	0.89(11)	$30.40^{+0.13}_{-0.14}$	$30.44^{+0.11}_{-0.13}$
	J0024-7204E	0.1	BB	$0.16^{+0.02}_{-0.02}$	0.67(8)	$30.56^{+0.10}_{-0.10}$	$30.62^{+0.09}_{-0.07}$
	J0024-7204F/S	0.1	BB	$0.21^{+0.01}_{-0.01}$	1.27(19)	$30.87^{+0.09}_{-0.08}$	$30.91^{+0.10}_{-0.12}$
	J0024-7204G/I	0.1	BB	$0.24^{+0.04}_{-0.03}$	1.20(10)	$30.66^{+0.15}_{-0.12}$	$30.67^{+0.12}_{-0.14}$
	J0024-7204H	0.1	BB	$0.19^{+0.08}_{-0.05}$	1.19(7)	$30.31^{+0.21}_{-0.17}$	$30.35^{+0.18}_{-0.11}$
	J0024-7204J	0.1	BB+PL	$0.16^{+0.06}_{-0.04} c/0.61^{+0.55}_{-0.26} d$	0.72(10)	$31.06^{+0.27}_{-0.25}$	$30.70^{+0.29}_{-0.26}$
	J0024-7204L	0.1	BB+BB	$0.15^{+0.02}_{-0.02}/1.95^{+0.58}_{-0.51}$	1.47(21)	$31.60^{+0.28}_{-0.21}$	$31.17^{+0.30}_{-0.26}$
	J0024-7204M	0.1	BB	$0.14^{+0.04}_{-0.04}$	0.99(4)	$30.49^{+0.14}_{-0.11}$	$30.59^{+0.13}_{-0.13}$
	J0024-7204N	0.1	BB	$0.48^{+0.18}_{-0.16}$	1.03(7)	$30.32^{+0.17}_{-0.21}$	$30.20^{+0.28}_{-0.34}$
	J0024-7204O	0.1	BB+PL	$0.15^{+0.02}_{-0.02} c/1.33^{+0.24}_{-0.22} d$	1.06(10)	$31.34^{+0.31}_{-0.25}$	$31.08^{+0.29}_{-0.18}$
	J0024-7204Q	0.1	BB	$0.30^{+0.11}_{-0.08}$	1.19(6)	$30.14^{+0.17}_{-0.13}$	$30.14^{+0.19}_{-0.15}$
	J0024-7204R	0.1	BB+PL	$0.18^{+0.04}_{-0.03} c/1.51^{+0.67}_{-0.65} d$	1.71(16)	$31.44^{+0.27}_{-0.31}$	$31.28^{+0.27}_{-0.29}$
	J0024-7204T	0.1	BB	$0.26^{+0.09}_{-0.07}$	0.99(5)	$30.18^{+0.13}_{-0.15}$	$30.19^{+0.16}_{-0.18}$
	J0024-7204U	0.1	BB	$0.26^{+0.03}_{-0.06}$	1.00(10)	$30.36^{+0.08}_{-0.13}$	$30.37^{+0.09}_{-0.11}$
J0024-7204W	0.1	BB+PL	$0.06^{+0.01}_{-0.03} c/1.72^{+0.16}_{-0.17} d$	0.97(19)	$31.39^{+0.12}_{-0.13}$	$31.39^{+0.11}_{-0.13}$	
J0024-7204Y	0.1	BB	$0.14^{+0.09}_{-0.05}$	1.73(5)	$30.34^{+0.16}_{-0.15}$	$30.43^{+0.15}_{-0.11}$	
M28 (NGC 6626)	J1824-2452A	$2.2 \pm 0.2$	PL	$1.13^{+0.03}_{-0.04}$	1.00(168)	$33.13^{+0.05}_{-0.03}$	$32.58^{+0.03}_{-0.03}$
	J1824-2452G	2.2	PL	$2.7^{+0.4}_{-0.5}$	0.83(12)	$31.14^{+0.07}_{-0.08}$	$31.49^{+0.29}_{-0.34}$
		2.2	BB	$0.3^{+0.1}_{-0.1}$	1.01(12)	$30.52^{+0.15}_{-0.24}$	$30.48^{+0.28}_{-0.36}$
	J1824-2452H	2.2	PL	$0.7^{+0.3}_{-0.4}$	0.77(13)	$31.20^{+0.36}_{-0.30}$	$30.53^{+0.18}_{-0.16}$
2.2		BB	$1.1^{+0.3}_{-0.2}$	0.73(13)	$31.12^{+0.22}_{-0.18}$	$30.49^{+0.35}_{-0.20}$	
NGC 6440	J1748-2021B (#947)	5.9	PL	$1.6^{+0.7}_{-0.5}$	1.49(7)	$32.32^{+0.46}_{-0.39}$	$32.10^{+0.44}_{-0.28}$
	J1748-2021B (#3799)	5.9	PL	$1.4^{+0.2}_{-0.2}$	0.93(14)	$32.89^{+0.16}_{-0.18}$	$32.54^{+0.10}_{-0.12}$
M62 (NGC 6266)	J1701-3006B	2.6	PL	$2.1^{+0.3}_{-0.3}$	0.93(13)	$31.95^{+0.14}_{-0.13}$	$31.98^{+0.21}_{-0.18}$
		2.6	BB	$0.5^{+0.1}_{-0.1}$	1.22(13)	$31.69^{+0.38}_{-0.26}$	$30.52^{+0.43}_{-0.27}$
	J1701-3006C	2.6	PL	$1.7^{+0.9}_{-0.9}$	0.10(3)	$31.49^{+0.55}_{-0.37}$	$31.33^{+0.50}_{-0.32}$
NGC 6752	J1911-6000C	0.2	PL	$1.9^{+0.8}_{-0.8}$	0.98(4)	$30.70^{+0.39}_{-0.23}$	$30.62^{+0.45}_{-0.26}$
		0.2	BB	$0.3^{+0.1}_{-0.1}$	0.56(4)	$30.40^{+0.36}_{-0.32}$	$30.62^{+0.39}_{-0.30}$
	J1910-5959D	0.2	PL	$2.6^{+0.5}_{-0.4}$	0.70(8)	$30.99^{+0.11}_{-0.06}$	$31.26^{+0.35}_{-0.27}$
M4 (NGC 6121)	B1620-26	2.0	PL	$2.8^{+0.6}_{-0.5}$	1.05(8)	$30.58^{+0.09}_{-0.23}$	$31.01^{+0.31}_{-0.54}$
		2.0	BB	$0.4^{+0.1}_{-0.1}$	1.23(8)	$30.09^{+0.23}_{-0.28}$	$30.05^{+0.19}_{-0.34}$
M71 (NGC 6838)	J1953+1846A	1.4	PL	$1.9^{+0.5}_{-0.4}$	0.50(5)	$31.15^{+0.36}_{-0.30}$	$31.10^{+0.31}_{-0.54}$
Terzan 5	J1748-2446	12.0	PL	$1.0^{+0.3}_{-0.2}$	0.44(10)	$33.01^{+0.19}_{-0.19}$	$32.51^{+0.19}_{-0.13}$
		12.0	BB	$1.0^{+0.2}_{-0.1}$	0.70(10)	$32.83^{+0.17}_{-0.22}$	$32.27^{+0.21}_{-0.25}$
NGC 6397	J1740-5340 (#79)	1.0	PL	$1.8^{+0.3}_{-0.3}$	0.75/6	$31.06^{+0.32}_{-0.27}$	$30.95^{+0.31}_{-0.41}$
		1.0	BB	$0.6^{+0.1}_{-0.1}$	0.67/6	$30.82^{+0.35}_{-0.38}$	$30.63^{+0.29}_{-0.33}$
	J1740-5340 (#2668)	1.0	PL	$1.5^{+0.3}_{-0.3}$	0.75/8	$31.08^{+0.30}_{-0.44}$	$30.81^{+0.32}_{-0.38}$
		1.0	BB	$0.6^{+0.1}_{-0.1}$	0.75/8	$30.77^{+0.37}_{-0.28}$	$30.59^{+0.19}_{-0.27}$
	J1740-5340 (#2669)	1.0	PL	$1.5^{+0.2}_{-0.2}$	1.14/8	$31.20^{+0.17}_{-0.25}$	$30.92^{+0.16}_{-0.22}$

Table 6.7: Continued

Cluster	Pulsar	$N_H/10^{21}$ $\text{cm}^{-2}$	Model <sup>a</sup>	$\Gamma/kT(\text{KeV})$	$\chi^2_\nu$ (d.o.f)	$\log L_{0.3-8 \text{ keV}}^b$ $\text{ergs s}^{-1}$	$\log L_{0.1-2.4 \text{ keV}}^b$ $\text{ergs s}^{-1}$
		1.0	BB	$0.7^{+0.1}_{-0.1}$	1.28/8	$30.97^{+0.29}_{-0.20}$	$30.70^{+0.22}_{-0.31}$
	J1740-5340 (#7460)	$0.9^{+1.0}_{-0.4}$	PL	$1.4^{+0.1}_{-0.1}$	0.97/11	$30.95^{+0.15}_{-0.14}$	$30.99^{+0.12}_{-0.09}$
	J1740-5340 (#7461)	$\lesssim 1.0$	PL	$1.7^{+0.4}_{-0.2}$	1.06/5	$30.95^{+0.26}_{-0.20}$	$30.99^{+0.13}_{-0.15}$

**Note:** The meaning of the columns are as follows: Cols. 1 & 2 list the cluster and pulsar name, Cols. 3 to 5 list the hydrogen column density, the spectral model and the best-fitted photon index or blackbody temperature, depending on the fitted model. Col.6 lists the reduced  $\chi^2$  together with the degrees of freedom given in brackets. Cols. 7 & 8 list the unabsorbed X-ray luminosity in the 0.3 – 8.0 and 0.1 – 2.4 keV energy ranges, respectively. Quoted errors indicate the 68% confidence level for one parameter of interest.

a.) PL = power-law; BB = blackbody

b.) Unabsorbed X-ray luminosities are computed at the distance of the GC (cf. Table 6.3 and Harris 1996, updated 2003).

c.) The value indicates the blackbody temperature in the unit of keV.

d.) The value indicates the photon index inferred from the power-law model.

# Chapter 7

## Chandra X-ray Observatory Observations of the Globular Cluster M71

This chapter is adopted from the refereed paper entitled “Chandra X-Ray Observatory Observations of the Globular Cluster M71” published in *Astrophysical Journal* (Elsner et al. 2008).

### 7.1 Abstract

We observed the nearby, low-density globular cluster M71 (NGC 6838) with the Chandra X-ray Observatory to study its faint X-ray populations. Five X-ray sources were found inside the cluster core radius, including the known eclipsing binary millisecond pulsar (MSP) PSR J1953+1846A. The X-ray light curve of the source coincident with this MSP shows marginal evidence for periodicity at the binary period of 4.2 h. Its hard X-ray spectrum and luminosity resemble those of other eclipsing binary MSPs in 47 Tuc, suggesting a similar shock origin of the X-ray emission. A further 24 X-ray sources were found within the half-mass radius, reaching to a limiting luminosity of  $1.5 \times 10^{30}$  ergs s<sup>-1</sup> (0.3-8 keV). From a radial distribution analysis, we find that  $18 \pm 6$  of these 29 sources are associated with M71, somewhat more than predicted, and that  $11 \pm 6$  are background sources, both galactic and extragalactic. M71 appears to have more X-ray sources between  $L_X = 10^{30}$ – $10^{31}$  ergs s<sup>-1</sup> than expected by extrapolating from other studied clusters using either mass or collision frequency. We explore the spectra and variability of these sources, and describe the results of ground-based optical counterpart searches.

### 7.2 Introduction

Globular cluster X-ray sources are of interest for many reasons. Dense globular clusters bring stars into close dynamical encounters that lead to the production of X-ray binaries (e.g. Hut, Murphy & Verbunt 1991), and studies of globular clusters with different structural parameters can elucidate the details of these mechanisms. Globular clusters provide concentrations of faint X-ray sources for study of X-ray populations at a known distance, age and metallicity. This is of

interest even in the least dense globular clusters, where dynamically formed X-ray binaries may be fewer than those descended from primordial binaries. Observations of globular clusters may provide science unique to individual X-ray sources that is enabled by knowledge of the X-ray source's distance, reddening, and other properties. An ensemble of such results for many clusters may shed light on the evolution of globular clusters and their binary populations.

Bright X-ray sources, associated with accreting neutron stars, have long been understood to be produced in globular clusters (Clark 1975). Fainter X-ray sources, composed of combinations of accreting neutron stars in quiescence, cataclysmic variables (CVs), millisecond radio pulsars (MSPs), and chromospherically active binaries (ABs), were known in the 1980s (Hertz & Grindlay 1983) and have been resolved with Chandra's high spatial resolution (e.g. Grindlay *et al.* 2001a, Verbunt & Lewin 2006). A number of globular clusters have been observed with Chandra to fairly low X-ray luminosities ( $< 10^{32}$  ergs  $s^{-1}$ ). Studies of dense clusters have identified large numbers of accreting neutron stars, CVs, ABs and MSPs (e.g. Grindlay *et al.* 2001a, 2001b, Pooley *et al.* 2002b, Becker *et al.* 2003). Two relatively sparse nearby clusters have been carefully studied with Chandra: M4 (Bassa *et al.* 2004) and NGC 288 (Kong *et al.* 2006). Those studies have indicated that ABs are prevalent in sparse clusters, and that CVs are few in number, but possibly larger in number than predicted by empirical extrapolations with the density and mass of the cluster core.

M71 (NGC 6838) is of particular interest due to its close proximity to Earth (4 kpc). A moderately short Chandra study can identify X-ray sources down to a few  $10^{30}$  ergs  $s^{-1}$  (0.5–2.5 keV), probing the populations of faint CVs, MSPs, and ABs. This cluster is of moderate central density ( $\rho_c = 10^{3.05} L_\odot/\text{pc}^3$ ) and shows no evidence for core collapse (its central concentration parameter (Djorgovski 1993) is 1.15). It is moderately reddened ( $E(B-V)=0.25$ ) and has a globular cluster metallicity ( $[\text{Fe}/\text{H}]=-0.73$ , Harris 1996, updated 2003) slightly higher than average. The core, half-mass, and tidal radii are  $r_c = 0'.63$ ,  $r_h = 1'.65$ , and  $r_t = 8'.96$ , respectively (Harris 1996, updated 2003). Neither Einstein (Hertz & Grindlay 1983) nor ROSAT (Verbunt 2001) detected X-ray sources obviously associated with the cluster, with the 0.5–2.5 keV ROSAT HRI upper limit being  $2.6 \times 10^{31}$  ergs  $s^{-1}$  (for an assumed bremsstrahlung spectrum with temperature 0.9 keV). The ROSAT HRI did detect 10 sources in its field of view, but none of these were within the cluster half-mass radius (Verbunt 2001).

Ransom *et al.* (2003, 2005) and Hessels *et al.* (2007) reported the presence of a binary MSP in M71, with  $P_{\text{PSR}} = 4.89$  ms and  $P_{\text{orb}} = 4.24$  h, and the presence at 20 cm of eclipses which last roughly 20% of the orbital period.

In this paper, we report on Chandra X-ray Observatory observations of M71. We discuss the observations, data processing, and source detection, providing source lists, in § 7.3, and the radial distribution of sources with respect to the nominal cluster center in § 7.4. In § 7.5 we present the results of power-law spectral fits to the brighter detected X-ray sources, and in § 7.6 we present and discuss the X-ray color-color diagram for these same sources. We then discuss candidate counterparts in § 7, including those extracted from the 2MASS, USNO B1.0, and TYCHO-2 catalogs (§ 7.7.1), a recent tabulation of variable stars (§ 7.7.3), X-ray source catalogs (§ 7.7.4), and the MSP in M71 (§ 7.7.5). Comparison with Hubble Space Telescope (HST) observations

of M71 (§ 7.7.2) will be reported in Huang *et al.* (2009, submitted to A&A). In § 7.8 we discuss spectral and temporal properties of the brightest detected sources. A summary of our results is given in § 7.9.

### 7.3 Observations, Data Reprocessing, and Source Detection

We obtained a 52.4-ks Chandra observation (ObsID 5434) of M71 (nominal center of cluster at J2000 RA  $19^h 53^m 46.1^s$ , Dec  $18^\circ 46' 42''$ ) on 20–21 December 2004 using the Advanced CCD Imaging Spectrometer (ACIS) in very faint (VF), timed-exposure mode, with 3.141-s frame time. Starting from the standard Chandra X-ray Center (CXC) processing (ASCDS version number 7.6.7.1 and CALDB 3.2.1; third reprocessing) level 1 files, we reprocessed the data without applying pixel randomization. The reprocessing included applying the current charge transfer inefficiency correction; selection of the standard ASCA grades 0, 2, 3, 4 and 6; and application of the good time filter. We column-cleaned the data using a variant of a method developed at Pennsylvania State University<sup>1</sup>. As is appropriate for data taken in VF mode, we used CLEAN55<sup>2</sup> to reduce the background and remove cosmic ray afterglows. In analyzing data and unless otherwise specified, we utilized events in pulse-invariant channels corresponding to 0.3 to 8 keV.

We searched for X-ray sources in the observed field employing techniques described in Tennant (2006) which use a circular-Gaussian approximation to the point spread function (PSF). That author gives a rather detailed account of the method in an Appendix, and there shows that for the Chandra Deep Field-North (Brandt et al. 2001) it gives results consistent with those obtained using the CIAO script `wavdetect`. Using a 30 ks subset of the much longer Deep Field-North observation made it possible to know exactly which sources should be found. The method has been used previously in other published work (*e.g.* Chandra observations of the globular cluster M28 reported in Becker *et al.* 2003). As a result of operating in VF mode, background levels were low throughout the observation (*e.g.*  $\sim 1.4 \times 10^{-7}$  counts/s/pixel over 0.3–8.0 keV for  $r_{M71} \leq r_h$ ). Therefore within twice the M71 half-mass radius ( $r_h = 1.65'$ ), we set the signal-to-noise threshold,  $S/N$ , for detection to 2.0, but also required the number of source counts to be at least 5 times the statistical uncertainty in the local background estimate. The empirical relation derived by Tennant,  $C_{min} = (S/N)^2/0.81$  then implies a point-source sensitivity limit of about 4.9 counts for  $r_{M71} \leq 2r_h$  and in the energy band 0.3–8.0 keV. Because of the increase in PSF size with off-axis distance and the associated increase in background within a detection cell, for  $r_{M71} > 2r_h$  we set the S/N threshold for detection to 2.4, and again required the number of source counts to be at least 5 times the statistical uncertainty in the local background estimate. The point-source sensitivity limit rises to about 7 counts. Following Tennant (2006) we expect a completeness limit of about 10 counts. We discuss the luminosities corresponding to these count sensitivity limits in § 7.4 and § 7.5.

The positions of X-ray sources found in this manner inside  $2r_h$  are listed in Table 7.1, which is divided into those inside  $r_h$  and those with  $r_h < r_{M71} \leq 2r_h$ . The positions of both sets of

<sup>1</sup>See <http://www.astro.psu.edu/xray/acis/recipes/index.html>

<sup>2</sup>See <http://cxc.harvard.edu/cont-soft/software/clean55.1.0.html>

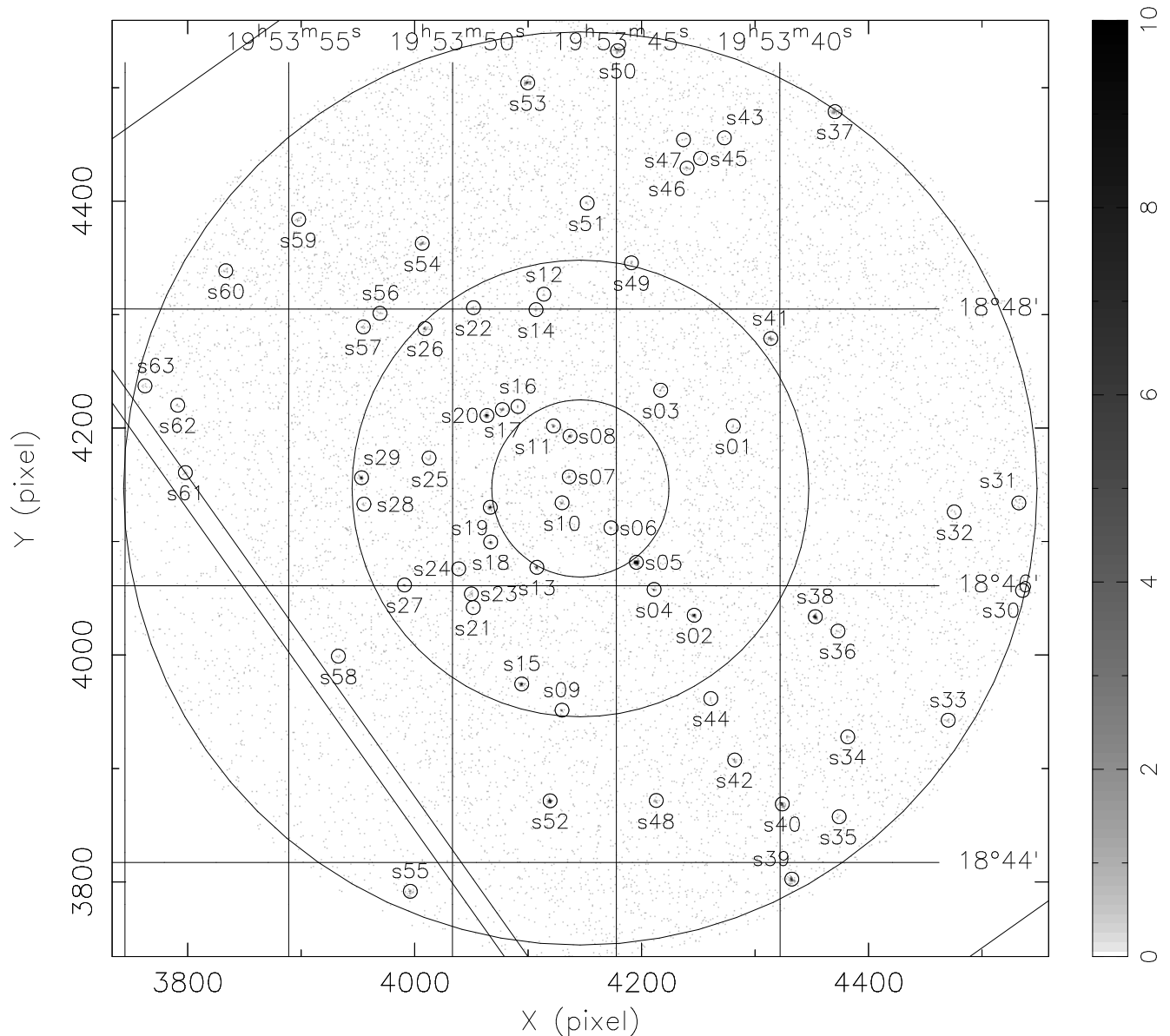


Figure 7.1: ACIS-S S3 0.3–8.0 keV image of the globular cluster M71 for  $r_{M71} \leq 2r_h$ . The small circles show the positions of the 29 X-ray sources listed in Table 7.1 with  $r_{M71} \leq r_h$  and the 34 X-ray sources also listed in Table 7.1 with  $r_h < r_{M71} \leq 2r_h$ . The large circles are centered on the nominal center of the cluster and have radii  $r_c$  (inner circle),  $r_h$  (middle circle), and  $2r_h$  (outer circles). Straight lines mark the nominal boundaries of the S3 and S2 CCDs, with most of the figure falling on S3 and the lower left hand portion on S2.

sources are displayed in Figure 7.1. As can be seen in Figure 7.1, the circle with radius  $2r_h$  extends slightly off the S3 CCD toward S2, which is a front-side illuminated CCD. We find one source, *s55*, inside  $2r_h$  on S2 and include it in Table 7.1. In this table, columns 2–5 give right ascension RA (J2000), declination DEC (J2000), detect cell radius,  $r_{ext}$ , and the approximate number of X-ray source counts,  $C_x$ , detected from the source in the 0.3–8.0 keV band. Column 6 lists the radius about the source position for inclusion of the source with 68% confidence. The corresponding radii for inclusion with 95% or 99% confidence,  $r_{95}$  and  $r_{99}$ , are found by multiplying column 6 by 1.62 or 2.01, respectively. Column 7 gives the distance,  $r_{M71}$ , of the source from the nominal center of M71. The remaining columns have to do with candidate counterparts and are discussed in § 7.7.1.

Uncertainties in the aspect solution for ACIS-S<sup>3</sup> imply  $\sigma_{sys} \approx 0'.2$  (radial,  $\sim 0'.4$  at 90% confidence); to be conservative, we set  $\sigma_{sys} = 0'.2$  per axis. A re-registration (boresight) analysis using the positions of the 18 2MASS candidate counterparts listed in Table 7.1 leads to the following conclusions: (a) the existing aspect solution leads to a statistically acceptable fit with  $\chi^2 = 40.4$  for 36 degrees of freedom (1 for each axis per counterpart); and (b) the best-fit changes in pointings position and roll angle are small ( $\Delta\alpha = 0'.03 \pm 0'.07$ ,  $\Delta\delta = 0'.03 \pm 0'.07$ , and  $\Delta\theta = -2'.3 \pm 2'.0$ ) and, using the f-test, statistically insignificant. Including the candidate counterpart for the MSP in M71 in this analysis does not change these conclusions.

The positions of X-ray sources detected outside  $2r_h$  are listed in Table 7.2. In this table, column 7 now lists the CCD on which the source was detected. The CCD S3 is back-illuminated and therefore its response extends to lower energies than does the response of the other CCDs which are front-illuminated. Due to dither, sources detected close to CCD boundaries may have counts on two CCDs as indicated in Table 7.2. The sources *ss33* and *ss34* are separated by  $\sim 6''$ , which is significantly larger than the corresponding values for  $r_{99}$  so we conclude that these are two different sources.

<sup>3</sup>See <http://cxc.harvard.edu/cal/ASPECT/celmon/>, upper left panel of the first figure

Table 7.1: CXO X-ray sources detected with  $r_{M71} \leq 2r_h$ .

(1)	(2)	(3)	(4)	(5)	(6)	(7)	(8)	(9)	(10)	(11)	(12)	(13)
Source	RA(J2000) h m s	Dec(J2000) ° ' "	$r_{\text{ext}}^a$ "	$C_x^b$ "	$\sigma_x^c$ "	$r_{M71}^d$ "	Offset <sup>e</sup> "	$J^f$ mag	$R^g$ mag	$VT^h$ mag	$P_{\text{coinc}}^i$ %	Comment
Sources with $r_{M71} \leq r_h$												
s01	19 53 41.431	18 47 9.25	1.5	4.4	0.52	1.20						
s02	19 53 42.624	18 45 47.21	1.3	88.2	0.31	1.23						
s03	19 53 43.651	18 47 24.69	1.4	5.6	0.47	0.92						
s04	19 53 43.853	18 45 58.27	1.2	26.6	0.33	0.91						
s05	19 53 44.389	18 46 10.18	1.2	301.7	0.30	0.67						
s06	19 53 45.165	18 46 25.11	1.2	8.9	0.38	0.36						In core
s07	19 53 46.430	18 46 47.25	1.2	12.7	0.36	0.11						In core
s08	19 53 46.424	18 47 4.91	1.2	37.5	0.32	0.39						In core, MSP
s09	19 53 46.663	18 45 6.05	1.3	18.4	0.35	1.61						
s10	19 53 46.662	18 46 35.89	1.1	14.7	0.35	0.17						In core
s11	19 53 46.916	18 47 9.18	1.2	20.3	0.34	0.49	0.29	14.002			0.12	In core
s12	19 53 47.211	18 48 6.15	1.5	4.8	0.52	1.42						In core
s13	19 53 47.427	18 46 7.98	1.1	40.0	0.32	0.65						2MASS
s14	19 53 47.453	18 47 59.57	1.5	6.7	0.46	1.33						
s15	19 53 47.888	18 45 17.47	1.2	61.3	0.32	1.47						
s16	19 53 48.007	18 47 17.72	1.2	8.8	0.39	0.74						
s17	19 53 48.473	18 47 16.39	1.2	28.6	0.33	0.80						
s18	19 53 48.837	18 46 18.96	1.1	56.4	0.32	0.66						
s19	19 53 48.849	18 46 34.04	1.1	56.4	0.32	0.66	0.29	15.545			0.58	2MASS
s20	19 53 48.950	18 47 13.88	1.2	90.3	0.31	0.85	0.05	12.598			0.060	2MASS
s21	19 53 49.369	18 45 50.58	1.2	6.1	0.41	1.16						
s22	19 53 49.368	18 48 0.55	1.5	6.5	0.47	1.52	0.48	15.289			0.88	2MASS
s23	19 53 49.421	18 45 56.54	1.1	10.3	0.37	1.09	0.18	16.271			0.35	2MASS
s24	19 53 49.798	18 46 7.52	1.1	6.6	0.40	1.05						
s25	19 53 50.702	18 46 55.00	1.2	6.7	0.41	1.11						
s26	19 53 50.846	18 47 51.58	1.5	28.7	0.35	1.61	0.29	16.245			1.13	2MASS
s27	19 53 51.470	18 46 0.35	1.2	10.3	0.38	1.45	0.27	12.454			0.12	2MASS
s28	19 53 52.719	18 46 35.32	1.3	6.1	0.44	1.57						
s29	19 53 52.780	18 46 46.86	1.3	51.7	0.32	1.58						
Sources with $r_h < r_{M71} \leq 2r_h$												
s30	19 53 32.644	18 45 58.21	2.8	6.0	0.75	3.27						
s31	19 53 32.723	18 46 36.74	2.8	6.9	0.70	3.17						
s32	19 53 34.679	18 46 31.92	2.4	5.5	0.68	2.71						
s33	19 53 34.876	18 45 1.67	2.5	8.6	0.60	3.14						
s34	19 53 37.948	18 44 54.57	2.1	11.1	0.48	2.64						
s35	19 53 38.231	18 44 19.88	2.3	5.3	0.66	3.02						
s36	19 53 38.252	18 45 40.38	1.8	7.1	0.51	2.13						
s37	19 53 38.331	18 49 25.52	3.0	45.3	0.41	3.29	0.18	13.070			0.18	2MASS
"							0.38		14.8(14.4)		0.32	USNO 1088-0475990
s38	19 53 38.933	18 45 46.61	1.7	102.7	0.32	1.94						

Table 7.1: Continued

(1)	(2)	(3)	(4)	(5)	(6)	(7)	(8)	(9)	(10)	(11)	(12)	(13)
s39	19 53 39.648	18 43 52.84	2.3	71.1	0.35	3.21						
s40	19 53 39.943	18 44 25.46	2.0	64.6	0.34	2.71						
s41	19 53 40.290	18 47 47.23	1.8	32.3	0.36	1.75						
s42	19 53 41.397	18 44 44.55	1.7	18.9	0.38	2.26	0.18	12.676			0.11	2MASS
s43	19 53 41.706	18 49 14.34	2.5	5.8	0.69	2.74	0.98	15.751			1.51	2MASS
s44	19 53 42.119	18 45 11.14	1.5	4.8	0.51	1.79						
s45	19 53 42.438	18 49 5.27	2.3	5.8	0.65	2.54	0.89	14.866			1.35	2MASS
"							0.51		15.1			USNO 1088-0476353
"							1.10		14.8(14.5)		1.14	USNO 1088-0476355
s46	19 53 42.835	18 49 1.01	2.2	14.8	0.46	2.44						
s47	19 53 42.953	18 49 13.41	2.4	6.3	0.65	2.63						
s48	19 53 43.794	18 44 26.65	1.7	15.2	0.40	2.33	0.72	16.071			1.28	2MASS
s49	19 53 44.536	18 48 20.00	1.7	8.6	0.47	1.67	0.35	14.940			0.64	2MASS
s50	19 53 44.967	18 49 52.03	2.8	31.6	0.43	3.17						
s51	19 53 45.904	18 48 45.91	1.9	5.7	0.57	2.06						
s52	19 53 47.022	18 44 26.78	1.5	85.9	0.32	2.27	0.01	9.812			0.011	2MASS
"							0.08		10.5(10.5)		0.035	USNO 1087-0482780
"							0.06			10.87		TYC 1620-1232-1
s53	19 53 47.711	18 49 38.07	2.5	63.4	0.36	2.95						
s54	19 53 50.931	18 48 28.42	1.8	27.2	0.37	2.11	0.65	13.359			0.16	2MASS
s55/	19 53 51.292	18 43 47.55	2.0	23.0	0.39	3.16						
s56	19 53 52.201	18 47 58.22	1.6	5.0	0.53	1.92	0.54	16.063			2.38	2MASS
s57	19 53 52.738	18 47 52.18	1.6	8.8	0.44	1.95	0.72	16.018			1.16	2MASS
s58	19 53 53.482	18 45 29.41	1.4	5.3	0.48	2.13						
s59	19 53 54.710	18 48 38.75	2.2	12.7	0.47	2.81	0.81		17.8(17.5)		1.85	USNO 1088-0477382
s60	19 53 56.921	18 48 16.53	2.2	8.5	0.55	3.00						
s61	19 53 58.155	18 46 49.10	1.9	11.0	0.46	2.85	0.07	15.680			0.99	2MASS
s62	19 53 58.396	18 47 18.34	2.0	6.1	0.58	2.97						
s63	19 53 59.410	18 47 26.64	2.2	5.2	0.67	3.23						

a. Radius of the detect cell for collecting X-ray counts.

b. Number of 0.3–8.0 keV source counts collected in the detect cell.

c. Radius enclosing the true source position with 68% confidence. The corresponding radii for inclusion with 95% or 99% confidence are found by multiplying this column by 1.62 or 2.01, respectively.

d. Radius from the nominal center of the cluster (J2000 RA  $19^{\text{h}} 53^{\text{m}} 46.1^{\text{s}}$ , DEC  $+18^{\circ} 46' 42''$ ).

e. Radial offset of candidate counterparts found by searching the HEASARC 2MASS (B/2mass; see <http://www.ipac.caltech.edu/2mass/>), USNO-B1.0 (I/284; Monet *et al.* 2003), and TYCHO-2 (tycho2; Høg *et al.* 2000) catalogs, requiring that the candidate counterpart lie within the 99% confidence radius of a CXO source. There are 6,414 and 3,376 2MASS sources, 15,324 and 9,196 USNO sources, and 7 and 9 TYCHO sources, appearing within the S2-S3-S4 and I2-I3 boundaries shown in Figures 3 and 4, respectively. If blank, no candidate counterpart was found in these catalogs.

f.  $J$  magnitude of a candidate counterpart found in the 2MASS catalog (HEASARC B/2mass; see <http://www.ipac.caltech.edu/2mass/>).

g.  $R1(R2)$  magnitude of a candidate counterpart found in the USNO-B1.0 catalog (HEASARC I/284; Monet *et al.* 2003).

h.  $VT$  magnitude of a candidate counterpart found in the TYCHO-2 catalog (HEASARC tycho2; Høg *et al.* 2000).

i. Probability of chance coincidence (see §6.1).

j. This source is on the S2 front-side CCD. All other sources in this table are on the S3 back-side CCD.

Table 7.2: CXO X-ray sources detected with  $2r_h \leq r_{M71}$ .

(1)	(2)	(3)	(4)	(5)	(6)	(7)	(8)	(9)	(10)	(11)	(12)	(13)
Source	RA(J2000) h m s	Dec(J2000) ° ' "	$r_{\text{ext}}^a$ "	$C_x^b$	$\sigma_x^c$	Chip <sup>d</sup>	Offset <sup>e</sup> "	$J^f$ mag	$R^g$ mag	$VT^h$ mag	$P_{\text{cont}}^i$ %	Comment
ss01	19 52 56.900	18 51 8.75	22.7	49.9	1.97	S4						
ss02	19 53 2.976	18 49 23.95	16.7	45.2	1.53	S4						
ss03	19 53 3.490	18 51 59.52	19.4	7980.2	0.33	S4		8.813	10.7(10.6)		0.0035	2MASS
"							0.14				0.0028	USNO 1088-0473175
"							0.13			11.737		TYC 1624-1644-1
ss04	19 53 4.399	18 48 38.23	15.4	38.2	1.53	S4						
ss05	19 53 9.151	18 53 50.29	19.1	85.0	1.29	S4		14.360			3.33	2MASS
"							1.02		16.2(15.8)		6.33	USNO 1088-0473600
ss06	19 53 10.843	18 50 18.08	13.0	251.6	0.58	S4		13.918			0.50	2MASS
ss07	19 53 12.205	18 47 59.83	10.6	32.5	1.16	S4						
ss08	19 53 14.354	18 51 57.83	13.3	386.1	0.51	S4						
ss09	19 53 14.636	18 50 23.35	11.2	25.7	1.36	S4		14.577			3.63	2MASS
"							1.92		17.3(16.6)		9.20	USNO 1088-0474040
ss10	19 53 16.567	18 46 37.74	8.1	59.9	0.70	S3		15.345			1.82	2MASS
ss11	19 53 21.991	18 48 39.87	6.6	35.9	0.73	S3		14.916			1.35	2MASS
ss12	19 53 24.427	18 49 53.59	6.7	20.6	0.94	S3-S4						
ss13	19 53 25.045	18 52 43.85	10.1	14.8	1.62	S4		16.431			14.41	2MASS
"							1.62		18.5(17.0)		15.91	USNO 1088-0474864
ss14	19 53 25.618	18 51 17.83	7.9	14.9	1.27	S4		14.397			3.42	2MASS
"							2.44		14.5(13.9)		2.05	USNO 1088-0474902
ss15	19 53 26.671	18 50 40.09	6.8	19.2	0.98	S3-S4						
ss16	19 53 27.949	18 47 4.78	4.0	12.6	0.74	S3		13.743			0.81	2MASS
"							1.16		14.7(14.4)		1.12	USNO 1087-0481208
ss17	19 53 28.475	18 49 51.63	5.4	14.7	0.90	S3						
ss18	19 53 28.617	18 46 58.16	3.8	89.9	0.39	S3						
ss19	19 53 29.129	18 47 13.87	3.7	16.8	0.63	S3		12.603			0.36	2MASS
"							0.49		13.9(13.5)		0.48	USNO 1087-0481286
ss20	19 53 29.353	18 46 17.54	3.6	29.8	0.50	S3						
ss21	19 53 29.427	18 46 39.79	3.6	98.9	0.37	S3		15.358			0.76	2MASS
ss22	19 53 29.494	18 50 8.47	5.4	12.6	0.97	S3						
ss23	19 53 29.996	18 45 19.29	3.5	7.3	0.84	S3						
ss24	19 53 30.251	18 51 57.63	7.4	20.1	1.04	S3-S4					16.82	USNO 1088-0475303
ss25	19 53 31.144	18 47 39.25	3.3	12.6	0.64	S3						
ss26	19 53 31.853	18 48 33.84	3.6	12.8	0.68	S3		13.051			0.40	2MASS
"							0.68		14.9(14.6)		0.78	USNO 1088-0475453
ss27	19 53 35.327	18 50 44.09	4.8	7.9	1.06	S3						
ss28	19 53 37.543	18 43 57.35	2.6	8.9	0.60	S3		13.577			0.54	2MASS
ss29	19 53 40.997	18 43 26.37	2.5	28.8	0.41	S3		15.379			0.88	2MASS
ss30	19 53 41.110	18 50 42.30	3.9	8.6	0.86	S3					5.40	USNO 1088-0476227
"							1.17		17.1(16.9)		0.96	USNO 1088-0476239
ss31	19 53 43.012	18 42 14.78	3.4	14.6	0.61	S3		14.522			1.13	USNO 1087-0482479
"							0.47		15.2(15.0)			

Table 7.2: Continued

(1)	(2)	(3)	(4)	(5)	(6)	(7)	(8)	(9)	(10)	(11)	(12)	(13)
ss32	19 53 44.491	18 51 28.40	4.6	28.9	0.60	S3						
ss33	19 53 46.137	18 42 52.38	2.6	8.3	0.63	S2-S3	0.53	14.809	15.3(15.0)		1.09	2MASS
"							0.76				1.03	USNO 1087-0482712
ss34	19 53 46.572	18 42 55.24	2.6	8.2	0.62	S2-S3						
ss35	19 53 48.153	18 43 15.76	2.3	10.2	0.53	S2-S3						
ss36	19 53 48.183	18 50 7.69	3.0	14.8	0.56	S3						
ss37	19 53 51.772	18 40 42.93	5.2	9.5	1.06	S2						
ss38	19 53 52.141	18 42 10.21	3.4	14.0	0.63	S2						
ss39	19 53 57.803	18 43 20.46	2.9	11.2	0.61	S2	0.79		(17.7)		4.50	USNO 1087-0483662
ss40	19 53 58.657	18 48 26.15	2.5	38.6	0.39	S3						
ss41	19 54 0.169	18 39 29.30	8.1	44.7	0.79	S2						
ss42	19 54 0.240	18 41 27.64	5.2	30.2	0.65	S2	0.40	14.693			1.02	2MASS
"							1.02		16.1(15.5)		1.41	USNO 1086-0482319
ss43	19 54 0.960	18 43 29.97	3.3	8.2	0.77	S2						
ss44	19 54 1.376	18 44 27.20	2.9	22.8	0.47	S2						
ss45	19 54 2.852	18 42 50.70	4.3	797.2	0.32	S2	0.39	10.654			0.015	2MASS
"							0.62		12.3(12.2)		0.053	USNO 1087-0484047
ss46	19 54 5.729	18 40 58.72	7.0	18.3	1.04	S2						
ss47	19 54 6.665	18 42 5.32	5.9	9.7	1.19	S2						
ss48	19 54 6.637	18 42 42.25	5.3	41.6	0.58	S2						
ss49	19 54 7.447	18 47 17.84	4.0	17.4	0.65	S2						
ss50	19 54 7.856	18 44 13.20	4.5	10.8	0.88	S2						
ss51	19 54 9.007	18 46 36.24	4.3	40.6	0.51	S2	0.95		18.1(18.4)		3.46	USNO 1087-0484528
ss52	19 54 9.562	18 47 22.66	4.7	16.7	0.75	S2	0.88	15.866			2.72	2MASS
"							0.70		18.0(17.7)		5.56	USNO 1087-0484568
ss53	19 54 10.927	18 39 50.05	10.3	15.1	1.62	S2						
ss54	19 54 11.625	18 46 47.69	5.2	19.3	0.78	S2						
ss55	19 54 11.738	18 43 12.42	6.4	35.6	0.72	S2						
ss56	19 54 12.698	18 43 45.91	6.4	21.9	0.88	S2						
ss57	19 54 13.904	18 37 45.12	15.3	30.6	1.69	S2	2.70	15.158			8.33	2MASS
"							2.32		19.04		50.39	USNO 1086-0483424
ss58	19 54 16.297	18 39 3.75	13.6	72.7	1.01	S2	1.15		19.9(19.7)			USNO 1086-0483626
ss59	19 54 18.319	18 43 39.81	8.7	46.6	0.82	S2						
is01	19 52 54.455	18 40 11.34	26.3	106.3	1.57	I3						
is02	19 53 17.086	18 42 34.97	9.7	25.3	1.20	I3						
is03	19 53 22.003	18 38 42.71	13.2	26.6	1.58	I3	1.08	16.278			10.62	2MASS
"							0.31		18.1(17.7)		13.33	USNO 1086-0479228
is04	19 53 24.281	18 33 12.71	27.1	71.4	1.96	I2	2.92		19.5		35.44	USNO 1086-0479239
"							3.60	16.215			15.03	2MASS
is05	19 53 25.238	18 39 14.66	11.2	42.0	1.08	I3	3.09		16.5(15.0)		4.83	USNO 1085-0482335
is06	19 53 26.354	18 39 55.13	9.6	144.5	0.57	I3						
is07	19 53 26.619	18 41 3.48	7.8	26.4	0.97	I3						
is08	19 53 28.215	18 40 53.31	7.6	20.7	1.05	I3	0.80	15.494			3.75	2MASS
"							0.20		15.8(15.4)		2.47	USNO 1086-0479720

Table 7.2: Continued

(1)	(2)	(3)	(4)	(5)	(6)	(7)	(8)	(9)	(10)	(11)	(12)	(13)
"	19 53 28.730	18 40 7.81	8.6	9.3	1.73	13	1.92	18.6	18.6		2.27	USNO 1086-0479736
is09							3.44	18.2	18.2		38.88	USNO 1086-0479755
"							2.83	19.1(19.3)	19.1(19.3)		37.82	USNO 1086-0479756
is10	19 53 31.432	18 39 40.69	8.6	12.3	1.52	12						
is11	19 53 34.916	18 38 28.26	10.2	14.2	1.65	12						
is12	19 53 38.072	18 37 44.80	11.2	13.1	1.89	12						
is13	19 53 47.875	18 33 16.88	22.8	37.9	2.26	12	3.39	15.124			9.89	2MASS
"							2.97		(15.2)			USNO 1085-0484067
"							3.42		15.8(15.7)		10.93	USNO 1085-0484068
is14	19 53 55.822	18 34 51.53	18.3	65.7	1.40	12						

a. Radius of the detect cell for collecting X-ray counts.

b. Number of 0.3–8.0 keV source counts collected in the detect cell.

c. Radius enclosing the true source position with 68% confidence. The corresponding radii for inclusion with 95% or 99% confidence are found by multiplying this column by 1.62 or 2.01, respectively.

d. CCD on which the X-ray source appears. In a few cases, the source is dithered across the gap between CCDs.

e. Radial offset of candidate counterparts found by searching the HEASARC 2MASS (B/2mass), USNO-B1.0 (l/284; Monet *et al.* 2003), and TYCHO-2 (tycho2; Hog *et al.* 2000) catalogs, requiring that the candidate counterpart lie within the 99% confidence radius of a CXO source. There are 6,414 and 3,376 2MASS sources, 15,324 and 9,196 USNO sources, and 7 and 9 TYCHO sources, appearing within the S2-S3-S4 and I2-I3 boundaries shown in Figures 3 and 4, respectively. If blank, no candidate counterpart was found in these catalogs.

f.  $J$  magnitude of a candidate counterpart found in the 2MASS catalog (HEASARC B/2mass; see <http://www.ipac.caltech.edu/2mass/>).

g.  $R1(R2)$  magnitude of a candidate counterpart found in the USNO-B1.0 catalog (HEASARC l/284; Monet *et al.* 2003).

h.  $VT$  magnitude of a candidate counterpart found in the TYCHO-2 catalog (HEASARC tycho2; Hog *et al.* 2000).

i. Probability of chance coincidence (see §6.1).

## 7.4 Distributions

M71 lies near the plane of the Galaxy, with galactic longitude  $56.74$  and latitude  $-4.56$ , suggesting a significant contribution to the detected X-ray sources from galactic field sources as well as a contribution from extragalactic sources. In order to determine the radial distribution of the X-ray sources detected in the S3 field, we follow the standard analysis by adopting the generalized King model profile (see Lugger et al. 1995; Grindlay et al. 2002; Heinke et al. 2006; Lugger et al. 2007) for the projected radial distribution function,  $s(r)$ , given by

$$s(r) = c_0 + \frac{s_0}{[1 + (r/r_0)^2]^\beta}, \quad (7.1)$$

where  $c_0$  is the number of background field X-ray sources (galactic and extragalactic) per unit solid angle on the sky, and  $s_0$  the number of globular cluster X-ray sources per unit solid angle at the cluster center. We make the usual assumption that the projected distribution for the visible stars is given by Eq. (1) with  $\beta = 1$  and  $r_0$  equal to the core radius of  $0.63'$ . We also assume the globular cluster X-ray sources are in thermal equilibrium with the stars. Then the X-ray core radius of X-ray sources with mass  $M_x = qM_0$ , where  $M_0$  is the nominal mass of the visible stars, is given by

$$r_{c,x} = (2^{1/\beta_x} - 1)^{1/2} r_0, \quad (7.2)$$

with  $\beta_x = (3q - 1)/2$ .

In contrast to the previous analyses cited above, where the background source level was assumed to be entirely of extragalactic origin and thus known a priori, we treated the background level as a fitting parameter on an equal basis with the other parameters in Eq. (1). In order to determine the best-fit values for  $c_{0,x}$ ,  $s_{0,x}$ , and  $\beta_x$ , we carried out a maximum-likelihood fit of Eq. (1) to the radial distances of the sources from the center of M71 given in Table 7.1, but excluded the source on S2. We followed the procedure described in Grindlay *et al.* (2002), which directly fits the unbinned radial distribution, using nonlinear optimization to maximize the likelihood. We estimated the parameter value errors using the bootstrap method, by generating and fitting 1000 random resamplings, with replacement, of the source radial distribution. We took the equivalent  $1-\sigma$  error estimate for each parameter to be one half of the 68% range about the median of the distribution of its fitted values from the bootstrap resamplings.

We note that the bootstrap method accounts for Poisson errors in the numbers of both cluster and background sources, since each resampling represents a particular realization of the underlying probability distribution defined by the original source sample. The total number of sources included with any region of the cluster varies over the distribution of bootstrap resamplings, since an individual source may be included in each resampling 0, 1, 2, or more times. For a distribution of 1000 resamplings of the 62-source sample within  $2r_h$ , we find that the mean and standard deviation of the number of sources in the core is  $5.0 \pm 2.2$ , in close agreement with the expectation from Poisson statistics. Thus the King-model parameter error estimates produced by the bootstrap method include the contribution from Poisson error.

Table 7.3: Best-fit King model parameters.

(1)	(2)	(3)
King model parameter	S3 X-ray sources	S3 sources with $C_x \geq 10$
$N_X$	62	33
$c_{0,x}^a$	$1.28 \pm 0.60$	$0.63 \pm 0.31$
$s_{0,x}^a$	$6.92 \pm 3.42$	$7.17 \pm 3.65$
$\beta_x$	$1.13 \pm 0.61$	$1.54 \pm 0.70$
$q_x$	$1.08 \pm 0.40$	$1.36 \pm 0.47$
$r_{c,x}(')$	$0.58 \pm 0.26$	$0.48 \pm 0.16$

<sup>a</sup>Units are sources per square-arcminute.

We determined best-fit parameter values using all S3 sources in Table 7.1 (i.e. all S3 sources within  $2r_h$  of the cluster center) and also using just the subset of these sources with  $C_x \geq 10$ . Our choice of  $2r_h$  for the outer radius of the fit, rather than the more common choice of  $r_h$ , was based on experiments with a range of values for the outer radius. We found that the relatively small ratio of  $r_h/r_c = 2.6$  for M71 required that we adopt an outer radius of at least  $2r_h$  in order to stably determine both the surface density slope,  $\beta_x$ , and the background level,  $c_{0,x}$ . In comparison, 47 Tuc, for which Heinke *et al.* (2005) adopted  $r_h$  as the outer radius of the fit, has a ratio of  $r_h/r_c = 7.0$ . In performing the fits, we corrected for the portion of the circular region ( $r \leq 2r_h$ ) that lies beyond the edge of S3. The best-fit parameters are given in Table 7.3 and the best-fit model for the radial profile is shown in Figure 7.2. This figure shows the fit to the observed cumulative radial profile, together with the separate cluster and background components of the model.

The large parameter uncertainties listed in Table 7.3 are the consequence of the high background source level, relative to the size of the cluster source population. Table 7.4 compares the number of X-ray sources actually detected on CCD S3 within the radii  $r_c$ ,  $r_h$ , and  $2r_h$  with the number of background (field) X-ray sources predicted by the best-fit generalized King model. The two-sided errors on these numbers were calculated by adding in quadrature the errors propagated from the best-fit and small number Poisson errors using Eqs. (7) and (11) from Gehrels (1986). We average the two-sided errors when they differ by  $\leq 20\%$ . This results in substantial uncertainties for all parameters of the cluster source population, *e.g.*, the size of the cluster source population within  $r_h$  is  $N_x = 18 \pm 6$ .

Examination of Table 7.3 indicates that for the entire set of X-ray sources the best-fit value of the mass ratio is  $q = 1.08 \pm 0.40$ , suggesting that the masses of the sources are typically of order the mass of the visible stars that dominate the potential (*i.e.*, the turnoff-mass stars). However, we note that the large uncertainty in this parameter precludes any definitive conclusions about the typical source mass. Similarly, the subsample of brighter X-ray sources has a larger best-fit value for the mass ratio,  $q = 1.36 \pm 0.47$ , but the two  $q$  values do not differ at a statistically significant level, precluding a test of the dependence of source mass on luminosity.

We may estimate the extragalactic contribution to the background sources as follows. Given

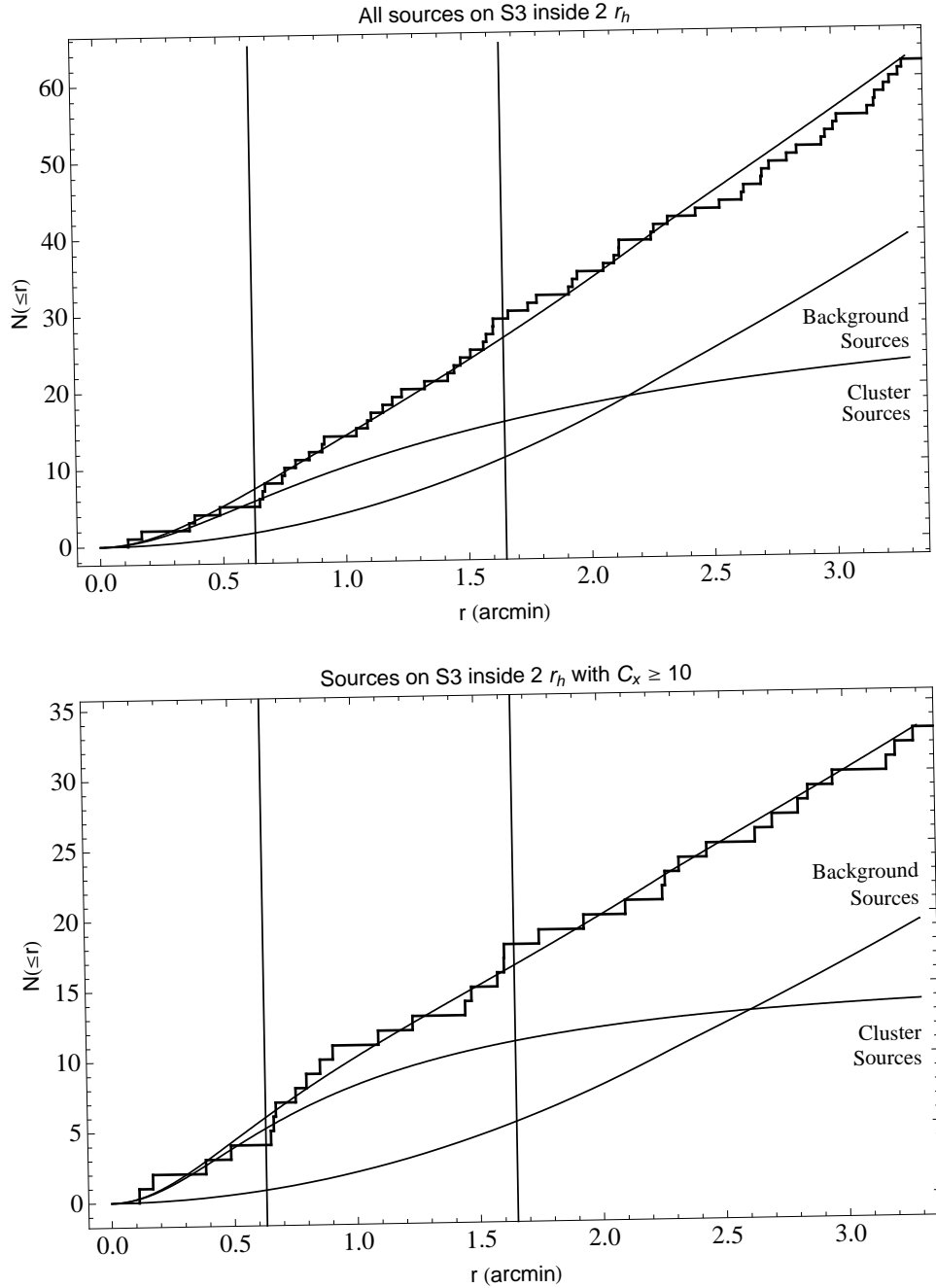


Figure 7.2: Number of sources,  $N(\leq r_{M71})$ , inside radius  $r_{M71}$  (') vs.  $r_{M71}$ . The top panel is for all S3 sources inside  $2r_h$ , and the bottom panel for those sources inside  $2r_h$  with numbers of 0.3–8.0 keV counts  $C_x \geq 10$ . The histogram shows the actual number of detected sources inside the corresponding radius, while the upper solid curve shows the number predicted by the best-fit King model. The lower curves are the model predicted background and cluster contributions, as indicated. The vertical lines mark the core radius,  $r_c$ , and half-mass radius,  $r_h$ .

Table 7.4: Predicted No. of S3 sources inside radius  $r_{M71}$  (').

(1)	(2)	(3)	(4)	(5)
Radius <sup>a</sup>	No. detected <sup>b</sup>	Predicted no. of <sup>c</sup> background sources	Extragalactic contribution <sup>d</sup> CDF-S <sup>e</sup>	CDF-N <sup>f</sup>
All X-ray sources				
$r_c = 0.63'$	5	$1.6^{+2.6}_{-1.4}$	$0.5^{+2.1}_{-0.5}$	$0.6^{+2.1}_{-0.6}$
$r_h = 1.65'$	29	$11.0 \pm 6.4$	$3.3^{+3.1}_{-1.9}$	$3.8^{+3.2}_{-2.0}$
$2r_h = 3.30'$	62	$39.4 \pm 19.7^g$	$10.8 \pm 4.6^g$	$12.2 \pm 4.7^g$
X-ray sources with $C_x \geq 10$				
$r_c = 0.63'$	4	$0.8^{+2.3}_{-0.8}$	$0.3^{+2.0}_{-0.3}$	$0.3^{+2.0}_{-0.3}$
$r_h = 1.65'$	18	$5.4^{+4.4}_{-3.5}$	$1.8^{+2.6}_{-1.3}$	$2.3^{+2.8}_{-1.5}$
$2r_h = 3.30'$	33	$19.4 \pm 10.8^g$	$5.8^{+3.8}_{-2.7}^g$	$7.5^{+4.1}_{-3.0}^g$

a. Radius in '.

b. No. of X-ray sources detected on CCD S3 inside this radius.

c. Predicted no. of background (field) X-ray sources on S3 inside this radius, based on the value for  $c_{0,x}$  from Table 7.3. See the §3 text for discussion of the assigned errors.

d. Predicted no. of extragalactic X-ray sources on S3 inside this radius, based on results from the Chandra Deep Fields North and South. See the §3 text for discussion of the assigned errors.

e. Giacconi *et al.* (2001).

f. Brandt *et al.* (2001).

g. Reduced by the amount of area inside  $2r_h$  that falls off S3.

the value for  $E_{B-V}$  from Harris (1996), the relationships  $A_V = 3.1E_{B-V}$  (Rieke & Lebofsky 1985) and  $n_H/A_V = 1.79 \times 10^{21}$  (Predehl & Schmitt 1995) imply a value for the hydrogen column density to M71 of  $n_H = 1.39 \times 10^{21}$  H atoms  $\text{cm}^{-2}$ . Assuming this value for  $n_H$  and a power-law spectrum with photon index 1.53 from the Chandra Deep Field-South (CDF-S; Giacconi *et al.* 2001), our detection limit of 4.9 counts in the 0.3–8.0 keV band corresponds to a 0.3–8.0 keV flux of  $1.32 \times 10^{-15}$  ergs  $\text{cm}^{-2} \text{s}^{-1}$  and a luminosity at the distance of M71 of  $2.5 \times 10^{30}$  ergs  $\text{s}^{-1}$ . The corresponding value for the 0.5–2.0 keV flux is  $4.2 \times 10^{-16}$  ergs  $\text{cm}^{-2} \text{s}^{-1}$ . Then from the CDF-S (Giacconi *et al.* 2001, Eq. (1)), we find for the expectation value for the number of extragalactic sources above a 0.3–8.0 keV band detection limit of 4.9 counts of  $(0.39 \pm 0.09) r_{M71}^2$  arcmin $^{-2}$  inside a radius  $r_{M71}$  (in arcmin). Repeating this exercise for a detection limit of 10 counts in the 0.3–8.0 keV band leads to an expectation value for the number of extragalactic sources of  $(0.21 \pm 0.05) r_{M71}^2$  arcmin $^{-2}$  inside a radius  $r_{M71}$  (in arcmin). Assuming the same value for  $n_H$  but using the power-law index 1.4 from the Chandra Deep Field-North (CDF-N; Brandt *et al.* 2001) increases these detection limits by 3%.

Table 7.4 also lists the number of extragalactic X-ray sources inside the radii  $r_c$ ,  $r_h$ , and  $2r_h$  predicted by these results. The errors quoted in the table were again calculated by adding in quadrature the expectation value errors and small number Poisson errors using Eqs. (7) and (11) from Gehrels (1986), resulting as before in substantial uncertainties. Because of the large uncertainties, we cannot conclusively say whether Galactic or extra-galactic X-ray sources dominate the sources not associated with M71. Probably both are important. Figure 7.3 shows the distribution of the number of sources with 0.3–8.0 keV band counts greater than  $C$ ,  $N(> C)$  vs  $C$  for the

sources detected inside  $2r_h$ . For  $C \leq 50$  the best unweighted-least-squares fit power-law index for this distribution is -0.68, while for  $50 < C < 110$  the corresponding value for this index is -2.64.

## 7.5 Power-law Spectral Fits

In order to estimate X-ray luminosities for the brighter sources within  $2r_h$ , we carried out fits in XSPEC (Arnaud 1996) to power-law spectra for sources with at least 45 source counts in the energy band 0.3–8.0 keV plus the candidate counterpart for the MSP in M71 with 37.5 source counts, with the results shown in Table 7.5. For each source we constructed response files using the CIAO tool *mkacisrmf*, and we extracted source and local background spectral files using *lextract* (Tennant 2006). In all cases we fixed the hydrogen column density at the value,  $n_H = 1.39 \times 10^{21} \text{ cm}^{-2}$ , appropriate for M71. In this table, column 1 gives the Chandra source name from Table 7.1 (see also Figure 7.1), column 2 lists the minimum number of counts used to group the spectral data for fitting in XSPEC, and columns 3–5 give the best-fit power-law index, the best-fit normalization, and the value obtained for  $\chi^2$  together with the number of degrees of freedom,  $\nu$ . Whenever  $\chi^2/\nu \leq 2$ , we provide the single parameter 67% confidence errors calculated by XSPEC using the *error* command with  $\Delta\chi^2 = 1$ ; when  $\chi^2/\nu > 2$ , as is the case for source *s52*, we do not quote any errors. Letting the hydrogen column density vary for *s52* produces an improved but still unacceptable fit. Note that the fits for the sources *ss03* and *ss45*, while satisfying  $\chi^2/\nu \leq 2$ , are not acceptable with better than 99.9% confidence. Column 6 lists the probability of obtaining by chance that value for  $\chi^2$  or greater. Column 7 gives the corresponding unabsorbed X-ray luminosity in the bands 0.5–2.5 keV and 0.3–8.0 keV.

In order to determine X-ray flux and luminosity limits for the fainter sources within  $r_h$ , we divided the sources with  $C_x < 45$ , but not including the MSP candidate counterpart, into two groups, one with counts in the range  $15 \leq C_x < 45$  (Group 1 with 7 sources), one with  $C_x < 15$  (Group 2 with 15 sources). We summed the PI spectra for each group, averaged the corresponding responses, and fit the results to power-law spectra as above, with the results also shown in Table 7.5. The total number of counts for the sources in Group 2 (the faintest group) is 119.1. Our source count sensitivity limit of 4.9 counts then corresponds to a 0.3–8.0 keV unabsorbed X-ray flux of  $\sim 8.0 \times 10^{-16} \text{ ergs cm}^{-2} \text{ s}^{-1}$ , and a 0.3–8.0 keV unabsorbed X-ray luminosity of  $\sim 1.5 \times 10^{30} \text{ ergs s}^{-1}$  at the distance of M71. Corresponding limits in the 0.5–2.5 keV and 0.5–6.0 keV energy bands are  $\sim 7.9 \times 10^{29} \text{ ergs s}^{-1}$  and  $\sim 1.1 \times 10^{30} \text{ ergs s}^{-1}$ , respectively. Very similar limits were found for the somewhat brighter, but fewer, sources in Group 1.

We divided the faint sources with cluster radii between  $r_h$  and  $2r_h$  into two groups as above, Group 3 with  $15 \leq C_x < 45$  (5 sources) and Group 4 with  $C_x < 15$  (22 sources). The summed spectra for Group 4 do not fit a power-law spectrum with  $n_H = 1.39 \times 10^{21} \text{ cm}^{-2}$  particularly well, so we allowed  $n_H$  to also vary. We then found an acceptable fit to a power-law spectrum, with a single parameter 67% upper limit for  $n_H \leq 2 \times 10^{20} \text{ cm}^{-2}$ .

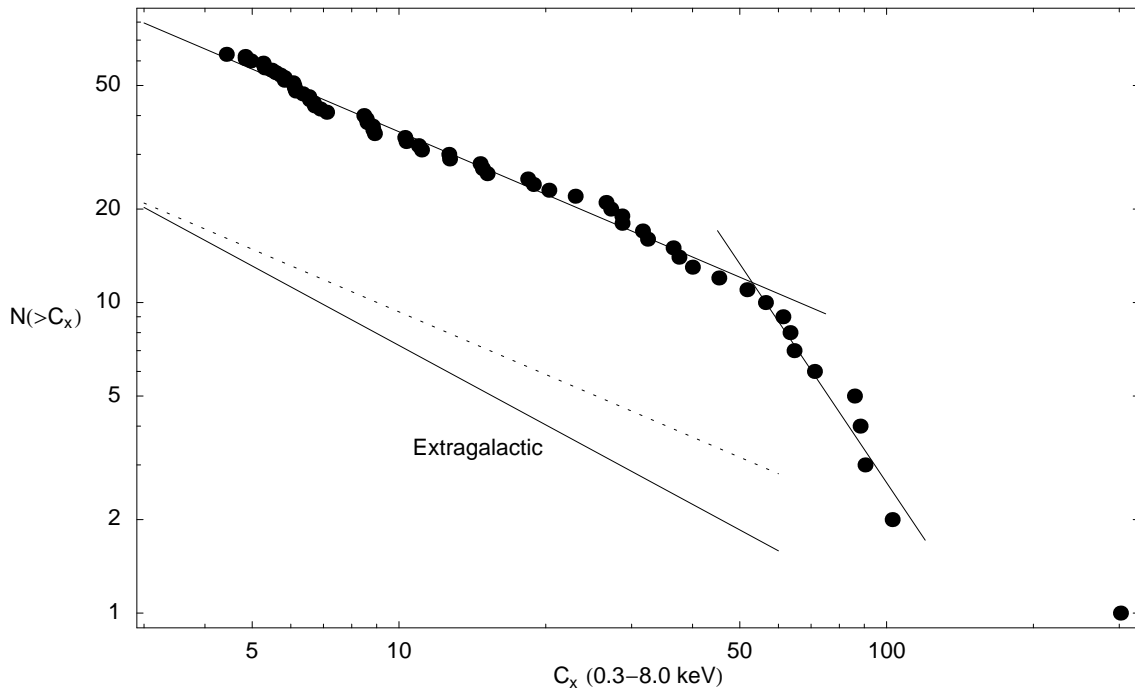


Figure 7.3: The M71  $\log N$ – $\log C_x$  distribution for sources with  $r_{M71} \leq 2r_h$ . The solid lines through the data represent unweighted least-squares fits to a power-law for  $C_x(0.3\text{--}8.0 \text{ keV}) < 50$  and  $C_x(0.3\text{--}8.0 \text{ keV}) > 50$ . The functions are  $N(> C_x) = 10^a / C_x^b$ , with  $(a, b) = (2.22, 0.67)$  for  $C_x(0.3\text{--}8.0 \text{ keV}) < 50$ , and  $(a, b) = (5.10, 2.34)$  for  $C_x(0.3\text{--}8.0 \text{ keV}) > 50$ . The lower lines show the estimated contribution from extragalactic sources (solid Giacconi *et al.* 2001, dotted Brandt *et al.* 2001).

Table 7.5: Power-law spectral fits for selected X-ray sources.

(1)	(2)	(3)	(4)	(5)	(6)	(7)	(8)	(9)
Source	Grouping <sup>a</sup>	$n_H/10^{22}$	$\gamma$	$A^b$	$\chi^2/\nu^c$	$P(\geq \chi^2)^d$	$L_x^e$	Comment
X-ray sources on S3 with $r_{M71} \leq 2r_h$ <sup>f</sup>								
s02	15	0.139	$3.09 \pm 0.22$	$3.01 \pm 0.34$	$5.82/3$	0.12	15 (31)	
s05	20	0.139	$1.57 \pm 0.11$	$7.83 \pm 0.62$	$17.41/12$	0.14	41 (103)	
s08	12	0.139	$1.89 \pm 0.32$	$1.12 \pm 0.23$	$0.80/1$	0.37	6 (12)	MSP
s15	15	0.139	$2.18 \pm 0.24$	$2.04 \pm 0.30$	$2.10/2$	0.35	10 (19)	
s19	15	0.139	$2.35 \pm 0.29$	$1.95 \pm 0.30$	$0.0011/1$	0.97	9 (18)	
s20	15	0.139	$2.17 \pm 0.19$	$3.03 \pm 0.37$	$4.91/3$	0.18	15 (29)	
s29	15	0.139	$1.44 \pm 0.26$	$1.30 \pm 0.26$	$0.020/1$	0.89	7 (19)	
s37	15	0.139	$2.56 \pm 0.33$	$1.59 \pm 0.26$	$1.37/1$	0.24	8 (14)	
s38	20	0.139	$1.40 \pm 0.18$	$2.44 \pm 0.34$	$2.60/2$	0.27	13 (37)	
s39	15	0.139	$1.36 \pm 0.22$	$1.75 \pm 0.30$	$0.16/2$	0.92	10 (28)	
s40	15	0.139	$0.20 \pm 0.21$	$0.66 \pm 0.16$	$1.40/2$	0.50	6 (47)	
s52	15	0.139	3.69	2.21	$23.98/3$	0.000025	12 (31)	$\chi^2/\nu \geq 2$
s53	20	0.139	$2.87 \pm 0.28$	$2.43 \pm 0.32$	$1.37/1$	0.24	12 (23)	
Summed spectra for faint sources on S3 with $r_{M71} \leq 2r_h$								
Group 1 <sup>g</sup>	20	0.139	$1.72 \pm 0.14$	$5.43 \pm 0.52$	$6.37/7$	0.50	28 (64)	
Group 2 <sup>h</sup>	20	0.139	$2.25 \pm 0.20$	$3.99 \pm 0.43$	$2.90/4$	0.58	19 (37)	
Groups 1+2 <sup>i</sup>	20	0.139	$1.89 \pm 0.11$	$9.44 \pm 0.68$	$8.34/13$	0.82	47 (100)	
Group 3 <sup>j</sup>	20	0.139	$1.74 \pm 0.16$		$3.30/4$	0.51	19 (43)	
Group 4 <sup>k</sup>	20	0.139	2.04	5.28	$14.00/7$	0.051	26 (52)	$\chi^2/\nu \geq 2$
Group 4	20	$\leq 0.02$ <sup>l</sup>	$1.44 \pm 0.16$	$3.32^{+0.40}_{-0.30}$	$5.86/6$	0.44	18 (49)	
Groups 3+4 <sup>m</sup>	20	0.139	$1.90 \pm 0.14$	$9.07 \pm 0.74$	$16.30/13$	0.23	45 (96)	
X-ray sources with $2r_h < r_{M71}$ <sup>n</sup>								
ss03	20	$0.24 \pm 0.013$	$2.55 \pm 0.047$	$6.01 \pm 0.24$	$225.55/169$	0.0014	2900 (5400)	on S4
ss06	20	$0.19^{+0.060}_{-0.076}$	$3.52^{+0.49}_{-0.26}$	$20.54^{+8.85}_{-5.19}$	$9.12/9$	0.43	110 (260)	on S4
ss08	20	$0.29^{+0.11}_{-0.075}$	$1.84^{+0.19}_{-0.12}$	$20.79^{+6.32}_{-4.22}$	$15.97/16$	0.46	100 (230)	on S4
ss45	20	$0.23 \pm 0.031$	$3.11 \pm 0.15$	$58 \pm 8$	$56.35/31$	0.0035	290 (600)	on S2
is01	20	$0.17^{+0.25}_{-0.14}$	$1.50^{+0.26}_{-0.48}$	$5.57^{+4.06}_{-2.16}$	$1.28/5$	0.94	30 (78)	on I3
is06	20	0.46	5.43	31.27	$12.96/4$	0.011	300 (1700)	on I3; $\chi^2/\nu \geq 2$

a. Minimum number of counts per spectral bin for fitting in XSPEC.

b. Power-law spectra normalization in units of  $10^{-6}$ .

c. Value of  $\chi^2$  for best-fit and the number of degrees of freedom,  $\nu$ .

d. Probability of finding a value for  $\chi^2 \geq$  the value actually found.

e. Unabsorbed X-ray luminosity in units of  $10^{30}$  ergs  $s^{-1}$ , assuming the distance to M71; energy bands are 0.5–2.5 (0.3–8.0) keV.

f.  $dN/dE(E) = e^{-n_H \sigma_{ISM} A} E^\gamma$  in units of photons/ $s$ - $cm^2$ -keV with  $E$  in keV, with  $n_H$  fixed at the value  $1.39 \times 10^{21}$  H atoms per  $cm^2$ . The quoted errors are the one-parameter 67% confidence level errors given by the XSPEC command error with  $\Delta\chi^2 = 1$ . Errors are not quoted when  $\chi^2/\nu \geq 2$ , as is the case for source s52 and Group 4 with  $n_H$  fixed.

g. Results of fit for summed power-law spectrum for Group 1, which contains the 7 faint sources on S3 not included in the table but with  $C_x \geq 15$  and with  $r_{M71} \leq r_h$ : s04, s09, s11, s13, s17, s18, and s26. From Table 7.1, the number of source counts in this group is 199.0.

h. Results of power-law spectral fit for summed power-law spectrum for Group 2, which contains the 15 faintest sources with  $r_{M71} \leq r_h$ : s01, s03, s06, s07, s10, s12, s14, s16, s21, s22, s23, s24, s25, s27, and s28. From Table 7.1, the number of source counts in this group is 119.1.

i. Results of fit for summed power-law spectrum for all sources in Groups 1 and 2. The number of source counts in these groups is 318.1.

- j. Results of fit for summed power-law spectrum for Group 3, which contains the 5 faint sources on S3 not included in the table but with  $C_x \geq 1.5$  and with  $r_{th} < r_{M71} < 2r_{th}$ : s41, s42, s48, s50, s54. From Table 7.1, the number of source counts in this group is 125.1.
- k. Results of fit for summed power-law spectrum for Group 4, which contains the 22 faintest sources with  $r_{th} < r_{M71} < 2r_{th}$ : s30, s31, s32, s33, s34, s35, s36, s43, s44, s45, s46, s47, s49, s51, s56, s57, s58, s59, s60, s61, s62, s63. From Table 7.1, the number of source counts in this group is 165.1.
- l. Since the fit for Group 4 with  $n_H$  fixed is not very good, we also fit these data with  $n_H$  free. This produced an acceptable fit with a single parameter 67% upper limit for  $n_H$  of  $\sim 2 \times 10^{20} \text{ cm}^{-2}$ .
- m. Results of fit for summed power-law spectrum for all sources in Groups 3 and 4.
- n.  $dN/dE(E) = e^{-n_H \sigma_{\text{B.M.A}}/E^2}$  in units of photons/s-cm<sup>2</sup>-keV with  $E$  in keV. The quoted errors are the one-parameter 67% confidence level errors given by the XSPEC command error with  $\Delta\chi^2 = 1$ . Errors are not quoted when  $\chi^2/\nu \geq 2$ , as is the case for source s06.

## 7.6 X-ray Color–Color Diagram

Figure 7.4 shows an X-ray color–color diagram for sources inside  $2r_h$ , using the three energy bands  $S = C(0.3\text{--}0.8 \text{ keV})$ ,  $M = C(0.8\text{--}2.0 \text{ keV})$ , and  $H = C(2.0\text{--}8.0 \text{ keV})$ , plotted using  $(H - S)/T$  as the  $x$ -axis and  $M/T$  as the  $y$ -axis, where  $T = C(0.3\text{--}8.0 \text{ keV})$ . We included results for *s52* and Group 4 on this plot, even though power-law models with  $n_H$  fixed at the value appropriate for M71 did not provide acceptable fits to the X-ray spectra from these sources. Also shown are three curves representing power-law spectra with indices ranging from -1 (right end point of curves) to -6 (left end point of curves). The three curves are for Hydrogen column densities  $n_H = 0.1, 1.39$  (the value for M71), and  $10.0$  in units of  $10^{21} \text{ cm}^{-2}$ .

As described by Tennant (2006), using these axes all sources should lie inside the triangle defined by  $S = 0$ ,  $M = 0$ , and  $H = 0$ . Soft sources will lie to the left, hard sources to the right, and centrally peaked sources in the middle. Sources to the left are more likely to be stars in our Galaxy, and sources to the right more likely to be pulsars or background AGN. Indeed, as we describe in § 7.7.1, *s37* and *s52*, which both have candidate counterparts from the 2MASS and USNO catalogs and are likely stars, lie near the line  $H = 0$ , while the MSP candidate counterpart *s08* lies near the line  $S = 0$ . The candidate counterpart for *s52* is also listed in the Tycho-2 catalog and is undoubtedly a foreground star.

## 7.7 Searches for Counterparts

### 7.7.1 2MASS, USNO, & TYCHO-2 Catalogs

Using the *HEASARC BROWSE* tool in batch mode, we searched the 2MASS<sup>4</sup>, USNO B1.0 (Monet *et al.* 2003), and TYCHO-2 (Hog *et al.* 2000) catalogs for possible optical and infrared counterparts. The TYCHO-2 catalog is a subset of the USNO B1.0 catalog containing the 2.5 million brightest stars. Thus coincidence with a TYCHO-2 catalog member potentially restricts the nature of the X-ray source. We required that candidates lie inside the radius  $r_{99}$ , given in Tables 7.1 and 7.2 from the Chandra X-ray source position. The results are listed in Tables 7.1 for sources with  $r_{M71} \leq 2r_h$  and Table 7.2 for sources with  $2r_h < r_{M71}$ , in columns 9–11. As noted in § 7.3, we carried out a re-registration (boresight) analysis using the X-ray positions and 2MASS positions for the 18 sources in Table 7.1 with 2MASS candidate counterparts. This analysis demonstrated that for our observation there is no need to shift the on-axis pointing position or spacecraft roll angle, thus eliminating the need to search the catalogs a second time. Column 8 lists the radial offset from the Chandra position in ″. If there is a candidate from the 2MASS catalog, column 9 lists the quoted  $J$  (the catalog also lists  $H$  and  $K$  magnitudes when available). If there is a candidate from the USNO catalog, column 10 lists the  $R1$  magnitude or average of  $R1$  and  $R2$  magnitudes (the catalog also lists  $B$  and  $I$  magnitudes when available). If there is a candidate from the TYCHO-2 catalog, column 11 lists the TYCHO-2  $VT$  magnitude. Column 12 lists the catalog and name (if there is one) for the candidate counterpart, and in a few cases other

<sup>4</sup>See <http://www.ipac.caltech.edu/2mass/>

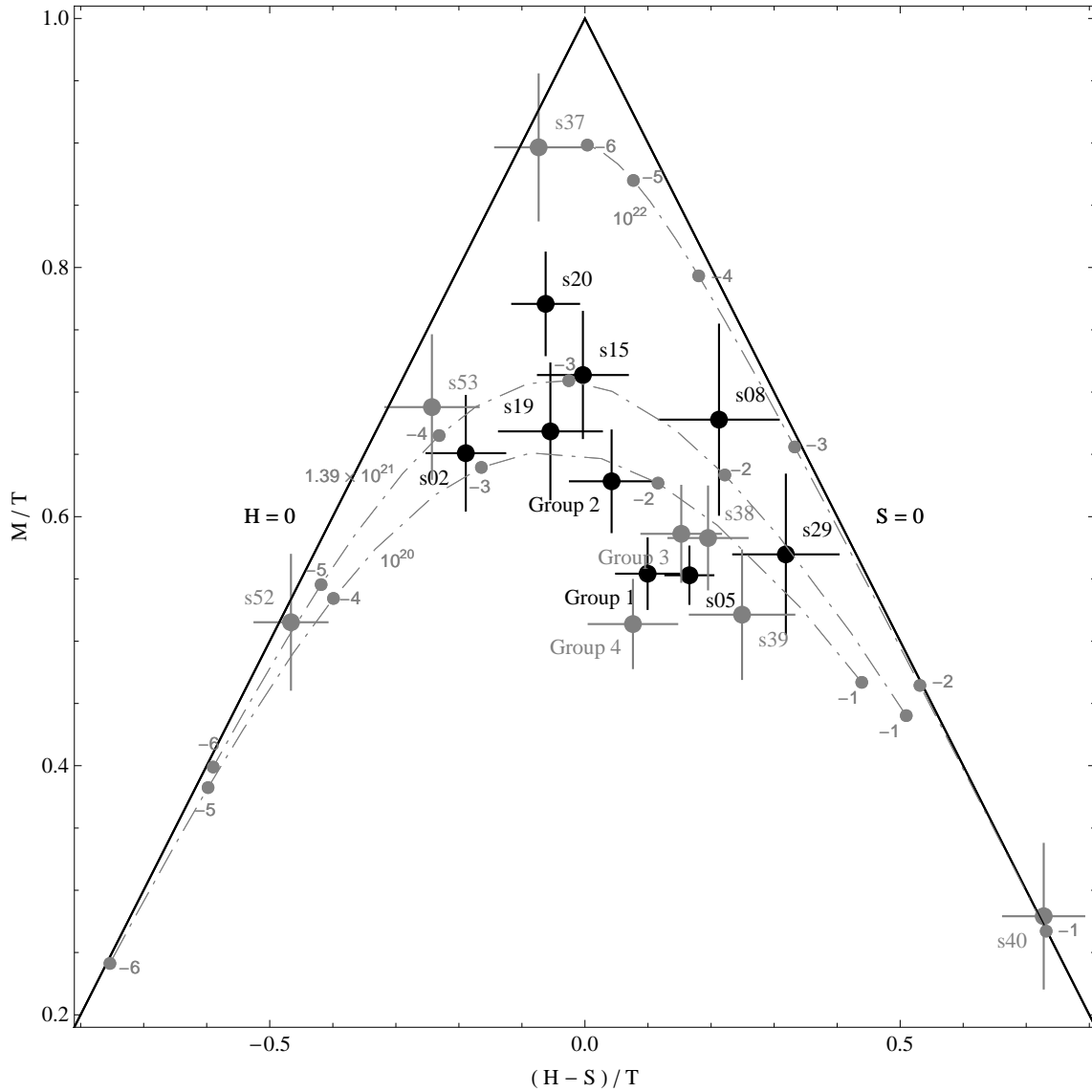


Figure 7.4: Color-color diagram for sources with  $r_{M71} \leq 2r_h$  having 45 or more source counts in the energy band  $T = 0.3\text{--}8.0$  keV, plus *s08*, the MSP candidate counterpart, and the summed spectra for Groups 1–4. Sources inside  $r_h$  are shown with large black dots while sources between  $r_h$  and  $2r_h$  are shown with large grey dots. The bands are  $S = 0.3\text{--}0.8$  keV,  $M = 0.8\text{--}2.0$  keV, and  $H = 2.0\text{--}8.0$  keV. The dot-dashed curves are the PIMMS predicted values for power-law spectra with indices ranging from -1 (hardest) to -6 (softest), and column densities  $n_H = 1.0 \times 10^{20}$  (bottom),  $1.39 \times 10^{21}$  (middle), and  $1.0 \times 10^{22}$  (top)  $\text{cm}^{-2}$ . The labeled small grey dots show the positions along these curves of the photon indices -1 to -6, from right (hardest) to left (softest), in increments of -1. Although we have included results for 52 and Group 4 on this plot, power-law models with  $n_H$  fixed at the value appropriate for M71 did not provide acceptable fits to the X-ray spectra from these sources.

pertinent information. Column 13 lists the probability of a chance coincidence in %, calculated from

$$P_{coinc} = N(> m)\pi r_{99}^2/A_{search}, \quad (7.3)$$

where  $N(> m)$  is the number of sources in the corresponding catalog inside the search area,  $A_{search}$ , with magnitude greater than that of the candidate counterpart, and  $r_{99}$  the radius enclosing the X-ray source location with 99% confidence. For the 2MASS catalog we set  $m = K$ , and for the USNO B1.0 catalog  $m = I$ . The number of possibilities from the TYCHO-2 catalog is very small, so  $P_{coinc} \ll 1$  in the few cases where a potential TYCHO-2 candidate counterpart exists. We set the search area,  $A_{search}$ , to the area inside the S-array boundaries for X-ray sources detected on CCDs S2, S3, or S4, and to the area inside the I-array boundaries for X-ray sources detected on CCDs I2 and I3.

As one might expect, we found no candidates from these catalogs for X-ray sources in the core of M71. We found 18 X-ray sources with  $r_c < r_{M71} \leq 2r_h$  having a single candidate counterpart in the 2MASS catalog, none with multiple counterparts. Of these 18 X-ray sources, 3 also have a single USNO B1.0 candidate counterpart, and one (*s45*) has two USNO B1.0 candidate counterparts. We found just one X-ray source, *s59*, having a USNO B1.0 candidate counterpart but not a candidate counterpart in the 2MASS catalog. The X-ray source *s52* has a single counterpart in each of the 2MASS, USNO B1.0, and TYCHO-2 and is likely a bright foreground star.

For X-ray sources with  $2r_h < r_{M71}$ , we found 24 had single candidate counterparts in the 2MASS catalog (20 of these on CCDs S2-S3-S4, 4 on I2-I3), none with multiple counterparts. Of these 24, 16 also have a single USNO B1.0 candidate counterpart, and three have two USNO B1.0 candidate counterparts. There are three X-ray sources with a single USNO B1.0 candidate counterpart but no 2MASS candidate counterpart, and two X-ray sources with two USNO B1.0 candidate counterparts but no 2MASS candidate counterpart. The X-ray source *ss03* has a single counterpart in each of the 2MASS, USNO B1.0, and TYCHO-2 and is likely a bright foreground star.

Color-color diagrams of  $J - H$  vs.  $J - K$ ,  $B - R$  vs.  $B$ , and  $R - I$  vs.  $R$  show nothing unusual about the candidate counterparts to the Chandra X-ray sources, except that the counterparts to *s52* and *ss03* are both bright in  $B$  and  $R$ , as might be expected since both appear in the TYCHO-2 catalog.

### 7.7.2 HST data

There are two sets of HST observations of the M71 field currently in the public domain, (see HST proposal 8118, Piotto, G., also Piotto *et al.* 2002; and HST proposal 10524, Ferraro, F.). These data consist of 2183 s of WFPC2 data divided among four filters, and 628 s of ACS data. Results from comparing these data to the Chandra list of sources presented here will be reported in Huang *et al.* (2008, in preparation).

### 7.7.3 Variable Sources

We also compared our source positions to those listed for faint variable sources in Table 9 of Park & Nemec (2000). Of the 23 variable sources listed, 7 lie inside a radius  $2r_h$  of the nominal center of M71 but none of them are positionally coincident with a Chandra X-ray source position. Two sources from Park & Nemec are coincident with Chandra X-ray sources outside  $2r_h$ , namely *ss14* on CCD S4 and *ss52* on CCD S2. The X-ray source *ss14* lies  $0''.88$  from Park & Nemec source *v21*, a W UMa binary with period 0.353 d which lies in the subgiant region in the Color-Magnitude Diagram. The X-ray source *ss52* lies  $1''.09$  from Park & Nemec source *v19*, which may be an eclipsing binary of thus far unknown type. They observed a rise of 0.5 magnitude over  $\sim 5$  h on 1996 July 12-13 (see Park & Nemec 2000, Figure 20). Both of these sources have 2MASS and USNO candidate counterparts (see Table 7.2).

### 7.7.4 X-ray Catalogs

As previously mentioned, Verbunt (2001) reanalyzed all the ROSAT data containing M71 and found no X-ray sources inside the cluster's half-mass radius. Again using the *HEASARC BROWSE* tool in batch mode, we searched the *HEASARC* Master X-ray Catalog for sources within  $30''$  of a Chandra X-ray source, with the results listed in Table 7.6. Inside  $2r_h$ , one source, 1BMW 195344.3+184610, from the Brera Multi-scale Wavelength ROSAT High Resolution Imager Catalog (BMWHRICAT, Panzera *et al.* 2003), lies within  $1''$  of the relatively bright Chandra X-ray source *s05* lying just outside the M71 core radius, and within  $20''$  or less of the sources *s04* and *s06*. We found no other coincidences inside  $2r_h$ .

Outside  $2r_h$ , the bright Chandra X-ray *ss03* on CCD S4 is positionally coincident within  $1''$  of the ROSAT HRI X-ray source 1RXH J195303.5+18520. This source is probably the same as other coincidences listed in the table for *ss03* drawn from the ROSAT catalogs ROSPSPC, WGACAT, and BMWHRICAT. As noted previously, this source is probably a bright foreground star. Other coincidences within  $30''$  are listed in the table for the X-ray sources *ss08*, *ss45*, *is06*, and, with low probability, *is14*.

### 7.7.5 The Milli-second Pulsar

The position of PSR J1953+1846A = M71A, the 4.89 ms MSP in a 4.24 h eclipsing binary in the core of M71 reported by Ransom *et al.* (2003, 2005; also see Hessels *et al.* 2007), is separated by  $0.12''$  from the position of the X-ray source *s08* in Table 7.1, well inside the  $r_{99}$  value of  $0.65''$  found for this source. The radio timing data yield a minimum companion mass of  $0.032 M_\odot$  (Ransom *et al.* 2005, Hessels *et al.* 2007). As given in Table 7.5, its X-ray spectrum is consistent with a power-law spectrum with photon index  $\gamma = 1.89 \pm 0.32$ , and an X-ray luminosity at the distance of M71 of  $6 \times 10^{30}$  ergs  $s^{-1}$  in the 0.5–2.5 keV band and  $12 \times 10^{30}$  ergs  $s^{-1}$  in the 0.3–8.0 keV band. The neutron star atmosphere model (nsa in XSPEC; Zavlin *et al.* 1996, Pavlov *et al.* 1995) for magnetic field strengths of 0,  $10^{12}$ , and  $10^{13}$  Gauss, with the distance held fixed at 4 kpc, produces bad fits, with the best null hypothesis probability being  $6.2 \times 10^{-6}$ . We

Table 7.6: X-ray sources within 30'' of a CXO source.

(1)	(2)	(3)	(4)	(5)	(6)	(7)	(8)
Source	CCD	Catalog <sup>a</sup>	Name	Offset ''	RA(J2000) h m s	Dec(J2000) ° ' ''	$R^b$ 10 <sup>-3</sup> c/s
s05	S3	ROSAT BMWHRICAT	1BMW 195344.3+184610	0.88	19 53 44.33	18 46 9.98	0.46±0.12
s04	S3			13.52	19 53 44.33	18 46 9.98	0.46±0.12
s06	S3			19.24	19 53 44.33	18 46 9.98	0.46±0.12
ss03	S4	ROSAT ROSHRI	1RXH J195303.5+18520	0.91	19 53 3.5	18 52 0.41	10.69±0.73
			1RXH J195303.2+18520	5.67	19 53 3.19	18 52 3.29	8.72±0.73
		ROSAT ROSPSPC	2RXP J195303.4+18515	3.35	19 53 3.34	18 51 56.99	32.42±2.31
		ROSAT BMWHRICAT	1BMW 195303.3+185201	3.69	19 53 3.24	18 52 0.52	8.89±0.56
			1BMW 195303.8+185201	4.08	19 53 3.77	18 52 0.59	10.65±0.58
		ROSAT WGACAT	1WGA J1953.0+1852	6.26	19 53 3.29	18 52 5.09	33.6±2.60
ss08	S4	ROSAT BMWHRICAT	1BMW 195314.4+185157	0.61	19 53 14.38	18 51 57.31	2.22±0.29
			1BMW 195314.0+185200	5.58	19 53 13.99	18 52 0.01	1.46±0.23
ss45	S2	ROSAT ROSHRI	1RXH J195402.9+18424	2.58	19 54 2.93	18 42 48.35	1.85±0.36
			1RXH J195402.6+18425	3.71	19 54 2.59	18 42 50.94	2.13±0.37
		ROSAT BMWHRICAT	1BMW 195402.8+184249	2.09	19 54 2.81	18 42 48.71	1.66±0.23
			1BMW 195402.5+184252	5.94	19 54 2.45	18 42 52.2	2.23±0.28
is06	I3	ROSAT BMWHRICAT	1BMW 195326.2+183955	2.10	19 53 26.21	18 39 55.4	0.79±0.17
is14	I2	ROSAT BMWHRICAT	1BMW 195355.5+183516	24.44	19 53 55.49	18 35 15.5	1.74±0.35

a. Sources in this table were extracted from the *HEASARC* Master X-ray Catalog, requiring that an entry lie within 30'' of a CXO source. ROSHRI and ROSPSPC are the standard catalogs of pointed observations with the ROSAT HRI and PSPC instruments. WGACAT is another catalog of PSPC pointed observations analyzed using the XIMAGE tool (White et al. 1994). BMWHRICAT is the Brera Multi-scale Wavelet ROSAT High Resolution Imager Source Catalog (BMW-HRI) (Panzer et al. 2003), derived from all ROSAT HRI pointed observations with exposure time longer than 100 seconds available in the ROSAT public archives, and analyzed using a wavelet detection algorithm.

b. Measured count rate.

therefore conclude that the X-ray emission from this MSP is largely nonthermal, and is due either to magnetospheric radiation or to an intrabinary shock formed due to interaction between the relativistic pulsar wind and matter from the stellar companion (as in the eclipsing MSPs in 47 Tuc, Bogdanov *et al.* 2006).

The X-ray luminosity of M71A falls inside the range of X-ray luminosities of the MSPs in the well studied globular cluster 47 Tuc (Bogdanov *et al.* 2006, see their Table 4). It also shares the non-thermal nature of its X-ray spectrum with MSPs J, O and W in 47 Tuc, with a photon power-law index of  $\gamma = 1.89 \pm 0.32$  vs.  $\sim 1-1.5$  for those three MSPs. All four of these binary MSPs show radio eclipses, and PSR J1953+1846A is also eclipsed for  $\sim 20\%$  of its orbit (Hessels *et al.* 2007). Bogdanov et al. (2005) reported variability in the X-ray emission from MSP W in 47 Tuc. Setting zero binary phase using the radio ephemeris (Stairs *et al.*, in preparation), and folding with 5 phase bins at the binary period of 0.1768 d = 4.2431 h = 15.2751 ks leads to the light curve shown in Figure 7.5. Testing this light curve using Pearson's  $\chi^2$  leads to a single trial confidence level of 2.2% for acceptance of a steady source model, providing marginal (just under  $3\sigma$ ) evidence in the X-ray band for periodicity at the radio binary period. The phase spanned by the radio eclipse ( $\sim 0.18-0.36$ , also shown in the Figure) does not quite line up with the minimum in the X-ray light curve. The error in eclipse phase due to extrapolation from the time of the radio observations to the time of the X-ray observation is negligible. For 47 Tuc W Bogdanov *et al.* (2006) found that X-ray minimum precedes the optically derived superior conjunction of the pulsar, which may therefore also explain the displacement of the radio eclipse from the minimum in the folded X-ray light curve. Bogdanov *et al.* (2006) suggest the X-ray

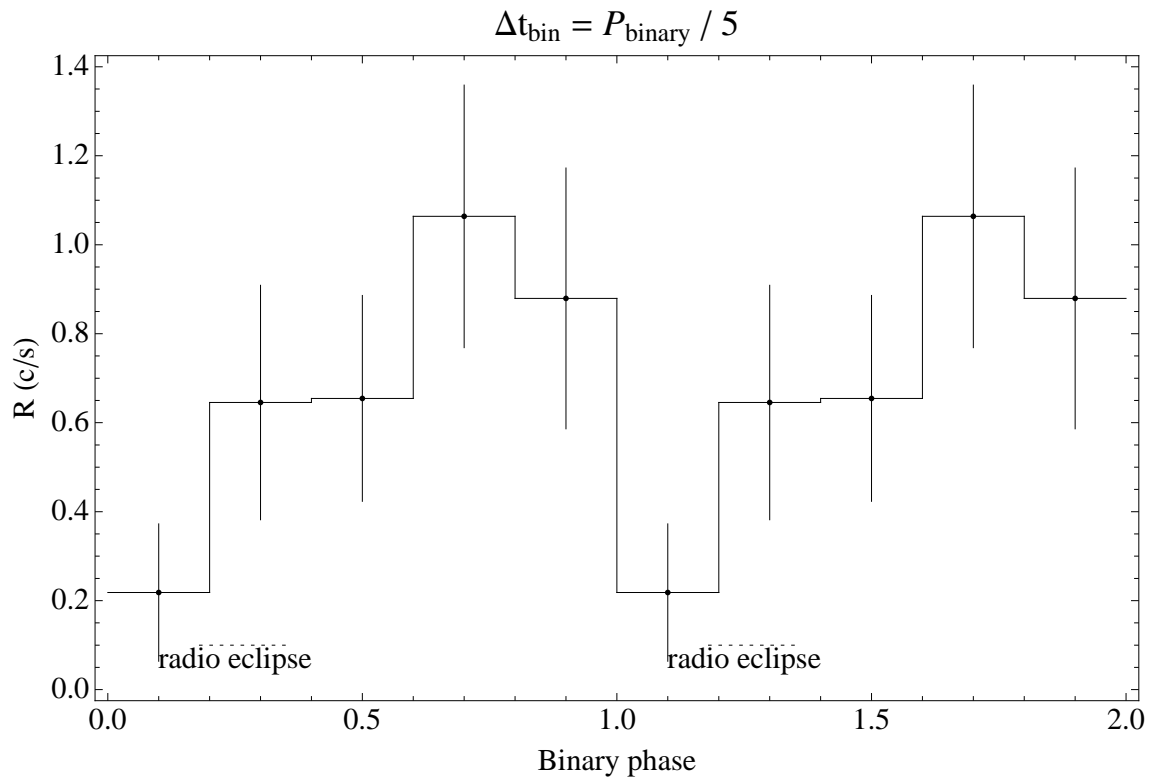


Figure 7.5: The 0.3–8.0 keV light curve for PSR J1953+1846A, folded at the reported radio binary period of 0.1768 d = 4.2431 h = 15.2751 ks. The bin size is 1/5 the binary period. The single period probability of chance occurrence of the corresponding value of  $\chi^2$  is 2.2%. Also shown is the phase spanned by the radio eclipse.

emission for the three eclipsing binary MSPs in 47 Tuc originates in a shock forming from the collision of a relativistic wind from the pulsar with material from its low-mass companion, a model which is as likely to apply to M71A as to the 47 Tuc sources.

## 7.8 Individual Sources

Figure 7.6 displays source and local background light curves in the 0.3–8.0 keV band for the 14 X-ray Chandra detected sources in Tables 7.1 and 7.2 with 0.3–8.0 keV counts  $C_x > 80$ , plus the source, *s08*, in M71’s core coincident with the MSP. Four of these sources, *s02*, *s05*, *s08*, and *s20*, lie inside the half-mass radius  $r_h$ . At the timescales shown, most of these 15 sources are inconsistent with being steady at 99.9% confidence or greater, except for *s08* (the source coincident with the MSP), *s52*, *ss21*, and *is01*. Source *s02* shows a steady rise over nearly the last half of the observation. The source *ss06* is extremely faint for over half of our observation, suddenly flares up strongly, then decays back to a faint level, with the flare lasting  $\sim 10$  ks. This source has a 2MASS candidate counterpart. The strong temporal variations in *s02* and *ss06* suggest flaring on coronally active stars.

X-ray source *s52* is positionally coincident with single 2MASS, USNO B1.0, and TYCHO-2 sources (see § 7.7.1), and its Tycho-2 counterpart has significant proper motion. As shown in Table 7.7, its X-ray spectrum fits acceptably to a single MEKAL model with no interstellar absorption. These facts suggest that *s52* is likely a nearby foreground star. Source *s38* shows evidence for time variability (Figure 7.6). The USNO catalog provides morphological star/galaxy classifications, which allow us to suggest that sources *s45* and *s59* are stars while *s37* is a galaxy.

The brightest of the 73 X-ray sources found outside  $2r_h$ , indeed the brightest in our field, is *ss03*. This X-ray source is positionally coincident with single 2MASS, USNO B1.0, and TYCHO-2 sources (see § 7.7.1), and on that basis is likely a nearby foreground star. It is also coincident with what is likely a single ROSAT X-ray source (see § 7.7.4). The fit of its X-ray spectrum to a power-law model is statistically not very good, but a fit to a single MEKAL model is statistically far worse. A fit to a MEKAL+MEKAL model with no interstellar absorption is an improvement over a single MEKAL model, but is still statistically worse than the fit to a power-law model (compare Tables 7.5 and 7.7). In addition, the source is time variable, showing a definite decline during our observation. A single MEKAL model does not fit the X-ray spectrum for source *ss45*, but a MEKAL+MEKAL model with no interstellar absorption does fit acceptably. There is one 2MASS object and one USNO B1.0 object within this source’s  $r_{99}$  radius (see § 7.7.1) as well as two ROSAT HRI sources within 2–6″. Table 7.7 shows that the X-ray spectrum for source *is06* is fit acceptably by a single MEKAL model with no interstellar absorption. We find no counterpart in the 2MASS or USNO B1.0 catalogs, but this source is within 2.1″ of a faint ROSAT HRI source (see § 7.7.4).

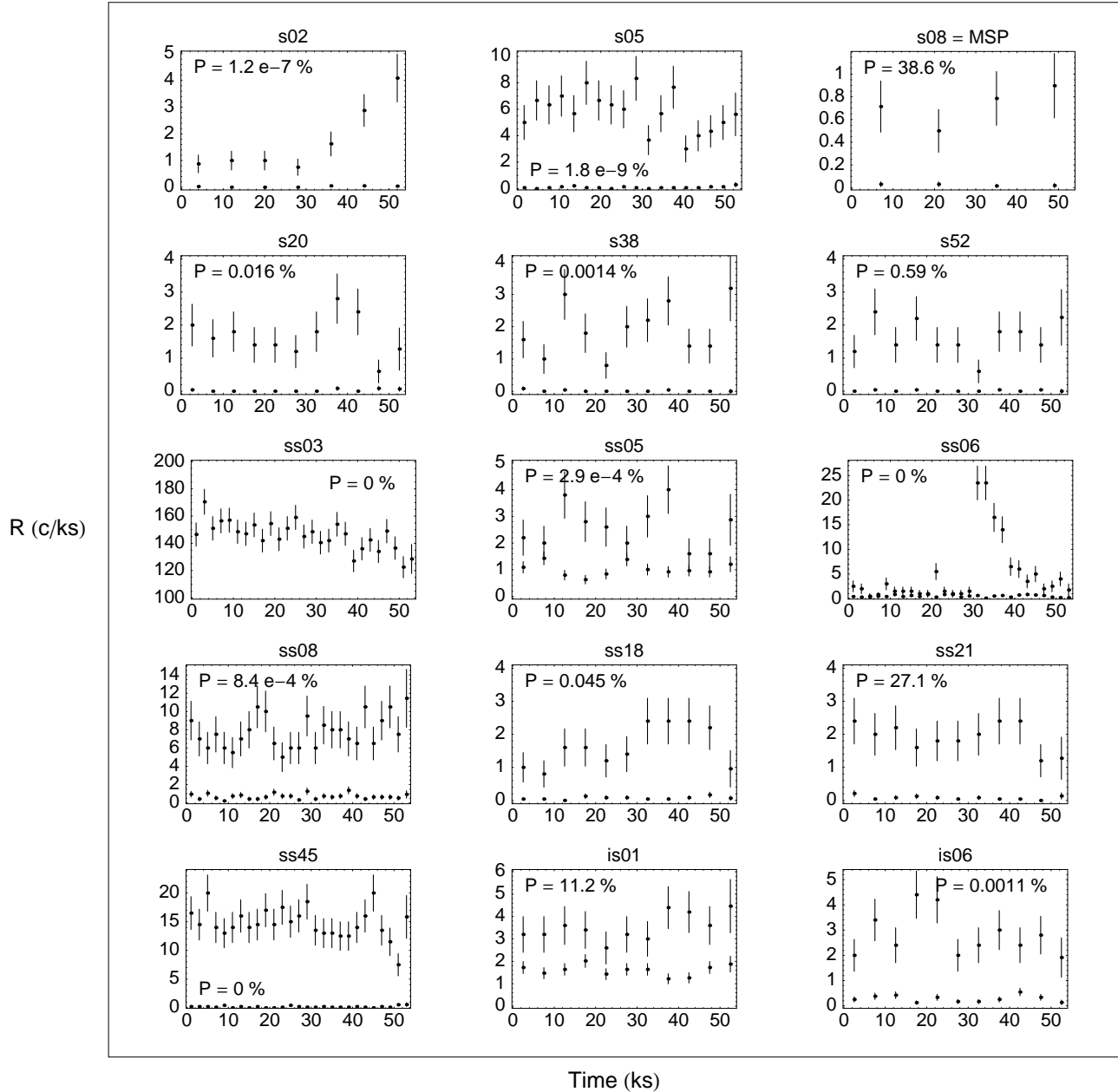


Figure 7.6: Light curves (0.3–8.0 keV rate in c/ks vs. time in ks) for the 14 Chandra detected X-ray sources in Tables 7.1–7.2 with 0.3–8.0 keV counts  $C_x > 80$ , plus the X-ray source, *s08*, coincident with the MSP in M71. Both the source and the local background light curves are shown.

Table 7.7: MEKAL and MEKAL+MEKAL spectral fits.

(1)	(2)	(3)	(4)	(5)	(6)	(7)	(8)	(9)	(10)
Source	Model <sup>a</sup>	Grouping <sup>b</sup>	$T_1$	$A_1/10^6$	$T_2$	$A_2/10^6$	$\chi^2/\nu$ <sup>c</sup>	$P(\geq \chi^2)$ <sup>d</sup>	$F_x$ <sup>e</sup>
s52	MEKAL	15	$0.41 \pm 0.06$	$2.17 \pm 0.29$			0.81/3	0.85	10(11)
ss03	MEKAL+MEKAL	20	$4.00 \pm 0.21$	$790_{20}^{30}$	$0.96 \pm 0.06$	$49 \pm 12$	322/165	3.37e-12	1470(2800)
ss45	MEKAL+MEKAL	20	$0.83 \pm 0.06$	$9.9 \pm 1.8$	$2.84 \pm 0.33$	$51 \pm 4$	28.1/30	0.56	130(200)
is06	MEKAL	20	$1.03 \pm 0.08$	$8.12 \pm 0.90$			6.12/5	0.29	29(34)

a. The XSPEC MEKAL model calculates the emission from a hot diffuse gas at temperature  $T$  and with normalization  $A$  as given at <http://heasarc.gsfc.nasa.gov/docs/xanadu/xspec/manual/XSmodelMekal.html> (Mewe et al. 1985, 1986; Liedahl et al. 1995; Arnaud & Rothenflug 1985; Arnaud & Raymond 1992). The quoted errors are the one-parameter 67% confidence level errors given by the XSPEC command error with  $\Delta\chi^2 = 1$ .

b. Minimum number of counts per spectral bin for fitting in XSPEC.

c. Value of  $\chi^2$  for best-fit and the number of degrees of freedom,  $\nu$ .

d. Probability of finding a value for  $\chi^2 \geq$  the value actually found.

e. X-ray luminosity in units of  $10^{30}$  ergs  $s^{-1}$ ; energy bands are 0.5–2.5 (0.3–8.0) keV.

## 7.9 Discussion

We have found five X-ray sources (including the millisecond pulsar M71A) located within the cluster core radius. Our radial distribution analysis indicates 1-2, and possibly all four other than M71A, are background sources. M71A shows marginal evidence for modulation at the the binary period, slightly before the radio eclipse phase, suggesting similarity with the eclipsing millisecond radio pulsar 47 Tuc W (Bogdanov *et al.* 2006). We identify 29 X-ray sources within the half-mass radius of M71, down to a limiting X-ray luminosity (0.3-8.0 keV)  $\sim 1.5 \times 10^{30}$  ergs  $s^{-1}$ , of which 5-17 may be foreground or background sources. Seven of these (all outside the core) have candidate 2MASS counterparts. We also identify a further 108 sources outside this radius, of which the majority (71) have candidate 2MASS, USNO, or TYCHO-2 optical or near-IR counterparts.

It is of great interest to compare the populations of faint X-ray sources in different globular clusters. Our radial distribution analysis shows that the X-ray sources associated with M71 seem to be largely confined within the half-mass radius, as seen in denser clusters (*e.g.* NGC 6440, Pooley *et al.* 2002). This is in contrast to the similarly low-density cluster  $\omega$  Cen, where a quiescent low-mass X-ray binary lies outside the half-mass radius (Rutledge et al. 2003). Three likely RS CVn and eclipsing Algol stars (all cluster members) have also been astrometrically identified with Chandra or XMM-Newton sources outside the half-mass radius (Cool et al. 2002; Gendre et al. 2003). We suggest that this contrast may be due to the particularly low level of mass segregation in  $\omega$  Cen, and its much longer half-mass relaxation time (in agreement with Verbunt & Johnston 2000).

Studies of globular clusters show that above  $L_X = 10^{31}$  ergs  $s^{-1}$ , the X-ray sources seem to be dominated by CVs, while below  $L_X = 10^{31}$  ergs  $s^{-1}$ , ABs seem to be the dominant population (see Fig. 14 in Heinke *et al.* 2005, or Fig. 6 in Kong *et al.* 2006). (Neutron stars contribute to both populations—as qLMXBs for the brighter population, and as MSPs for the fainter—but do not approach 50% of either population in any studied cluster.) Therefore, some constraints upon the relative frequency of ABs in different cluster environments are possible even before completion of detailed counterpart identification studies.

Table 7.8: Background-subtracted source numbers for selected globular clusters.

(1)	(2)	(3)	(4)	(5)
	M 4	M 71	47 Tuc	NGC 6397
Distance (kpc)	1.73	4.0	4.5	2.55
$\Gamma^a$	1	0.11	24.9	2.52
$M_h^b$	1	0.30	10.2	0.78
$10^{31} < L_x(\text{ergs s}^{-1})^c$	1 <sup>d</sup>	2.2	23	8
$10^{30} < L_x(\text{ergs s}^{-1})^c < 10^{31}$	6.6	12.5	116	7
Error	3.0	6.2	3.9	2.4
References <sup>e</sup>	1	2	3	4

a. Collision number,  $\Gamma \propto \rho_0^{1.5} r_c^2$ , normalized to the value for M4, where  $\rho_0$  is the cluster central density and  $r_c$  the core radius. Cluster parameters come from Harris (1996; updated Feb. 2003), except M4 for which  $\rho_0$  and  $M_V$  are computed from the distance and reddening of Richer *et al.* (1997).

b. Scaled cluster mass  $M_h$  inside  $r_h$ . Following Kong *et al.* (2006), scaled values for  $M_h$  were calculated from  $M_h = 10^{-0.4(M_V - M_{V,M4})}$ , where  $M_V$  is the cluster absolute visual magnitude from Harris (1996, updated 2003). The value  $M_{V,M4}$  for the cluster M4 is -7.2.

c.  $L_x$  is the X-ray luminosity of individual sources in the 0.5–2.5 keV energy band.

d. M4 possesses one optically identified X-ray source and likely CV with  $L_x > 10^{31}$  ergs s<sup>-1</sup>.

e. For each cluster, the basic data for this table were extracted from: 1 Bassa *et al.* 2004; 2 this work; 3 Heinke *et al.* 2005, but correcting for a distance of 4.5 kpc; 4 Grindlay *et al.* 2001b.

We count the total numbers of sources with: a)  $10^{31} < L_x$ ; and b)  $10^{30} < L_x < 10^{31}$  ergs s<sup>-1</sup>, in the 0.5–2.5 keV band, inside the half-mass radii of four clusters: M4, M71, 47 Tucanae, and NGC 6397. We calculate the numbers of background sources within each half-mass radius (except NGC 6397, where we use the 2' radius studied by Grindlay *et al.* 2001b) predicted by the Chandra Deep Field-North studies (Brandt *et al.* 2001). For M71, we use the counts from Table 1 and derive (0.5–2.5 keV) luminosities using the spectral fit to groups 1 and 2 in Table 5, giving  $L_x = 1.48 \times 10^{29}$  ergs/s/photon for on-axis sources. M71's high foreground source contamination (attributable to its low Galactic latitude and low density) requires correction for foreground contamination using the results of §3. We find a total of  $12.5 \pm 6.2$  X-ray sources within M71's half-mass radius between  $10^{30} < L_x < 10^{31}$  ergs/s. The background-subtracted source numbers in these  $L_x$  ranges are listed in Table 7.8, and plotted in Figure 7.7. The errors on the source numbers are derived from the Poisson statistics of the numbers of background sources, as in Table 7.4.

Figure 7.7 shows that a linear relation between scaled mass,  $M_h$ , inside the half-mass radius and the number,  $N_h$ , of X-ray sources inside the half-mass radius in the luminosity range dominated by ABs appears acceptable for most clusters. In computing this linear fit ( $N_h = aM_h$ ), we add in quadrature the errors on the predicted number of sources at each cluster's mass, with the actual errors on the cluster sources. M71 stands out as having an excess of likely ABs for its mass ( $12.5 \pm 6.2$ ) sources with  $10^{30} < L_x < 10^{31}$  ergs s<sup>-1</sup>, compared to 3.5 expected, although it is less than a  $2\sigma$  excess. Similar radial profile analyses have not yet been done for most of the other comparison clusters; if they also suffer foreground contamination, then the discrepancy will be increased.

The central density of M71 is relatively low,  $\log \rho_c \simeq 3.0$ , suggesting that M71 may have lost fewer binaries (and hence ABs) through binary destruction mechanisms (Ivanova *et al.* 2005).

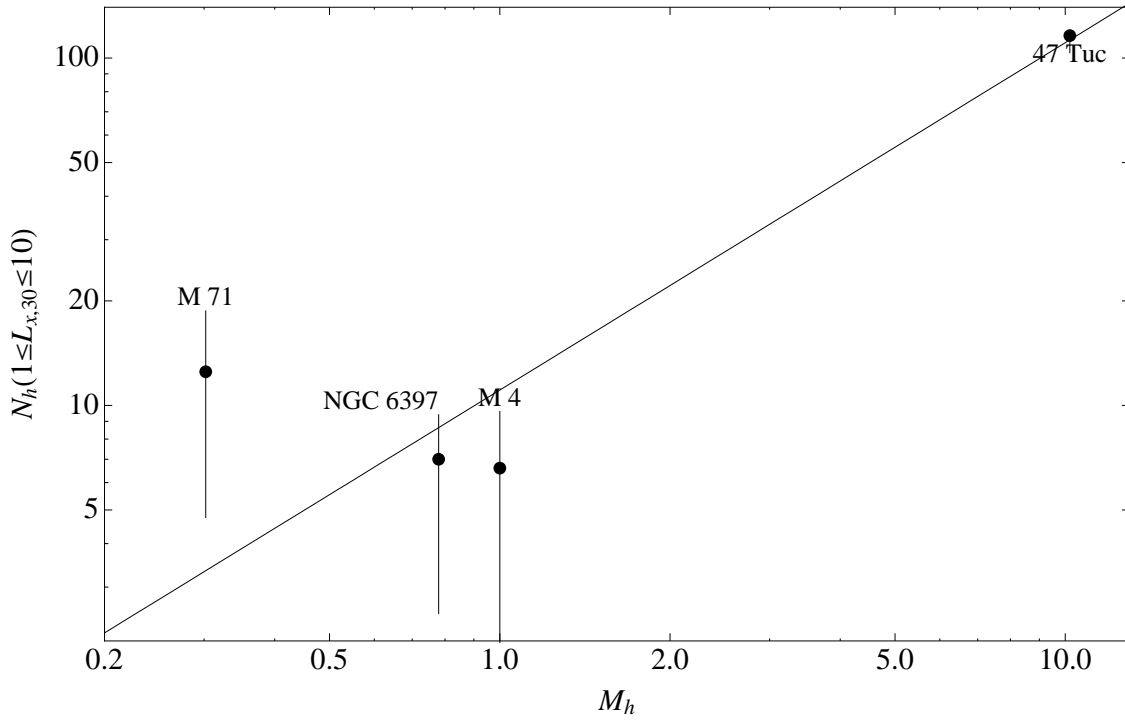


Figure 7.7: For four clusters, number of background-subtracted sources inside  $r_h$  with 0.5–2.5 keV X-ray luminosities,  $L_{x,30}$ , in the range 1–10, vs. scaled values for the mass,  $M_h$ , inside  $r_h$ . Following Kong *et al.* (2006), scaled values for  $M_h$  were calculated from  $M_h = 10^{-0.4(M_V - M_{V,M4})}$ , where  $M_V$  is the cluster absolute visual magnitude from Harris (1996, updated 2003). The value  $M_{V,M4}$  for the cluster M4 is -7.2. The result of a weighted linear fit to the data ( $N_h = aM_h$ ), including M71, is also plotted, with slope  $a = 11.1$ .

Contamination of the sample by collisionally produced X-ray sources (e.g. CVs) cannot explain M71's likely abundance of X-ray sources, since M71 is a very low-density and low-Gamma cluster (Table 8). Thorough optical identification campaigns (to reduce the uncertainties in cluster membership), and deep observations of additional globular clusters, will enable progress in understanding the formation and destruction of faint X-ray sources.

# Chapter 8

## Study of HST counterparts to Chandra X-ray sources in M71

This chapter is adopted from the refereed paper entitled “Study of HST counterparts to Chandra X-ray sources in the Globular Cluster M71” published in *Astronomy & Astrophysics* (Huang et al. 2010).

### 8.1 Abstract

We report on archival Hubble Space Telescope (HST) observations of the globular cluster M71 (NGC 6838). These observations, covering the core of the globular cluster, were performed by the Advanced Camera for Surveys (ACS) and the Wide Field Planetary Camera 2 (WFPC2). Inside the half-mass radius ( $r_h = 1'.65$ ) of M71, we find 33 candidate optical counterparts to 25 out of 29 Chandra X-ray sources while outside the half-mass radius, 6 possible optical counterparts to 4 X-ray sources are found. Based on the X-ray and optical properties of the identifications, we find 1 certain and 7 candidate cataclysmic variables (CVs). We also classify 2 and 12 X-ray sources as certain and potential chromospherically active binaries (ABs), respectively. The only star in the error circle of the known millisecond pulsar (MSP) is inconsistent with being the optical counterpart. The number of X-ray faint sources with  $L_X > 4 \times 10^{30}$  ergs s<sup>-1</sup> (0.5–6.0 keV) found in M71 is higher than extrapolations from other clusters on the basis of either collision frequency or mass. Since the core density of M71 is relatively low, we suggest that those CVs and ABs are primordial in origin.

### 8.2 Introduction

There are 158 Galactic globular clusters (GGCs) found in the halo of our galaxy and typically contain  $10^4 - 10^7$  stars. They are very old and dense star systems and tightly bound by gravity, which gives them their spherical shapes and relative high stellar density toward the center. The dense stellar environment in globular clusters triggers various dynamical interactions, ie. exchanges in encounters with binaries, direct collisions, destruction of binaries, and tidal capture.

These dynamical interactions not only can change the evolution of individual stars, but also can produce tight binary systems (see, e.g., Ashman & Zepf 1998; Verbunt & Lewin 2004, for review).

One of the most powerful ways to probe the binary content of globular clusters is by studying the X-ray source population. In the early 1970s, X-ray sources with luminosity greater than  $10^{36}$  ergs  $s^{-1}$  were first detected by using the Uhuru and OSO-7 Observatories. Following the Einstein and ROSAT era, the number of faint X-ray sources ( $L_X < 10^{34.5}$  ergs  $s^{-1}$ ) was dramatically increased. Those bright X-ray sources have been identified with low-mass X-ray binaries (LMXBs; Grindlay et al. 1984) while the identification of the weaker sources remained limited due to low photon statistics and insufficient spatial resolution. The launch of the Chandra X-ray Observatory ushered in a new age of studying the crowded centers of Galactic globular clusters with a far greater sensitivity and resolving power than ever before (e.g., Grindlay et al. 2001a,b). With the aid of the Hubble Space Telescope (HST), many of these faint X-ray sources were identified as quiescent low-mass X-ray binaries (qLMXBs; in which a neutron star accretes matter from its companion at a low rate), cataclysmic variables (CVs; in which a white dwarf accretes from its low-mass companion), and millisecond pulsars (MSPs), as well as chromospherically active binaries (ABs; e.g., RS CVn and BY Dra systems) (e.g., Grindlay et al. 2001b; Pooley et al. 2002; Edmonds et al. 2003a,b; Heinke et al. 2005; Bassa et al. 2004; Kong et al. 2006; Lugger et al. 2007; Bassa et al. 2008).

The globular cluster M71 (NGC 6838) lies close to the Galactic plane with Galactic longitude  $l = 56.74$  and latitude  $b = -4.56$ . Similarly to 47 Tuc, it is a fairly metal-rich globular cluster with metallicity of  $[Fe/H] = -0.73$ . Due to its relatively small distance ( $d \sim 4$  kpc) to Earth and low central luminosity density ( $\rho_c = 10^{3.05} L_\odot/\text{pc}^3$ ), M71 is a good target for both optical and X-ray observations. The core, half-mass, and tidal radii are  $r_c = 0.63$ ,  $r_h = 1.65$ , and  $r_t = 8.96$ , respectively. M71 shows no evidence for core collapse. Its moderate optical reddening  $E_{B-V} = 0.25$  may be converted into a nominal X-ray absorption column of  $N_H = 1.39 \times 10^{21} \text{cm}^{-2}$  (Predehl & Schmitt 1995). The aforementioned parameters related to M71 were obtained from Harris (1996, updated 2003<sup>1</sup>).

In this work we report on archival Chandra and HST observations of the globular cluster M71. We have obtained a 52.4-kilosecond Chandra observation of M71 taken with the Advanced CCD Imaging Spectrometer (ACIS), reaching the limiting X-ray luminosities of  $1.5 \times 10^{30}$  ergs  $s^{-1}$  and  $7.9 \times 10^{29}$  ergs  $s^{-1}$  in the energy ranges of 0.3–8.0 and 0.5–2.5 keV, respectively. In Elsner et al. (2008), we reported the identification of 29 X-ray sources within the cluster half-mass radius, including the known millisecond pulsar PSR J1953+1846A (M71A), and their X-ray properties, and found that  $18 \pm 6$  of these 29 sources are likely to be associated with M71 from a radial distribution analysis. The present paper extends our study of the X-ray sources in M71 by using archival HST data to identify optical counterparts to the majority of M71's X-ray sources, improving our understanding of their nature.

In §2 we discuss the Chandra X-ray observations and spectral analysis. HST observations, data reduction and analysis are described in §3. In §4 we present the source identification. A

<sup>1</sup><http://physwww.mcmaster.ca/harris/Databases.html>

discussion and comparison with other globular clusters is given in §5.

### 8.3 X-ray Observations

Elsner et al. (2008) described the Chandra X-ray observations of M71. We here note some relevant information for our analysis and extend the spectral fitting in this paper to test alternative models besides the power-laws considered by Elsner et al. (2008). Only seven of the 29 detected X-ray sources have sufficient counts (six sources with at least 50 source counts and one known MSP with 37.5 source counts<sup>2</sup>) to warrant a detailed spectral analysis. We used the CIAO tool *dmextract* to extract spectra of the brighter sources and the source-free background regions near to those sources. Response files were constructed by using the CIAO tool *mkacisrmf* and *mkarf*. The extracted spectra were binned with at least 5 source counts per bin. Background-subtracted spectral modeling was performed with XSPEC using data in the energy band 0.3–8.0 keV. To characterize the spectra of these sources, we fitted each of the 7 brightest X-ray sources with several different models (i.e., power-law (PL), thermal bremsstrahlung (TB), and blackbody (BB)) by using Cash (1979) statistics. Assuming all the X-ray sources within the half-mass radius are associated with the globular cluster M71, we fixed the hydrogen column density at the value of  $N_{\text{H}} = 1.39 \times 10^{21} \text{ cm}^{-2}$  from optical extinction to attempt spectral fitting.

In Table 8.1, column 1 shows the Chandra source name given in Elsner et al. (2008), and column 2 lists the spectral model we used (we omitted the models that could not provide any physically acceptable description of the observed spectra). Column 3 gives the minimum number of counts used to group the spectral data for fitting, column 4 shows the best-fit photon index ( $\Gamma$ ) or the temperature (keV), column 5-6 gives the C-statistic and the number of PHA<sup>3</sup> bins, and the last column lists the unabsorbed X-ray flux in units of  $10^{-14} \text{ ergs s}^{-1} \text{ cm}^{-2}$  in the energy bands 0.3–8.0 and 0.5–2.5 keV.

The X-ray spectra discussed here can help us to classify the faint X-ray sources. The brightest X-ray sources with  $L_{\text{X}} \geq 10^{32} \text{ ergs s}^{-1}$  in the energy band 0.5–2.5 keV and soft spectra ( $f_{0.5-2.0 \text{ keV}}/f_{2.0-6.0 \text{ keV}} \geq 1$ ) are mostly quiescent low-mass X-ray binaries (qLMXBs; Verbunt et al. 2008). None of the X-ray sources in our sample shows this characteristic, and we conclude that M71 does not contain this kind of binary systems. Cataclysmic variables (CVs) usually have hard spectra (power-law photon indices  $\Gamma < 2$ ) and their X-ray luminosities are typically between a few  $10^{30}$  and a few  $10^{32} \text{ ergs s}^{-1}$ . Most faint ( $L_{\text{X}} < 3 \times 10^{31} \text{ ergs s}^{-1}$ ) sources with soft spectra belong to chromospherically active binaries (ABs; Verbunt et al. 2008). Looking at the brightest seven X-ray sources within the half-mass radius, we see that three have soft spectra ( $\Gamma > 2$ ), three have hard spectra ( $\Gamma < 2$ ), and one (s20) is borderline, with  $\Gamma \sim 2$ . These spectra suggest that s05, s08, and s29 might be CVs, AGN, or MSPs, while the softer spectra of s02, s15, s19 and s20 may indicate that these are ABs. Definitive classifications require optical identification, which we turn to now.

<sup>2</sup>The number of source counts is a result of modelling the background and the PSF, and represents a background subtracted expectation value for the source counts within the detect cell.

<sup>3</sup>PHA: Pulse Height Analysis

Table 8.1: Spectral fits of the X-ray sources with source counts  $C_{0.3-8.0 \text{ keV}} \geq 50$ 

X-ray Source	Model	Grouping <sup>a</sup>	$\Gamma/\text{kT}$	C-statistic/bins	$f_{0.3-8.0}(f_{0.5-2.5})^b$
s02	PL	8	$3.08 \pm 0.3$	12.11/9	1.49(0.74)
	TB	8	$0.62 \pm 0.1$	10.99/9	1.26(0.82)
s05	PL	30	$1.55 \pm 0.1$	8.20/9	5.67(2.25)
	TB	30	$9.96^{+9.2}_{-3.0}$	10.33/9	5.48(2.23)
	BB	30	$0.69^{+0.04}_{-0.03}$	59.72/9	2.63(0.91)
s08	PL	5	$1.70 \pm 0.5$	2.56/6	0.74(0.32)
	TB	5	0.53	20.18/6	0.67(0.45)
s15	PL	5	$2.57 \pm 0.3$	9.34/11	1.18(0.63)
	TB	5	$1.31^{+0.5}_{-0.3}$	8.23/11	0.84(0.57)
s19	PL	5	$2.61 \pm 0.4$	1.19/9	1.14(0.60)
	TB	5	$1.23^{+0.7}_{-0.3}$	2.77/9	0.80(0.55)
s20	PL	8	$1.92 \pm 0.4$	9.52/9	1.71(0.83)
	TB	8	$1.90^{+2.1}_{-0.7}$	8.58/9	1.40(0.89)
	BB	8	$0.35^{+0.04}_{-0.03}$	0.84/7	0.83(0.72)
s29	PL	5	$1.29 \pm 0.4$	4.94/8	1.12(0.36)

<sup>a</sup>Minimum number of counts used to group the spectral data for fitting in XSPEC.

<sup>b</sup>Unabsorbed X-ray flux in units of  $10^{-14} \text{ ergs s}^{-1} \text{ cm}^{-2}$ ; energy bands are 0.3–8.0 (0.5–2.5) keV.

## 8.4 Optical Observations

Two fields located inside the half-mass radius of the globular cluster M71 were observed with the Wide Field and Planetary Camera 2 (WFPC2) on board the Hubble Space Telescope (HST) in 2000 and 2006. An image of the observations is shown in Figure 8.1. For these observations, the PC camera was centered on the cluster center and the F336W (similar to  $U$ , hence  $U_{336}$  hereafter), F439W ( $B_{439}$ ), and F555W ( $V_{555}$ ) filters were used. Exposure times were 800 sec in F336W (GO10524) and 240 sec in F439W (GO8118). Two exposure times correspond to the F555W filter are 80 sec and 63 sec for GO10524 and GO8118, respectively. GO10524 also contains F255W images which did not go deep enough to identify our targets. To estimate whether the nondetections may be meaningful, we used Ferraro et al. (2000) to estimate that CVs may be up to 3 magnitudes brighter (absolute magnitude) in F255W than  $V$ . Using Seaton (1979), we estimate the extinction  $A_{255} = 7.0$  for M71, and thus any CVs would be observed to be at least 3.2 magnitudes fainter in F255W than  $V$ . Using the WFPC2 exposure time calculator (ETC), we estimate that the brightest CV candidate in our WFPC2 field, s29, could attain a signal-to-noise ratio (SNR) of 1.4 in the F255W data if it showed the maximum F255W/ $V$  excess, which many of Ferraro et al.'s UV-selected objects do not. Therefore we did not discuss the F255W data further in this paper. The  $5\text{-}\sigma$  limiting magnitudes of  $U_{336}$ ,  $B_{439}$ , and  $V_{555}$  for point sources are 21.09, 20.87, and 21.87, respectively. M71 was also observed with the HST Advanced Camera for Surveys (ACS). The observations (GO10775) consist of F606W ( $V_{606}$ ) and F814W ( $I_{814}$ ) im-

ages covering the entire half-mass radius of the cluster (see Fig. 8.1). The exposure times for the F606W and F814W filters were 304 and 324 sec with  $5\text{-}\sigma$  limiting magnitudes of  $V_{606} = 25.17$  and  $I_{814} = 23.91$  for point sources. We note that the median value of the point sources with the signal to noise ratio  $S/N \sim 5$  is used to define the 5-sigma limiting magnitude.

This section outlines the data reduction, photometry, and astrometry of the HST/WFPC2 and ACS images.

### 8.4.1 Data Reduction and Photometry

The HST/WFPC2 data obtained from the ESO archive were processed through the WFPC2 Associations Science Products Pipeline<sup>4</sup>. For each filter, single exposures were calibrated, including full bias subtraction and flat-fielding, and combined together in order to remove the cosmic-ray events and correct the geometrical distortions<sup>5</sup>. We also downloaded the archival HST/ACS drizzled images. Those images were combined from two Wide Field Channel (WFC) images and calibrated with MultiDrizzle package (Koekemoer et al. 2002), which corrected for geometric distortion and performed cosmic ray rejection.

Although M71 is a globular cluster, its stellar surface density is not as dense as that of a typical globular cluster. Even in the central region of M71, the average distance between stars is around  $2''$ , which is about 10 times larger than the typical FWHMs of WFPC2 and ACS cameras. Therefore, a simple aperture photometry method with the aperture correction is applicable to our data. We tested the flux measurement using several different psf-fitting photometry methods and the simple aperture photometry. We found that aperture photometry method had better signal-to-noise ratio and less magnitude error. Therefore, we decided to use aperture photometry to measure the fluxes of our data.

For the data taken with WFPC2, we basically followed the instruction of aperture photometry described in Holtzman et al. (1995). To deal with the PSF variances within each chip and between chips, we further separated the images into 4 and 9 equal-size regions for the PC and WF chips, respectively, and performed the aperture photometry with aperture correction for each separated regions individually. We used an aperture with the size of  $0'.5$  in radius to measure fluxes, for all the objects with  $3\sigma$  detection found using the IRAF *daofind* task. We note that only less than 1% objects in each chip with separation of  $\leq 0'.5$  to their neighbors, so that using an aperture with the size of  $0'.5$  does not suffer from the PSF overlapping problem. The local sky values were measured using an inner sky annulus of 4 arcsecs with a width of 2 arcsecs, and the aperture correction value was calculated using the averages of the differences between the magnitudes measured using apertures with sizes of  $0'.5$  and  $4''$  in radius for 4 to 5 isolated stars in each separated region. The aperture correction value is  $0.11 \pm 0.02$  mag, which is consistent with the value shown in Holtzman et al. (1995). The final output magnitudes, in the VEGAMAG system, were corrected for the appropriate zeropoints based upon the sensitivity information in each header and the charge transfer efficiency effect (Dolphin 2000).

<sup>4</sup>See <http://archive.eso.org/archive/hst/wfpc2.asn/>

<sup>5</sup>see <http://archive.stsci.edu/hst/wfpc2/pipeline.html>

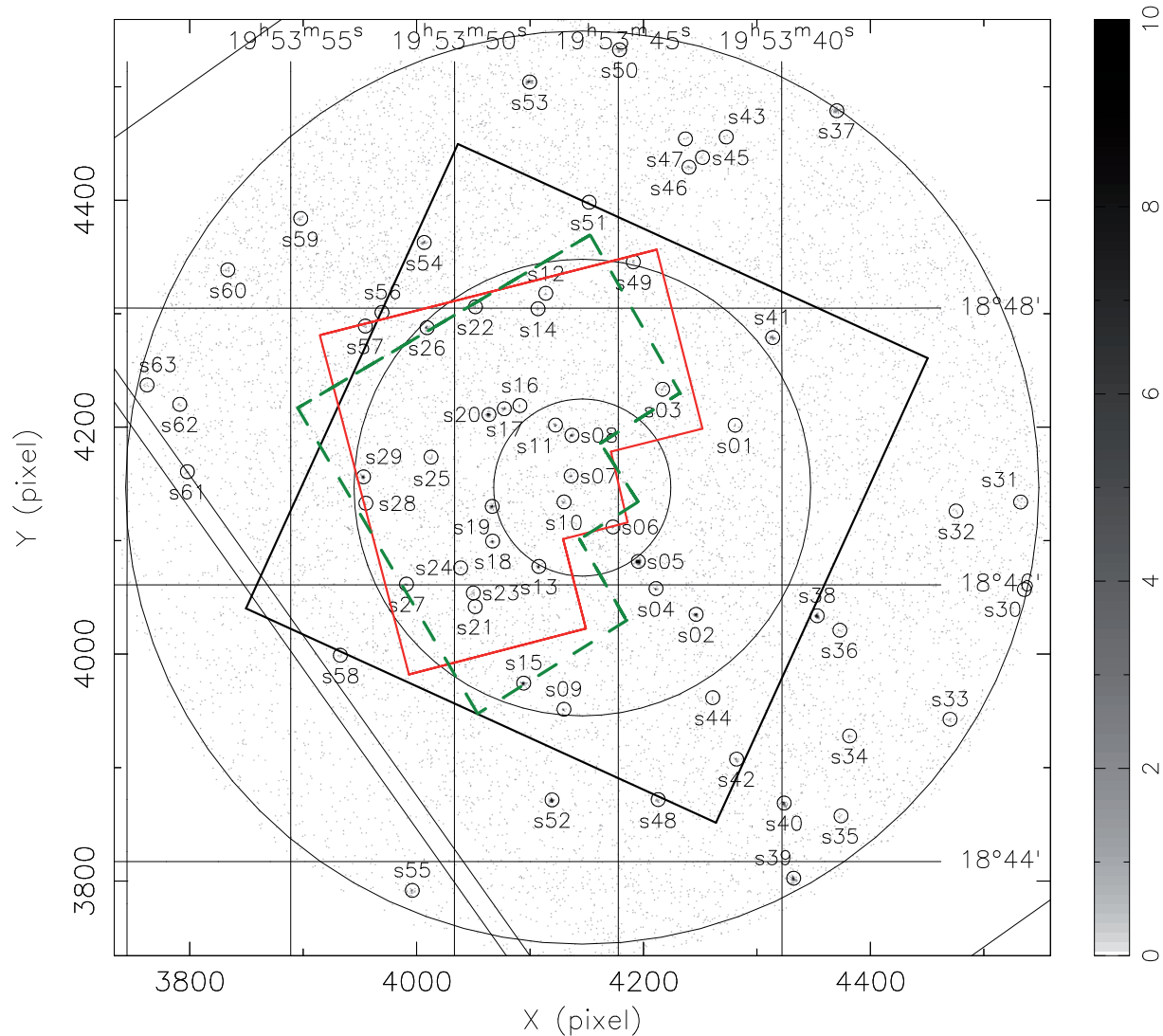


Figure 8.1: Chandra ACIS-S3 image of the globular cluster M71 within the energy range of 0.3 – 8.0 keV. The large circles are centered on the nominal center of the cluster and have radii  $r_c$  (inner circle),  $r_h$  (middle circle), and  $2r_h$  (outer circles). The small circles show the positions of the 63 X-ray sources within  $r_{\text{M71}} \leq 2r_h$  (Elsner et al. 2008). Straight lines mark the nominal boundaries of the ACIS-S3 and ACIS-S2 CCDs, with most of the figure falling on S3 and the lower left hand portion on S2. The field of view of the HST ACS (GO10775) marked by the black square covers the entire half-mass radius. The green (dashed) and red (solid) polygons are the field of view of the HST WFPC2 for GO10524 and GO8118, respectively.

For the data taken with ACS, we performed the aperture photometry based on the method described in Sirianni et al. (2005). The method is very similar to what we did for WFPC2. We also separated the ACS drizzled images into 9 equal-size regions to deal with the PSF variances. We used an aperture size of  $0''.5$  in radius to measure the fluxes with sky annulus from 4 arcsecs to 6 arcsecs. The aperture correction value is  $0.08 \pm 0.01$ , which agrees with the values shown in Sirianni et al. (2005). However, several optical counterparts, e.g., s08, s19, suffer from the PSF overlapping problem since the distances between them and their neighbors are  $\lesssim 1''.0$ . In order to measure accurate fluxes for these counterparts, we first subtracted their neighbors by using the PSF generated from isolated stars which are close to the counterparts, and then performed the aperture photometry on these sources. By doing this, we can minimize the photometric effect from the PSF wings of neighbors.

Comparing with the photometry of M71 kindly provided by Anderson et al. (2008) for the ACS images and reported by Piotto et al. (2002) for the WFPC2 B-band and V-band images, their results are consistent with what we have obtained by using aperture photometry, but have the main sequence and the giant branch with less noise. We therefore used their photometry in our study. In addition, for those possible optical counterparts undetected in their photometry, we used our own results for the magnitudes which have been corrected for the appropriate zeropoint.

The most informative of these diagrams are shown in Fig. 8.2, on which all stars located within the 95% confidence error circles (see Section 2 and Table 1 of Elsner et al. 2008) of the Chandra source positions are indicated by red squares. Numbers have been assigned to all candidate counterparts corresponding to the ‘s’ designation given in Elsner et al. (2008), with ‘a’, ‘b’, or ‘c’ appended if multiple potential optical counterparts exist.

### 8.4.2 Astrometry

To search for optical counterparts to the Chandra X-ray sources we aim to place both the X-ray and the optical frames onto the International Celestial Reference System (ICRS). We use this approach to improve the absolute pointing accuracy of Chandra and HST,  $0''.6$  and  $1''.0$  ( $1\sigma$ ) respectively (Aldcroft et al. 2000; Heyer et al. 2004).

For the X-ray sources, the positions listed in Elsner et al. (2008) are already on the ICRS. In this paper, we aim to tie the HST pointing to the ICRS by finding matches between stars appearing on HST images and stars with accurate positions in the Two Micron All Sky Survey (2MASS) Point Source Catalog (Skrutskie et al. 2006). On the basis of the HST pointing information contained in each image header, we used the `WCSTools/imwcs`<sup>6</sup> task on each corrected image to do the cross-correlation. The resulting positions were matched to those stars from the 2MASS catalog. There are hundreds of 2MASS stars within each HST image. By using those 2MASS stars as reference, the astrometric solution yielded root-mean-square residuals of  $0''.057$  in right ascension (RA) and  $0''.065$  in declination (Dec) relative to the 2MASS astrometry for the ACS images. The resultant solution gave the residual errors of  $0''.068$  and  $0''.148$  in RA and  $0''.066$  and  $0''.149$  in Dec relative to the 2MASS astrometry for the PC and WF images, respec-

<sup>6</sup>See <http://tdc-www.harvard.edu/software/wcstools/index.html>

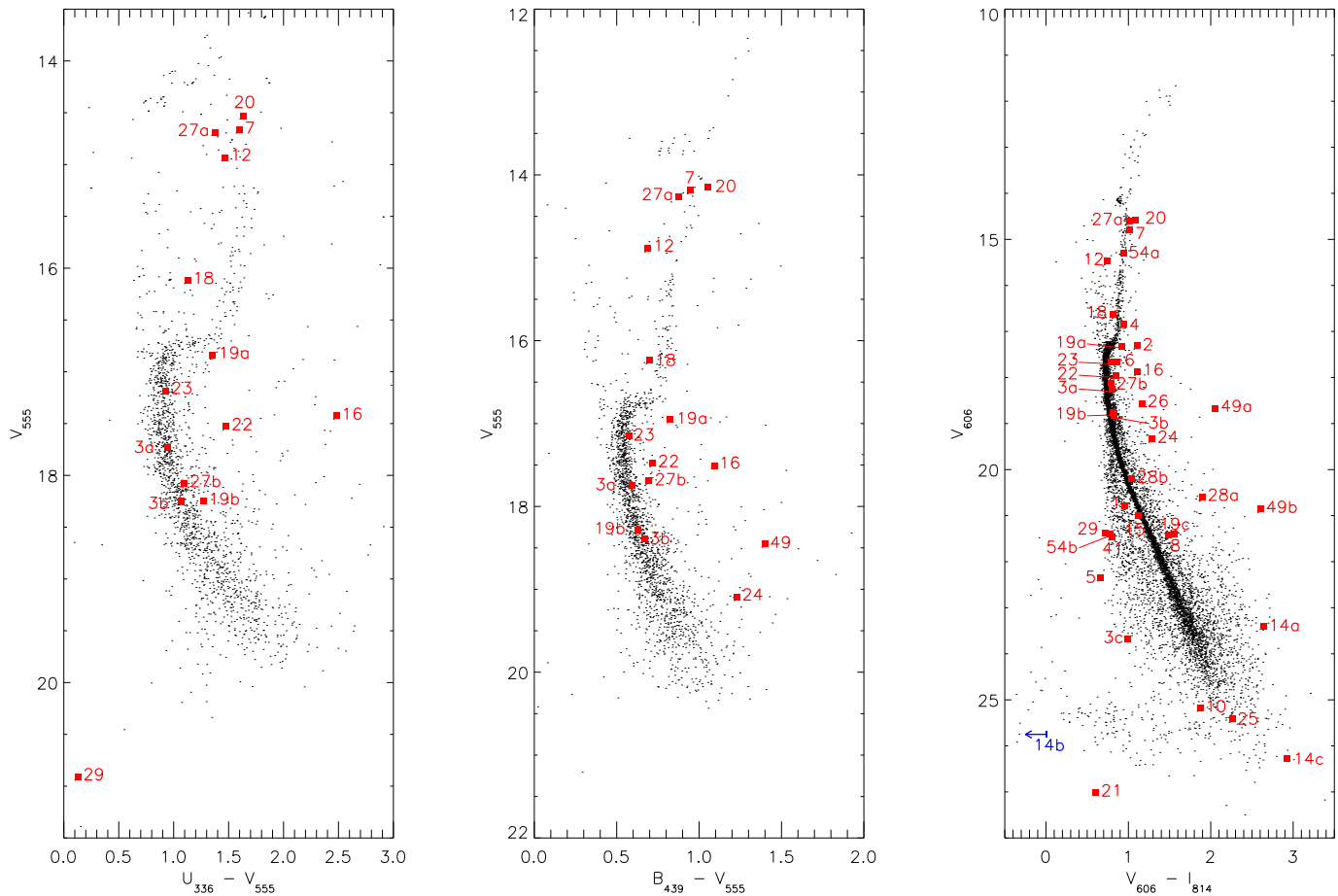


Figure 8.2: Color magnitude diagrams (CMDs) for all the sources detected in the WFPC2 and ACS field of view. The HST candidate counterparts matched to the X-ray sources are indicated by red squares. We note here s14b in the (V, V-I) CMD is plotted as a leftward-pointing arrow since its  $I_{814}$ -band magnitude is far below the 5-sigma limiting magnitude and with a large magnitude error.

tively. The final uncertainties of the optical source position in RA and Dec are the root of the square sum of the uncertainty of the astrometry in 2MASS and HST image alignment and the general uncertainties of 2MASS point source astrometry of typically  $\sim 0''.1$  relative to the ICRS (Skrutskie et al. 2006).

## 8.5 Source Identification and Classification

To obtain optical identifications for the X-ray sources we use the precise astrometry described in Section 3. We search for optical counterparts within the 95% Chandra error circle of the source positions (see Table 1 of Elsner et al. 2008), which includes the positional uncertainty of X-ray sources reported by the wavelet source detection algorithm, the uncertainty in the X-ray bore-sight correction, and the uncertainty in the optical astrometry. Within the half-mass radius of M71, there are 29 sources detected by Chandra and we suggest optical counterparts based on positional coincidence alone to 25 of them. In case of multiple sources inside the X-ray error circle, we include all the candidates. The results of each candidate optical counterpart are summarized in Table 8.2, and finding charts are shown in Fig. 8.3 and Fig. 8.4.

The first step in classifying faint ( $L_X \leq 10^{34.5}$  ergs s $^{-1}$ ) X-ray sources is to study their X-ray properties, e.g. their X-ray luminosity and spectral behavior (see §2). The second step in the identification process can be made when the sources have other information coming from different wavelengths. The coincidence between accurate radio timing positions of millisecond pulsars and the positions of X-ray sources can provide reliable identification. In the optical band, the color-magnitude diagrams (CMDs) of globular clusters have been studied for a long time because they reflect the fundamental properties of these stars and the evolutionary stage of the globular clusters. We extract further information from the locations of the optical stars in the CMDs of Fig. 8.2. CVs usually lie much bluer than the main sequence stars in the (V, U–V) and (V, B–V) CMDs while the X-ray ABs may be located on or slightly above the main sequence or on the giant branch. Stars on the main sequence in the V vs. V–I CMD cannot be clearly classified: they could either be CVs or ABs since their optical flux is dominated by the donor stars or brighter stars of the binary systems.

The ratio of X-ray to optical flux is also useful to distinguish CVs from X-ray ABs (see Bassa et al. 2004). In Fig. 8.5 we show the X-ray luminosity as a function of the absolute magnitude for low-luminosity X-ray sources from 47 Tuc, NGC 6397, NGC 6752, M4, NGC 288, M55, NGC 6366 (data from Grindlay et al. 2001a; Edmonds et al. 2003a; Cool et al. 1998; Grindlay et al. 2001b; Taylor et al. 2001; Pooley et al. 2002; Bassa et al. 2004; Kong et al. 2006; Bassa et al. 2008), and M71. The large symbols in this figure indicate the X-ray sources with possible optical counterparts in the field of view of the Chandra observation of M71, while the smaller symbols show classified objects found in other clusters. We note that the absolute magnitudes and X-ray luminosities for the sources in the observations are computed under the assumption that they are cluster members. As discussed in Elsner et al. (2008), we caution that  $\sim 40\%$  of the 29 X-ray sources within the half-mass radius are background or foreground objects.

Now we turn to those stars unrelated to the globular clusters. Foreground stars are likely

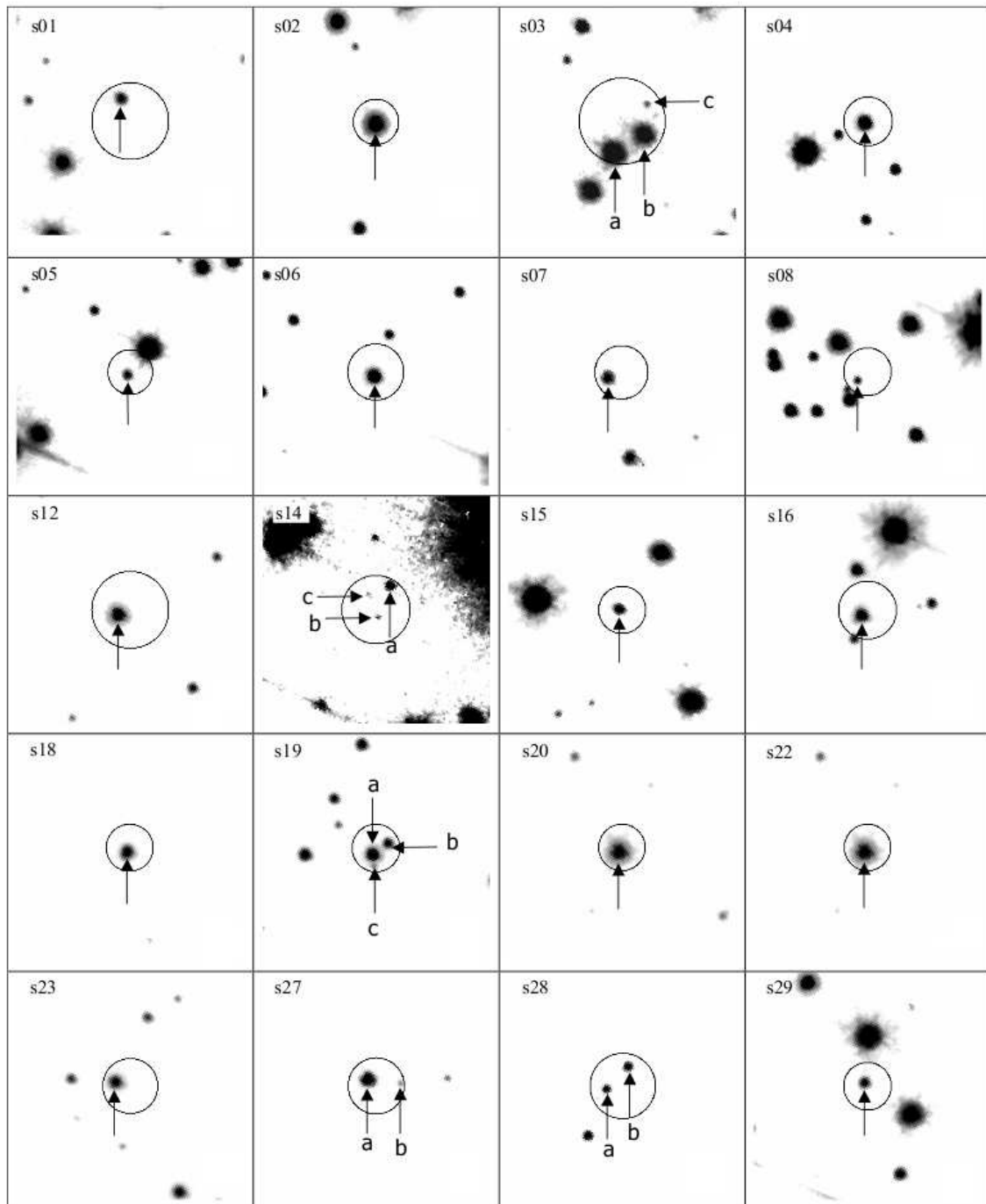


Figure 8.3:  $5'' \times 5''$  finding charts for candidate optical counterparts within the half-mass radius of M71. The finding charts are obtained from the HST/ACS  $V_{606}$  images. The 95% confidence uncertainties on the Chandra positions are overlaid on these charts, while the candidate counterparts are indicated with an arrow. The finding charts are set with their dynamic range. The greyscale of these images is chosen to enhance the visibility of the candidate counterparts. All images have North to the top and East to the left.

Table 8.2: Optical counterparts to Chandra X-ray sources within the HST/ACS field of view

X-ray Source	Offset From CXO position <sup>a</sup>		$U_{336}$ (mag)	$B_{439}$ (mag)	$V_{555}$ (mag)	$V_{606}$ (mag)	$I_{814}$ (mag)	$\log(L_X)^b$ ergs s <sup>-1</sup>	$\log(f_X/f_O)^c$	FAP <sup>d</sup>	Classification <sup>e</sup>
	$\Delta RA$ (")	$\Delta Dec$ (")									
Inside the half-mass radius											
s01	0.22	0.49	...	...	...	20.85(0)	19.94(2)	29.85	-2.02	26.06	AB?
s02	0.0	-0.05	...	...	...	17.38(1)	16.32(1)	31.18	-2.08	1.08	AB
s03a	0.18	-0.69	18.68(6)	18.35(4)	17.78(4)	18.33(1)	17.56(0)	29.95	-2.93	7.01	AB?
s03b	-0.50	-0.29	19.32(9)	19.09(4)	18.44(4)	18.90(1)	18.11(0)	29.95	-2.70	10.36	AB?
s03c	-0.57	0.37	x <sup>g</sup>	x	x	23.8(1)	22.81(6)	29.95	-0.76	37.35	CV/AGN?
s04	0.07	-0.02	...	...	...	16.92(1)	16.01(1)	30.63	-2.82	0.73	AB?
s05	0.06	-0.05	...	...	...	22.42(5)	21.79(0)	31.61	0.37	11.98	CV/AGN?
s06	0.04	-0.08	...	...	...	17.74(1)	16.91(1)	30.15	-2.96	2.67	AB?
s07	0.33	-0.11	16.26(2)	15.16(5)	14.30(5)	14.86(0)	13.89(0)	30.31	-3.96	0.25	AB?
s08	0.24	-0.17	x	x	x	21.48(2)	19.96(1)	30.78	-0.84	11.31	MSP
s10	0.27	0.05	x	x	x	25.25(6)	23.4(1)	30.37	0.26	21.96	CV/AGN?
s12	0.28	-0.10	16.40(2)	15.60(3)	14.93(3)	15.55(0)	14.82(0)	29.88	-4.11	0.72	AB?
s14a	-0.29	0.54	x	x	x	23.47(6)	20.87(2)	30.03	-0.80	33.60	F?
s14b	-0.04	-0.18	x	x	x	25.8(1)	28(2)	30.03	0.12	48.35	CV/AGN?
s14c	0.18	0.36	x	x	x	26.4(2)	23.46(6)	30.03	0.36	51.13	CV/AGN?
s15	0.10	0.06	...	...	...	21.06(6)	19.98(4)	31.0	-0.79	10.37	CV/AB?
s16	0.15	-0.09	19.9(1)	18.62(4)	17.55(3)	17.95(1)	16.88(0)	30.15	-2.88	3.44	F?
s18	0.08	-0.08	17.25(3)	16.96(6)	16.28(6)	16.69(1)	15.92(1)	30.77	-2.77	0.58	AB
s19a	0.08	-0.12	18.20(5)	17.79(3)	16.99(3)	17.39(0)	16.50(0)	30.95	-2.30	1.16	AB?
s19b	-0.28	0.10	19.52(9)	18.93(4)	18.32(4)	18.83(1)	18.05(1)	30.95	-1.73	4.62	AB?
s19c	0.18	0.36	x	x	x	21.48(1)	20.04(2)	30.95	-0.66	11.33	AB?
s20	0.08	-0.07	16.16(2)	15.21(3)	14.18(4)	14.65(0)	13.61(0)	31.18	-3.17	0.16	AB
s21	0.17	-0.15	x	x	x	27.09(9)	26.5(3)	29.99	0.61	42.03	CV/AGN?
s22	0.14	-0.15	19.01(7)	18.22(5)	17.52(3)	18.03(0)	17.22(1)	30.02	-2.98	5.48	F?
s23	0.32	0.09	18.11(5)	17.75(3)	17.19(3)	17.73(1)	16.73(1)	30.22	-2.91	2.49	AB?
s24	0.21	0.05	x	20.3(1)	19.13(4)	19.4(1)	18.16(1)	30.02	-2.43	9.81	F
s25	0.08	0.06	x	x	x	25.49(8)	23.3(1)	30.03	0.01	30.34	CV/AGN?
s26	-0.07	-0.08	...	19.3(2)	18.33(7)	18.63(7)	17.50(3)	30.66	-2.10	4.88	F
s27a	0.19	0.17	16.06(2)	15.15(4)	14.23(4)	14.68(0)	13.70(0)	30.22	-4.12	0.24	AB?
s27b	-0.57	0.06	19.18(8)	18.41(3)	17.73(3)	18.19(1)	17.45(1)	30.22	-2.72	4.09	AB?
s28a	0.35	-0.06	x	...	...	20.67(0)	18.81(0)	29.99	-1.96	17.96	F?
s28b	-0.15	0.44	x	...	...	20.28(1)	19.28(1)	29.99	-2.11	16.12	AB?
s29	0.05	0.06	21.0(2)	...	20.9(2)	21.44(1)	20.76(1)	30.85	-0.79	11.20	CV
Outside the half-mass radius											
s41	0.13	-0.12	...	...	...	21.53(1)	20.77(1)	30.69	-0.91	14.47	CV/AGN?
s49a	-0.24	0.09	...	19.87(7)	18.49(3)	18.74(1)	16.72(1)	30.13	-2.59	9.43	F
s49b	-0.31	-0.38	...	x	x	20.93(2)	18.35(1)	30.12	-1.71	21.64	F
s54a	0.68	0.20	...	...	...	15.36(0)	14.46(0)	30.62	-3.45	0.65 <sup>h</sup>	AB?
s54b	-0.23	-0.05	...	...	...	21.46(1)	20.72(1)	30.62	-1.01	19.76 <sup>h</sup>	CV/AGN?

<sup>a</sup>The position offsets of sources detected in the  $V_{606}$  band are given relative to their Chandra positions (see Elsner et al. 2008 for details)

<sup>b</sup> $L_X$ : unabsorbed X-ray luminosity in the energy band is 0.5–2.5 keV (see Table 5 of Elsner et al. 2008)

<sup>c</sup>Ratio of X-ray to optical ( $V_{606}$ ) flux is computed by using  $\log(f_X/f_O) = \log f_X + 0.4V_{606} + 5.07$ ;  $f_X$  is derived in the 0.5–2.5 keV band.

<sup>d</sup>FAP: False Alarm Probability (%). The probability of a chance coincidence in % is calculated from  $P_{\text{coinc}} = N(< m)\pi r_{95}^2/A_{\text{search}}$  (see §6.1 of Elsner et al. 2008). The search area,  $A_{\text{search}}$ , is the central region of M71 with the radius of  $2'$  (see Anderson et al. 2008) and the considered magnitude,  $m$ , is  $V_{606}$  band magnitude.

<sup>e</sup>MSP: millisecond pulsar; CV: cataclysmic variable; AB: X-ray active binary; AGN: active galactic nucleus; F: foreground source; ?: all cases where we are not certain about the nature of the X-ray source.

<sup>f</sup>Sources lying outside the field-of-view of the WFPC2 chips do not have F336W, F439W or F555W data

<sup>g</sup>Under detection limit.

<sup>h</sup>Since the source is outside the searching region of the  $2'$ -radius central circle (Anderson et al. 2008), the  $A_{\text{search}}$  for the probability of a chance coincidence is calculated with the HST/ACS field of view, i.e.  $202'' \times 202''$ .

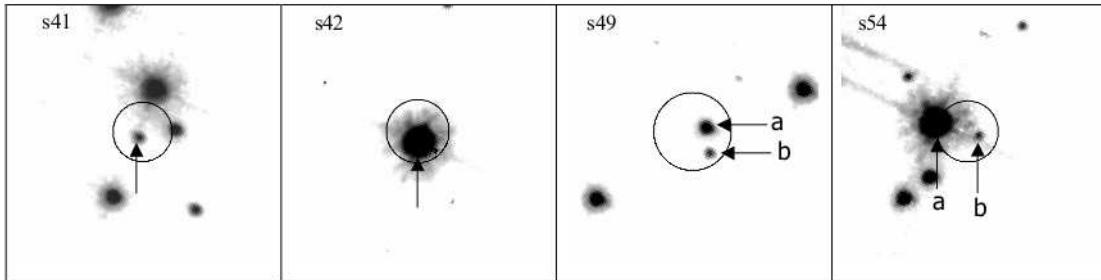


Figure 8.4:  $5'' \times 5''$  finding charts for candidate optical counterparts outside the half-mass radius of M71. The finding charts are obtained from the HST/ACS  $V_{606}$  images. The 95% confidence uncertainties on the Chandra positions are overlaid on these charts, while the candidate counterparts are indicated with an arrow. The finding charts are set with their dynamic range. The greyscale of these images is chosen to enhance the visibility of the candidate counterparts. All images have North to the top and East to the left.

to have counterparts not on the main sequence, have soft spectra, and have low  $f_X/f_0$  ratios (Krautter et al. 1999). For background active galactic nuclei (AGN), they will also have counterparts not on the main sequence, but with hard spectra; their  $f_X/f_0$  ratios can be high (Krautter et al. 1999). However, the AGN won't necessarily be detected at all; in some cases, the only object in an error circle may be a cluster main-sequence star that is not related to the X-ray source.

We first consider those X-ray sources with only one suggested counterpart in the Chandra error circle. S08 is a known millisecond pulsar, PSR J1953+1846A = M71A, with a spin period of 4.89 ms. It is in a 4.24 hr eclipsing binary system with a low-mass ( $\geq 0.032 M_\odot$ ) companion. It was discovered with Arecibo (Ransom et al. 2003, 2005; Hessels et al. 2007) and its radio emission is partially eclipsed in the orbital phase interval 0.18 – 0.36 for approximately 20% of each orbit (Hessels et al. 2007). The X-ray counterpart was detected by Elsner et al. (2008). Within the Chandra error circle we find a possible optical counterpart of this pulsar in the  $V_{606}$  and  $I_{814}$  band. The candidate optical counterpart to s08 lies on the main sequence in our V-I CMD with an absolute magnitude  $M_V \sim 8.5$ , which implies that it has a mass of about  $0.5 M_\odot$ . The radio timing indicates a minimum mass of  $0.03 M_\odot$  (Hessels et al. 2007) for the companion star. In order to allow for such a massive companion (i.e.  $\sim 0.5 M_\odot$ ), conceivably the orbit could be seen nearly face-on (within 4 degrees). However, in that (extremely unlikely) case we do not expect regular radio eclipses, as are observed. M71A's radio properties are very similar to those of other very low-mass binary pulsars such as PSR J1701–3006E (M62E, Freire 2005), and therefore we conclude that M71A's companion is not this star. Although this star's position agrees within  $0'.1$  with M71A's position from radio timing (I. Stairs 2009, private comm.), transferred with  $0'.1$  accuracy ( $1\sigma$ ) onto the 2MASS frame (Skrutskie et al. 2006), this could be coincidence due to the crowding in this field (Fig. 8.3); alternatively, M71A could be a hierarchical triple system. Future radio timing may determine this.

The star in the error circle of s02 is nearly located on the main-sequence turn-off point

(MSTO) in the (V, V-I) CMD of Fig. 8.2 and slightly below the subgiant branch, which is similar to the “red straggler” active binaries seen as X-ray sources in other clusters (Albrow et al. 2001; Edmonds et al. 2003a,b; Bassa et al. 2008). Its ratio of the X-ray to optical flux locates in the region of ABs in Fig. 8.5. Since s02 has a soft spectrum and shows significant time variability in the X-ray band (Elsner et al. 2008) we suggest that s02 is a chromospherically AB and its temporal variation can be explained as flaring on the coronally active star. S04 and s18 are also believed to be in the same group as ABs since both of them are located slightly above the main-sequence turn-off point, have soft X-ray spectra, and have lower X-ray to optical flux ratios.

S05 is the brightest X-ray source within the half-mass radius of M71. It is worth noting that s05 is the only X-ray source detected with ROSAT (Panzer et al. 2003; Elsner et al. 2008) inside the half-mass radius. Its optical counterpart is bluer than the main-sequence, and it has a relatively high X-ray luminosity ( $L_X \sim 4 \times 10^{31}$  ergs  $s^{-1}$ ). It is unlikely to be an AB. Its X-ray spectrum is too hard to consider it as a quiescent low-mass X-ray binary (qLMXB). S05 gives a bremsstrahlung temperature consistent with  $\sim 10$  keV, as appropriate for luminous magnetic CVs (Eracleous et al. 1991; Mukai 2003). During the 52.4 ks observation time, it is not consistent with being steady at 99.9% confidence. We suggest that a CV interpretation is plausible. In addition, s05 has a high value of  $\log(f_X/f_O) \sim 0.37$  and the blue color, which implies this source could be a background AGN. However, the power-law fit of its X-ray spectrum, with photon index  $\Gamma = 1.55 \pm 0.1$ , might be considered as arising from the intra-binary shock formed due to interaction between the relativistic pulsar wind and material from its companion star. An irradiated main-sequence companion could be this blue; e.g. 47 Tuc W (Bogdanov et al. 2005). MSPs with main-sequence companions of the mass of  $\sim 0.5M_\odot$  have not yet been detected, but may well be hidden from radio detection by clouds of ionized gas from the companion (e.g. Freire et al. 2004). Therefore, we cannot rule out the interpretation that it is a binary MSP system though this unusual scenario must be judged unlikely.

The candidate cluster counterpart to s29 has ultraviolet excess with respect to the main sequence (Fig. 8.2) and has a high X-ray to optical flux ratio. The source can be well fitted with a power-law model with a photon index of  $\Gamma = 1.29 \pm 0.4$ , and its X-ray luminosity is  $L_{X,0.3-8.0 \text{ keV}} \sim 2.1 \times 10^{31}$  ergs  $s^{-1}$ . Its U-V color is far too blue to be an AB while the optical color is redder, almost on the main sequence. That indicates s29 is a CV with two spectral components, a blue disk and a red companion star.

Source s15 is a good AB candidate since there is no evidence for a blue color in the VI CMD and it has a soft X-ray spectrum ( $f_{0.5-2.0 \text{ keV}}/f_{2.0-6.0 \text{ keV}} \geq 1$ ). On the other hand, without the information from the U-V or B-V color, a CV interpretation is still plausible. Its relatively high value of  $\log(f_X/f_O) \sim -0.79$  suggests that s15 could be a CV, although it doesn't rule out an AB.

The star in the error circle of s20 lies on the giant branch and has a soft X-ray spectrum, which gives strong evidence that it is a chromospherically active binary containing a giant star (i.e., a RS CVn system). Its temporal variation in the X-ray band (Elsner et al. 2008) can be explained by magnetic activity. Since s07 and s12 are located on the giant branch and have relatively low X-ray to optical flux ratios, we believe that they are likely RS CVn systems as well.

The optical counterparts associated with those X-ray sources having lower photon statistics,

s01, s06, and s23, are located on the main-sequence and have lower X-ray to optical flux ratios. We then consider that all of them may be X-ray ABs. S22 exhibits rather interesting colors. In the V–I CMD it is on the main sequence, but as we shift to progressively bluer colors its color gets redder and redder while in the U–V CMD it is way off the main sequence. Thus we suggest that it is either a foreground or background source, not associated with M71.

We turn now to the sources with more than one possible counterpart in the error circle. We find two or three possible optical counterparts within each of the Chandra error circles for s03, s14, s19, s27, and s28. S03a and s03b both fall on the main-sequence in the (V, U–V), (V, B–V), and (V, V–I) CMDs. Their colors and low X-ray to optical flux ratios suggest that either s03a or s03b is a chromospherically AB. However, the blue color and the relatively high X-ray to optical flux ratio of s03c indicates that it is a CV or a background AGN. S14a and s28a are located far from the main sequence, suggesting that they do not belong to M71, while s28b located on the main sequence could be an active binary system since it has the relatively low X-ray to optical flux ratio. In Fig. 8.3, we find two additional possible optical counterparts, s14b and s14c, within the Chandra error circle of s14, which are fainter than the  $5\text{-}\sigma$  limiting magnitudes of  $V_{606}$  and  $I_{814}$ . Based on the blue color and the high value of  $f_x/f_o$ , s14b could be either a CV or a background AGN. The optical-faint source s14c is located near the downward-extended part of the main sequence, suggesting that it could be a main-sequence star. However, it is located in the  $L_x$  vs.  $M_V$  diagram in a region where no authentic cluster members have been found if we compute its X-ray luminosity and absolute magnitude under the assumption that it belongs to M71. We then rule out the AB interpretation. Therefore, due to its high X-ray to optical flux ratio of this source, s14c is considered as either a good candidate for background AGN with a optically faint object inside the error circle not related to the X-ray source or a CV candidate with a secondary star that dominates the optical flux in the (V, V–I) CMD. There are three optical counterparts within the Chandra error circle of s19. The position of s19a is near the MSTO point and slightly below the subgiant branch, which is similar to the case of s02, while s19b is located on the main sequence. Both of their X-ray to optical flux ratios are located in the region that is primarily populated by ABs (Fig. 8.5). For the third optical counterpart, s19c, its location in the VI CMD and soft X-ray spectrum indicate that s19c is an active binary as well. However, without the information from the UV color we cannot eliminate the CV interpretation due to its relatively high X-ray to optical flux ratio, which is similar to the case of s15. We suggest that s19a is the most likely counterpart, as red stragglers are very often associated with X-ray sources (e.g. Heinke et al. 2005). According to the positions of two possible optical counterparts to s27 in the CMDs and in the absolute magnitude vs. X-ray luminosity diagram, we believe that either s27a or s27b is likely to be an active binary.

The optical counterparts of s16, s24, and s26 are located further above or to the right of the main sequence than the binary sequence. Hence we believe that they are foreground objects and unrelated to M71. The positions of two faint optical counterparts to s10 and s25 in the (V, V–I) CMD and their relatively high X-ray to optical flux ratios are very similar to the case of s14c so that s10 and s25 could be either CVs or background AGN. The highest X-ray to optical flux ratio among 39 possible counterparts and blue color suggests that s21 is the most likely background AGN although we cannot eliminate the interpretation of a CV. Furthermore, the regions of the

X-ray sources, s09, s11, s13, and s17, were also observed with the HST/WFPC2 and ACS, but we do not find any optical counterparts inside their Chandra error circles. If we set the  $5\text{-}\sigma$  limiting magnitude of  $V_{606} = 25.17$  as the upper limit for these sources, their X-ray to optical flux ratios fall on a range of  $\sim 0.2\text{--}0.6$ , which are higher than the highest  $\log(f_x/f_o)$  value known for an AB in a cluster, e.g. W64 in 47 Tuc (Edmonds et al. 2003a). Therefore, an AB interpretation can be rejected. If we take their X-ray colors into account, s11 and s17 are located near the bottom-right corner and close to the position of s40 in the X-ray color-color diagram shown in Fig. 4 of Elsner et al. (2008), which implies they have very hard spectra with over half of their counts above 2 keV. This infers a high intrinsic  $N_H$ , which strongly suggests that these are background AGN. For the other three sources with medium X-ray colors, we then tentatively classify them all as CVs, MSPs, or background AGN, though AGN are probably the most likely category.

Outside the half-mass radius of M71, we find 6 optical counterparts to X-ray sources, s41, s42, s49 and s54 in the ACS field-of-view. The candidate counterpart to s42, located on the edge of the ACS, is saturated in the optical band, which prevents us from obtaining a reliable magnitude of this optical source or searching for any other faint optical sources inside the Chandra error circle. There are 2 possible optical counterparts to s49. Both of them are located far from the main sequence, hence we suggest that they are not associated with M71. Inside the error circle of s54, the brighter object s54a is on the giant branch while the fainter one, s54b, is located blueward of the main sequence in the CMD and has a relatively high X-ray to optical flux ratio, suggesting that s54b might be a CV. However, s54b lies on the spikes produced by s54a, which prevents us from obtaining an accurate magnitude for s54b. S41's color is bluer than the main sequence, and its X-ray to optical flux ratio is higher than that of an AB. We then suggest that s41 is a CV candidate. Furthermore, a background AGN scenario is also plausible for s41 and s54b due to their blue colors, high  $\log(f_x/f_o)$  values, and their locations outside the half-mass radius of M71, where they are more likely to be background sources.

## 8.6 Summary and Discussion

In summary, we find one certain CV (s29), seven possible candidate CVs (s05, s10, s14, s21, s25, s41, and s54), and two certain ABs (s02 and s20) and 12 good candidate ABs (s01, s03, s04, s06, s07, s12, s15, s18, s19, s23, s27, and s28) in the globular cluster M71. Some of our candidate CVs (and/or candidate ABs) might be MSPs in binary systems or AGN, which often (but not always) show blue colors.

To interpret our results, understanding how many of our objects are likely false matches will be critical. We calculated the expected number of false matches in several ways. First, we shifted all our X-ray source positions by  $9''$  and  $18''$  (somewhat arbitrary, but chosen to be larger than the largest uncertainties) in four directions, and searched for matches against the  $V_{606}$  frame. From this exercise, we expect  $11_{-8}^{+4}$  false matches among our 39 possible matches, indicating that  $\geq 70\%$  of the 34 total X-ray sources in our field of view have a true match. By chance, then, 70% of our false matches should occur with sources which have a true match—suggesting that  $\sim 7.7$  sources should have two possible optical counterparts. We see seven sources that have two

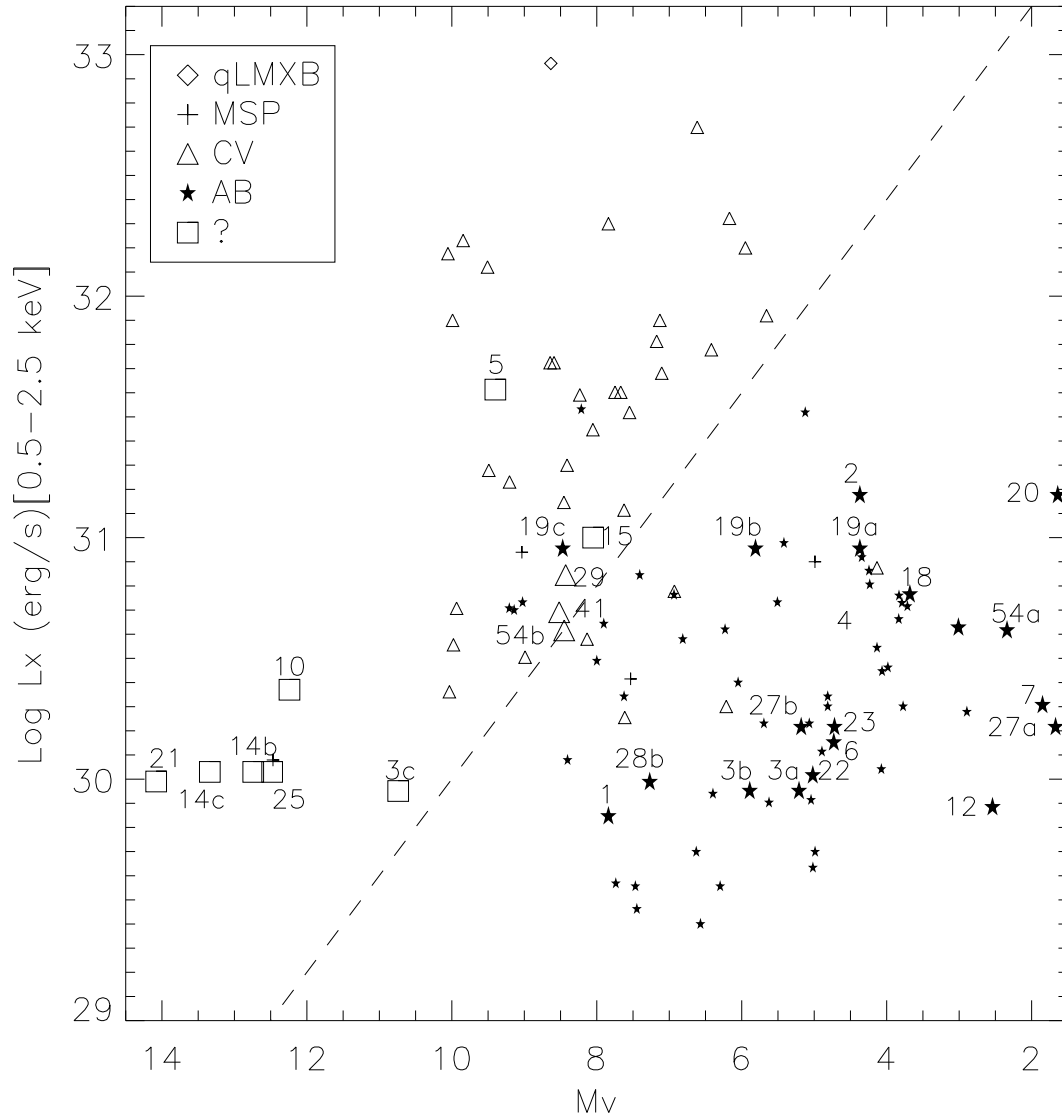


Figure 8.5: X-ray luminosity as a function of absolute magnitude, for low-luminosity X-ray sources in globular clusters. Five types of X-ray sources are shown, qLMXBs (diamonds), MSPs (crosses), CVs (triangles), ABs (stars), and unclassified sources (squares). The larger and numbered symbols in this figure correspond to the optically identified X-ray sources in the field of view of the Chandra observation of M71, where we compute absolute magnitude and X-ray luminosity under the assumption that the sources are associated with M71. The smaller symbols in this figure indicate objects found in other clusters, i.e. 47 Tuc, NGC 6397, NGC 6752, M4, NGC 288, M55, and NGC 6366. We note that ambiguous sources coming from other clusters were discarded in this figure. The dashed line of constant X-ray to optical flux ratio given by  $\log L_{X,0.5-2.5 \text{ keV}}(\text{ergs s}^{-1}) = 34.0 - 0.4 M_V$  (after Bassa et al. 2004) roughly separates CVs from ABs.

or more possible  $V_{606}$  counterparts, which is nicely consistent.

In order to know which sources are more likely to have false matches, we calculated the probability of a chance coincidence in % shown in Col. 10 of Table 8.2 by using Eq. (3) from Elsner et al. (2008) (see also Verbunt et al. 2008). Within the half-mass radius, there are 6 sources with a false alarm probability smaller than 1%, which indicates that those associations between X-ray sources and optical counterparts have a >99% confidence level. Adding up the false alarm probabilities gives a total expected number of false matches of  $\sim 5$ , which is consistent with the expectation of  $11_{-8}^{+4}$  false matches above. Among the 10 X-ray sources with optical counterparts and  $L_{X,0.5-6.0 \text{ keV}} > 4 \times 10^{30} \text{ ergs s}^{-1}$ , adding the false alarm probabilities indicates that roughly one of them is expected to be a false match. (Note that we believe s08 to be a false match, but to be a true cluster member; and that s19 has three potential counterparts.)

Inside the half-mass radius of M71, we find 14 X-ray sources with  $L_{X,0.5-6.0 \text{ keV}} > 4 \times 10^{30} \text{ ergs s}^{-1}$ , of which 10 have optical counterparts. Assuming that all X-ray sources outside the half-mass radius are fore- or background sources, we can estimate that  $\sim 3.7_{-1.8}^{+3.1}$  X-ray sources among 14 are unrelated to M71. The error quote here is from the Poisson statistic (Gehrels 1986). This is consistent with our estimate above that we have identified true optical counterparts for  $\sim 9$  X-ray sources.

Pooley et al. (2003) have shown that for 12 globular clusters observed by Chandra, the number of globular cluster X-ray sources which are above the lower limit of  $4 \times 10^{30} \text{ ergs s}^{-1}$  (0.5–6 keV) can be approximately linearly fitted with the predicted stellar encounter rate  $\Gamma' \propto \rho_o^{1.5} r_c^2 \equiv \Gamma$ , where  $\Gamma$  is referred to as the collision number (Verbunt 2003). Here  $\rho_o$  is the central density of the cluster, and  $r_c$  is the core radius. In order to examine if M71 fits this relation we compare its number of X-ray sources and its collision number  $\Gamma$  with those of some other clusters, NGC 6266, 47 Tuc, M28, M4, NGC 6366, M55, and NGC 288 (see Fig. 8.6), using the parameters listed in Table 8.3. We note that the core-collapsed globular clusters are not considered in our study since their core parameters are generally uncertain, introducing strong uncertainties into interaction rates derived from those parameters. The encounter number for M71 is  $\sim 230$  and  $\sim 10$  times smaller than those of 47 Tuc and M4, respectively. Pooley et al. (2003) reports  $41 \pm 2$  sources above the lower luminosity limit in 47 Tuc, which are revised by Heinke et al. (2005) to  $63 \pm 4$  (for a distance of 4.5 kpc); the uncertainty is due to the estimated number of background sources. Thus, if the number of sources scales with the encounter rate, the presence of  $\sim 10 \pm 3$  sources with  $L_{X,0.5-6.0 \text{ keV}} > 4 \times 10^{30} \text{ ergs s}^{-1}$  in M71 is a very significant overabundance, even if we take into account the errors due to Poissonian fluctuations. The same conclusion is reached on the basis of comparison with any other globular clusters listed in Table 8.3 except for M55 and NGC 288, in which the number of the X-ray sources is also in excess of the predicted value. This indicates that most of the sources in M71, M55, and NGC 288 are not formed via stellar encounters.

As suggested by Verbunt (2002), ABs are most likely primordial binaries, and thus to first order their numbers should scale with mass. Following Kong et al. (2006), we calculated the half masses with  $10^{-0.4M_v}$ , assuming the visual mass-to-light ratio is the same for all clusters listed in Table 8.3. M71 has the lowest half-mass, containing only  $\sim 30\%$  of the mass within the half-mass

Table 8.3: Scaling parameters of NGC 6266, 47 Tuc, M28, M4, M71, NGC 6366, M55, and NGC 288

(1) Cluster	(2) $\log \rho_0$ ( $L_\odot \text{pc}^{-3}$ )	(3) $r_c$ (")	(4) $d$ (kpc)	(5) $M_V$	(6) $\Gamma$	(7) $M_h$	(8) Source	(9) Background	(10) Member	(11) IDs.	(12) Reference <sup>a</sup>
NGC 6266	5.14	10.8	6.9	-9.19	37.07	8.24	51	2-3	48-49	2 <sup>c</sup>	1,2,3
47 Tuc	4.81	24.0	4.5	-9.4	24.91	10.0	79	~16	63±4	53-63	4
M 28	4.75	14.4	5.6	-8.33	11.29	3.73	26	2-3	23-24	2 <sup>c</sup>	1,5,6
M 4	4.01	49.8	1.73	-6.9	1.0	1.0	6	1-3	3-5	5	1,7
M 71	3.05	37.8	4.0	-5.6	0.11	0.30	14	1-7	10±3	4-9	8
NGC 6366	2.42	109.8	3.6	-5.77	0.08	0.33	5	2-5	1 <sup>+2</sup> <sub>-1</sub>	~1	9
M 55	2.15	169.8	5.3	-7.6	0.18	1.82	16	5-12	8 <sup>+3</sup> <sub>-4</sub>	2-4	9
NGC 288 <sup>b</sup>	1.80	85.0	8.4	-6.7	0.03	0.83	11	4-11	4 <sup>+3</sup> <sub>-4</sub>	2-5	10

Note: Cols. 2–5 give the values for central density ( $\rho_0$ ), core-radius ( $r_c$ ), distance ( $d$ ) and absolute visual magnitude ( $M_V$ ) originate from Harris (1996, version of February 2003). For M4, the values of  $\rho_0$  and  $M_V$  are computed for the distance and reddening of Richer et al. (1997). Cols. 6 and 7 are the collision number which is computed from  $\Gamma \equiv \rho_0^{1.5} r_c^2$  and the half-mass from  $M_h \propto 10^{-0.4M_V}$  (Kong et al. 2006). Values for  $\Gamma$  and  $M_h$  are normalized to the value of M4. Col. 8 shows the total number of sources detected within the half-mass radius. Col. 9 is the number of expected fore/background sources. Col. 10 gives the number of expected cluster members plus error. Col. 11 shows the number of X-ray sources (with  $L_{X,0.5-6.0 \text{ keV}} > 4 \times 10^{30} \text{ ergs s}^{-1}$ ) which have optical or/and radio counterparts associated with the cluster, or spectrally confirmed qLMXBs. The last column gives the reference paper. These globular clusters are ordered on the central density.

a. For each cluster, the basic data for this table were extracted from: 1. Pooley et al. (2003); 2. Cocozza et al. (2008); 3. Trepl (2007); 4. Heinke et al. (2005); 5. Becker et al. (2003); 6. Becker & Hui (2007); 7. Bassa et al. (2004); 8. this work; 9. Bassa et al. (2008); 10. Kong et al. (2006).

b. NGC 288 was not observed long enough to reach this luminosity limit of  $L_X \sim 4.0 \times 10^{30} \text{ ergs s}^{-1}$  in the 0.5–6.0 keV range. Its limiting luminosity is  $\sim 5.7 \times 10^{30} \text{ ergs s}^{-1}$ . However, we keep this cluster's data, as a lower limit, since we have so few constraints on low-density clusters.

c. No information about the optical counterparts to X-ray sources.

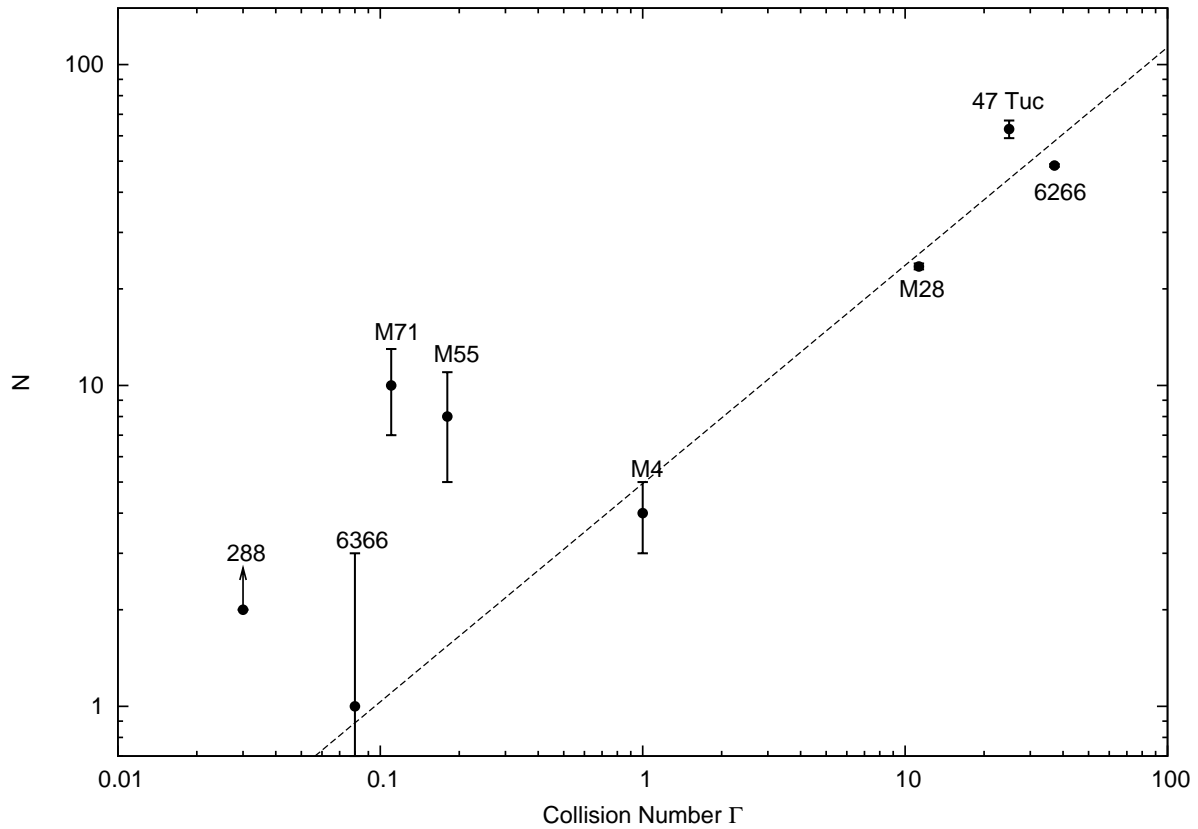


Figure 8.6: Number of globular cluster X-ray sources ( $N$ ) with  $L_{X,0.5-6.0 \text{ keV}} \geq 4 \times 10^{30} \text{ ergs s}^{-1}$  inside the half-mass radius vs. the normalized collision number  $\Gamma$  of the cluster. The dashed line indicates the best power-law fit of the data points from 47 Tuc, NGC 6266, M28, M4, and NGC 6366 (cf. Table 8.3). The relation between  $N$  and  $\Gamma$ , i.e.  $N \propto \Gamma^{0.74 \pm 0.03}$ , is consistent with the result derived from Pooley et al. (2003).

radius of M4. Scaled by mass, the predicted number of ABs with  $L_{X,0.5-6 \text{ keV}} > 4 \times 10^{30} \text{ ergs s}^{-1}$  in M71 should be similar to that of NGC 6366 and smaller than those in any other cluster shown in Table 8.3, but this is in contrast to our results.

The scaling of source number with the collision number for the sources with  $L_{X,0.5-6 \text{ keV}} > 4 \times 10^{30} \text{ ergs s}^{-1}$  suggests that CVs are mostly made via stellar encounters (Pooley et al. 2003). If we assumed that all of the CVs in M71 were formed dynamically, we would not expect to find more than one CV by scaling with the encounter numbers from any other cluster listed in Table 8.3. However, most of the globular clusters studied by Pooley et al. (2003) have high  $\Gamma$  numbers and many dynamically produced CVs. It is reasonable to suspect that primordial CVs may dominate in the low-density clusters. According to the computations by Davies (1997), a cluster core with a star density of  $1000 \text{ pc}^{-3}$  allows most of the CV progenitors to evolve into a CV. This could explain the existence of at least one (and several candidate) CVs within the half-mass radius of M71.

It is interesting to mention that in M71  $\sim 7$  optical counterparts to Chandra X-ray sources are classified as potential RS CVn systems, in which X-ray emission is produced primarily in (sub)giant flare outbursts. A couple possible RS CVn X-ray sources have been identified in 47 Tuc (Heinke et al. 2005) and  $\omega$  Centauri (Cool et al. 2002), but, besides M71, only the low-density clusters M55 and NGC 6366 (Bassa et al. 2008) have significant fractions of X-ray sources identified as possible RS CVns. Considering the even lower density case, the total X-ray luminosity of the old open cluster M67 is dominated by binaries with giants (van den Berg et al. 2004). From the ROSAT census, the X-ray emission of most globular clusters per unit mass is lower than that of the old open cluster M67 (Verbunt 2001, 2002). There are three possible explanations for this: a) M67 is a very sparse cluster, which is evaporating its lowest-mass stars (Hurley et al. 2005). Open clusters don't survive very long. As a cluster evaporates its lowest-mass stars, it tends to retain its heaviest systems—binaries—which are more likely to be X-ray sources. b) M67 is a rather young cluster. Younger stars may produce more X-rays (Randich 1997), since they tend to be rotating faster than older stars. c) A large fraction of binary systems are destroyed in globular clusters (see Ivanova et al. 2005), in particular those with longer orbits. RS CVn systems involve giants that are spun up by stellar companions. These systems must be relatively wide binaries, in order to avoid the giant swallowing its companion as it evolves; but such wide binaries are destroyed in globular clusters. Thus there are fewer RS CVn binaries in globulars. Since RS CVn binaries tend to be brighter than BY Dra binaries (main-sequence ABs), low-density clusters can have startlingly high X-ray luminosities per unit mass.

To summarize the results of this paper, the number of X-ray faint sources with  $L_{X,0.5-6 \text{ keV}} > 4 \times 10^{30} \text{ ergs s}^{-1}$  found in M71 is higher than the predicted value on the basis of either the collision frequency or the half mass. We suggest that those CVs and ABs in M71 are primordial in origin. The last interpretation above may explain the X-ray overabundance of low-density clusters like M71, where fewer primordial binaries may have been destroyed through binary interactions. Study of other low-density globular clusters will help us to better understand their evolution and dynamics.

# Chapter 9

## Conclusion and Future Prospect

In this thesis I have presented several results of investigations of millisecond pulsars in the Galactic disk and in the globular clusters and studies of X-ray sources in the globular cluster M71, which are discussed individually in the conclusion and discussion of each chapter. I emphasize below some of the important, often recurring, themes and discuss possible future directions.

### 9.1 Eclipsing Binary Pulsars

Eclipsing binary pulsars have the potential of providing a wealth of information on both the evolutionary history of isolated millisecond pulsars (MSPs) and the relativistic winds and pulse emission mechanisms of the general pulsar population. Alpar et al. (1982) and Radhakrishnan & Srinivasan (1982) proposed that MSPs could be formed through accretion from a low-mass companion on to an inert neutron star. As mass is accreted on to the neutron star, it is spun up to millisecond periods. During this accretion phase the system may be observable as a low-mass X-ray binary (LMXB). A gamma-ray flux is generated by the interaction of the magnetic field of the neutron star with the accretion disc and this can severely ablate the secondary star (Ruderman 1989). Once the accretion has stopped, the neutron star may be able to ablate its companion which has survived the LMXB phase (Rasio et al. 1989). The discovery of the “Black Widow pulsar”, PSR B1957+20 (Fruchter et al. 1988b), gave support to this formation scenario. Since then, 21 (plus one potential) other eclipsing binary pulsars have been detected (see Table 9.1). Of these systems, only two are situated in the Galactic field while the rest is located in globular clusters (GCs).

In Table 9.1, we show that there are two fundamentally different groups of eclipsing binary pulsars; separated by their companion masses. The binary systems with more massive companions ( $M_c \sim 0.1 - 0.4 M_\odot$ ) will henceforth be called eclipsing low-mass binary pulsars (ELMBPs; Freire 2005). However, the less massive eclipsing binaries consisting of a companion with the mass of  $M_c \sim 0.02 - 0.04 M_\odot$  belong to a class of objects that we will henceforth call very low-mass binary pulsars (VLMBPs; Freire 2005), also known as “black-widow” binaries. ELMBPs are believed to be formed by exchange encounters in globular clusters, and for that reason are exclusive to those environments, while VLMBPs are a product of predictable stellar evolution

in binary pulsars. This class of systems can be used to learn about the neutron star recycling fraction in the globular clusters actively forming pulsars.

Until now only less than half of these eclipsing systems have been studied in the X-ray regime (cf. Table 9.1). It is obvious that our current understanding of the X-ray emission nature of these systems is seriously biased. Therefore, it is very important to enlarge the X-ray population of them and study their emission properties. This provides the motivation for my study. In this thesis, I have reported on X-ray observations of four eclipsing millisecond pulsars in binary systems by utilizing the Chandra and XMM-Newton observatories. Two are VLMBPs, i.e. PSR B1957+20 in the field and PSR J1953+1846A in the globular cluster M71, and the others are ELMBPs, i.e. PSR J1740–5340 and PSR J1824–2452H in the globular cluster NGC 6397 and M28, respectively.

The observed non-thermal X-ray emission from these eclipsing binary systems is believed to come from the magnetosphere of the pulsar or from the intra-binary shock. On the other hand, the thermal emission is proposed to originate from the magnetic polar caps of the underlying neutron stars, heated by the backflow of energetic particles from the pulsar magnetosphere (see, e.g., Harding & Muslimov 2002; Zhang & Cheng 2003, and reference therein). Through the spectral analysis, the X-ray emission of PSR B1957+20, PSR J1953+1846A and PSR J1824–2452H is found to be non-thermal and best modeled with a single power-law spectrum, which points to an intra-binary shock origin of the X-rays. The intra-binary shock model predicts that synchrotron emission is expected to be the primary energy loss mechanism in the shock wave resulting from the interaction of the relativistic pulsar wind with the interstellar medium or with the ablated material from the companion star. This model can be used to interpret the origin of the non-pulsed non-thermal X-ray emission of PSR B1957+20. In addition, PSR J1953+1846A and PSR J1824–2452H share the non-thermal nature of their X-ray spectra with MSPs J, O and W in 47 Tuc. Bogdanov et al. (2006) suggest the X-ray emission for the three eclipsing binary originates in a shock forming from the collision of a relativistic wind from the pulsar with material from its low-mass companion, a model which is as likely to apply to PSR J1953+1846A and PSR J1824–2452H as to these 47 Tuc sources. However, the PSR J1740–5340 pulsar is bound to a peculiar “red-straggler” (sub-subgiant) companion (cf. Albrow et al. 2001; Edmonds et al. 2003a,b; Bassa et al. 2008) with the mass of  $\sim 0.2 - 0.3M_{\odot}$  in a relatively long-period binary orbit. Its X-ray spectrum can be fitted equally well by either a single power-law model or a thermal bremsstrahlung model. The possible origin of the X-ray flux was discussed in § 5.3 with three different scenarios. Besides two aforementioned possible origins of the non-thermal X-ray emission, the coronal emission from the companion star should be taken into account as well. Based on the present data, we are not able to firmly distinguish these possible contributions of X-ray emission of the binary system of PSR J1740–5340.

Interaction between the relativistic pulsar wind and the surrounding interstellar medium (ISM) is expected to create the detectable diffuse emission. In our study, such emission is only seen from the field pulsar, PSR B1957+20. The extended emission with the orientation to the north-east and the size of about 16 arcsec detected with the MOS1/2 cameras onboard the XMM-Newton is consistent with the previous result derived from the Chandra observations. The PSR B1957+20 binary system provides us with an excellent opportunity to study the wind of a recy-

Table 9.1: A set of eclipsing binary pulsars in Galactic globular clusters and in the Galactic disk. The minimum companion masses ( $m_c$ ) are calculated assuming a pulsar mass of  $1.4 M_\odot$ . All the parameters are obtained from <http://www.naic.edu/~pfreire/GCpsr.html>

Pulsar	GC, letter	P(ms)	$P_{\text{orb}}$ (days)	$m_c(M_\odot)$	X-ray detected
<b>ELMBPs</b>					
J0024–7204V	47 Tuc V (?) <sup>a</sup>	4.81	~0.2	~0.3	-
J0024–7204W	47 Tuc W	2.35	0.133	0.127	Y
J1701–3006B	M62 B	3.59	0.145	0.124	Y
B1718–19	NGC 6342 A	1004	0.258	0.117	-
J1740–5340	NGC 6397 A	3.65	1.354	0.188	Y
J1748–2021D	NGC 6440 D	13.50	0.286	0.14	-
J1748–2446A	Terzan 5 A	11.56	0.076	0.089	-
J1748–2446P	Terzan 5 P	1.73	0.363	0.44	-
J1748–2446ad	Terzan 5 ad	1.40	1.094	0.16	-
J1824–2452H	M28 H	4.63	0.435	0.20	Y
J1824–2452I	M28 I	3.93	0.459	0.20	-
J2140–2310A	M30 A	11.02	0.174	0.101	-
<b>VLMBPs</b>					
J0023–7203J	47 Tuc J	2.10	0.121	0.021	Y
J0024–7204O	47 Tuc O	2.64	0.136	0.022	Y
J0024–7204R	47 Tuc R	3.48	0.066	0.026	Y
J1518+0204C	M5 C	2.48	0.087	0.038	-
J1641+3627E	M13 E	2.49	0.117	0.02	-
J1701–3006E	M62 E	3.23	0.158	0.035	-
J1748–2446O	Terzan 5 O	1.68	0.260	0.04	-
J1953+1846A	M71 A	4.89	0.177	0.032	Y
B1957+20	(Galaxy)	1.61	0.382	0.022	Y
J2051–0827	(Galaxy)	4.51	0.099	0.027	-
J1823-3021F	NGC 6624 F	4.85	– <sup>b</sup>	– <sup>b</sup>	-

a. The eclipse of this system cannot be characterized yet.

b. Not published elsewhere.

pled neutron star. The wind is ablating, and may eventually evaporate, its low-mass companion. Ablation and heating of the companion star are believed to be caused by X- or  $\gamma$ -rays generated in an intrabinary shock between the pulsar wind and that of the companion star. Furthermore, the pulsar moves through the sky with a supersonic velocity of  $\sim 220 \text{ km s}^{-1}$ . The interaction of a relativistic wind flowing away from the pulsar with the ISM produces an  $\text{H}\alpha$  bow shock (see Figure 4.1) which was the first one seen around a recycled pulsar (Kulkarni & Hester 1988).

Now I turn to the other three binary systems located in the globular clusters. If the diffused emissions caused by the intra-binary shock do exist, we are not able to resolve them due to the limited spatial resolution. However, for PWN from the interaction with the ISM, so far we do not find any positive evidence as well. This might reflect that the emission mechanism and the surrounding environment for the MSPs in the GCs and in the Galactic plane can be quite different.

In the temporal domain, no coherent X-ray pulsations at the spin period of PSR B1957+20 was reported by using the XMM-Newton PN observations operated in the fast timing mode, which provided the evidence that the non-thermal X-rays were produced by the interaction of the pulsar wind with the binary companion or the ISM. On the other hand, given the limited timing resolution of the Chandra ACIS and XMM-Newton MOS1/2 observations with a frame time of 3.24 sec and 2.6 sec, respectively, I was refrained from searching for the spin periods of the other three MSPs.

Furthermore, the X-ray flux from the shock is expected to undergo modulations at the binary period (Arons & Tavani 1993). I have also investigated if the pulsar's X-ray emission is a function of its orbital phase by examining how significant the orbital light curve differs from a constant level for these three eclipsing binary systems. I give a detailed description for these systems in the following:

- The previous ROSAT (Kulkarni et al. 1992) and Chandra (Stappers et al. 2003) data of the PSR B1957+20 system revealed a suggestive but insignificant orbital modulation. However, in this thesis, I have reported that no variation during  $\sim 90\%$  of one binary orbit was found by using the XMM-Newton data (see Figure 4.5). The limited photon statistics and the incomplete orbital coverage prevent us from searching for the flux modulation in a fully-covered orbit.
- Setting zero binary phase using the radio ephemeris and folding with 5 phase bins at the binary period of 15.2751 ks of the PSR J1953+1846A system leads to the light curve shown in Figure 7.5. Testing this light curve using Pearson's  $\chi^2$  leads to a single trial confidence level of 2.2% for acceptance of a steady source model, providing marginal (just under  $3\sigma$ ) evidence in the X-ray band for periodicity at the radio binary period.
- The millisecond pulsar, PSR J1740–5340, has its radio emission eclipsed for  $\sim 40\%$  of its orbit which suggests the pulsar is orbiting within an extended envelope of matter released from the companion. It has long been speculated that the X-ray emission of this binary system should also vary across the orbital phase. Utilizing two archival Chandra observations of PSR J1740–5340, we have performed a systematic analysis of this binary system.

A marginal temporal variability for the whole orbit of the binary system was reported (see Figure 5.2).

- The eclipsing binary system PSR J1824–2452H in M28 has an orbit period of 10.87 h and has been observed to show radio eclipses (Bégin 2006). Inspecting the light curves may reveal a X-ray flux variability with the pulsar’s orbital motion at the  $\sim 2 - 4\sigma$  confidence level, depending on the number of phase bins used to construct the light curve (see Figure 6.11). The minimum in the X-ray light curve at the orbital phase  $\phi \sim 0.25$  can be plausibly interpreted as a geometric occultation of the shock by the companion star.

So far only the MSP W in 47 Tuc has been detected with the orbital variability in the X-ray emission (Bogdanov et al. 2005). The shape of the light curve as well as the orbital phase-resolved spectroscopy are the important tools to constrain the nature of these eclipsing binary system. A repeated coverage of the binary orbit in a longer X-ray observation and a comparison with the present data would provide us not only a better photon statistic but would also allow us to determine the emission geometry with a much higher accuracy than currently possible. Besides, further multiwavelength studies of these interesting eclipsing binary systems are required to place tighter constraints on their emission properties.

## 9.2 Millisecond Pulsars in Galactic Globular Clusters

Globular clusters have long been known to be breeding grounds for millisecond and binary pulsars (Camilo & Rasio 2005). The main reason for this is the high stellar density and high rate of stellar interaction in globular clusters relative to most of the rest of the Galaxy. As a result, low-mass X-ray binaries are almost 10 times more abundant in clusters than in the Galactic disk. In addition, exchange interactions between binary and multiple systems in the cluster can result in the formation of exotic binary systems (Nice et al. 1999). To date, searches have revealed 140 pulsars in 26 globular clusters<sup>1</sup>.

We have conveyed a systematic census of the X-ray population of radio pulsars in Galactic globular clusters by using the imaging data obtained with Chandra X-ray observatory. Among 140 pulsars, only  $\sim 20\%$  have been identified with X-ray counterparts. Therefore, our current understanding of the high-energy emission nature of the cluster pulsars is seriously prejudiced. By cross-correlating the radio timing positions of the cluster pulsars with the high resolution X-ray images, thirty-one possible X-ray counterparts have been identified in nine different globular cluster systems, including the 47 Tuc pulsar population. These include the newly identified X-ray counterparts of PSR J1824–2452G and PSR J1824–2452H in M28 and PSR J1748–2021B in NGC 6440. We have also characterized their spectral properties as well as searched for the possible temporal variability. We have found that the X-ray emission from some cluster pulsars, i.e. PSR J1740–5340 in NGC 6397, PSR J1824–2452G and J1824–2452H in M28, and PSR J1748–2021B in NGC 6440, are variable. These pulsars are in binary systems. Therefore, the variability can possibly be resulted from the intra-binary shocks.

<sup>1</sup><http://www.naic.edu/~pfreire/GCpsr.html>

Millisecond pulsars in GCs inhabit an environment with a much higher stellar density than those in the Galactic plane. Therefore, the stellar dynamical interactions in GCs are more frequent. GC millisecond pulsars can possibly change their companions a few times throughout their lives. In addition, the magnetic field structure at the neutron star surface might be influenced by the accretion (Cheng 2008), this would result in a much more complicated field structure of the millisecond pulsars in GCs than those in the disk. Therefore, the physical properties of the millisecond pulsars in the globular clusters are suspected to be different from those in the Galactic field. As an example, the X-ray emission of millisecond pulsars in the field were found to have a non-thermal component (Becker & Trümper 1997, 1999; Zavlin 2006). However, Grindlay et al. (2002) and Bogdanov et al. (2006) suggested that the X-ray spectra of most millisecond pulsars in 47 Tuc are consistent with blackbody models. In addition, Grindlay et al. (2002) suggested the X-ray conversion efficiency (i.e. the dependence of  $L_X$  on  $\dot{E}$ ) for 47 Tuc pulsars to be  $L_X \propto \dot{E}^{0.5}$ , where  $\dot{E}$  is the spin-down power of the pulsar. Such dependence is obviously shallower than the linear relation  $L_X \sim 10^{-3}\dot{E}$  found for the pulsars in the Galactic field and in the globular clusters (see Becker & Trümper 1997, 1999, 2009).

In order to better constrain the physical properties of the millisecond pulsars in the globular clusters, we have systematically studied the X-ray emission from 31 GC pulsars and re-examined the relation between the X-ray luminosity and the spin-down power of pulsar population in globular clusters by using the enlarged sample reported in this work. Their X-ray conversion efficiency was found to span a wide range, which is not consistent with the linear  $L_X - \dot{E}$  relation.

As suggested by Becker (2009), the  $L_X = 10^{-3}\dot{E}$  relation represents as an upper bound to the X-ray efficiency instead of a fixed correlation. Since the beaming correction of the X-ray luminosity is not applied, the X-ray efficiency for those faint pulsars appears to be smaller. An alternative possible reasons for the flatter  $L_X - \dot{E}$  relation for GC pulsars may be due to the lack of reliable measurement of the spin-down rate  $\dot{P}$  of many GC pulsars. This can be ascribed to two facts. First, the radio signals from these pulsars are relatively weak and therefore an accurate timing solution is difficult to obtain. Moreover, the proper motion of the GC pulsars and gravitational effect of a cluster further complicates the estimation of  $\dot{P}$ . Besides the aforementioned possibilities, the various origins of the X-ray emission for the GC pulsars may lead to this flatness of the  $L_X - \dot{E}$  relation. The X-ray emission of some GC pulsars (excluding 47 Tuc pulsars) may come from the intra-binary shock since they are located in the binary systems, which is not that case for most field pulsars.

We have also constructed the cumulative luminosity functions for the millisecond pulsar population in globular clusters as well as in the Galactic field. No significant difference between these two cumulative luminosity functions was found in our study. Therefore, we cannot conclude the discrepancy between the globular cluster pulsar population and the Galactic millisecond pulsars in terms of the current knowledge of their X-ray conversion efficiency and luminosity functions. Deeper observations of these GC pulsars may help to reduce the errors in determining their X-ray luminosities. Enlarging the X-ray population of the GC pulsars may allow us not only to study their emission properties but also to better constrain the  $L_X - \dot{E}$  relation for the GC pulsars.

Searching and studying millisecond pulsars in GCs not only provide us with the knowledge of the pulsars themselves, but also enable us to probe the interactions as well as the evolution of X-ray binaries inside the clusters. Traditional pulsar searches based on radio timing observations still play an important role in expanding the GC millisecond pulsar population. However, one should be aware of some selection effects in radio timing observations. It is difficult to detect pulsars with short spin periods, and/or with large dispersion measure, and/or in very tight binaries which have the orbital period as short as a few hours. These facts further complicate the pulsar searches. Since the signals from the GC millisecond pulsars are typically weak, the inferred pulsar parameters can possibly suffer from large errors. It is interesting to notice that the X-ray emission from a number of GC pulsars (e.g. PSR J1824–2452H in M28) reported in this thesis has already been detected before the radio pulsations were detected. This suggests that combining X-ray imaging with radio timing solution can be an efficient way for searching pulsars. With the aid of X-ray spectro-imaging analysis, not only the pulsar positions but also their emission properties can be better constrained.

### 9.3 Globular Clusters

Globular clusters provide us with unique laboratory conditions to investigate various aspects of astrophysics. Due to the high stellar densities, globular clusters have a high efficiency in producing tight binary systems, such as LMXBs, CVs, MSPs, and chromospherically ABs (e.g., RS CVn and By Dra systems), through frequent dynamical interactions. Binaries are thought to play a key role in the dynamical evolution of the clusters. One of the most powerful ways to probe their binary content is by studying the X-ray source populations.

We have observed the nearby, low-density globular cluster M71 (NGC 6838) with the Chandra X-ray Observatory to study its faint X-ray populations. Five X-ray sources were found inside the cluster core radius ( $r_h = 0'.63$ ), including the known eclipsing binary MSP PSR J1953+1846A. The X-ray light curve of the source coincident with this MSP shows marginal evidence for periodicity at the binary period of 4.2 h. Its hard X-ray spectrum and luminosity resemble those of other eclipsing binary MSPs in 47 Tuc, suggesting a similar shock origin of the X-ray emission. A further 24 X-ray sources were found within the half-mass radius ( $r_h = 1'.65$ ), reaching to a limiting luminosity of  $1.5 \times 10^{30}$  ergs  $s^{-1}$  (0.3–8 keV). From a radial distribution analysis, we found that  $18 \pm 6$  of these 29 sources are associated with M71, somewhat more than predicted, and that  $11 \pm 6$  are background sources, both galactic and extragalactic.

We have also reported on archival Hubble Space Telescope observations of M71. Inside the half-mass radius of M71, we found 33 candidate optical counterparts to 25 out of 29 Chandra X-ray sources. Outside the half-mass radius, 6 possible optical counterparts to 4 X-ray sources were detected. Based on the X-ray and optical properties of the identifications, we found 1 certain and 7 candidate CVs. We have also classified 2 and 12 X-ray sources as certain and potential chromospherically ABs, respectively. The only star in the error circle of the known MSP is inconsistent with being the optical counterpart. The number of X-ray faint sources with  $L_X > 4 \times 10^{30}$  ergs  $s^{-1}$  (0.5–6.0 keV) found in M71 is higher than extrapolations from other

clusters on the basis of either collision frequency or mass. Since the core density of M71 is relatively low, fewer primordial binaries may have been destroyed through binary interactions. We then suggest that those CVs and ABs in M71 are primordial in origin. This interpretation may also explain the X-ray overabundance of low-density clusters, e.g., NGC 288, M55, and NGC 6366. Study of other low-density globular clusters will help us to better understand their evolution and dynamics.

## 9.4 Future Prospects

After four decades of studies of neutron stars, still a lot of questions remain unanswered. In this section, I point out some questions raised by the studies presented in this thesis and also briefly discuss the feasibilities of the future astronomical facilities in answering these questions.

Pulsars, in general, have long been known to have space velocities at least an order of magnitude larger than those of their main sequence progenitors, which have typical values between 10 and 50 km s<sup>-1</sup>. The first direct evidence for large velocities came from optical observations of the Crab pulsar (Trimble 1968), showing that the neutron star has a velocity in excess of 100 km s<sup>-1</sup>. Proper motions for 233 pulsars have subsequently been measured largely by radio timing and interferometric techniques (Lyne et al. 1982; Bailes et al. 1990; Fomalont et al. 1992; Harrison et al. 1993; Hobbs et al. 2005; Zou et al. 2005). These data imply a broad velocity spectrum ranging from 0 to over 1000 km s<sup>-1</sup> (Lyne & Lorimer 1994). Such large velocities are given the violent conditions under which neutron stars are formed. Shklovskii (1970) demonstrated that, if the explosion is only slightly asymmetric, an impulsive “kick” velocity of up to 1000 km s<sup>-1</sup> can be imparted to the neutron star. In addition, if the neutron star progenitor was a member of a binary system prior to the explosion, the pre-supernova orbital velocity will also contribute to the resulting speed of the newly-formed pulsar. The relative contributions of these two factors to the overall pulsar birth velocity distribution is currently not well understood.

The distribution of pulsar velocities has a high velocity component with the mean transverse velocity ( $V_T$ ) of  $246 \pm 22$  km s<sup>-1</sup> for the normal pulsars (Lyne & Lorimer 1994; Hobbs et al. 2005; Faucher-Giguère & Kaspi 2006), and a lower velocity component from binary and millisecond pulsars with the averaged value of  $V_T = 83 \pm 13$  km s<sup>-1</sup> (Lorimer 1995; Cordes & Chernoff 1997; Lyne et al. 1998; Hobbs et al. 2005). One reason for the lower velocities appears to be that, in order to survive and subsequently form recycled pulsars through the accretion process, the binary systems contain only those neutron stars with lower birth velocities. In addition, the surviving neutron star has to pull the companion along with it, thus slowing the system down. However, the average escape velocity for the MSPs in globular clusters are even lower than the field MSPs. A question may be raised if the formation of these MSPs in GCs is different from those in the Galactic plane, i.e. if most of the neutron stars in GCs were formed via accretion-induced supernovae with typical natal kicks smaller than in core-collapse supernovae that produce the majority of neutron stars in the Galactic field.

A natural explanation for those pulsar with the space velocity of a few tens to well over 1000 km s<sup>-1</sup> is that supernova explosions are asymmetric, and provide kicks to nascent neutron

stars. While the evidence for such kicks is unequivocal, the physical origin remains unclear. A natal kick could be generated by an asymmetric explosion due to global hydrodynamical perturbations in the supernova core, asymmetric neutrino emission in the presence of superstrong magnetic fields ( $B \gtrsim 10^{15}$  G) in the proto-neutron star, or asymmetric electromagnetic radiation from an off-centered dipole in a rapidly rotating pulsar (see Lai et al. 2001, and reference therein). Johnston et al. (2005, 2007) and Rankin (2007) found strong evidence for an alignment between the spin axis and the velocity vector at birth from analyses of proper motion and polarization data, which further implies that slow moving pulsars may not be aligned, whereas fast moving pulsars should have their spin and velocity vectors aligned. More proper motions will become available in the next few years both from interferometry and from timing. The Jodrell Bank data archive will be able to provide values or limits on the proper motions of many hundreds of pulsars in the near future. These will further improve the constraints on the distribution and origin of pulsar velocities.

Searching and studying MSPs in GCs not only provides us with the information of the physical properties and emission mechanism of the pulsars themselves, but also enable us to probe the stellar interactions inside the globular clusters so as to better understand the dynamics of the globular cluster. So far only  $\sim 20\%$  of the 140 radio pulsars in 26 globular clusters have been identified with X-ray counterparts. Our current understanding of the high-energy emission nature of the cluster pulsars is limited. Therefore, extensive surveys are necessary.

Traditional pulsar searches are based on the radio timing observations. These studies have successfully expanded the populations of the GC MSPs. However, some limitations of timing observations indeed exist. Pulsars with very short spin periods, with large dispersion measure and within very tight binaries are very difficult to be detected. The fitted parameters, including the positions, inferred from minimizing the pulse arrival-time residuals can possibly suffer from large errors since the signals from the GC MSPs are typically weak. The case of PSR J1824–2452H in M28 mentioned in the Section 9.2 suggests that combining X-ray imaging with radio timing can probably open another window to search for pulsars in GCs.

Pulsar astronomy remains an extremely active area of modern astrophysics and the next decade will undoubtedly continue to produce new results from currently known objects as well as new surprises. In the coming decades, all-sky surveys will be performed from radio to  $\gamma$ -rays. These surveys will have unprecedented sensitivities and take astronomers to leap further. In the radio band, the Square Kilometer Array (SKA) and the LOw Frequency ARray (LOFAR) will ultimately provide a far more complete census of the Galactic pulsar population in our Galaxy. Simulations suggest (Smits et al. 2008) that at least 14000 normal pulsars and  $\sim 6000$  millisecond pulsars could be detected with SKA in the blind survey. With the huge collecting power and better sensitivities up to 15 keV, the all-sky survey performed with eROSITA is expected to expand the X-ray populations of neutron stars. The successful launch of the *Fermi* Gamma-Ray Space Telescope (formerly the *Gamma-Ray Large Area Space Telescope*, or GLAST) on June 11, 2008 has led us into a new era of high energy astrophysics. The Large Area Telescope (LAT) onboard the *Fermi* Telescope has much better sensitivity and time resolution than its predecessor, the Energetic Gamma-Ray Experiment Telescope (EGRET) onboard the *Compton Gamma-Ray Observatory* (CGRO), making it to be very efficient in pulsar search. With all the upcoming

missions, a new and full exploration of the neutron stars is about to start.

# Bibliography

- Albrow, M. D., Gilliland, R. L., Brown, T. M., et al. 2001, *ApJ*, 559, 1060
- Aldcroft, T. L., Karovska, M., Cresitello-Dittmar, M. L., Cameron, R. A., & Markevitch, M. L. 2000, in Presented at the Society of Photo-Optical Instrumentation Engineers (SPIE) Conference, Vol. 4012, Proc. SPIE Vol. 4012, p. 650-657, X-Ray Optics, Instruments, and Missions III, Joachim E. Truemper; Bernd Aschenbach; Eds., ed. J. E. Truemper & B. Aschenbach, 650-657
- Alpar, M. A., Cheng, A. F., Ruderman, M. A., & Shaham, J. 1982, *Nature*, 300, 728
- Anderson, J., Sarajedini, A., Bedin, L. R., et al. 2008, *AJ*, 135, 2055
- Angeletti, L., Dolcetta, R., & Giannone, P. 1980, *Ap&SS*, 69, 45
- Arnaud, K. A. 1996, in *Astronomical Society of the Pacific Conference Series*, Vol. 101, *Astronomical Data Analysis Software and Systems V*, ed. G. H. Jacoby & J. Barnes, 17
- Arnaud, M. & Raymond, J. 1992, *ApJ*, 398, 394
- Arnaud, M. & Rothenflug, R. 1985, *A&AS*, 60, 425
- Arons, J. 2002, in *Astronomical Society of the Pacific Conference Series*, Vol. 271, *Neutron Stars in Supernova Remnants*, ed. P. O. Slane & B. M. Gaensler, 71
- Arons, J. & Tavani, M. 1993, *ApJ*, 403, 249
- Arzoumanian, Z., Fruchter, A. S., & Taylor, J. H. 1994, *ApJ*, 426, L85
- Ashman, K. M. & Zepf, S. E. 1998, *Globular cluster systems* (Cambridge University Press)
- Atoyan, A. M. & Aharonian, F. A. 1996, *A&AS*, 120, C453
- Bailes, M., Manchester, R., Kesteven, M., Norris, R., & Reynolds, J. 1990, *Mon. Not. R. Astron. Soc.*, 247, 322
- Bailyn, C. D. & Pinsonneault, M. H. 1995, *ApJ*, 439, 705
- Bassa, C., Pooley, D., Homer, L., et al. 2004, *ApJ*, 609, 755

- Bassa, C. G., Pooley, D., Verbunt, F., et al. 2008, *A&A*, 488, 921
- Becker, W. 2009, in *Astrophysics and Space Science Library*, Vol. 357, *Astrophysics and Space Science Library*, ed. W. Becker, 91–140
- Becker, W. & Aschenbach, B. 2002, in *Neutron Stars, Pulsars, and Supernova Remnants*, ed. W. Becker, H. Lesch, & J. Trümper, 64
- Becker, W. & Hui, C. Y. 2007, ArXiv: astro-ph/07050119
- Becker, W., Swartz, D. A., Pavlov, G. G., et al. 2003, *ApJ*, 594, 798
- Becker, W. & Trümper, J. 1993, *Nature*, 365, 528
- Becker, W. & Trümper, J. 1997, *A&A*, 326, 682
- Becker, W. & Trümper, J. 1999, *A&A*, 341, 803
- Bégin, S. 2006, Ph.D. thesis, University of British Columbia
- Bell, J. F., Bailes, M., Manchester, R. N., Weisberg, J. M., & Lyne, A. G. 1995, *ApJ*, 440, L81
- Benacquista, M. J. 2006, *Living Reviews in Relativity*, 9, 2
- Binney, J. & Tremaine, S. 1987, *Galactic Dynamics*, Princeton Series in Astrophysics (Princeton, U.S.A.: Princeton University Press)
- Blandford, R. & Teukolsky, S. A. 1976, *ApJ*, 205, 580
- Bogdanov, S., Grindlay, J. E., Heinke, C. O., et al. 2006, *ApJ*, 646, 1104
- Bogdanov, S., Grindlay, J. E., & van den Berg, M. 2005, *ApJ*, 630, 1029
- Brandt, W. N., Alexander, D. M., Hornschemeier, A. E., et al. 2001, *AJ*, 122, 2810
- Brown, E. F., Bildsten, L., & Rutledge, R. E. 1998, *ApJ*, 504, L95
- Buccheri, R., Bennett, K., Bignami, G. F., et al. 1983, *A&A*, 128, 245
- Burderi, L., D’Antona, F., & Burgay, M. 2002, *ApJ*, 574, 325
- Camilo, F. & Rasio, F. A. 2005, in *Astronomical Society of the Pacific Conference Series*, Vol. 328, *Binary Radio Pulsars*, ed. F. A. Rasio & I. H. Stairs, 147
- Campana, S., Stella, L., Mereghetti, S., et al. 1998, *ApJ*, 499, L65
- Canizares, C. R. & Neighbours, J. E. 1975, *ApJ*, 199, L97
- Cash, W. 1979, *ApJ*, 228, 939

- Chadwick, J. 1932, *Nature*, 129, 312
- Cheng, K. S. 2009, in *Astrophysics and Space Science Library*, Vol. 357, *Astrophysics and Space Science Library*, ed. W. Becker, 481
- Cheng, K. S., Ho, C., & Ruderman, M. 1986, *ApJ*, 300, 500
- Cheng, K. S., Taam, R. E., & Wang, W. 2004, *ApJ*, 617, 480
- Cheng, K. S., Taam, R. E., & Wang, W. 2006, *ApJ*, 641, 427
- Chernyakova, M., Neronov, A., Lutovinov, A., Rodriguez, J., & Johnston, S. 2006, *MNRAS*, 367, 1201
- Clark, G. W., Markert, T. H., & Li, F. K. 1975, *ApJ*, 199, L93
- Cocozza, G., Ferraro, F. R., Possenti, A., et al. 2008, *ApJ*, 679, L105
- Cool, A. M., Grindlay, J. E., Cohn, H. N., Lugger, P. M., & Bailyn, C. D. 1998, *ApJ*, 508, L75
- Cool, A. M., Haggard, D., & Carlin, J. L. 2002, in *Astronomical Society of the Pacific Conference Series*, Vol. 265, *Omega Centauri, A Unique Window into Astrophysics*, ed. F. van Leeuwen, J. D. Hughes, & G. Piotto, 277
- Cordes, J. & Chernoff, D. 1997, *Astrophys. J.*, 482, 971
- D'Amico, N., Lyne, A. G., Manchester, R. N., Possenti, A., & Camilo, F. 2001a, *ApJ*, 548, L171
- D'Amico, N., Possenti, A., Fici, L., et al. 2002, *ApJ*, 570, L89
- D'Amico, N., Possenti, A., Manchester, R. N., et al. 2001b, *ApJ*, 561, L89
- Danner, R., Kulkarni, S. R., Saito, Y., & Kawai, N. 1997, *Nature*, 388, 751
- Davies, M. B. 1997, *MNRAS*, 288, 117
- de Jager, O. C. & Djannati-Ataï, A. 2008, *ArXiv: astro-ph/0803.0116*
- de Jager, O. C. & Harding, A. K. 1992, *ApJ*, 396, 161
- Djorgovski, S. 1993, in *Astronomical Society of the Pacific Conference Series*, Vol. 50, *Structure and Dynamics of Globular Clusters*, ed. S. G. Djorgovski & G. Meylan, 373
- Djorgovski, S. & Meylan, G. 1994, *AJ*, 108, 1292
- Dolphin, A. E. 2000, *PASP*, 112, 1397
- Dull, J. D., Cohn, H. N., Lugger, P. M., et al. 1997, *ApJ*, 481, 267
- Duncan, R. C. & Thompson, C. 1992, *ApJ*, 392, L9

- Edmonds, P. D., Gilliland, R. L., Camilo, F., Heinke, C. O., & Grindlay, J. E. 2002a, *ApJ*, 579, 741
- Edmonds, P. D., Gilliland, R. L., Heinke, C. O., & Grindlay, J. E. 2003a, *ApJ*, 596, 1177
- Edmonds, P. D., Gilliland, R. L., Heinke, C. O., & Grindlay, J. E. 2003b, *ApJ*, 596, 1197
- Edmonds, P. D., Gilliland, R. L., Heinke, C. O., Grindlay, J. E., & Camilo, F. 2001, *ApJ*, 557, L57
- Edmonds, P. D., Heinke, C. O., Grindlay, J. E., & Gilliland, R. L. 2002b, *ApJ*, 564, L17
- Elsner, R. F., Heinke, C. O., Cohn, H. N., et al. 2008, *ApJ*, 687, 1019
- Elson, R. A. W. 1999, in *Globular Clusters*, ed. C. Martínez Roger, I. Perez Fournón, & F. Sánchez, 209–248
- Eracleous, M., Halpern, J., & Patterson, J. 1991, *ApJ*, 382, 290
- Faucher-Giguère, C.-A. & Kaspi, V. 2006, *Astrophys. J.*, 643, 332
- Ferraro, F. R., Paltrinieri, B., Rood, R. T., Fusi Pecci, F., & Buonanno, R. 2000, *ApJ*, 537, 312
- Ferraro, F. R., Possenti, A., D'Amico, N., & Sabbi, E. 2001, *ApJ*, 561, L93
- Fomalont, E., Goss, W., Lyne, A., Manchester, R., & Justtanont, K. 1992, *Mon. Not. R. Astron. Soc.*, 258, 497
- Frail, D. A. & Scharringhausen, B. R. 1997, *ApJ*, 480, 364
- Fregeau, J. M. 2008, *ApJ*, 673, L25
- Fregeau, J. M. & Rasio, F. A. 2007, *ApJ*, 658, 1047
- Freire, P. C., Gupta, Y., Ransom, S. M., & Ishwara-Chandra, C. H. 2004, *ApJ*, 606, L53
- Freire, P. C. C. 2005, in *Astronomical Society of the Pacific Conference Series*, Vol. 328, *Binary Radio Pulsars*, ed. F. A. Rasio & I. H. Stairs, 405
- Freire, P. C. C., Ransom, S. M., Bégin, S., et al. 2008, *ApJ*, 675, 670
- Fruchter, A. S., Gunn, J. E., Lauer, T. R., & Dressler, A. 1988a, *Nature*, 334, 686
- Fruchter, A. S., Stinebring, D. R., & Taylor, J. H. 1988b, *Nature*, 333, 237
- Gaensler, B. M. & Slane, P. O. 2006, *ARA&A*, 44, 17
- Gaensler, B. M., Stappers, B. W., Frail, D. A., et al. 2000, *MNRAS*, 318, 58

- Gallant, Y. A., Jacholkowska, A., Khélifi, B., et al. 2006, in COSPAR, Plenary Meeting, Vol. 36, 36th COSPAR Scientific Assembly, 3306
- Gao, B., Goodman, J., Cohn, H., & Murphy, B. 1991, *ApJ*, 370, 567
- Gehrels, N. 1986, *ApJ*, 303, 336
- Gendre, B., Barret, D., & Webb, N. A. 2003, *A&A*, 400, 521
- Giacconi, R., Murray, S., Gursky, H., et al. 1972, *ApJ*, 178, 281
- Giersz, M. & Heggie, D. C. 2003, *MNRAS*, 339, 486
- Gil, J. & Krawczyk, A. 1996, *MNRAS*, 280, 143
- Gnedin, O. & Ostriker, J. 1997, *ApJ*, 474, 223
- Gold, T. 1968, *Nature*, 218, 731
- Goldreich, P. & Julian, W. H. 1969, *ApJ*, 157, 869
- Goodman, J. & Hut, P. 1989, *Nature*, 339, 40
- Gotthelf, E. V. 2003, *ApJ*, 591, 361
- Grabhorn, R. P., Cohn, H. N., Lugger, P. M., & Murphy, B. W. 1992, *ApJ*, 392, 86
- Greenstein, G. & Hartke, G. J. 1983, *ApJ*, 271, 283
- Grindlay, J. E., Camilo, F., Heinke, C. O., et al. 2002, *ApJ*, 581, 470
- Grindlay, J. E., Heinke, C., Edmonds, P. D., & Murray, S. S. 2001a, *Science*, 292, 2290
- Grindlay, J. E., Heinke, C. O., Edmonds, P. D., Murray, S. S., & Cool, A. M. 2001b, *ApJ*, 563, L53
- Grindlay, J. E., Hertz, P., Steiner, J. E., Murray, S. S., & Lightman, A. P. 1984, *ApJ*, 282, L13
- Harding, A. K. 2009, in *Astrophysics and Space Science Library*, Vol. 357, *Astrophysics and Space Science Library*, ed. W. Becker, 521
- Harding, A. K. & Muslimov, A. G. 2002, *ApJ*, 568, 862
- Harris, W. E. 1996, *AJ*, 112, 1487
- Harrison, P., Lyne, A., & Anderson, B. 1993, *Mon. Not. R. Astron. Soc.*, 261, 113
- Hayakawa, S. & Matsuoka, M. 1964, *Progress of Theoretical Physics Supplement*, 30, 204

- Heggie, D. & Hut, P. 2003, *The Gravitational Million-Body Problem: A Multidisciplinary Approach to Star Cluster Dynamics*, ed. D. Heggie & P. Hut (Cambridge University Press, 2003, 372 pp.)
- Heinke, C. O., Grindlay, J. E., Edmonds, P. D., et al. 2005, *ApJ*, 625, 796
- Heinke, C. O., Grindlay, J. E., Lugger, P. M., et al. 2003, *ApJ*, 598, 501
- Heinke, C. O., Wijnands, R., Cohn, H. N., et al. 2006, *ApJ*, 651, 1098
- Hertz, P. & Grindlay, J. E. 1983, *ApJ*, 275, 105
- Hessels, J. W. T., Ransom, S. M., Stairs, I. H., Kaspi, V. M., & Freire, P. C. C. 2007, *ApJ*, 670, 363
- Hewish, A., Bell, S. J., Pilkington, J. D. H., Scott, P. F., & Collins, R. A. 1968, *Nature*, 217, 709
- Heyer, I., Biretta, J., Brammer, G., et al. 2004, *WFPC2 Instrument Handbook, Version 9.0* (Baltimore: STScI).
- Hobbs, G., Lorimer, D., Lyne, A., & Kramer, M. 2005, *MNRAS*, 360, 974
- Høg, E., Fabricius, C., Makarov, V. V., et al. 2000, *A&A*, 355, L27
- Holtzman, J. A., Burrows, C. J., Casertano, S., et al. 1995, *PASP*, 107, 1065
- Horns, D., Aharonian, F., Santangelo, A., Hoffmann, A. I. D., & Masterson, C. 2006, *A&A*, 451, L51
- Hoyle, F., Narlikar, J. V., & Wheeler, J. A. 1964, *Nature*, 203, 914
- Huang, H. H. & Becker, W. 2007, *A&A*, 463, L5
- Huang, R. H. H. & Becker, W. 2009, *ArXiv: astro-ph/0910.2049*
- Huang, R. H. H. & Becker, W. 2010, *A&A*, 510, A67
- Hui, C. Y. & Becker, W. 2006, *A&A*, 448, L13
- Hurley, J. R., Aarseth, S. J., & Shara, M. M. 2007, *ApJ*, 665, 707
- Hurley, J. R., Pols, O. R., Aarseth, S. J., & Tout, C. A. 2005, *MNRAS*, 363, 293
- Hut, P., McMillan, S., Goodman, J., et al. 1992, *PASP*, 104, 981
- Hut, P., Murphy, B. W., & Verbunt, F. 1991, *A&A*, 241, 137
- in't Zand, J. J. M., Hulleman, F., Markwardt, C. B., et al. 2003, *A&A*, 406, 233

- Ivanova, N., Fregeau, J. M., & Rasio, F. A. 2005, in *Astronomical Society of the Pacific Conference Series*, Vol. 328, *Binary Radio Pulsars*, ed. F. A. Rasio & I. H. Stairs, 231
- Ivanova, N., Heinke, C. O., Rasio, F. A., Belczynski, K., & Fregeau, J. M. 2008, *MNRAS*, 386, 553
- Ivanova, N., Heinke, C. O., Rasio, F. A., et al. 2006, *MNRAS*, 372, 1043
- Johnston, H. M. & Verbunt, F. 1996, *A&A*, 312, 80
- Johnston, S., Hobbs, G., Vigeland, S., et al. 2005, *MNRAS*, 364, 1397
- Johnston, S., Kramer, M., Karastergiou, A., et al. 2007, *MNRAS*, 381, 1625
- Kargaltsev, O. & Pavlov, G. G. 2007, *ApJ*, 670, 655
- Kaspi, V. M., Manchester, R. N., Siegman, B., Johnston, S., & Lyne, A. G. 1994, *ApJ*, 422, L83
- Kaspi, V. M., Roberts, M. S. E., & Harding, A. K. 2006, in *Compact stellar X-ray sources*. Cambridge Astrophysics Series, No. 39, ed. W. H. G. Lewin & M. van der Klis, 279–339
- Katz, J. I. 1975, *Nature*, 253, 698
- Kawai, N. & Saito, Y. 1999, *Astrophysical Letters Communications*, 38, 1
- Kennel, C. F. & Coroniti, F. V. 1984, *ApJ*, 283, 694
- King, I. 1962, *AJ*, 67, 471
- King, I. R. 1966a, in *IAU Symposium*, Vol. 25, *The Theory of Orbits in the Solar System and in Stellar Systems*, ed. G. I. Kontopoulos, 51
- King, I. R. 1966b, *AJ*, 71, 64
- King, I. R. 1966c, *AJ*, 71, 276
- Koekemoer, A. M., Fruchter, A. S., Hook, R. N., & Hack, W. 2002, in *The 2002 HST Calibration Workshop : Hubble after the Installation of the ACS and the NICMOS Cooling System*, ed. S. Arribas, A. Koekemoer, & B. Whitmore, 337
- Kong, A. K. H., Bassa, C., Pooley, D., et al. 2006, *ApJ*, 647, 1065
- Krauss, L. M. & Chaboyer, B. 2003, *Science*, 299, 65
- Krautter, J., Zickgraf, F.-J., Appenzeller, I., et al. 1999, *A&A*, 350, 743
- Krongold, Y., Dultzin-Hacyan, D., & Marziani, P. 2001, *AJ*, 121, 702
- Kulkarni, S. R. & Hester, J. J. 1988, *Nature*, 335, 801

- Kulkarni, S. R., Phinney, E. S., Evans, C. R., & Hasinger, G. 1992, *Nature*, 359, 300
- Kundt, W. & Schaaf, R. 1993, *Ap&SS*, 200, 251
- Lai, D., Chernoff, D. F., & Cordes, J. M. 2001, *ApJ*, 549, 1111
- Lee, H. M. 2002, in *IAU Symposium*, Vol. 207, *Extragalactic Star Clusters*, ed. D. P. Geisler, E. K. Grebel, & D. Minniti, 584
- Liedahl, D. A., Osterheld, A. L., & Goldstein, W. H. 1995, *ApJ*, 438, L115
- Liu, Q. Z., van Paradijs, J., & van den Heuvel, E. P. J. 2001, *A&A*, 368, 1021
- Lorimer, D. 1995, *MNRAS*, 274, 300
- Lugger, P. M., Cohn, H. N., & Grindlay, J. E. 1995, *ApJ*, 439, 191
- Lugger, P. M., Cohn, H. N., Heinke, C. O., Grindlay, J. E., & Edmonds, P. D. 2007, *ApJ*, 657, 286
- Lyne, A., Anderson, B., & Salter, M. 1982, *Mon. Not. R. Astron. Soc.*, 201, 503
- Lyne, A. & Lorimer, D. 1994, *Nature*, 369, 127
- Lyne, A., Manchester, R., Lorimer, D., et al. 1998, *MNRAS*, 295, 743
- Lyne, A. G., Brinklow, A., Middleditch, J., Kulkarni, S. R., & Backer, D. C. 1987, *Nature*, 328, 399
- Lyne, A. G., Pritchard, R. S., & Smith, F. G. 1988, *MNRAS*, 233, 667
- Manchester, R. N., Hobbs, G. B., Teoh, A., & Hobbs, M. 2005, *AJ*, 129, 1993
- Manchester, R. N. & Taylor, J. H. 1977, *Pulsars.*, ed. Smith, F. G.
- Mardling, R. A. 1995a, *ApJ*, 450, 722
- Mardling, R. A. 1995b, *ApJ*, 450, 732
- Mewe, R., Gronenschild, E. H. B. M., & van den Oord, G. H. J. 1985, *A&AS*, 62, 197
- Mewe, R., Lemen, J. R., & van den Oord, G. H. J. 1986, *A&AS*, 65, 511
- Mineo, T., Cusumano, G., Massaro, E., Becker, W., & Nicastro, L. 2004, *A&A*, 423, 1045
- Monet, D. G., Levine, S. E., Canzian, B., et al. 2003, *AJ*, 125, 984
- Mukai, K. 2003, *Advances in Space Research*, 32, 2067

- Nice, D., Sayer, R., & Taylor, J. 1999, in *Pulsar Timing, General Relativity, and the Internal Structure of Neutron Stars*, ed. Z. Arzoumanian, F. van der Hooft, & E. van den Heuvel (Amsterdam, Netherlands: Royal Netherlands Academy of Arts and Sciences), 79–83
- Orosz, J. A. & van Kerkwijk, M. H. 2003, *A&A*, 397, 237
- Ostriker, J. P. & Gunn, J. E. 1969, *ApJ*, 157, 1395
- Ostriker, J. P., Spitzer, Jr., L., & Chevalier, R. A. 1972, *ApJ*, 176, L51
- Pacini, F. 1967, *Nature*, 216, 567
- Pacini, F. & Salvati, M. 1973, *ApJ*, 186, 249
- Padmanabhan, T. 2000, *Theoretical Astrophysics, Volume I: Astrophysical Processes* (Cambridge, U.K.; New York, U.S.A.: Cambridge University Press)
- Pallavicini, R., Golub, L., Rosner, R., et al. 1981, *ApJ*, 248, 279
- Panzera, M. R., Campana, S., Covino, S., et al. 2003, *A&A*, 399, 351
- Pavlov, G. G., Shibano, Y. A., Ventura, J., & Zavlin, V. E. 1994, *A&A*, 289, 837
- Pavlov, G. G., Shibano, Y. A., Zavlin, V. E., & Meyer, R. D. 1995, in *The Lives of the Neutron Stars*, ed. M. A. Alpar, U. Kiziloglu, & J. van Paradijs, 71
- Piotto, G., King, I. R., Djorgovski, S. G., et al. 2002, *A&A*, 391, 945
- Pooley, D. & Hut, P. 2006, *ApJ*, 646, L143
- Pooley, D., Lewin, W. H. G., Anderson, S. F., et al. 2003, *ApJ*, 591, L131
- Pooley, D., Lewin, W. H. G., Homer, L., et al. 2002, *ApJ*, 569, 405
- Possenti, A., D’Amico, N., Corongiu, A., et al. 2005, in *Astronomical Society of the Pacific Conference Series, Vol. 328, Binary Radio Pulsars*, ed. F. A. Rasio & I. H. Stairs, 189
- Predehl, P. & Schmitt, J. H. M. M. 1995, *A&A*, 293, 889
- Radhakrishnan, V. & Srinivasan, G. 1982, *Current Science*, 51, 1096
- Randich, S. 1997, *Memorie della Societa Astronomica Italiana*, 68, 971
- Rankin, J. 2007, *ApJ*, 664, 443
- Ransom, S., Hessels, J., Stairs, I., et al. 2005, in *Astronomical Society of the Pacific Conference Series, Vol. 328, Binary Radio Pulsars*, ed. F. A. Rasio & I. H. Stairs, 199

- Ransom, S. M. 2008, in American Institute of Physics Conference Series, Vol. 983, 40 Years of Pulsars: Millisecond Pulsars, Magnetars and More, ed. C. Bassa, Z. Wang, A. Cumming, & V. M. Kaspi, 415–423
- Ransom, S. M., Hessels, J. W. T., Stairs, I. H., et al. 2003, in Astronomical Society of the Pacific Conference Series, Vol. 302, Radio Pulsars, ed. M. Bailes, D. J. Nice, & S. E. Thorsett, 371
- Ransom, S. M., Stairs, I. H., Backer, D. C., et al. 2004, *ApJ*, 604, 328
- Rasio, F. A., Pfahl, E. D., & Rappaport, S. 2000, *ApJ*, 532, L47
- Rasio, F. A., Shapiro, S. L., & Teukolsky, S. A. 1989, *ApJ*, 342, 934
- Rees, M. J. & Gunn, J. E. 1974, *MNRAS*, 167, 1
- Reid, I. N. 1997, *AJ*, 114, 161
- Reynolds, S. P. & Chevalier, R. A. 1984, *ApJ*, 278, 630
- Richer, H. B., Brewer, J., Fahlman, G. G., et al. 2002, *ApJ*, 574, L151
- Rieke, G. H. & Lebofsky, M. J. 1985, *ApJ*, 288, 618
- Romani, R. W. 1987, *ApJ*, 313, 718
- Ruderman, M. 1989, in *Timing Neutron Stars*, ed. H. Ögelman & E. P. J. van den Heuvel, 329
- Ruderman, M. A. & Sutherland, P. G. 1975, *ApJ*, 196, 51
- Rutledge, R. E., Bildsten, L., Brown, E. F., Pavlov, G. G., & Zavlin, V. E. 2003, in *Bulletin of the American Astronomical Society*, Vol. 35, *Bulletin of the American Astronomical Society*, 655
- Rutledge, R. E., Fox, D. W., Kulkarni, S. R., et al. 2004, *ApJ*, 613, 522
- Sabbi, E., Gratton, R. G., Bragaglia, A., et al. 2003, *A&A*, 412, 829
- Saito, Y., Kawai, N., Kamae, T., et al. 1997, *ApJ*, 477, L37
- Seaton, M. J. 1979, *MNRAS*, 187, 73P
- Shapley, H. 1918, *ApJ*, 48, 154
- Shklovskii, I. 1970, *Sov. Astron.*, 13, 562
- Sirianni, M., Jee, M. J., Benítez, N., et al. 2005, *PASP*, 117, 1049
- Skrutskie, M. F., Cutri, R. M., Stiening, R., et al. 2006, *AJ*, 131, 1163
- Smits, R., Kramer, M., Stappers, B., et al. 2008, *ArXiv: astro-ph/0811.0211*

- Snedden, C. & Cowan, J. J. 2003, *Science*, 299, 70
- Spitzer, L. 1987, *Dynamical evolution of globular clusters*, ed. L. Spitzer (Princeton, NJ, Princeton University Press, 1987, 191 p.)
- Spitzer, Jr., L. 1984, *Science*, 225, 465
- Stappers, B. W., Gaensler, B. M., Kaspi, V. M., van der Klis, M., & Lewin, W. H. G. 2003, *Science*, 299, 1372
- Stella, L., Campana, S., Colpi, M., Mereghetti, S., & Tavani, M. 1994, *ApJ*, 423, L47
- Sturrock, P. A. 1971, *ApJ*, 164, 529
- Tavani, M. & Arons, J. 1997, *ApJ*, 477, 439
- Taylor, J. H. & Cordes, J. M. 1993, *ApJ*, 411, 674
- Taylor, J. M., Grindlay, J. E., Edmonds, P. D., & Cool, A. M. 2001, *ApJ*, 553, L169
- Tennant, A. F. 2006, *AJ*, 132, 1372
- Trepl, L. 2007, LMU Diploma Thesis
- Trimble, V. 1968, *Astrophys. J.*, 73, 535
- van den Berg, M., Tagliaferri, G., Belloni, T., & Verbunt, F. 2004, *A&A*, 418, 509
- van Paradijs, J., Allington-Smith, J., Callanan, P., et al. 1988, *Nature*, 334, 684
- Verbunt, F. 1993, *ARA&A*, 31, 93
- Verbunt, F. 2001, *A&A*, 368, 137
- Verbunt, F. 2002, in *Astronomical Society of the Pacific Conference Series*, Vol. 265, *Omega Centauri, A Unique Window into Astrophysics*, ed. F. van Leeuwen, J. D. Hughes, & G. Piotto, 289
- Verbunt, F. 2003, in *Astronomical Society of the Pacific Conference Series*, Vol. 308, *From X-ray Binaries to Gamma-Ray Bursts: Jan van Paradijs Memorial Symposium*, ed. E. P. van den Heuvel, L. Kaper, E. Rol, & R. A. M. J. Wijers, 201
- Verbunt, F. & Hut, P. 1987, in *IAU Symposium*, Vol. 125, *The Origin and Evolution of Neutron Stars*, ed. D. J. Helfand & J.-H. Huang, 187
- Verbunt, F. & Johnston, H. M. 2000, *A&A*, 358, 910
- Verbunt, F. & Lewin, W. H. G. 2004, ArXiv: astro-ph/0404136
- Verbunt, F. & Lewin, W. H. G. 2006, in *Compact stellar X-ray sources*, 341–379

- Verbunt, F., Pooley, D., & Bassa, C. 2008, in IAU Symposium, Vol. 246, Dynamical Evolution of Dense Stellar Systems, 301–310
- White, N. E. & Angelini, L. 2001, ApJ, 561, L101
- White, N. E., Giommi, P., & Angelini, L. 1994, in Bulletin of the American Astronomical Society, Vol. 26, Bulletin of the American Astronomical Society, 1372
- Zavlin, V. E. 2006, ApJ, 638, 951
- Zavlin, V. E. 2007, Ap&SS, 308, 297
- Zavlin, V. E., Pavlov, G. G., & Shibanov, Y. A. 1996, A&A, 315, 141
- Zavlin, V. E., Pavlov, G. G., Shibanov, Y. A., & Ventura, J. 1995, A&A, 297, 441
- Zeldovich, Y. B. & Guseynov, O. H. 1966, ApJ, 144, 840
- Zhang, L. & Cheng, K. S. 2003, A&A, 398, 639
- Zhang, W., Marshall, F. E., Gotthelf, E. V., Middleditch, J., & Wang, Q. D. 2001, ApJ, 554, L177
- Zou, W., Hobbs, G., Wang, N., et al. 2005, MNRAS, 362, 1189

# Acknowledgements

I would like to take this opportunity to thank these people who help me a lot during my PhD study. The first person I would like to thank is my research supervisor, Prof. Dr. Werner Becker. Without his patience and continuous guidance, I could not accomplish my PhD thesis. I would also like to thank my second supervisor, PD Dr. Markus Kissler-Patig, for giving me some useful suggestions to improve my thesis. Acknowledgements would also be given to Mrs. Christa Ingram and Mrs. Gabriele Kratschmann for helping me in every aspect of my life.

I cannot end without thanking my parents. Their continuous love and encouragement support me to overcome many difficulties. I would also like to thank them for providing me the final support so I can concentrate on my work.



# Curriculum Vitae

## Hsiu-Hui (Regina) Huang

Date of birth: 08 February 1980

Place of birth: Taiwan

Citizenship: Taiwan

Gender: Female

### Education

Institution	From	To	Subject	Qualifications
Ludwig-Maximilians-Universität (LMU) Munich, Germany	2005	2010	Physics	PhD (Dr. rer. nat.)
National Tsing Hua University (NTHU), Taiwan	2002	2004	Physics	Master of Science
National Tsing Hua University (NTHU), Taiwan	1998	2002	Physics	Bachelor of Science

### Honors & Awards

The International Max-Planck Research School (IMPRS) Fellowship	2005–2008
Marie Curie Host Fellowship For Early Stage Research Training (EST)	2005–2006
The Academic Achievement Award	2001, 2002
Cathay Life Insurance Co. Scholarship	2002
Ma Shang-Geng Memorial Scholarship	2001
Taipei Mayors Prize	1998